

Carbon nanosheets and their applications

Inaugural-Dissertation

zur

Erlangung der Doktorwürde

der Fakultät für Physik

der Universität Bielefeld

vorgelegt von

Dipl. Chem.

Christoph Thilo Nottbohm

aus Heidelberg

Bielefeld, August 2009

Gutachter: Prof. Dr. Armin Gölzhäuser

Prof. Dr. Andreas Hütten

Hiermit erkläre ich an Eides statt, dass ich die vorliegende Arbeit selbständig und ohne unerlaubte Hilfsmittel durchgeführt habe.

Bielefeld,

Abstract

Carbon nanosheets are a new kind of two-dimensional polymeric material that is fabricated by cross-linking aromatic self-assembled monolayers with electrons. Due to their uniform thickness of only about one nanometer, as well as their high chemical, mechanical, and thermal stability, such materials are of high interest for a wide variety of applications. Carbon nanosheets can be released from their original substrate and transferred to arbitrary new substrates. When placed on oxidized silicon wafers, nanosheets can be seen by the naked eye. Folds appear to be darker and blue shifted with respect to the substrate color. This effect was systematically studied for multilayer stacks of nanosheet by means of UV/Vis reflection spectroscopy and simulation. The oxide layer acts as an optical spacer, similar to an interferometer. Thus, the contrast was found to be dependent on the wavelength of light as well as the thickness of the oxide layer.

On perforated substrates such as transmission electron microscopy (TEM) grids, large freestanding membranes with the thickness of one monolayer were obtained with an aspect ratio of up to 1:225000. This way, for the first time, the bottom side of the nanosheet became accessible for functionalization, and it was possible to selectively couple fluorescent dyes to the nanosheet; this highlights the versatility of the nanosheets. Freestanding nanosheets have been used as sample supports to image nanoparticles by TEM. Due to the thickness of the nanosheets, the nanoparticles can be observed in intricate detail, with only minimal background from the nanosheet as compared to conventional carbon films. Also, the individual layers of multi-walled carbon nanotubes (MWNT) were resolved. In scanning TEM even single gold atoms were observed.

It is possible to deposit more than just nanoparticles onto freestanding nanosheets. The sheets can also be metalized in a variety of different ways either before transfer or afterwards; this was demonstrated by fabricating gold patterns onto freestanding nanosheets. As the nanosheet is stable under an electron beam, patterns can also be written by electron beam induced deposition (EBID).

By annealing nanosheets in ultra high vacuum their conductivity can be adjusted flexibly. This is due to a gradual transition to a graphitic phase that reaches a sheet resistivity of only $\approx 100 \text{ k}\Omega/\text{sq}$ at $\approx 1200 \text{ K}$. The structural changes that are associated with this transition are reflected in the TEM and Raman data. For multilayer stacks it was also possible to observe the transition to graphite by means of UV/Vis spectroscopy.

Because of their stability and flexibility, carbon nanosheets will likely find a multitude of applications, including potential use as sensors, filtration membranes, sample supports, and even conductive coatings.

Table of contents

Abstract.....	I
Table of contents	III
1 Introduction	1
2 Basics.....	5
2.1 Self-assembled monolayers	5
2.1.1 Interaction with electrons.....	6
2.2 X-ray photoelectron spectroscopy (XPS).....	7
2.2.1 Quantification	9
2.3 Electron microscopy.....	9
2.3.1 TEM	9
2.3.2 SEM	10
2.4 Atomic force microscopy (AFM).....	11
2.5 Optical Properties of thin films	13
2.5.1 Thin film interference	13
2.5.2 Fresnel's equations	14
2.5.3 Matrix method for multilayered systems	15
2.6 Fluorescence microscopy	20
2.7 Contact angle.....	20
2.8 Photolithography.....	21
2.8.1 Chemistry of photoresists.....	22
2.9 Supercritical drying.....	23
3 Materials and Methods.....	25
3.1 SAM preparation	25
3.1.1 Silane-SAMs.....	25
3.1.2 Thiol-SAMs	25
3.2 Transfer of cross-linked SAMs.....	26

3.2.1	Transfer medium	26
3.2.2	Release from substrate	26
3.2.3	Removal of transfer medium	27
3.3	Patterning of nanosheets	27
3.3.1	Photolithography.....	27
3.3.2	Plasma etching	28
3.3.3	Preparation of PDMS stamps	28
3.3.4	UV/ozone patterning.....	28
3.4	TEM sample supports	28
3.4.1	Cobalt nanoparticles	28
3.4.2	Gold nanoclusters.....	29
3.5	Metallization of nanosheets.....	30
3.6	Functionalization of nanosheets	30
3.6.1	Amino terminus.....	30
3.6.2	Thiol terminus	30
3.7	Annealing.....	30
3.8	Raman.....	31
3.9	Electrical measurements	31
3.10	X-ray photoelectron spectroscopy.....	31
3.11	Microscopy.....	31
4	Results and Discussion	33
4.1	Transfer.....	33
4.1.1	Transfer of silane based nanosheets.....	35
4.1.2	Freestanding nanosheets on conventional TEM grids.....	39
4.1.3	Transfer of thiol-based nanosheets	42
4.1.4	Critical Point Dryer	45

4.1.5	Summary	47
4.2	Asymmetric functionalization of nanosheets – Janus membranes	49
4.2.1	Modification of the Amino-terminus.....	50
4.2.2	Modification of the thiol group	52
4.2.3	Doubly labeled nanosheets.....	54
4.2.4	Summary	58
4.3	Patterning nanosheets	59
4.3.1	Irradiation through a shadow mask (proximity printing)	60
4.3.2	EUV-IL.....	62
4.3.3	Plasma etching	66
4.3.4	UV/ozon	71
4.3.5	Summary	78
4.4	Nanosheet multilayers	81
4.4.1	Structured nanosheet multilayers	82
4.4.2	XPS evaluation of multilayer samples.....	83
4.4.3	Optical Properties	86
4.4.4	Optical Properties of freestanding nanosheets.....	96
4.4.5	Summary	98
4.5	Nanosheets as TEM sample supports	99
4.5.1	Cobalt nanoparticles	100
4.5.2	Gold nanoclusters	104
4.5.3	Summary	108
4.6	Metallization of freestanding nanosheets	109
4.6.1	Underetching of metallized nanosheets.....	109
4.6.2	Transfer of metallized nanosheets	110
4.6.3	Evaporation onto freestanding nanosheets	111

4.6.4	Direct writing by electron beam induced deposition (EBID)	112
4.6.5	Summary	113
4.7	Annealing experiments.....	114
4.7.1	XPS and scanning Auger microscopy.....	116
4.7.2	Electrical properties	118
4.7.3	Raman.....	121
4.7.4	TEM.....	122
4.7.5	Outlook and Conclusion	123
4.8	Annealing experiments on multilayers.....	125
4.8.1	XPS evaluation	126
4.8.2	Raman.....	129
4.8.3	Optical Properties.....	130
4.8.4	Electrical properties	137
4.8.5	Summary	141
5	Conclusion and Outlook	143
6	References.....	149
7	Publikations	159
8	Abbreviations	161
9	List of Figures.....	163
10	Acknowledgements.....	175

1 Introduction

In the last 50 years technology has advanced to produce increasingly sophisticated devices. This development goes hand-in-hand with the miniaturization of those devices; for instance, Moore described that the number of transistors per computer chip doubles every two years [1]. Also, accelerometers and microphones have reached a size that makes it possible to integrate them into ever smaller chips, i.e. for cell phones. The driving force for this miniaturization is the reduction of cost, weight and size as well as power and resource consumption together with increased performance.

Two-dimensional (2D) materials with a thickness of only one molecule (or atom) represent the ultimate limit in miniaturization for membranes and foils. In a recent review about 2D-materials Schlüter et al. ask: “Can one hang them up on a rope for drying like laundry or feel them with ones fingers? Can one see them with the naked eye?” [2]. These questions address the unknown physical properties of such thin materials, namely their mechanical stability and optical properties. Despite these fundamental scientific questions, such materials are interesting for a wide variety of applications. They can be used as: (i) membranes for filtration or separation of gases. Material flow through a membrane is limited by the thickness of the membrane. Membranes of molecular thickness with a precisely controlled pore size can thus lead to higher throughput. (ii) These materials can also be utilized as (pressure) sensors. Due to their thickness the sensitivity of (pressure) sensors can be increased while at the same time decreasing their size, i.e. for lab-on-a-chip applications. Such sensors should also be extremely sensitive to the binding of molecular adsorbates. (iii) It is also possible to use 2D materials to modify the surface properties of other materials, such as resistance to corrosion, adhesion, friction, etc. (iv) Finally, these materials might be useful for the synthesis of new layered materials by stacking of multiple 2D-layers.

Since the work of Agnes Pockels in the 1890s, it is known that molecularly thin films can be prepared on the surface of water [3]. The boundary between the water and the air confines the space to two dimensions. Langmuir [4] and Blodgett [5] discovered that such films (later called Langmuir-Blodgett- or LB-films) could also be transferred to a solid substrate by simply pulling it out of the water through the film. The biggest problem with LB-films is that they are only held together by weak forces. Their stability,

however, can be enhanced by cross-linking, which was first described by Gee as early as 1935 [6, 7]. Such mechanically enhanced LB-films have been studied intensely for the fabrication of nanoporous membranes [2, 8].

Not only liquid interfaces, but also surfaces of solids are able to provide a template for the formation of 2D-materials. Self-assembled monolayers (SAMs) have been used to coat a variety of materials [9] and have found wide use for the modification of surface properties. Like LB-films they are held together only by weak interactions of the molecules, so that they must be cross-linked for enhancement of their stability. This can be achieved for example by irradiation with electrons [10]. In contrast to the LB-films though, it has not been possible so far to transfer them to new substrates. In this work a method was developed to release cross-linked SAMs (nanosheets) from their original substrate and transfer them to arbitrary new substrates; this could also have general implications on 2D materials that are prepared on solid supports by different methods.

The transfer procedure is described in detail for two classes of SAMs on different substrates in chapter 4.1. A special emphasis is put on the preparation of freestanding nanosheets that span over the holes of transmission electron microscopy (TEM) grids.

Due to the amphiphilic nature of the molecules in the SAM, the nanosheets inherently have two chemically different surfaces. In chapter 4.2 both sides were labeled separately by different fluorescent dyes to show that functionalization of both sides is feasible. Due to their asymmetry, such “Janus”-membranes could be efficacious for use in biomimetic ion pumps.

In the following chapter (4.3) strategies for creating and transferring patterned nanosheets are explored. For example, nanosheets with regular hole patterns can be fabricated that might find applications in filtration and separation.

It is peculiar that the nanosheets can be seen by the naked eye, if they are transferred to an oxidized silicon wafer with a defined oxide thickness. This effect is discussed in chapter 4.4 together with the preparation of multilayer stacks.

A first application for freestanding nanosheets is presented in chapter 4.5. Due to their thickness they are ideal as sample supports for the characterization of nano-sized

clusters in TEM. A strongly enhanced contrast could be observed for cobalt nanoparticles and gold nanoclusters as compared to conventional support films.

Due to their thickness, nanosheets are very interesting as a transparent support for novel optical components as well as membranes for micro-electromechanical systems (MEMS). To this end, it is necessary to have a means to fabricate metal structures on top of the nanosheet membranes. Different strategies to achieve such structures are discussed in chapter 4.6.

A different approach is to transform the nanosheets into a conducting state by annealing in vacuum. This method is well known for the production of highly oriented pyrolytic graphite (HOPG) from organic precursors. The results presented in chapter 4.7 show that by changing the annealing temperature, the conductivity of the nanosheets can be tuned over several orders of magnitude. As the nanosheets are only 1 nm thick, this could lead to a new route for the fabrication of graphene, a single layer of graphite. Graphene shows very interesting electrical properties, which make it a candidate for future microelectronics applications.

In chapter 4.8 the effect of annealing on multilayer stacks of nanosheet is examined. The changes in the optical properties are discussed with the help of simulations, and a model was developed to explain the differences in conductivity between layers of different thickness.

2 Basics

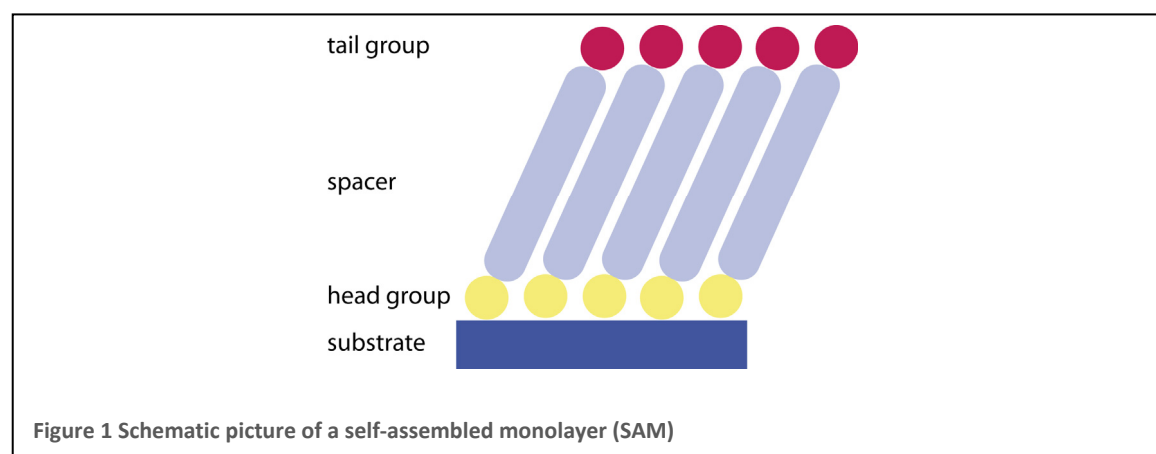
2.1 Self-assembled monolayers

Self-assembled monolayers (SAMs) are two-dimensional systems of organic molecules that spontaneously form into well ordered molecular films on a variety of solid surfaces. This phenomenon was first discovered in the beginning of the 1980's, when Sagiv [11] studied silane films on SiO_2 and Nuzzo and Allara [12] thiols on gold substrates. Since then SAMs have been the topic of intense research in diverse fields ranging from molecular electronics and materials science to biology [9].

Schematically, a SAM can be described by three parts: (i) a headgroup that is binding to the substrate, (ii) a spacer and (iii) a tail group. Thiol headgroups for example can bind to a variety of coinage metals, with gold being the most widely used due to its inertness. With a binding energy of ≈ 120 kJ/mol the interaction between the thiol and the gold is considered a chemisorption. A variety of different surfaces from metals to oxides can be functionalized by choosing a suitable headgroup. The intermolecular interactions are depending on the nature of the spacer. SAMs with non-polar spacers, such as alkane chains or phenyl rings, are stabilized by van-der-Waals forces. For alkane thiols it was found that the speed of self-organization increases with increasing chain length.

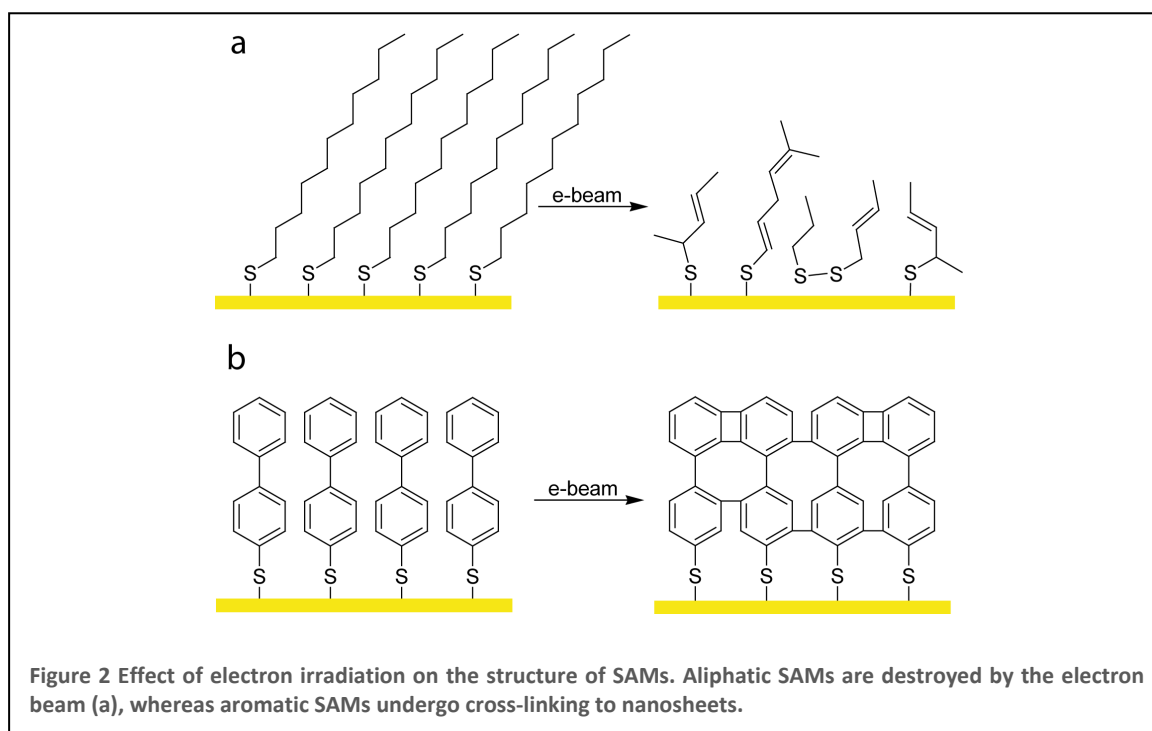
The tail group is responsible for the surface properties such as wettability, adhesion, friction and others. As an example, a carboxylic acid tail group yields a hydrophilic surface, whereas a hydrophobic coating can be achieved by a methyl tail group.

For a more detailed description of the properties of SAMs the reader is referred to the reviews by Ulman [13, 14], Schreiber [15] and Love [9].



2.1.1 Interaction with electrons

Irradiation of alkanethiol SAMs with electrons results in the destruction of the SAM, which is shown schematically in Figure 2a. Some of the associated processes are dehydrogenation, desorption and a loss of order [16-18]. These properties can be used by structured electron irradiation to generate templates for etching or electrochemical

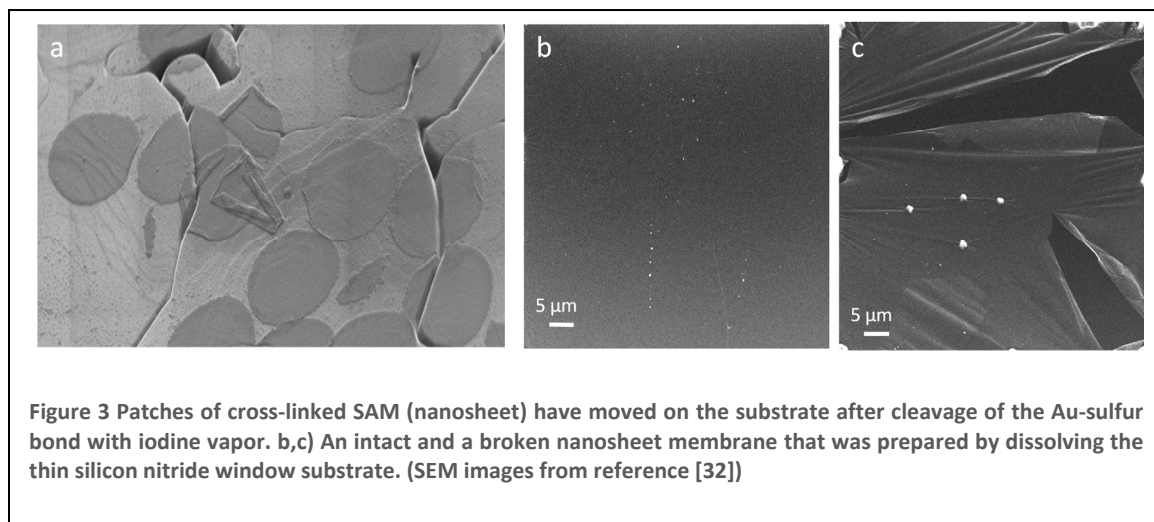


metal deposition [19-22].

Aromatic SAMs on the other hand are reacting opposite to electron irradiation. Here, a cross-linking of the aromatic rings can be observed, which renders the SAM more stable (Figure 2b) [10, 23, 24]. It is claimed by Tai et al. that the cross-linking is inhomogeneous and more pronounced at the SAM-ambient interface [25]. In addition, due to the release of hydrogen during electron irradiation, terminal nitro groups are reduced to amino groups. This has been termed “chemical lithography” [26, 27].

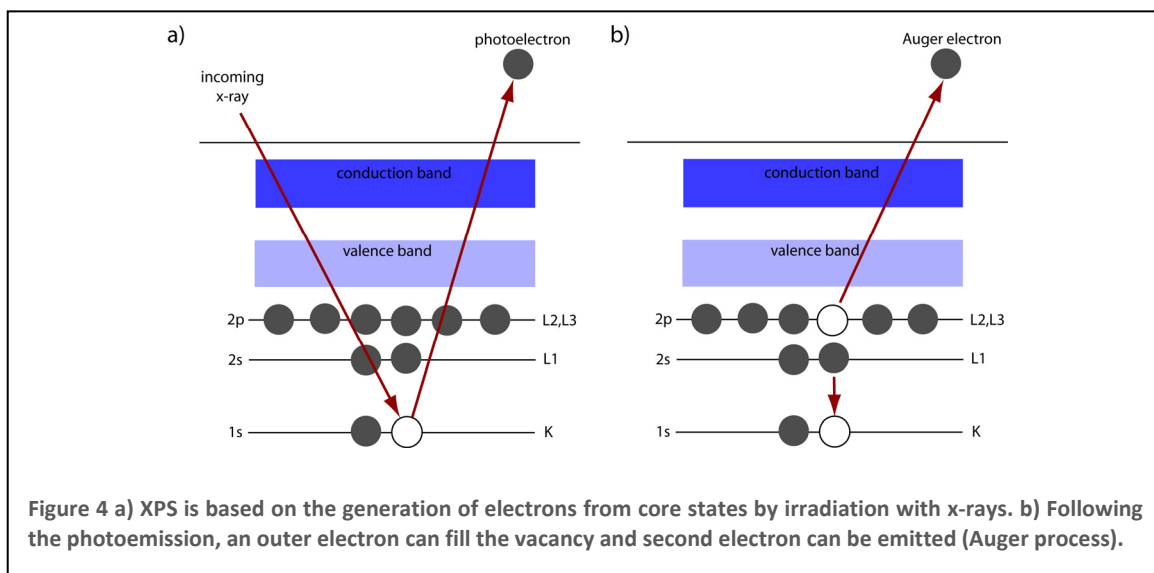
Patterns of cross-linked SAMs have been used as a resist for selective etching of the substrate [10, 24], as well as selective electrochemical [21, 22] and electroless [28] deposition of metal, immobilization of biomolecules [29, 30], and growth of polymer brushes [31]. It was shown that by cross-linking stable nanosheets are formed, that can be moved on the surface by sonication after cleaving the sulfur-gold bond by exposure to iodine vapor (Figure 3a) [32]. For a SAM that was prepared on thin silicon nitride

windows, it was also possible to dissolve the substrate to obtain freestanding nanosheet membranes [32]. Two of such membranes are shown in Figure 3. The one in (b) is totally intact, only a few traces of contamination are visible; the membrane in (c) was damaged during the preparation. Due to the folds and tears its visibility is greatly enhanced, it somewhat resembles “saran wrap”.



2.2 X-ray photoelectron spectroscopy (XPS)

X-ray photoelectron spectroscopy is one of the standard techniques in surface science [33, 34]. It is able to give insights into the chemical structure and composition at interfaces. Its scientific basis is the photoelectric effect that was first discovered by Hertz in 1887, however, the technique itself was developed in the 1950's in the group of Siegbahn (Nobel price 1981).



Samples are irradiated in ultra high vacuum (UHV) with soft x-rays. These are able to penetrate the sample several micrometers. If the energy is high enough, a core electron is ejected by the incident x-rays (photoionization). As a second process, an electron from an outer shell can relax to an inner shell by releasing a second electron (Auger electron). Both processes are schematically depicted in Figure 4. The kinetic energy E_K of all the emitted electrons can be measured by an analyzer that is in electrical contact with the sample. If the work function Φ_{SP} is known, the original binding energy E_B of the electron, which is characteristic for the element, can be calculated by:

$$E_B = h\nu - E_K - \Phi_{SP} \quad (1)$$

As the binding energy is independent of the x-ray energy, this convention makes it easy to compare signals. For the same reason, the kinetic energy scale is used for Auger electrons. In addition, the binding energy is dependent on the chemical environment of the element, making this a useful tool for chemical analysisⁱ.

The surface sensitivity of XPS is due to the attenuation of these photoelectrons in the solid. Only in close proximity of the surface, the electrons can be emitted into the vacuum (photoemission). The attenuation length is plotted as a function of the electron energy in Figure 5. At the minimum of this characteristic fundamental curve between 40 and 100 eV the maximum surface sensitivity is achieved.

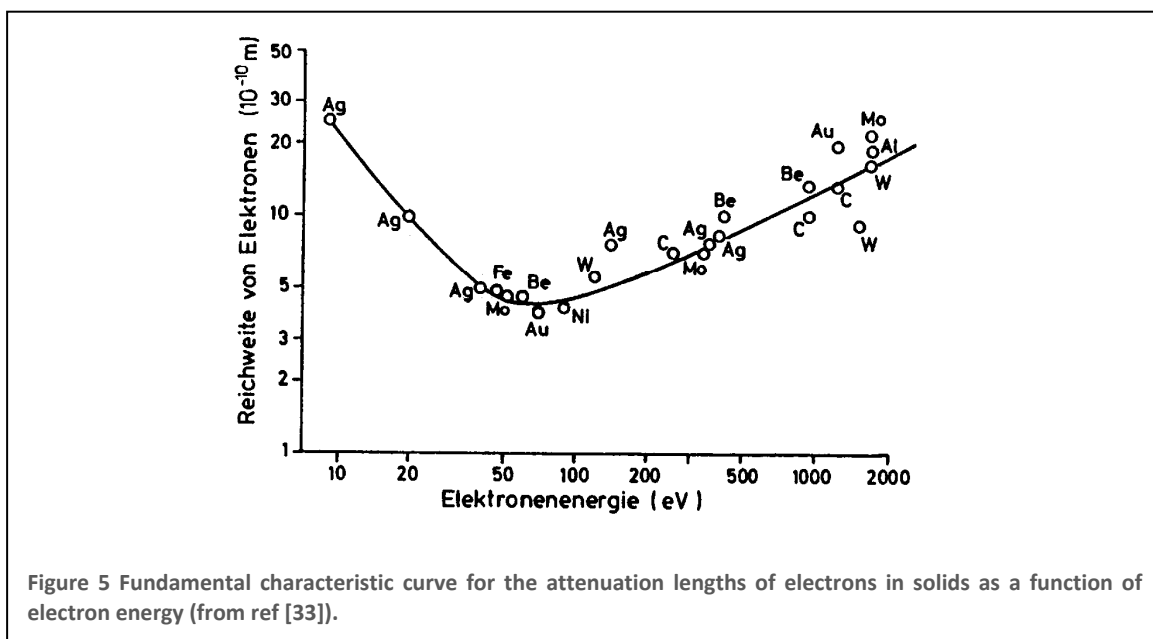


Figure 5 Fundamental characteristic curve for the attenuation lengths of electrons in solids as a function of electron energy (from ref [33]).

ⁱ XPS is also called electron spectroscopy for chemical analysis (ESCA)

2.2.1 Quantification

For samples that consist of a homogeneous layer on top of a (atomically) flat substrate, the thickness of this layer can be determined by comparison of the substrate signal intensity of the sample and a clean substrate. The intensities can then be described as:

$$\frac{I}{I_0} = \exp\left(-\frac{d}{\lambda \cos\Theta}\right) \quad (2)$$

where d is the thickness of the overlayer, λ is the attenuation length of electrons from the substrate in the overlayer and Θ is the take off angle of the electrons with respect to the surface normal. This method is limited to overlayer thicknesses between one monolayer and about 3λ . For thinner films, it is better to speak of a surface coverage, whereas in thicker films the substrate intensity is getting too low.

2.3 Electron microscopy

The resolution of the human eye is limited to $\approx 75 \mu\text{m}$ [35]. In order to observe objects that are smaller, it is necessary to use microscopes. The resolution limit d of a microscope depends on the wavelength λ of the radiation and the numerical aperture N_A :

$$d = \lambda/2N_A \quad (3)$$

Thus, with optical microscopes that use visible light, it is difficult to reach values of below 200 nm. To overcome this problem, a microscope that used electrons for imaging was constructed by Ruska in the 1930's [36]. This is based on the de-Broglie equation [37], which states that a particle of the mass m has a wavelength λ of:

$$\lambda = h/mv \quad (4)$$

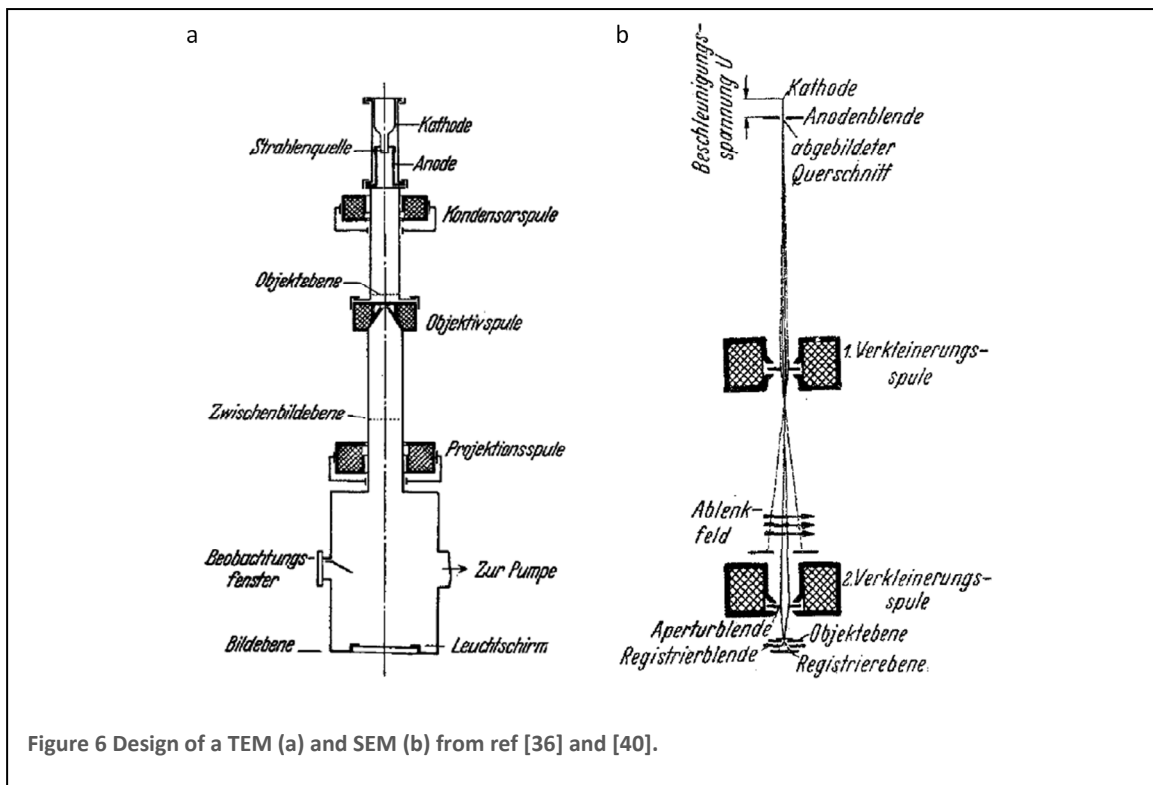
with the Planck constant h and the velocity v . For electrons that are accelerated to 50 kV, $\lambda \approx 0.005 \text{ nm}$, thus it should be theoretically possible to achieve atomic resolution. In practice the resolution is limited by diffraction and aberration [35].

Electron microscopes are generally divided into two different categories: transmission electron microscopes (TEM) and scanning electron microscopes (SEM).

2.3.1 TEM

The TEM follows the original design by Ruska and is very similar to an optical microscopy in transmission mode (Figure 6a). An electron energy of 100-300 keV is typically used.

The electrons shine through the sample and are then projected onto a phosphor screen. For small magnifications mainly thickness and composition of the sample play a role in image formation. Contrast originates from the absorption of electrons within the specimen. At very high magnifications, however, the interaction is more complex and computer simulation is necessary for the interpretation of the obtained images.



The newest generation of TEMs reaches a resolution of ≈ 0.08 nm [38, 39]. This is sufficient to resolve single atomic columns in all crystalline materials.

2.3.1.1 Scanning transmission electron microscopy (STEM)

In contrast to standard TEM, the electron beam is focused into one spot and scanned over the sample. That way it is possible to perform mapping experiments at atomic resolution. By using the high angle annular darkfield (HAADF) mode, only inelastically scattered electrons are detected. These are very sensitive to the atomic number of the elements in the observed samples.

2.3.2 SEM

In contrast to TEM, where always the whole field of view is irradiated with electrons, in SEM the electron beam is focused into one small spot and scanned over the object (Figure 6b)[35, 40]. Generally, samples are not examined in transmission, but in

reflection. The primary electron beam (typically 5-30 keV) interacts with the sample and gives rise to a variety of detectable secondary radiation, including backscattered electrons, secondary electrons and Auger electrons as well as x-rays. The image is composed in the computer from the detector intensities in each spot.

A typical detector is the Everhart-Thornley detector, also called SE2, where the backscattered and secondary electrons are collected by a positive bias. Due to its position with respect to the sample, objects facing towards the detector appear brighter than those facing away from it. This makes the resulting images appear to have shadows.

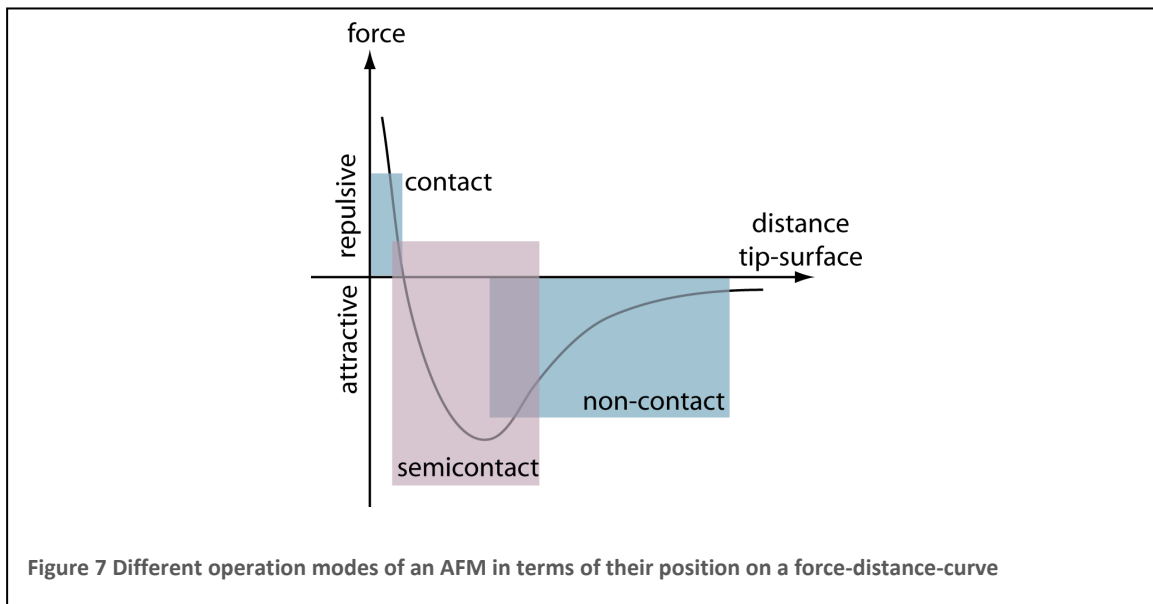
Also important is the so called inlens detector that was mostly used in this work. As the name says, it is located within the electron lenses. Only secondary electrons that are scattered backwards are detected. Due to the low energy of the secondary electrons, this detector is very sensitive to material contrast originating from the topmost surface of the sample.

2.4 Atomic force microscopy (AFM)

The atomic force microscope is a tool to image surfaces. It was developed by Binnig, Quate and Gerber in 1986 based on the scanning tunneling microscope (STM). It is in principle possible to obtain atomic resolution images. The main advantages over other techniques are the ability to image the topography of a sample with high accuracy, to work in vacuum, liquid or air, and to image insulating materials.

An AFM consists of a cantilever with a small tip on the end. This cantilever is brought into close contact with a sample and is scanned over its surface with the help of piezo scanners. Changes in topography result in a deflection of the cantilever, which can be detected by a laser that is reflected on top of the cantilever into a four quadrant photodiode.

The different modes of operation are characterized by the tip-surface distance, which is depicted in Figure 7.



In *contact mode* the tip is brought into mechanical contact with the sample. If the tip is scanned over the sample at a constant height, the deflection of the cantilever is a measure of the topography. The advantage of this mode is the fast operation, but it is limited to very clean and flat surfaces. More commonly the tip is scanned at constant force. By a feedback loop the distance of the tip to the surface (and thus the deflection of the cantilever) is controlled, so that the difference signal of the photodiode is minimized. The topography of the sample then results from the movement of the z-piezo. Additionally, the torsion of the cantilever during sideways movement can be measured with the four-quadrant photodiode. This signal is called “lateral force”, which can give insight into areas of different friction.

Non-contact mode is different in that the tip is kept at a distance to the surface where attractive forces are dominating. The tip is excited near its resonance frequency, which is shifted by the attractive forces. Both constant height and constant force modes are possible. Non-contact mode is especially important for soft samples that could be destroyed by contact with the tip.

Semi-Contact or tapping mode is the intermediate between the two other modes. The tip is also excited near its resonance frequency, but at a higher amplitude. At each oscillation the tip is “tapping” onto the sample, thus detecting repulsive forces. In

addition a phase shift of the oscillation with respect to the excitation can be measured, which is very sensitive to material properties such as adhesion, elasticity, etc.

2.5 Optical Properties of thin films

2.5.1 Thin film interference

If an electromagnetic wave hits a thin dielectric medium, it is split into two components, a wave that is reflected at the first interface and one that is refracted and then reflected at the second interface[41]. This leads to a difference of the optical path Γ for both waves that is dependent on the refractive index of the material n , the thickness of the thin film d and the wavelength of the light λ . Γ can be described by (Figure 8)

$$\Gamma = n(AB + BC) - AD \quad (5)$$

with

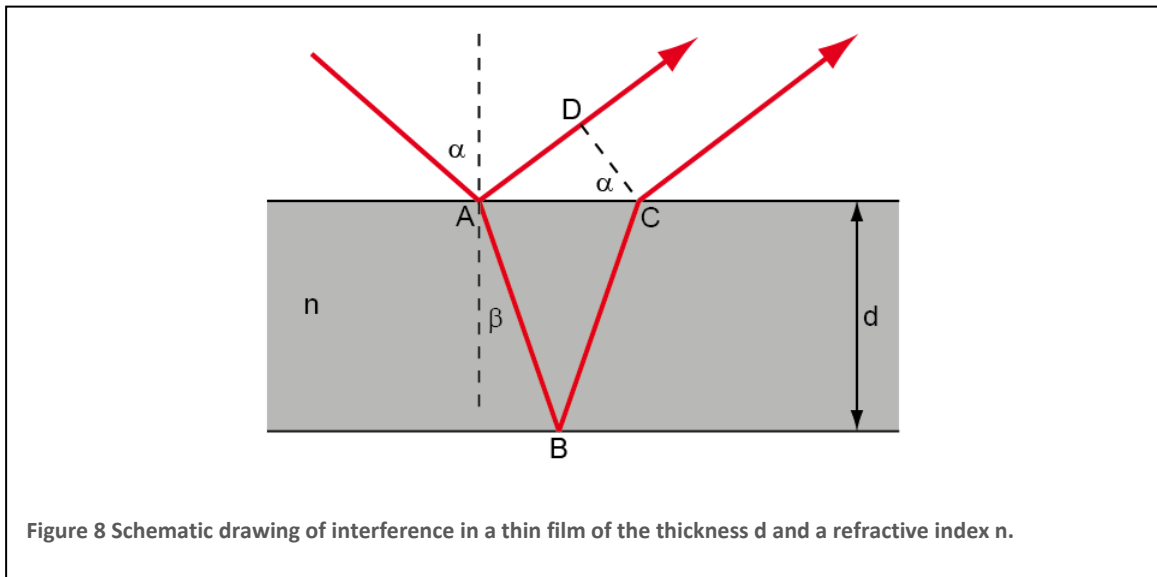
$$AB = d/\cos \beta \quad (6)$$

and

$$AD = (2d \tan \beta) \sin \alpha = 2d \tan \beta (n \sin \beta) \quad (7)$$

Inserting (6) and (7) into (5) gives

$$\Gamma = 2nd \left(\frac{1}{\cos \beta} - \tan \beta \sin \beta \right) = 2nd \left(\frac{1 - \sin^2 \beta}{\cos \beta} \right) = 2nd \cos \beta \quad (8)$$



The conditions for constructive and destructive interference are therefore given by:

$$\text{Constructive: } 2nd \cos \beta = m \lambda \quad (9)$$

$$\text{Destructive: } 2nd \cos \beta = (m - 1/2) \lambda \quad (10)$$

Light that is reflected from an optically denser medium (higher index of refraction) experiences an additional phase change of π . Hence, equation (10) then describes constructive and equation (9) destructive interference.

2.5.2 Fresnel's equations

Reflection and transmission of an electromagnetic wave at an interface can be described by Fresnel's equations in terms of reflection and transmission coefficients for light polarized parallel and perpendicular to the plane of incidence [42, 43].

The reflection coefficients are:

$$r_{\parallel} = \frac{n_t \cos \theta_i - n_i \cos \theta_t}{n_i \cos \theta_t + n_t \cos \theta_i} \quad (11)$$

$$r_{\perp} = \frac{n_i \cos \theta_i - n_t \cos \theta_t}{n_i \cos \theta_i + n_t \cos \theta_t} \quad (12)$$

with θ_i being the angle of incidence in a medium of the refractive index n_i and θ_t the angle of transmission in a medium of the refractive index n_t . The transmission coefficients are:

$$t_{\parallel} = \frac{2n_i \cos \theta_i}{n_i \cos \theta_t + n_t \cos \theta_i} \quad (13)$$

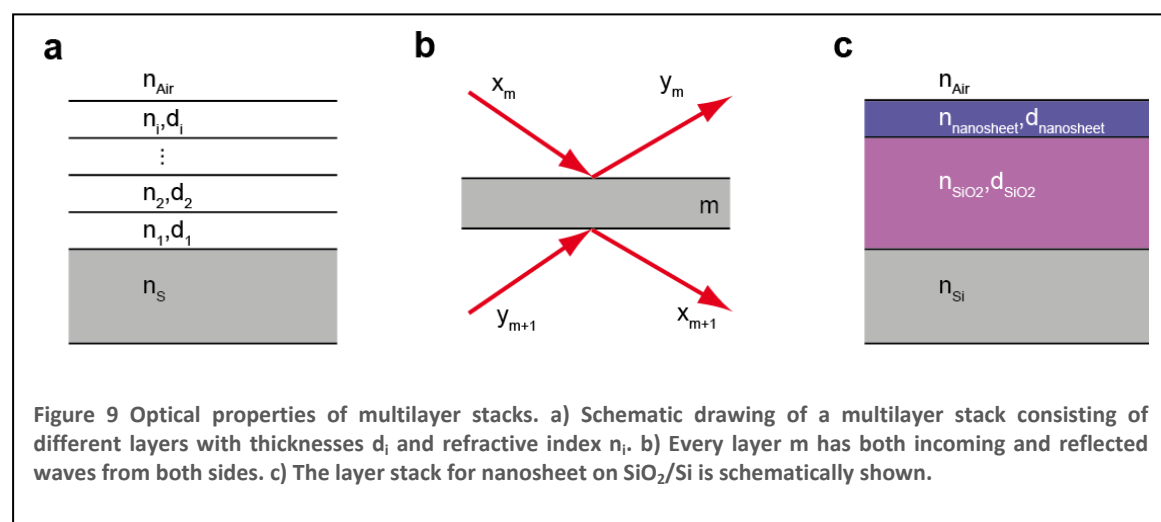
$$t_{\perp} = \frac{2n_i \cos \theta_i}{n_i \cos \theta_i + n_t \cos \theta_t} \quad (14)$$

The coefficients are given as amplitudes and have to be squared in order to give intensities.

2.5.3 Matrix method for multilayered systems

The above case where the maximum and minimum of reflection from a thin dielectric film is described simply by comparing the difference of the optical path is only valid for idealized non-absorbing materials with a constant refractive index. For multilayer systems (Figure 9a), the case is more complicated, as multiple reflections (from each layer) have to be considered. A generalized method for the analysis the optical properties of multilayer systems is the so called matrix method [42-45]. It considers the total electric and magnetic fields, as described by the Fresnel equations, in every layer. The boundary conditions are applied at every interface. Simplified this can be described by assuming M layers between the medium 0 and M+1. Every layer m has an incoming (x_m) and reflected wave (y_m) on the top side (Figure 9b) [43]. The incoming and outgoing waves on the bottom side (y_{m+1} and x_{m+1}) are the reflected and incoming waves of the next layer m+1. The relation between the waves on either side of the layer is then given by

$$\begin{pmatrix} x_m \\ y_m \end{pmatrix} = \tilde{M}_m \begin{pmatrix} x_{m+1} \\ y_{m+1} \end{pmatrix} \quad (15)$$



For a multilayer stack it is therefore

$$\begin{pmatrix} x_1 \\ y_1 \end{pmatrix} = \tilde{M}_1 \tilde{M}_2 \cdots \tilde{M}_m \cdots \tilde{M}_{M+1} \begin{pmatrix} x_{M+1} \\ y_{M+1} \end{pmatrix} = \tilde{M} \begin{pmatrix} x_{M+1} \\ y_{M+1} \end{pmatrix} \quad (16)$$

where \tilde{M} is the characteristic matrix for the given multilayer stack. It depends on the thickness of the layers, the angle of incident light and the complex, wavelength depended refractive index of each layer.

For the case of nanosheet on an oxidized Si wafer, two layers on the Si substrate have to be considered: SiO₂ and nanosheet (ns), Figure 9c. The reflectance R in such a system is then given by [46]

$$R = \left| \frac{M_{12}}{M_{22}} \right|^2 \quad (17)$$

where

$$M_{12} = \left[\cos \phi_{ns} \cos \phi_{SiO_2} \left(1 - \frac{n_{Air}}{n_{Si}} \right) - \sin \phi_{ns} \sin \phi_{SiO_2} \left(\frac{n_{ns}}{n_{SiO_2}} - \frac{n_{Air} n_{SiO_2}}{n_{ns} n_{Si}} \right) \right] - i \left[\cos \phi_{ns} \cos \phi_{SiO_2} \left(\frac{n_{SiO_2}}{n_{Si}} - \frac{n_{Air}}{n_{SiO_2}} \right) - \sin \phi_{ns} \sin \phi_{SiO_2} \left(\frac{n_{ns}}{n_{Si}} - \frac{n_{Air}}{n_{ns}} \right) \right] \quad (18)$$

$$M_{22} = \left[\cos \phi_{ns} \cos \phi_{SiO_2} \left(1 + \frac{n_{Air}}{n_{Si}} \right) - \sin \phi_{ns} \sin \phi_{SiO_2} \left(\frac{n_{ns}}{n_{SiO_2}} + \frac{n_{Air} n_{SiO_2}}{n_{ns} n_{Si}} \right) \right] - i \left[\cos \phi_{ns} \cos \phi_{SiO_2} \left(\frac{n_{SiO_2}}{n_{Si}} + \frac{n_{Air}}{n_{SiO_2}} \right) + \sin \phi_{ns} \sin \phi_{SiO_2} \left(\frac{n_{ns}}{n_{Si}} + \frac{n_{Air}}{n_{ns}} \right) \right] \quad (19)$$

with

$$\phi_i = \frac{2\pi n_i d_i}{\lambda_0} \quad (20)$$

The matrix method is implemented in a variety of commercial programs for simulation and optimization of antireflective coatings and filters. In this work the open source program OpenFilters by Larouche and Martinu has been used to simulate optical reflection spectra [47].

2.5.3.1 Angular dependence

The above equations (18) to (20) are valid for light perpendicular to the surface. For any other incident angles θ_0 the angle θ_i in each layer has to be calculated by Snell's law

$$\theta_i = \arcsin(\sin \theta_0 / n_i) \quad (21)$$

According to Fresnel's equations (11),(12),(13) and (14) [42, 43], n_i has to be substituted by $n_i \cos \theta_i$ for s-polarized light in equations (18) and (19), whereas for p-polarized light every ratio n_i/n_j changes to $n_i \cos \theta_j / n_j \cos \theta_i$. The phases change to

$$\phi_i = \frac{2\pi n_i d_i \cos \theta_i}{\lambda_0} \quad (22)$$

For a given experimental setup, a distribution of incident angles has to be taken into account for simulations. Two different setups have to be considered, reflection microscopy, using an objective lens and reflection spectroscopy, using fiber optics.

2.5.3.1.1 Reflection microscopy

In reflection microscopy the sample is normally illuminated and observed through the same objective lens. The acceptance angle at which light is reflected off the surface into the lens is defined by the numerical aperture of the objective lens (see Figure 10a):

$$NA = n * \sin \alpha \quad (23)$$

Where n is the refractive index of the surrounding medium. In air $n \approx 1$, so that

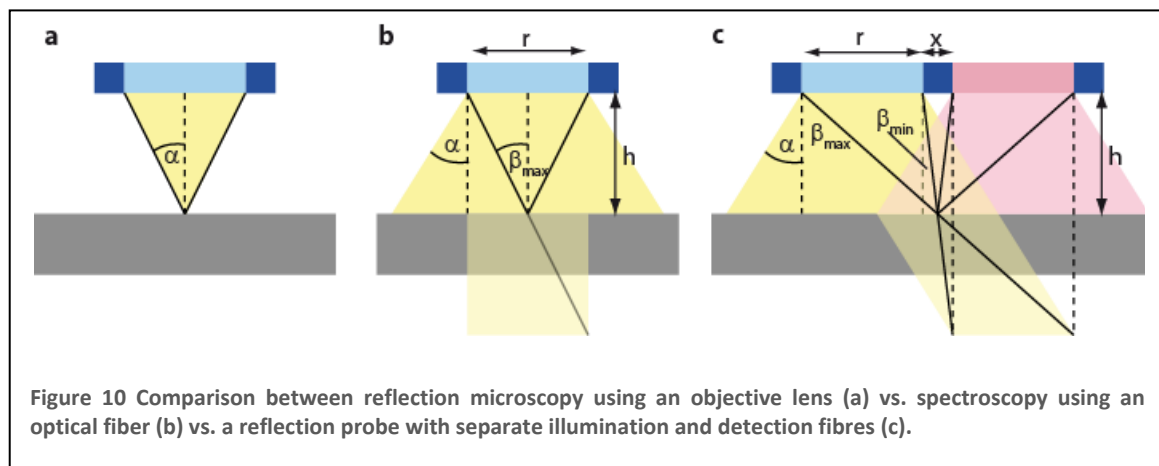
$$\alpha \approx \arcsin(NA) \quad (24)$$

Thus for high NA, the acceptance angle is large. For thin films this means that for a given wavelength there is a distribution of path differences.

2.5.3.1.2 Fiber optic probes

In fiber optics the numerical aperture is defined as:

$$NA = n * \sin \alpha = \sqrt{(n_1^2 - n_2^2)} \quad (25)$$



Where α is defined as the cone angle at that light exits the fiber, it is dependent on the refractive indices of the fiber material and the cladding (material around the fiber), representing the maximum acceptance angle (see Figure 10b). For a given distance of the probe to the surface, the highest angle at that reflected light can still enter the probe is determined by the distance to the surface and the diameter of the fiber. Simplified this can be described by a circular cylinder with a height of $2h$. Therefore

$$\beta_{max} = \arctan\left(\frac{r}{h}\right) \quad (26)$$

The minimum angle β_{min} is zero. Thus the numerical aperture NA is only important for the case $r/h > NA$; for a given radius r , i.e. small distances to the surface.

2.5.3.1.3 Reflection probe

The reflection probe that was used for measurements of the optical spectra consists of six illumination fibers that are arranged around a single detection fiber (Figure 11). As the detection of reflected light is separate from the illumination, the circular cylinder of Figure 10b has to be sheared by the diameter of the fibers plus the distance between them (Figure 10c). Equation (26) has to be modified to

$$\beta_{max} = \arctan\left(\frac{2r + x}{h}\right) \quad (27)$$

The minimum angle is changing to

$$\beta_{min} = \arctan\left(\frac{x}{h}\right) \quad (28)$$

For smaller angles the light will not be able to enter the detection fiber. The maximum



Figure 11 Reflection probe consisting of six illuminating fibers around one detection fiber (Ocean Optics)

angle for β_{\max} is α , which is dependent on the NA of the fiber (equation (25)).

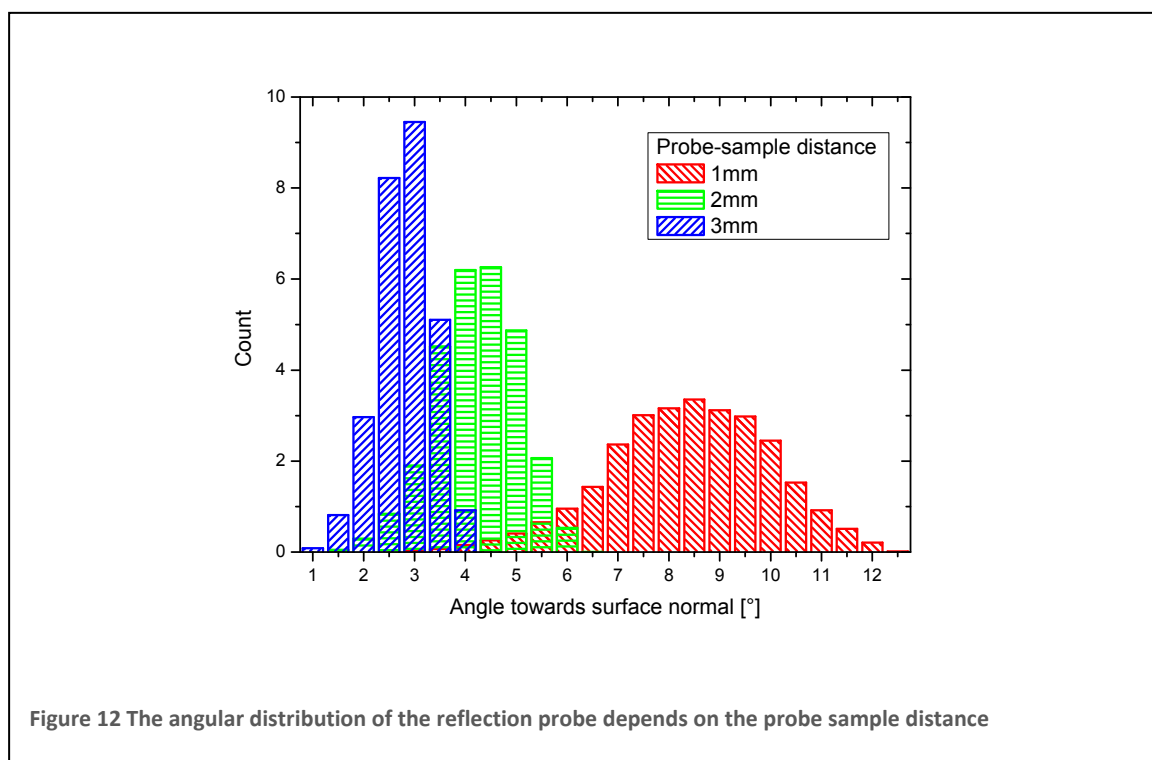
To account for all possible angles, the oblique cylinder was described in cylindrical coordinates and the angles were calculated for all vectors intersecting both the top and bottom circle. The calculation has been performed for a few probe-surface distances for the reflection probe with a fiber diameter of 200 μm and a spacing of 40 μm . A Gaussian angular distribution was found from fitting the resulting histograms in Figure 12:

$$y = \frac{A}{w\sqrt{\pi/2}} \exp\left(-2 \frac{(x - x_c)^2}{w^2}\right) \quad (29)$$

$$\text{Where } x_c = \frac{2}{3} \arcsin\left(\frac{2r+x}{h}\right) = \frac{2}{3} \arcsin\left(\frac{220\mu\text{m}}{h}\right) \text{ and}$$

$$w = \frac{1}{4} \arcsin\left(\frac{2r+x}{h}\right) = \frac{1}{4} \arcsin\left(\frac{220\mu\text{m}}{h}\right)$$

For the lowest angular spread it is thus best to put the probe far from the sample, however this is limited by the light intensity. A large distance also makes it difficult to determine the exact spot on the sample that is measured. During experiments the distance was chosen so that the light spot was roughly the size of the total probe diameter (1.5 mm) and could easily be positioned within the regions of interest (2-3 mm). This leads to a distance of ~ 2 mm, which was used in the Gaussian weight distribution for all simulated spectra.



2.6 Fluorescence microscopy

Fluorescence is a radiative relaxation of an electronically excited state of a molecule to its ground state [48]. The energy is given off as a photon that generally has a longer wavelength than that of the excitation (Stokes shift). This difference can be used in fluorescence microscopy to filter out the exciting radiation and only detect the fluorescence. Images can be obtained by either illuminating the sample in wide field or scanning over the sample with a focused laser.

2.7 Contact angle

The wetting of a surface by a drop of liquid is determined by the chemical properties of the surface. As a measure to quantify the wetting properties (hydrophilicity vs. hydrophobicity), the contact angle is defined as the angle at the tripelpoint between the drop, the surface and air.

In this work the contact angle of modified surfaces with water was determined by a homebuilt apparatus. The water droplets are dispensed through a small capillary by a gastight microliter syringe and a micrometer screw. The diameter of the droplet can be

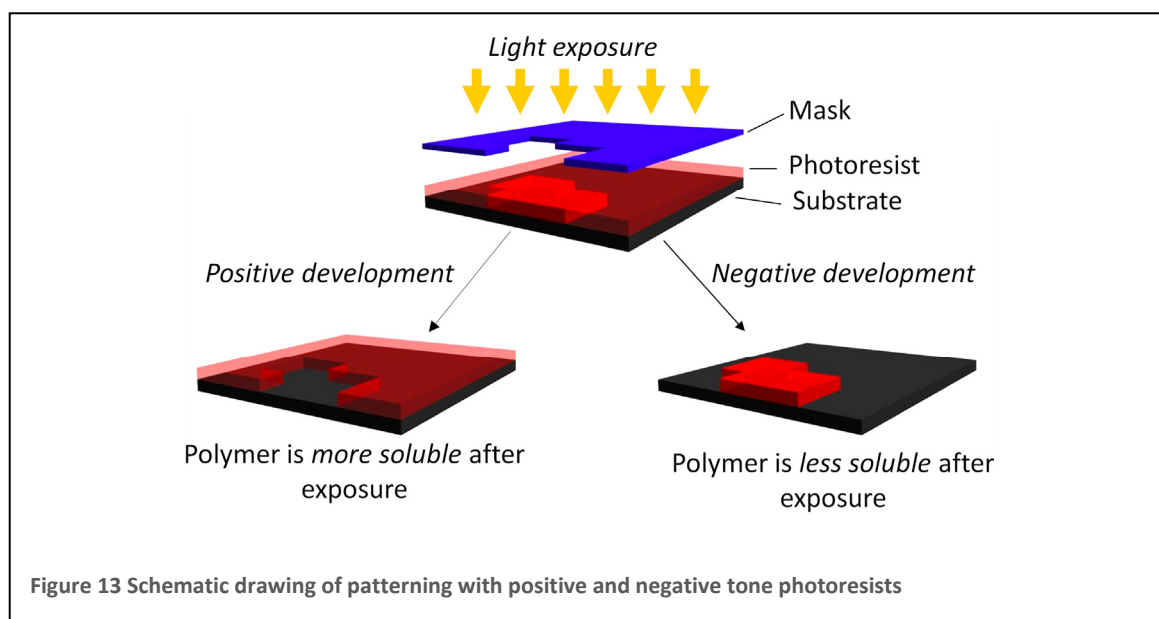
varied by variation of the capillary. The sample can then be brought into contact with the hanging droplet by an adjustable sample stage. A modified webcam with a zoom lens is mounted on the side for taking images. Opposite of the camera is a lamp behind a diffuser screen that ensures maximum contrast of the drop. The images can then be evaluated by the free software “ImageJ” with the plugin “ContactAngle”.

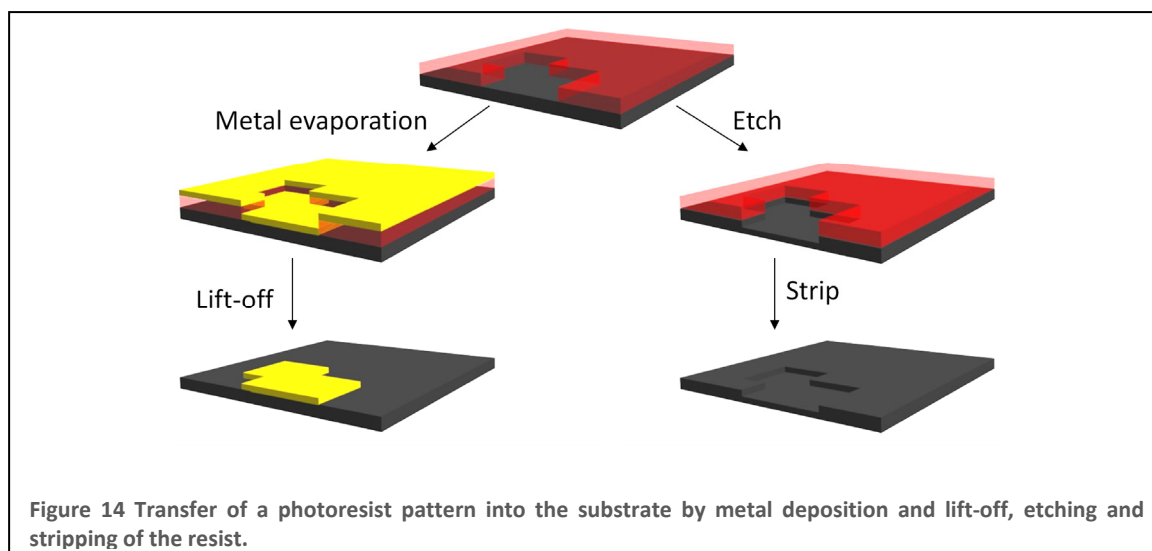
2.8 Photolithography

Lithography refers to the printing of patterns from a mask into a resist layer. In photolithography the pattern is transferred by exposure to visible or UV light through the mask. Other types of lithography utilize electrons, ions, stamps or scanning probe techniques for generating patterns. The resist layer is the crucial part of the photolithographic patterning process.

Generally, photoresists are polymeric coatings that change their properties upon exposure to light. They are applied to a substrate as a solution. The substrate is then rotated up to a few thousand rounds per minute, so that the resist evenly spreads over the surface. During this process the solvent evaporates, so that a residual polymeric film covers the surface. The thickness of this film depends on the concentration of the solution as well as on the speed of rotation.

Photoresists can be divided into two different categories: (i) positive tone and (ii) negative tone resists. In a positive tone resist the areas that are exposed to light become more soluble in a developer solution than the surrounding parts and can thus be washed





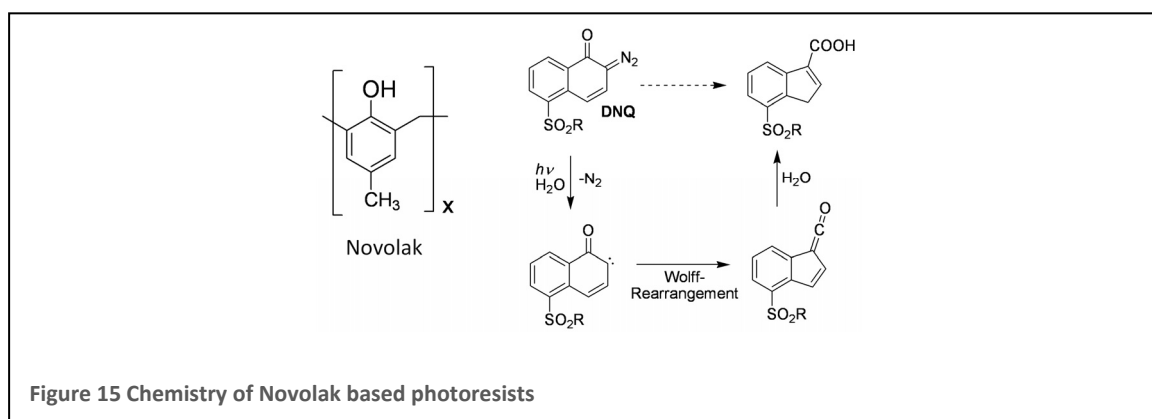
away to expose the substrate. For a negative tone resist, the process is exactly opposite, as the exposed regions stay behind after development. These differences are shown schematically in Figure 13.

After exposure and development, the patterned photoresist protects the substrates from further processing. This can be an etching step, either by wet chemical or dry etching techniques, to transfer the pattern into the substrate. Afterwards the photoresist is dissolved in a suitable solvent. Another possibility is the deposition of metal. The metal is coated on the whole substrate, but can easily be removed together with the photoresist (lift-off). Both pathways are shown in Figure 14.

2.8.1 Chemistry of photoresists

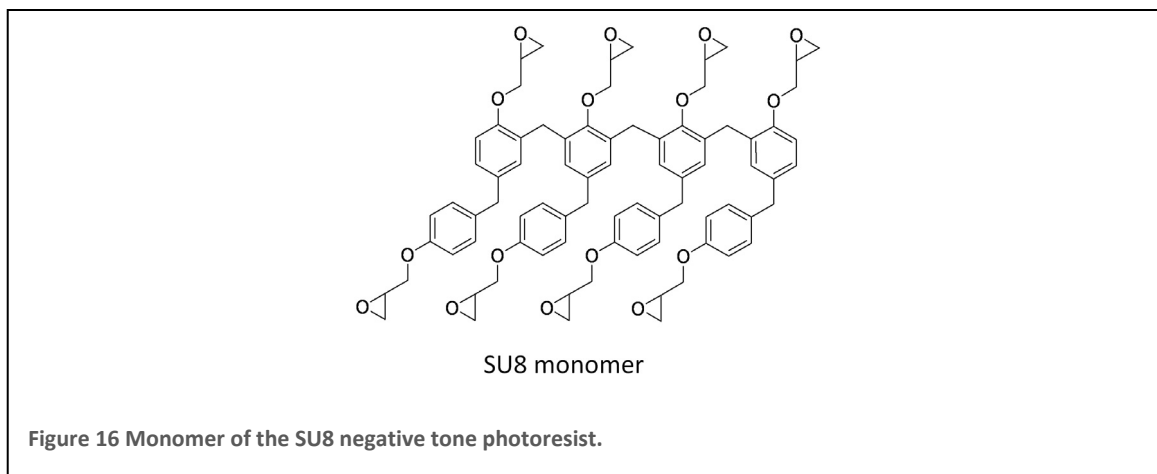
In this work several different types of photoresists have been used, and in this section the chemistry of these is shortly discussed.

Novolak based resists are very common positive tone photoresists based on a phenol-formaldehyde type resin, which is slowly soluble in aqueous base. The solubility can be



greatly enhanced by photochemically active ingredient such as diazonaphtaquinone (DNQ). Upon irradiation the DNQ undergoes a Wolf rearrangement that yields a carboxylic acid in the final step. This increases the dissolution rate of the exposed polymer by several orders of magnitude. After processing Novolak based resists can be removed easily by washing with acetone.

A widely used negative tone resist is SU8. It is based on a bisphenol epoxy resin, bearing eight epoxy groups per monomer (Figure 16). Due to the relatively low molecular weight, the unexposed resist is easily dissolvable in different solvents. The photosensitivity is achieved by a triarylsulfonium salt based photo initiator. This initiator decays upon exposure to UV light and releases acid that triggers the cationic polymerization of the epoxide. After cross-linking SU8 is insoluble, making it ideal for applications where the resist is part of the final structure.



Polymethylmethacrylate (PMMA, plexiglas) is technically not a photoresist, as it is used for electron beam lithography. It is used as a high molecular weight polymer (50K to 950K). In electron beam lithography the polymer is fragmenting, which makes it more soluble in the exposed regions (positive tone). Overexposure, however, can lead to cross-linking and thereby to a reversed contrast (negative tone). In this work PMMA was only used as a transfer medium, as it is easily processable and removable in acetone.

2.9 Supercritical drying

Upon evaporation of a solvent, the volume of the liquid phase is constantly decreasing. Due to surface tension and capillary forces fragile structures such as in biological samples and micromechanical devices can be destroyed. In supercritical drying the phenomena is

utilized that above the critical point there is no phase transition between liquid and gas. Due to the high critical point, both in terms of temperature and pressure of water (374°C, 218 bar), it is necessary to exchange the water with a more suitable solvent. Most commonly liquid CO₂ (31°C, 72 bar) is used, which is not miscible with water, so that an intermediate solvent such as ethanol or acetone needs to be usedⁱⁱ.

For drying, a sample is introduced into a pressure chamber in acetone or ethanol. The solvent is then exchanged by liquid CO₂ at a temperature below 0°C. Next, the temperature (and thus also the pressure) is raised above the critical point. Now, at constant temperature, the pressure is slowly lowered until ambient pressure is reached.

In this work two different critical point dryers were used. The main differences are the way the solvent exchange and cooling is handled. The Bal-Tec CPD 030 uses a compressor for cooling, the solvent exchange is done manually by lowering the solvent level and subsequently refilling it with CO₂. In the Tousimis Autosamdri 815-B the cooling is achieved by expansion of CO₂. The solvent is exchanged continuously over a predefined time interval.

ⁱⁱ Freon used to be another common solvent with a critical point slightly above room temperature at 35-40 bar, but is not available anymore due to environmental concerns.

3 Materials and Methods

3.1 SAM preparation

3.1.1 Silane-SAMs

For the preparation of 4'-[(3-Trimethoxysilyl)propoxy]-[1,1'-biphenyl]-4-carbonitril (CBPS)ⁱⁱⁱ SAMs silicon wafers with a thermal oxide layer of 300 nm and a layer of plasma enhanced chemical vapor deposited silicon nitride (200 nm) were used. Samples were cleaned with Piranha (H₂SO₄:H₂O₂ 3:1^{iv}) solution, rinsed with water and ethanol and blown dry with nitrogen. They were then immersed in a ≈10 mmol solution of CBPS in dry toluene^v at 80°C for 24h in a sealed flask under nitrogen. Samples were rinsed and sonicated with ethyl acetate and ethanol. Cross-linking by electron irradiation was achieved under high vacuum (<5*10⁻⁷ mbar) with an electron floodgun (Specs) at an electron energy of 100 eV and a dose of ≈40-60 mC/cm² which was monitored by a faraday cup close to the sample position. To prevent charging, the sample was contacted on the side by applying Ga-In alloy into a scratch and covering it with silver paint.

3.1.2 Thiol-SAMs

For the preparation of 1,1'-biphenyl-4-thiol (BPT) or 4'-Nitro-1,1'-biphenyl-4-thiol (NBPT) SAMs, 300 nm thermally evaporated Au on mica substrates (Georg Albert PVD-Coatings) were used. The substrates were cleaned in a UV/ozone-cleaner (UVOH 150 LAB from FHR, Germany) for 3-5 minutes at an oxygen flux of 1 l/min, rinsed with water and ethanol and blown dry in a stream of nitrogen. They were then immersed in a ≈10 mmol solution of BPT or NBPT in dry, degassed dimethylformamide^{vi} (DMF) for 72 h in a sealed flask under nitrogen. Afterwards samples were rinsed with DMF and ethanol and blown dry with nitrogen. Cross-linking was achieved in high vacuum (<5*10⁻⁷ mbar) with an electron floodgun (Specs) at an electron energy of 100 eV and typical dose of 50 mC/cm².

For patterning by proximity printing, a shadow mask (TEM grid) is placed on the sample during irradiation.

ⁱⁱⁱ By Küller this molecule is abbreviated as CEBP.

^{iv} Attention, special care has to be taken. This solution is highly oxidizing!

^v Toluene is freshly distilled after refluxing with sodium and benzophenone for at least 2 hours.

^{vi} DMF is dried over molecular sieve (4 Å)

3.2 Transfer of cross-linked SAMs

3.2.1 Transfer medium

The transfer procedure is shown schematically in Figure 19. First, a transfer layer is applied to the sample. To this end, PMMA (AR-P 671.04) is spincoated onto the nanosheet for 30 s at 4000 rpm as a transfer medium and cured on a hotplate for 5 min at 90°C.

Initial experiments were also performed using the photoresists AR-P 3510 (Allresist) and S1818 (Microchem). They are spincoated to a nominal thickness of 2 μm (30s@4000 rpm) and cured on a hotplate at 90°C for 2 min.

3.2.2 Release from substrate

3.2.2.1 $\text{SiO}_2/\text{Si}_3\text{N}_4$ substrates

The resist edge bead that was formed during spin coating is removed by either breaking off the edges of the sample, or by wiping the edges with a cleanroom cloth that is soaked in acetone. This ensures that the nanosheet/resist sandwich is easily released from the $\text{SiO}_2/\text{Si}_3\text{N}_4$ substrate by immersion in 48% hydrofluoric acid (HF)^{vii}. Completion of the removal can be observed by the naked eye as the color changes drastically. For very small samples it is useful to just let them float on top of the HF, after complete etching the substrate then sinks to the bottom of the beaker. Samples are then carefully taken out of the HF and transferred into water. The monolayer is then swimming on the water surface and can be transferred by fishing it out with a new substrate. It is then carefully dried with a cleanroom cloth and a gently flow of nitrogen. Best contact with the new substrate can be achieved by drying it on a hotplate at 90°C for several minutes.

For preparing freestanding nanosheets i.e. on TEM grids, care has to be taken that the nitrogen flow is not perpendicular to the grid. Also, the cleanroom cloth should only be applied from the sides, to avoid breaking of the nanosheet/resist sandwich.

3.2.2.2 Au/mica substrates

The $\text{Au}/\text{nanosheet}/\text{resist}$ sandwich can be removed from the mica substrate by immersion in 48 % HF for 15-60 min. The mica can then be separated by carefully dipping it into water. The $\text{Au}/\text{nanosheet}/\text{resist}$ sandwich is then swimming on the water surface.

^{vii} Attention, HF is extremely dangerous. Special care has to be taken!

By using a piece of silicon it can then be transferred to a KI/I₂ etching solution (0.6 mol/l KI, 0.09 mol/l I₂) where the Au is completely removed after 15 min[49]. The nanosheet/resist sandwich is then transferred back to water to prevent contamination with I₂. Transferring to the final substrate is done as described above.

3.2.3 Removal of transfer medium

3.2.3.1 Manual removal

The resist is removed by immersion of the sample in acetone under light stirring for at least 2 minutes. Afterwards the sample is dipped in methanol and blown dry with nitrogen. TEM grids have to be held by tweezers during the whole procedure and only moved parallel to the grid and perpendicular to the solvent surface.

3.2.3.2 Supercritical drying

Samples are built into the suitable sample holder and then introduced into the acetone filled chamber of the critical point dryer (Tousimis Autosamdri). After 45-60 min the chamber is sealed and the drying process is started by cooling down the chamber. Both the inlet and outlet valves are closed. Upon filling with CO₂ the inlet valve is slowly opened to minimize turbulences. Afterwards the outlet valve is also opened carefully. A time of 15-20 minutes (setting 3 or 4) is sufficient for exchanging the acetone with liquid CO₂. Samples can be taken out once ambient pressure is reached after the end of the process.

3.3 Patterning of nanosheets

3.3.1 Photolithography

Photoresist (AR-P 3510, Allresist) is spincoated onto the sample (30s@4000 rpm) and baked on a hot plate at 90°C for 2 min. Patterning is achieved by exposure through a chromium mask (delta mask) for 1.3 s in a mask aligner (Süss MJB 3). After development (AR-P 671.04, 60 s) the samples were rinsed with water and blown dry in a steam of nitrogen

Initial experiments were performed by flood exposure (1 s) using a UV-lamp (Modell 8011, Oriel Corporation, USA). Here, the mask was brought into contact with the sample manually. The photoresist is developed for 30 seconds with AR 300-35

3.3.2 Plasma etching

Removal of the nanosheet in exposed regions was done by an oxygen plasma (see [50] for details on the homebuilt system) for 1 min. Afterwards the photoresist was removed with acetone and water under sonication for 5 minutes each. In some experiments also photoresist stripper AZ 400T (Clariant) was used.

Some etching experiments were also performed with a PlasmaTherm 790 series reactive ion etching system (chamber pressure of ≈ 0.13 mbar, 20 sccm O_2 , 100 W). SiO_2 was etched in a CF_4 -Plasma (50 mTorr, 40 sccm, 100 W).

3.3.3 Preparation of PDMS stamps

Positive photoresist (Allresist, AR-P 3510) was spincoated (30 s @ 4000 rpm) onto a piece of silicon wafer and cured on a hotplate at $90^\circ C$ for 2 min. The relief pattern was generated by exposure (1.3 s) through a chrome mask using a maskaligner (Suss MJB 3). After development (AR-P 671.04, 45 s) the samples were rinsed with water and blown dry in a stream of nitrogen. PDMS was prepared according to the manufacturer with a ratio between prepolymer and curing agent of 10:1. It was poured over the photoresist master and cured overnight at $70^\circ C$. After peeling the stamp off the master, it was used without further treatment.

3.3.4 UV/ozone patterning

Samples were treated by UV/ozone at a constant oxygen flux of 1 l/min in a commercial UV/ozone cleaner (UVOH 150 LAB from FHR, Germany). TEM grids (Quantifoil) were used as masks. They were brought into contact with the sample with a small drop of ethanol that promotes adhesion upon evaporation, or by fixing them with a clamp. PDMS stamps were brought in contact by applying gentle pressure with the tips of a pair of tweezers. Afterwards samples were rinsed with water, ethanol and acetone and blown dry with nitrogen.

3.4 TEM sample supports

3.4.1 Cobalt nanoparticles

The Co nanoparticles with sizes ranging from 4 to 8 nm were prepared by thermolysis of metal carbonyl precursors according to the procedures by Puentes et al. [51]. 0.1–0.3 g of trioctylphosphine oxide (TOPO) and 0.2 ml of oleic acid were dissolved in 12 ml of 1,2-

dichlorobenzene. The solution was subsequently heated to reflux. Separately, 0.45–0.5 g of dicobaltoctacarbonyl, $\text{Co}_2(\text{CO})_8$, were dissolved in 3–6 ml of 1,2-dichlorobenzene. Under vigorous stirring, the second solution was injected into the refluxing bath. After a reaction time of 30 min the mixture was cooled to room temperature. Finally, the Co nanoparticles were dispersed in acetone and deposited onto the freestanding nanosheet.

For coupling of the Co nanoparticles to multi-walled carbon nanotubes (MWNT) the TOPO ligand was exchanged by 4-Pyrene-1-yl-butyric acid. The carboxylic acid moiety can bind to the Co particles, and the pyrene is able to bind to the MWNTs through π - π interactions. Coupling was achieved by mixing the suspensions of the Co nanoparticles and the MWNTs.[52]

3.4.2 Gold nanoclusters

Triphenylphosphine stabilized Au nanoclusters were synthesized by Simon et al. (Institute for Inorganic Chemistry, RWTH Aachen University) following the two-step procedure for the formation of Au nano-clusters from mononucleic gold precursor, described in [53]. First, the HAuCl_4 is dissolved in benzene and subsequently reduced with B_2H_6 yielding a solution of atomic gold. In the solvent, gold atoms aggregate to form small primary nano-clusters. These tend to grow or dissolve, and the stabilization of the cluster surface with a strongly binding ligand is required. Therefore, in the second step of the synthesis, a stabilizing agent, triphenylphosphine (TPP), $\text{C}_{18}\text{H}_{15}\text{P}$, is added to the suspension to passivate the surface of the growing gold clusters. The size of the resulting gold clusters in the solution is controlled by the amount of reducing agent, the rate of its addition, the time period between reduction and stabilization, and by the ratio of the stabilizing ligand to gold. The kinetic parameters of the synthesis were chosen such as to form clusters of 1.4 nm in size, though the diffusional character of the cluster formation implies occurrence of some dispersion in cluster size. Finally, the suspension of ligand stabilized gold nano-clusters in the solvent is repeatedly centrifuged and rinsed with methanol until a dry brownish powder of stabilized gold clusters can be collected and stored for months.

To suspend the Au clusters on the TEM grid, the powder of stabilized gold nano-clusters was dispersed in methanol by careful stirring. Deposition of the clusters onto the TEM

grid was achieved by carefully dropping a tiny amount of the suspension on the nanosheet covered side of the TEM grid, which was afterwards dried in air for about 10-15 minutes. In the present experiments, the foil was studied immediately after being deposited with nano-clusters. However, we found that in the case of a recurring study after longer storage time, the nanosheets can be plasma-cleaned for 15-20 sec in a 25% O₂ – 75% Ar gas mixture (using a Fishione Plasma Cleaner) to remove contamination prior to being introduced in the TEM instrument.

3.5 Metallization of nanosheets

Gold films were prepared on the nanosheet by sputter coating at a rate of ≈ 35 nm/min. The base pressure was $< 2 \cdot 10^{-6}$ mbar, during sputtering the argon plasma was kept at 25 W at an argon pressure of $2.1 \cdot 10^{-3}$ mbar. The apparatus is described in Ref [54].

3.6 Functionalization of nanosheets

3.6.1 Amino terminus

0.1 mg of tetramethylrhodamine isothiocyanate (TMR, Sigma-Aldrich) was dissolved in 50 μ l of dry DMF and then diluted with 1 ml of a 0.1 M sodium-bicarbonate buffer[29, 55]. Samples were immersed in this solution for ≈ 1 -2 h. Afterwards samples were washed with methanol and water and dried under nitrogen flow.

3.6.2 Thiol terminus

0.05 mg of Atto647N maleimide is dissolved in 25 μ l of dry DMF and diluted with 1 ml HEPES buffer (pH ≈ 7.5)[55]. The nanosheet was transferred to water three times for rinsing after the dissolution of the Au substrate and then transferred to the dye solution. After ≈ 30 min it was again transferred to water three times for rinsing and then transferred to the final substrate.

Reduction of possible disulfides was attempted by transfer to a dithioerythritol (DTE) solution right before labeling, followed by rinsing with water.

3.7 Annealing

Annealing of the cross-linked nanosheets on Au surfaces was conducted in UHV conditions in Mo sample holders with a resistive heater with the typical heating/cooling rates of ~ 150 K/h and the annealing time from 0.5 h to 3 h. Annealing temperature was

controlled with a Ni/Ni-Cr thermocouple and two-color pyrometer (SensorTherm). Cross-linked biphenylthiol nanosheets on gold films were annealed in vacuum up to ~ 1200 K, however, the mica substrate is substantially damaged at temperatures above ~ 1000 K, leading to damage of the gold-film/nanosheet as well. In order to maximize defect free areas, the Au-film was cleaved from the mica by immersion in hydrofluoric acid (48%) for 5 min and transferred it to a clean quartz substrate.

3.8 Raman

Raman spectra were measured at the PTB in Braunschweig by Rainer Stosch with a triple monochromator system Horiba Jobin-Yvon T64000 equipped with a liquid N₂-cooled CCD detector and an Olympus BH2 microscope. Data was collected in back-scattering geometry with a spectral resolution of 2 cm^{-1} using 514.5 nm line of an Ar⁺ laser (as the excitation source). The use of an 80 \times objective led to a spatial resolution of $\sim 2.5\text{ }\mu\text{m}$ and a laser power on the sample surface of 10 mW. Spectra were calibrated against the 520 cm^{-1} peak of the Si/SiO substrate.

3.9 Electrical measurements

Resistance measurements of suspended nanosheets on a gold grid were conducted in UHV by contacting with the tungsten tip of the scanning tunnelling microscope of an Omicron Multiscan Microscope. The sheet resistance of nanosheets transferred on SiO₂ was determined by a four-point measurement using Suss probes and a Keithley SMU Source-Measure Unit (Model 236) at a home built probe station.

3.10 X-ray photoelectron spectroscopy

XP-spectra were recorded with an Omicron Multiprobe spectrometer using monochromatic Al K α radiation. The spectra were calibrated by setting the Au 4f signal to 84.0 eV. Peak fitting was performed using Shirley backgrounds and symmetric Voigt functions.

3.11 Microscopy

Scanning electron micrographs (SEM) were acquired using the inlens detector of a Zeiss Leo1530 at 3 kV.

TEM investigations on the Co nanoparticles were performed in a FEI Tecnai F20 ST operated at 200 kV. The Au nanoclusters were also studied by employing two of the new

generation of C_s -corrected instruments (FEI Titan 80-300 TEM and STEM, both operated at 300 keV).

Atomic force microscopy (AFM) images were obtained with a NT-MDT Ntegra in contact mode using silicon cantilevers with a force constant of 0.1 N/m. For some experiments also a Digital Instruments Multiscan AFM was used. Optical microscopy was performed at an Olympus BX51.

4 Results and Discussion

4.1 Transfer

A variety of methods exists for the preparation of ultrathin films on different substrates. Metallic and oxide films are usually prepared by vapor deposition or epitaxy, whereas polymeric films are more commonly prepared by spin coating. For a number of applications, however, these methods are not applicable. This might be due to incompatibility of the processes or the requirement for special geometries, such as curved substrates or even windows for the fabrication of freestanding structures. It is therefore of interest to have means to transfer thin films from their original substrate to a new substrate. For thicker polymeric films (in the μm range) this can still be achieved by simply peeling the film off by hand and placing it onto a new substrate (similar to a sticker). For smaller objects that are not easily manipulated by hand, a number of different methods have been described in the literature.

Nanotransfer printing is a technique to transfer nanometer or micrometer sized objects from one substrate to another [56, 57]. The objects are normally only bound to the substrates by weak forces, such as van-der-Waals interactions. By bringing an elastomeric stamp (PDMS) in contact with the sample, the objects can then be released and transferred to a new substrate. Pickup and release can be controlled by the velocity of releasing the stamp from the substrate. This method is very versatile and has been applied for the transfer of semiconductor ribbons, carbon nanotubes, pollen and many more. The role of the stamp is not only that of a transfer-medium, but also to ensure the integrity and preservation of lateral patterns. In contrast to solution based processes, alignment of the structures is preserved during the transfer procedure. Nanotransfer printing is not possible, however, with objects that are bound to the surface by specific interactions. Also, to date no monomolecular films have been transferred by this method.

Another method that was mainly used for metallic films is the so called lift-off float-on (LOFO) process [58]. Here the metal film is released from the original substrate and then floated on a water surface where it can be picked up by a new substrate. The procedure was developed to have a way to form electrical contacts on i.e. SAMs without damage of the monolayer. One drawback of the method is that the integrity of a patterned film is

not preserved during the transfer procedure. However, this was solved by introducing a polymeric layer for support (polymer assisted lift-off, PALO) [59].

The above mentioned techniques are all limited to transferring films that are at least several ten nanometers thick. In this chapter, a method is described for transferring cross-linked SAMs (nanosheets) of ≈ 1 nm thickness to arbitrary new substrates. This method should also be applicable to any other molecularly or atomically thin film such as graphene.

To ensure a successful transfer of the nanosheet from one substrate to another, the nanosheet has to be mechanically supported during all transfer steps. This can be achieved by applying a transfer medium, similar to the stamp used in nanotransfer printing.

The transfer medium has to fulfill several criteria:

Easy applicability: The application of transfer medium to the sample should be as easy and fast as possible, ideally not requiring expensive equipment.

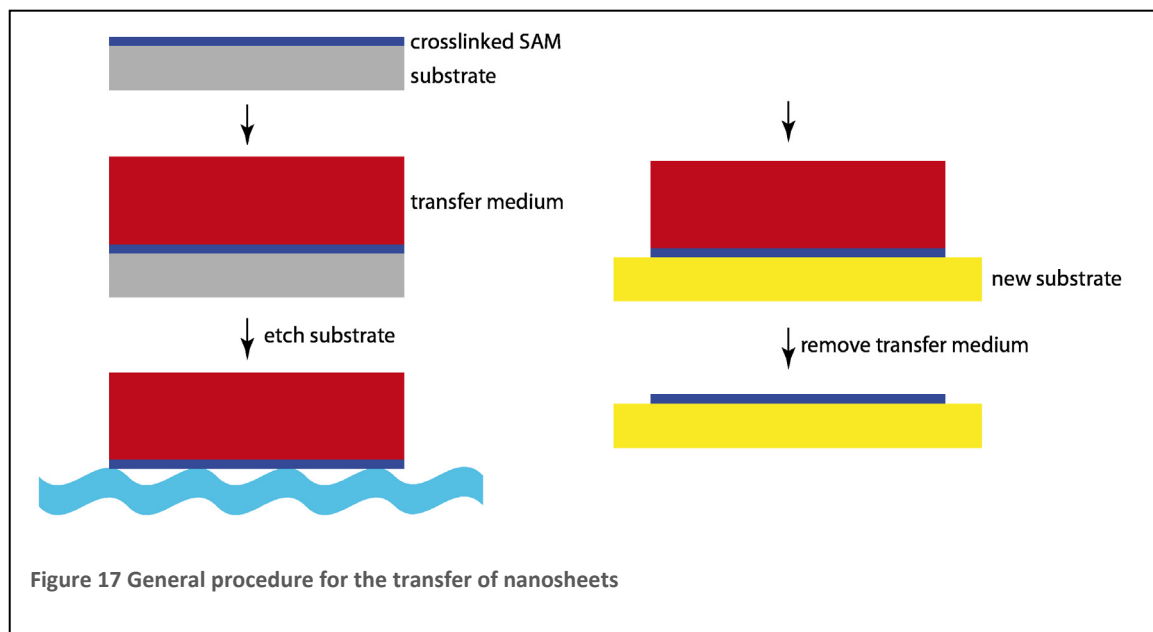
Chemical inertness: There should be no chemical reactions between the nanosheet (with possible functional groups) and the transfer medium.

Structural stability: The transfer medium needs to withstand the etching conditions for dissolving the substrate without losing its mechanical stability.

Removability: The transfer medium should be easily removable after the transfer procedure. The conditions should be mild, such that the nanosheet stays intact.

These criteria are fulfilled by a variety of photoresists. They can easily be applied to the sample by spincoating and baking on a hot plate. After transfer they can be removed by simply rinsing with acetone. Their chemical inertness has to be tested for each functional group in the nanosheet. Another key step is the handling of the nanosheet/photoresist sandwich during and after etching of the substrate. The structural stability depends on a large part on the thickness of the resist. Thinner films are more flexible but are also breaking more easily.

The whole transfer process is summarized in Figure 17. In a first step a layer of photoresist is spincast onto the sample as a transfer medium. The substrate can then be removed by etching. Due to the hydrophobic photoresist layer, the nanosheet-photoresist sandwich then floats to the surface of the aqueous solution, where it can be picked up with a new substrate. Alternatively, the sample can be placed to float directly



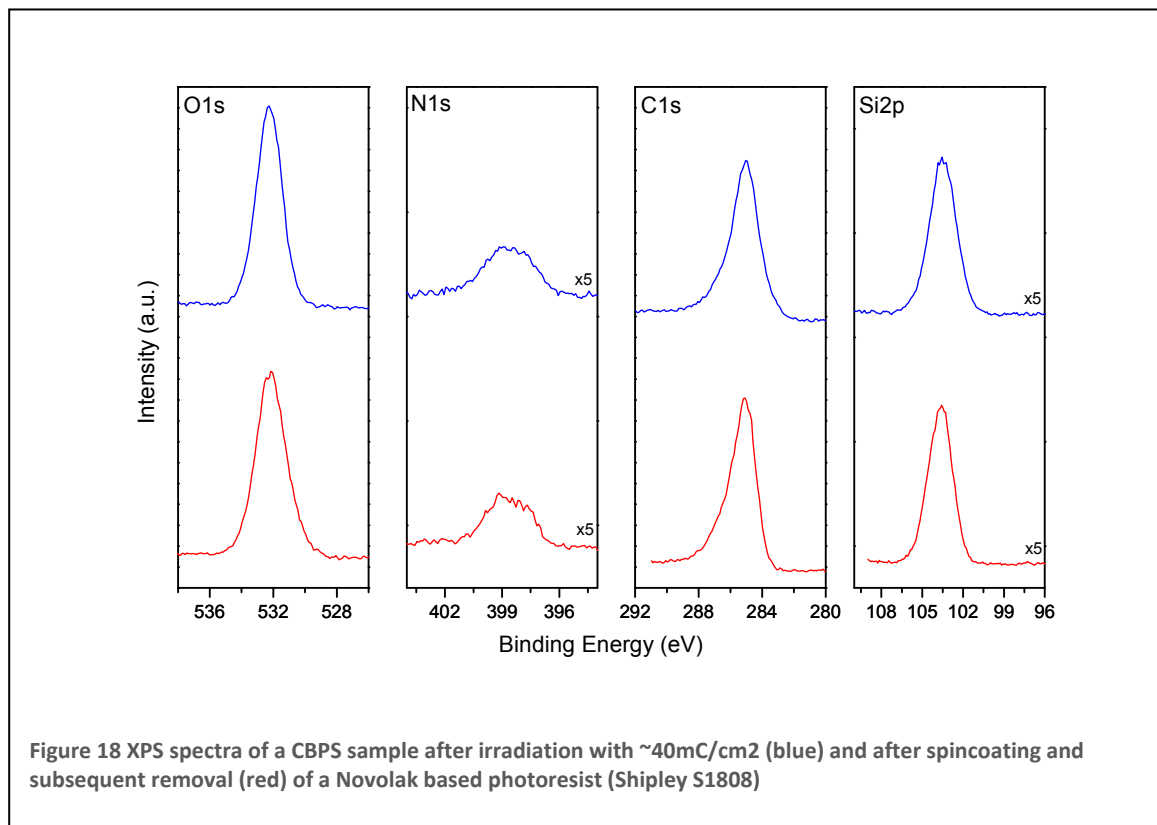
on top of the solution during etching, such that the buoyancy force is minimized. After the etching is complete, the remaining Si-substrate sinks to the bottom of the etching solution. In a final step the photoresist is dissolved.

In the following sections, the detailed procedure is shown for two kinds of nanosheet based on silanes on $\text{SiO}_2/\text{Si}_3\text{N}_4$ as well as thiols on gold substrates.

4.1.1 Transfer of silane based nanosheets

The possibility to underetch a CBPS nanosheet that was prepared on ultrathin silicon nitride membranes has been demonstrated by Küller and Eck [32, 60]. CBPS binds to a SiO_2 or Si_3N_4 surface via its methoxysilane anchor group, both of these substrates can be etched by hydrofluoric acid. The resulting freestanding membranes showed the enormous stability of the nanosheets, but a release from the substrate was not possible.

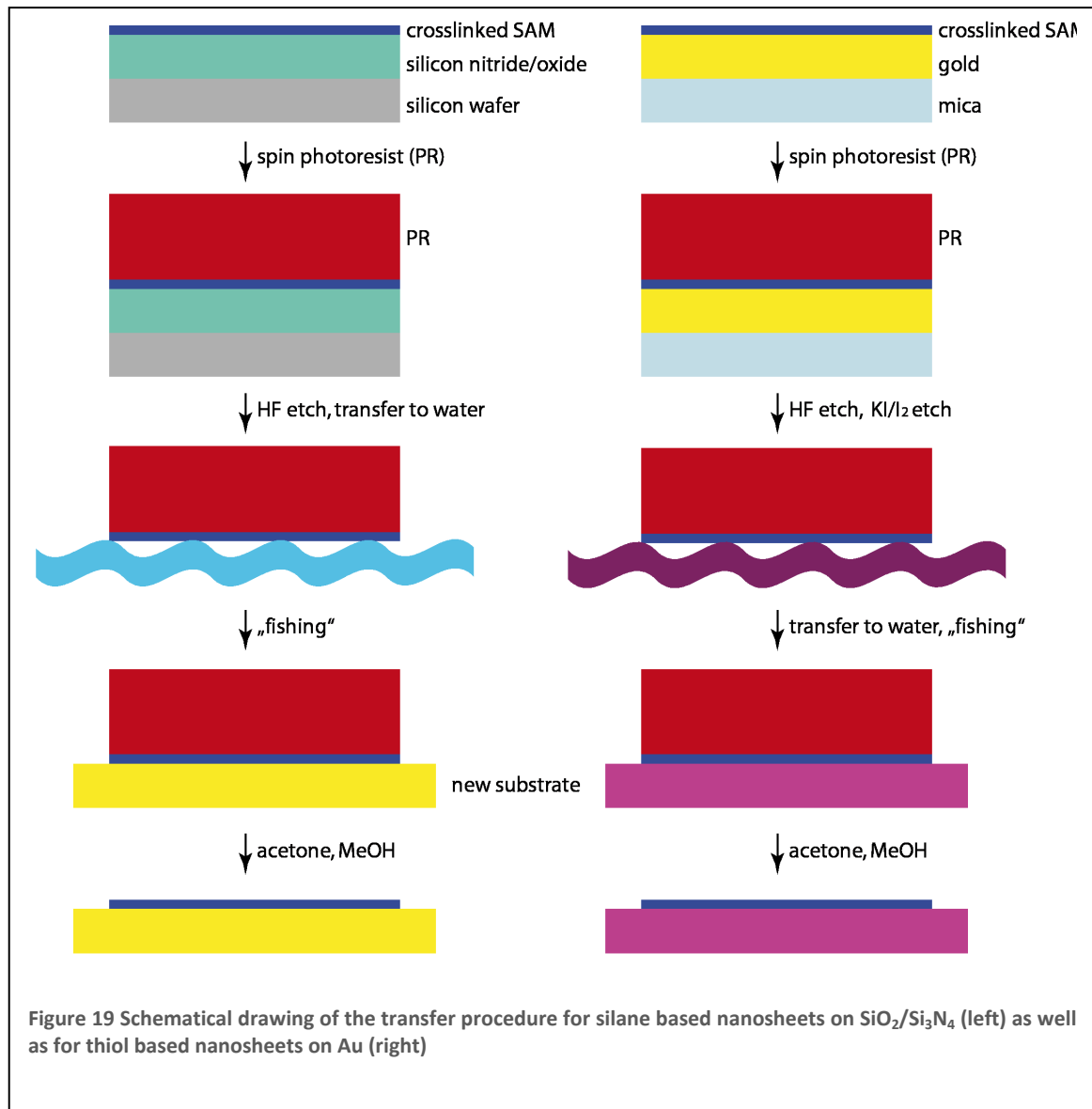
In order to transfer the CBPS nanosheet, as a first step the interaction of the CBPS nanosheet with photoresist was studied by XPS. Figure 18 shows XP spectra of the O1s, N1s, C1s and Si2p regions of CBPS on SiO₂/Si₃N₄ after cross-linking and after spincoating of photoresist and subsequent removal by rinsing with acetone. It can clearly be seen that no additional carbon contamination is left on the nanosheet. Also no attenuation of



the substrate signals is observed. The photoresist is therefore suitable as a transfer medium for the CBPS nanosheet.

The whole transfer process is schematically shown in Figure 19. The CBPS monolayer is prepared on a SiO₂/Si₃N₄ wafer and subsequently cross-linked with electrons. A layer of photoresist is applied by spincoating and dried on a hotplate. The SiO₂/Si₃N₄ layers can be rapidly removed by etching in hydrofluoric acid. The nanosheet is underetched from the sides, releasing the nanosheet/photoresist sandwich from the substrate. The nanosheet can then be placed onto a new substrate. This can be solid, but can also have holes, such as a TEM grid.

The choice of the original substrate is crucial for transferring the nanosheet. If the SAM is prepared on a Si wafer with a layer of SiO₂, it is also possible to remove the SiO₂ layer in



HF, however, the etch process is so fast that the nanosheet stays in close proximity of the Si wafer and forms a conformal contact. It is then impossible to release it. In case of the SiO₂/Si₃N₄ double layer system, both layers are etched at different rates, allowing the removal of the nanosheet.

4.1.1.1 First successfully transferred nanosheet

As a first test the nanosheet was transferred to a Si-wafer with etched trenches. These trenches were meant to represent a first test to see if it is possible to obtain freestanding nanosheet spanning over these trenches by the transfer process. Figure 20a shows an optical micrograph of such a sample with some pieces of transferred nanosheet before removal of the photoresist. In the SEM image after dissolution of the photoresist in (b) it is clearly visible that the nanosheet was successfully transferred. The outline of the piece from (a) is still visible due to some dirt, the nanosheet got folded at the edges, some parts at the top of the image are also missing completely. In some spots, especially on folds, the nanosheet also spanned over the trenches of the substrate, as is shown in (d) of a spot indicated by the arrow in (b). Mostly, the nanosheet was broken at the trenches, which is shown in (c), which is most likely due to capillary forces in the trenches during the drying process. However, these first results were very promising, as it was shown that the transfer is in general possible.

As a next step to fabricating freestanding nanosheets by the transfer process, Si-window

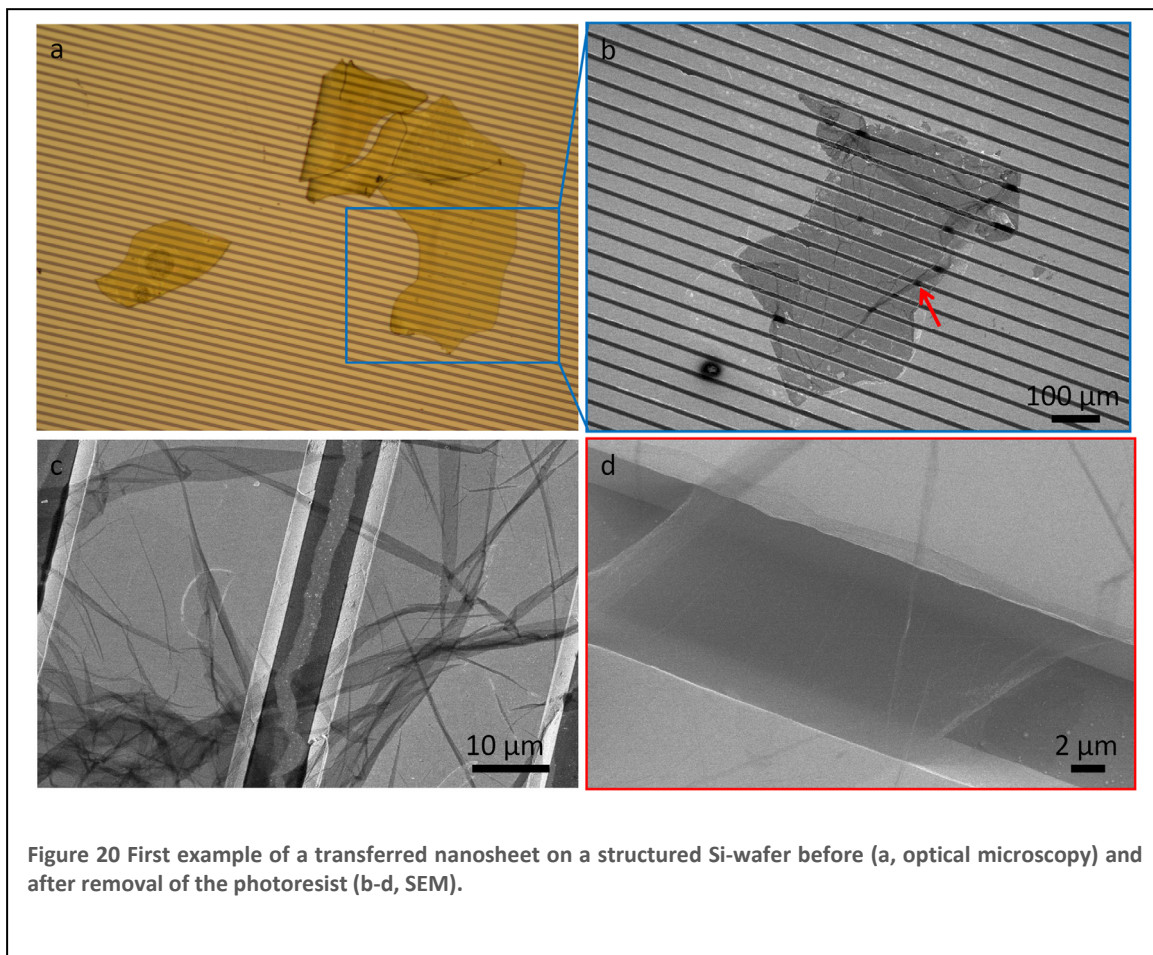
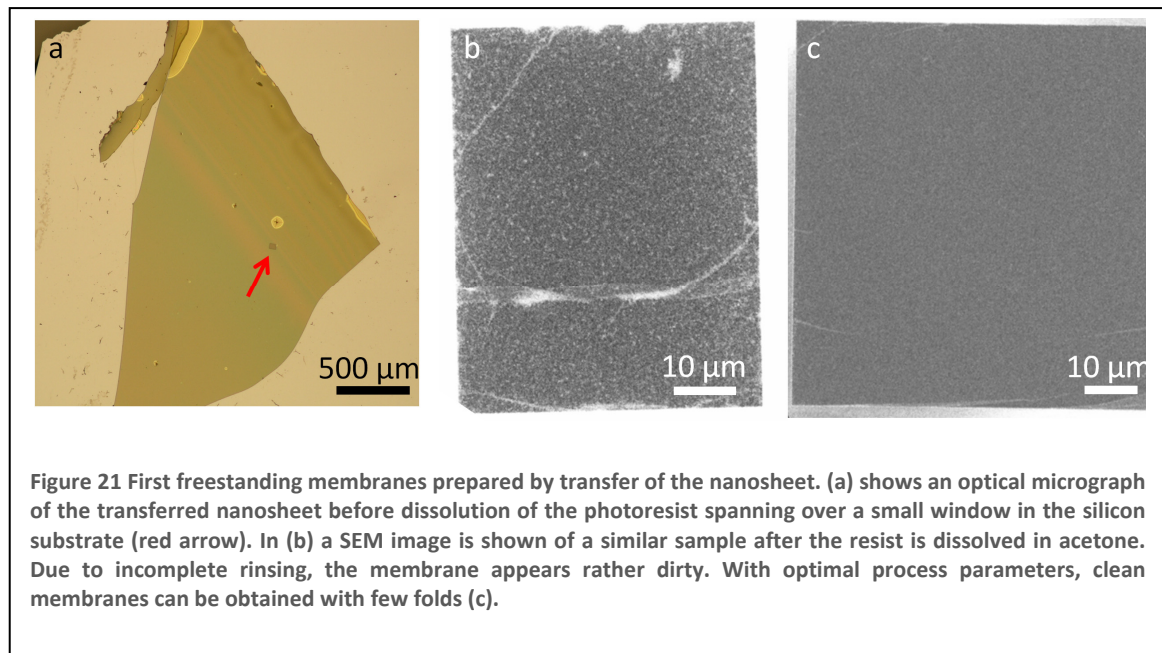


Figure 20 First example of a transferred nanosheet on a structured Si-wafer before (a, optical microscopy) and after removal of the photoresist (b-d, SEM).



substrates were used similar to those used previously by Eck and Küller [32, 60] but without the nitride membranes. These samples have the advantage that the solvent is not confined between the sample and the nanosheet, so that capillary forces during drying should be minimized. Also, the nanosheet has a large contact area to the sample.

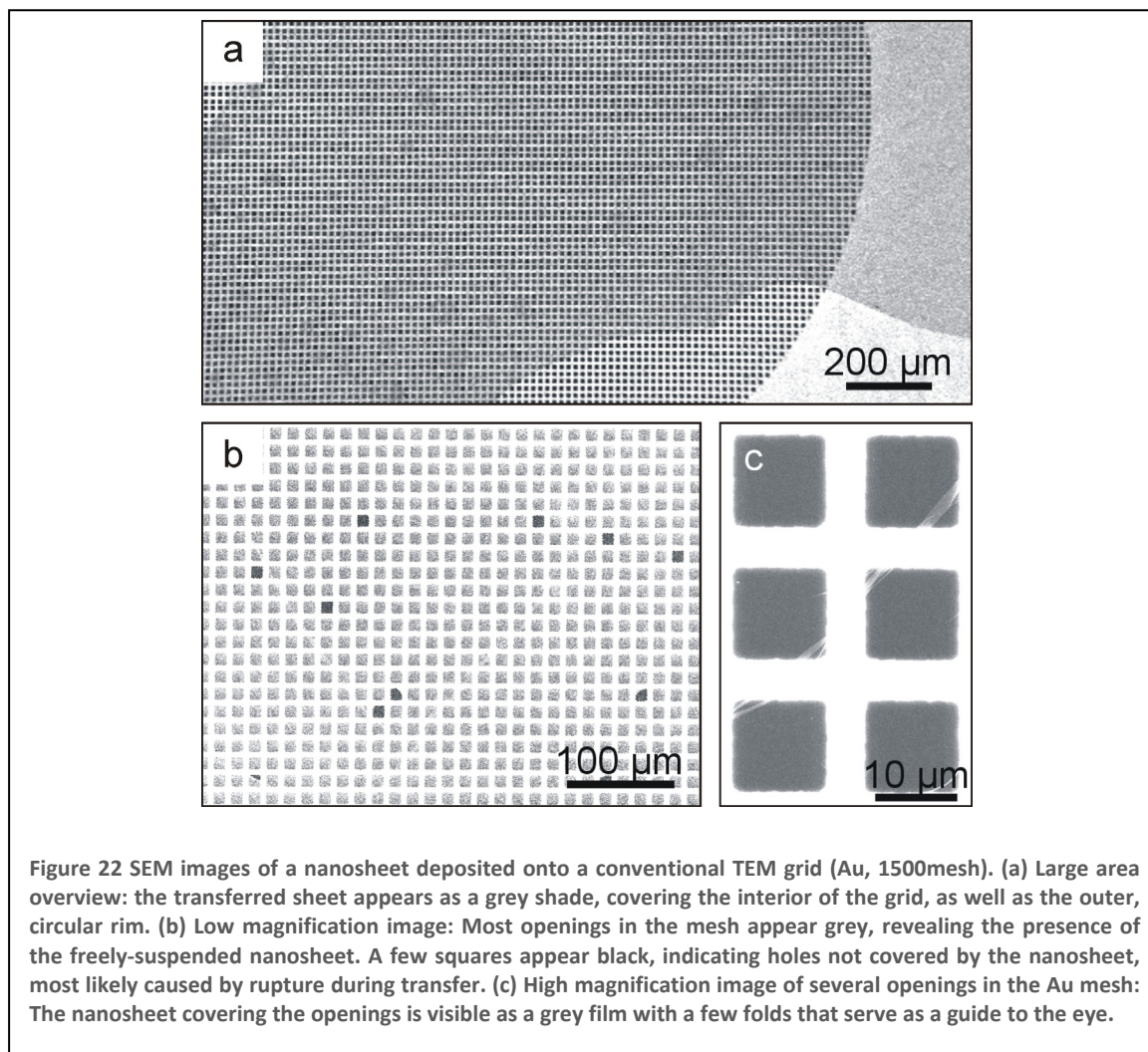
An example of such a window substrate is shown in Figure 21. Again, (a) shows a sample before removal of the photoresist, the location of the window is indicated by the arrow. To visualize the nanosheet in an SEM, a very high value of image contrast must be chosen, such that the contrast of the substrate is saturated. The freestanding membrane in (b) is one of the first successfully transferred membranes, it appears rather dirty as the rinsing time was not sufficient to remove all photoresist. By carefully adjusting the processing parameters, clean nanosheet membranes can be obtained, as shown in (c).

4.1.2 Freestanding nanosheets on conventional TEM grids

The main advantage of the transfer process is the possibility to coat arbitrary substrates with nanosheet. It is therefore not necessary to use silicon windows for preparing freestanding nanosheet membranes. Conventional TEM grids are cheaper, have larger numbers of openings, and are available with a variety of hole sizes from $\sim 1 \mu\text{m}$ to several hundred μm . In principle, all available TEM grids can be used as a support for the

nanosheets. However, it was found that the nanosheets are more stable the smaller the free-standing areas are.

Figure 22 shows scanning electron microscope (SEM) micrographs of the nanosheet covering the square holes of a TEM grid (Au, 1500 mesh). With these contrast settings



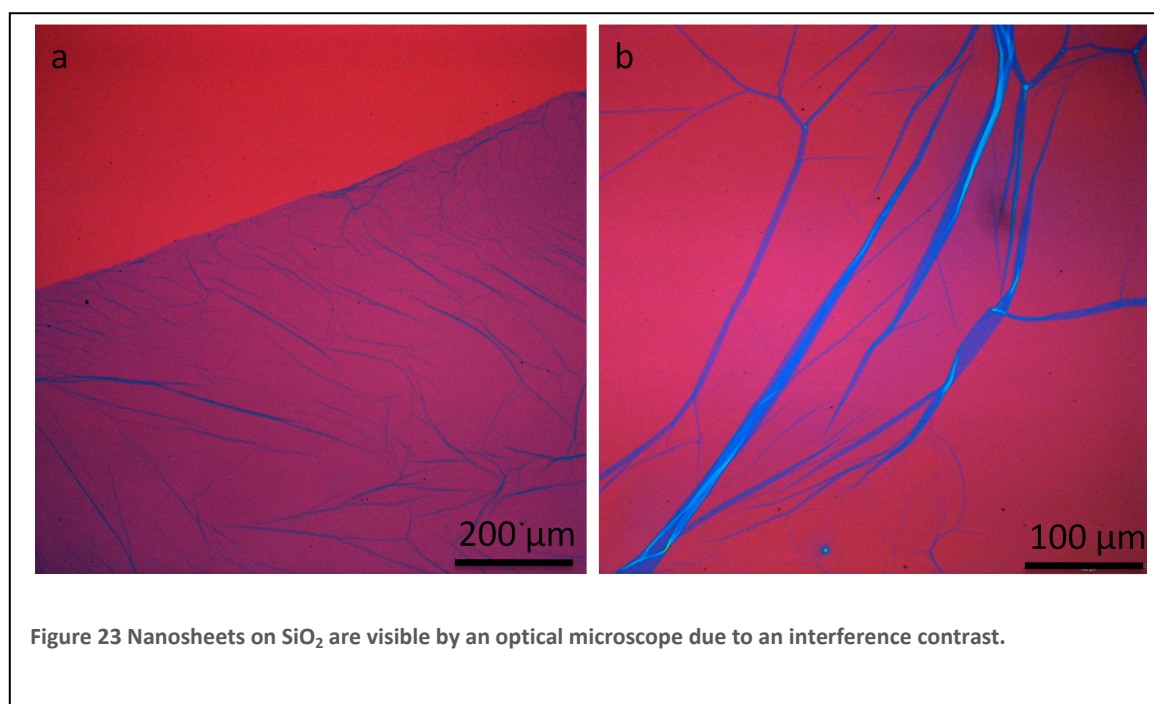
only the nanosheet on top of the Au grid can be seen. The grid in this case is homogeneously coated, only the area in the bottom right is not covered by the nanosheet. To also visualize the nanosheet also in the freestanding areas, the contrast is set so that the gold grid is saturated, while the rectangular openings covered with the nanosheet appear grey. Some of the openings appear black, indicating the absence of the nanosheet in these areas, presumably caused by film rupture. (c) shows the $11 \times 11 \mu\text{m}^2$ rectangles covered by the freestanding nanosheet at higher magnification. The sheet shows occasional folding most likely resulting from the handling of the grid during

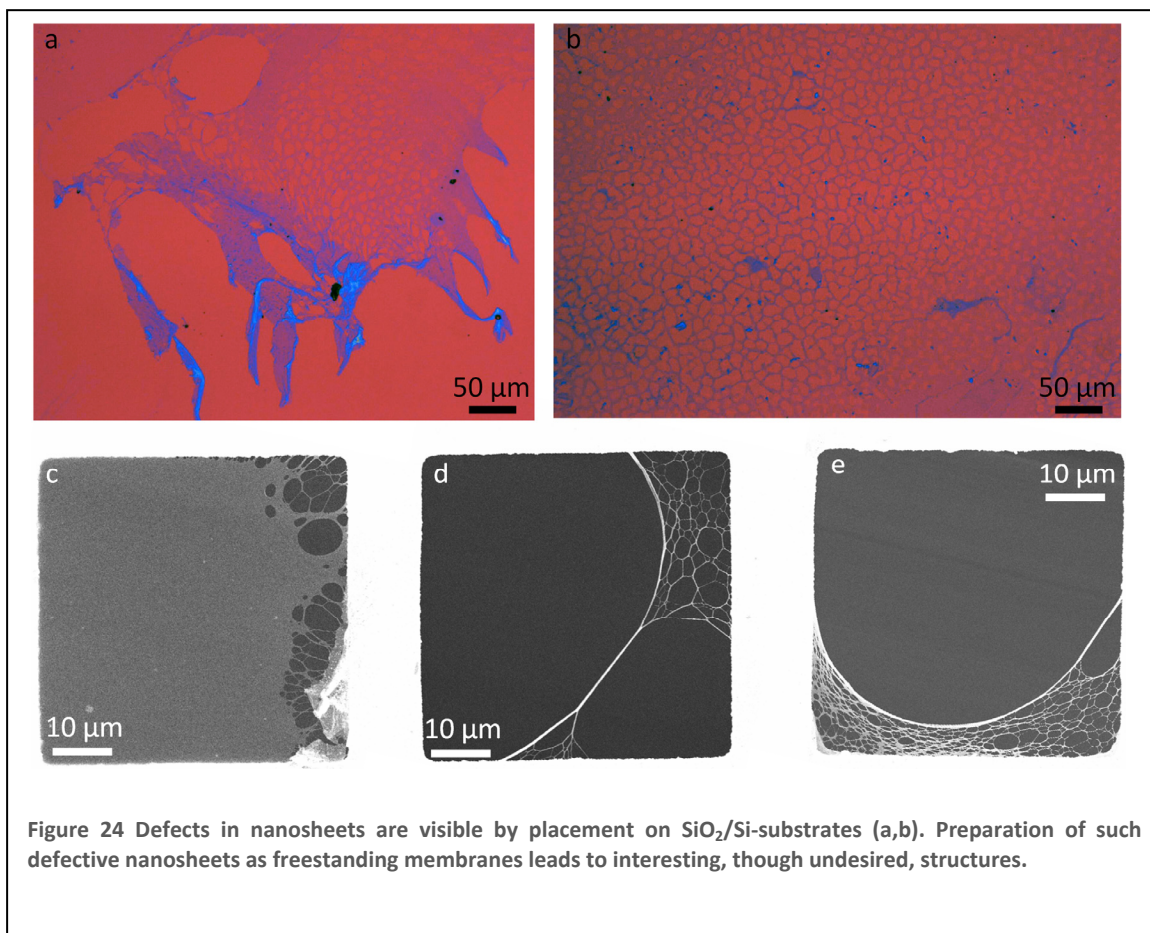
the preparation process. The major part of the area, however, is defect-free, which renders the nanosheet practically invisible for SEM studies.

4.1.2.1 Visibility of nanosheets on SiO_2

Similar to graphene, the nanosheet can be seen by optical microscopy by means of an interference contrast, if it is placed on a Si wafer with a 300 nm thick thermal oxide layer [46, 61]. The nanosheet appears darker than the substrate and the color is shifted slightly towards blue as can be seen in Figure 23. The origin of this contrast will be discussed later (chapter 4.4.3). Folded areas can easily be seen, as well as defects. This provides an easy and quick method for monitoring the quality of the nanosheet

An example of a transferred, defective sheet is shown in Figure 24. The nanosheet forms a porous network, where the size of the pores and intact parts varies. The origin of the defects could be due to incomplete cross-linking as a result of charging. An alternative explanation would be that the monolayer was not homogeneously formed on the substrate. When prepared freestanding, the majority of the windows are ruptured, however a few of them are showing stable networks that have a similar appearance to lacey carbon films (Figure 24c-e).





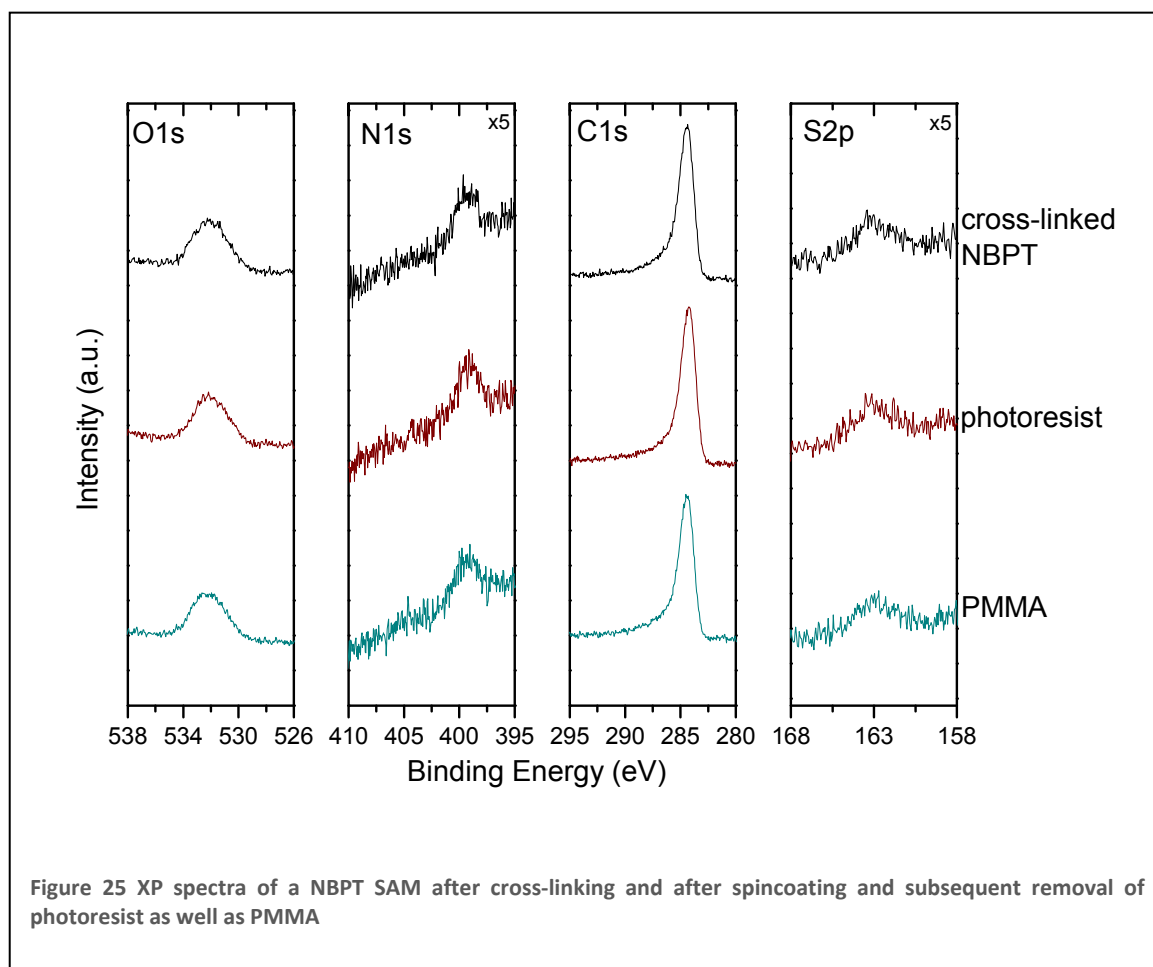
4.1.3 Transfer of thiol-based nanosheets

In principle, thiol based nanosheets prepared on Au-substrates can be transferred in the same manner as was described for the silane/SiO₂/Si₃N₄ system, substituting the hydrofluoric acid by a specific Au-etchant (KI/I₂/H₂O). As the etch rates of Au are several orders of magnitude slower, it is not feasible though to only rely on the underetching from the sides of the sample. Ideally the whole bottom surface of the Au is accessible by the etchant. A possible solution is the preparation of cross-linked SAMs on thin Au foils, however, these are lacking the stability needed for easy handling and the use of stable gold foils is too costly.

An alternative are thin Au films that can be released from their substrate after preparation of the nanosheet and application of the transfer medium. Au films on mica have been used for years to have access to ultraflat Au substrates for scanning probe experiments (“template stripped gold”). Normally the gold is released from the mica substrate by immersion in tetrahydrofuran (THF) or hydrofluoric acid. THF would be

more desirable, as it is not as dangerous, unfortunately it is not compatible with photoresists though.

The modified process for transferring thiol based nanosheets is shown in Figure 19. As an additional step, the cleavage of the gold film off the substrate is shown. Again, the suitability of the photoresist as a transfer medium has to be checked. This is shown for a



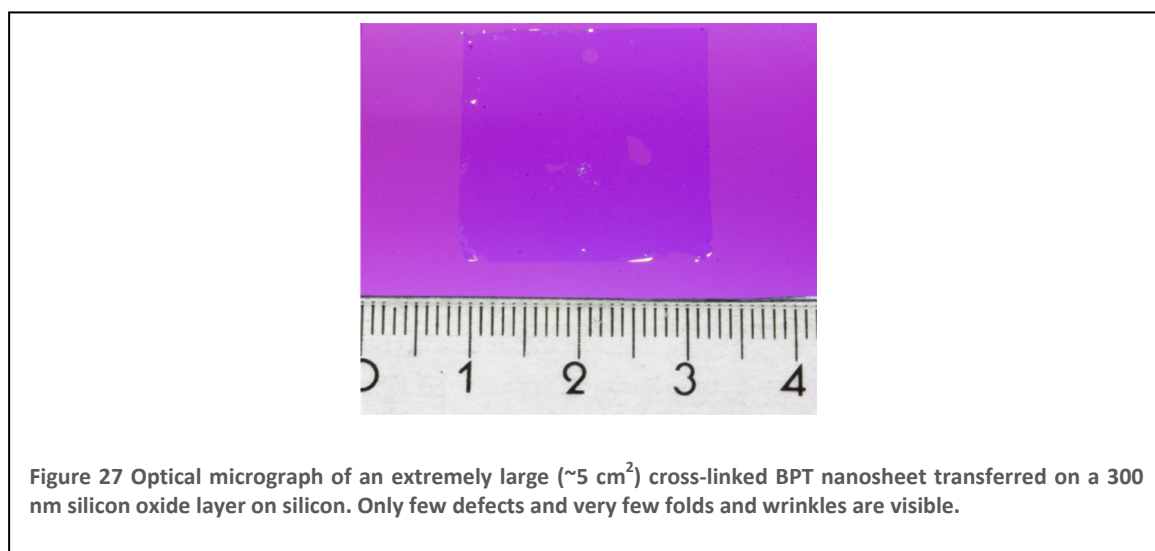
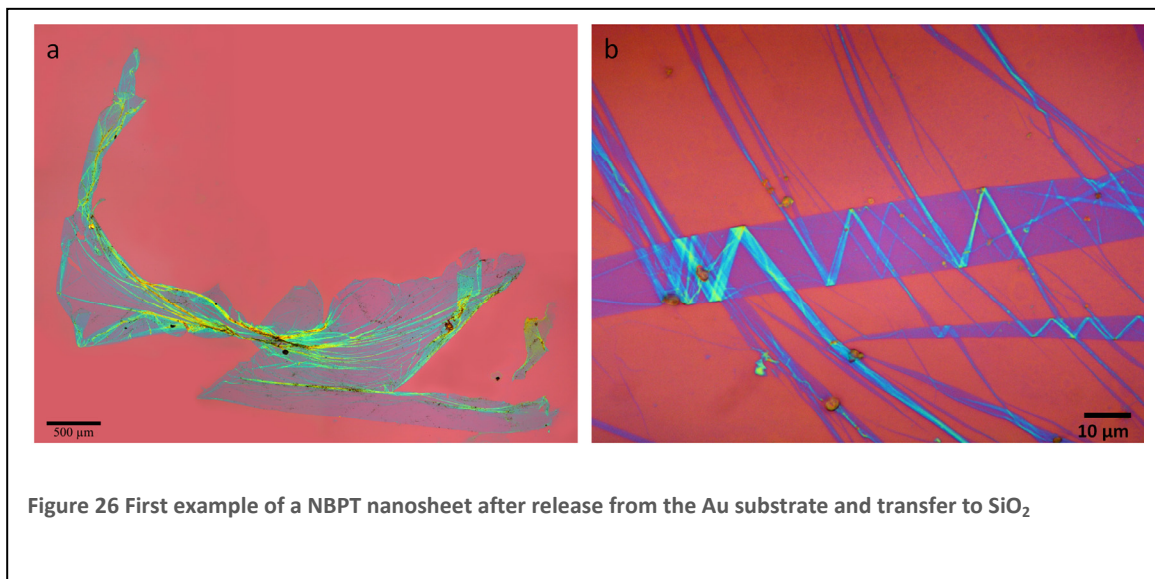
cross-linked NBPT SAM, bearing an Amino functional group, in

Figure 25. As an alternative transfer medium polymethyl methacrylate (PMMA) was also tested. PMMA is able to withstand long exposures to HF better than the Novolak based photoresists, which are losing their structural stability and become brittle. Both the photoresist as well as PMMA can be totally removed from the NBPT nanosheet.

The first example of a successfully transferred NBPT nanosheet is shown in Figure 26. The adhesion to the substrate in this case was not ideal, so that lots of folds are visible.

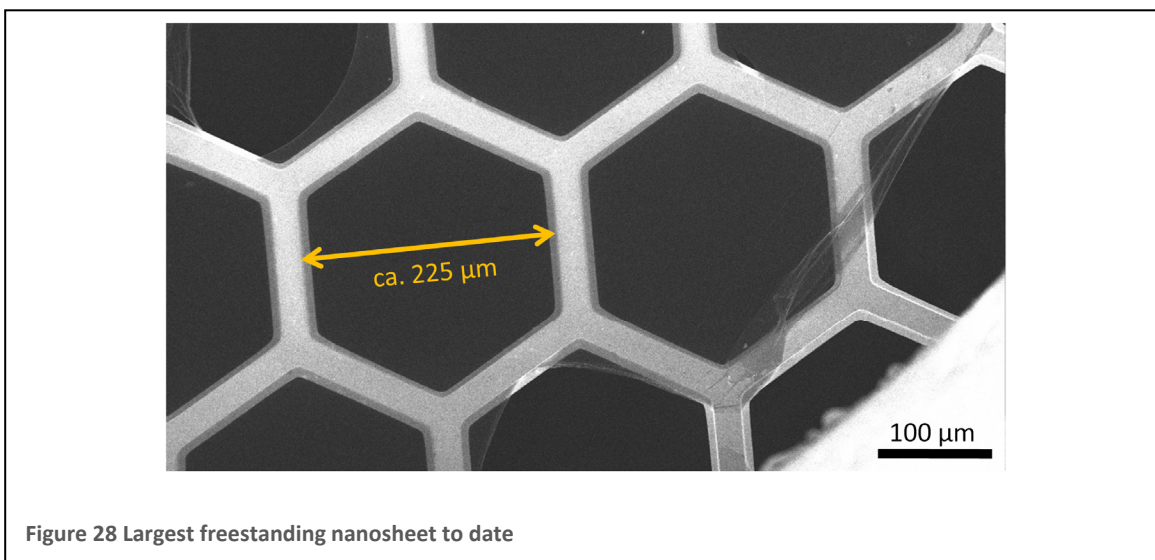
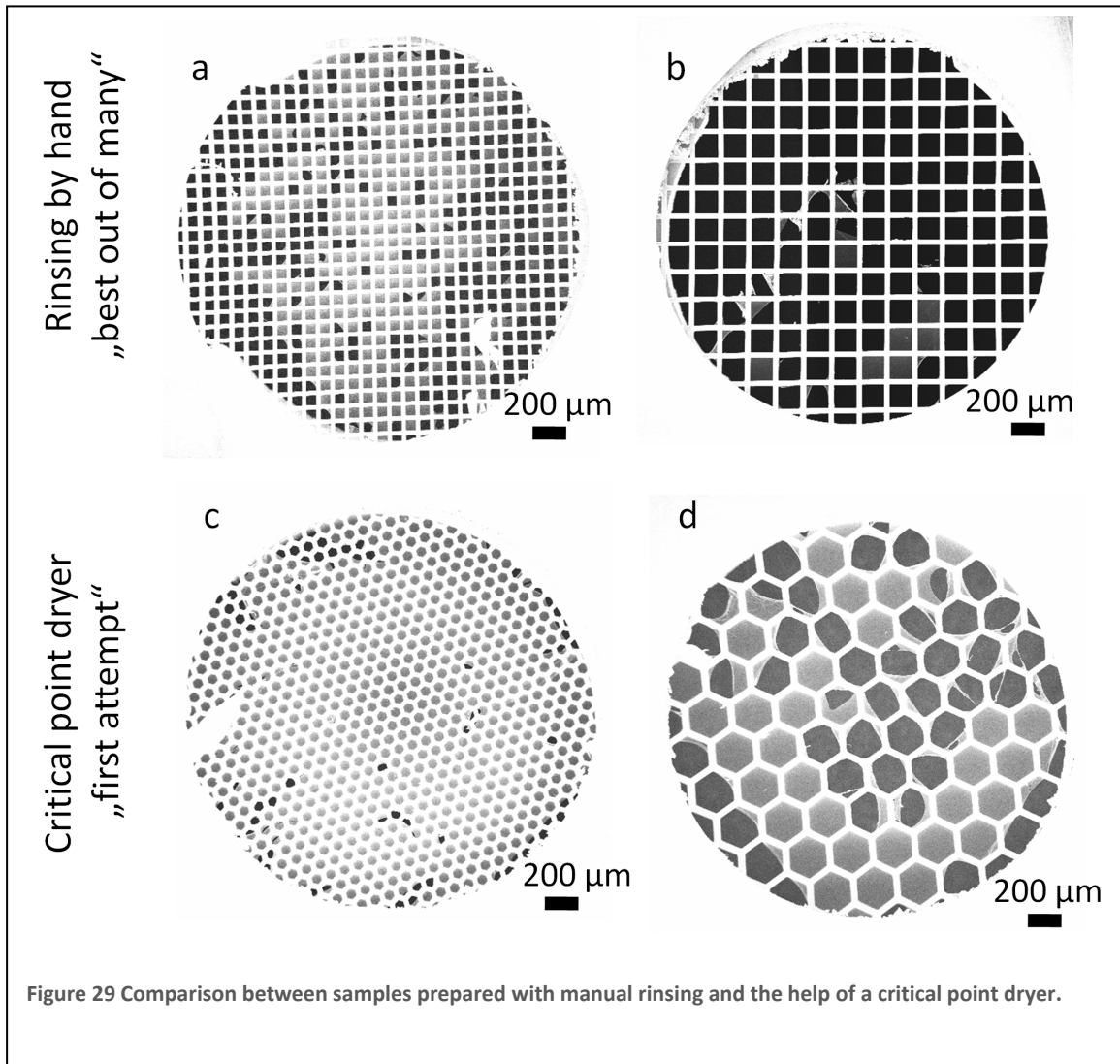
These give rise to esthetically pleasing structures, especially when folding occurs in two directions, as is the case in (b).

However, by optimizing the conditions during transfer and rinsing of the sample, it is possible to obtain very large nanosheets with very few folds and wrinkles. The size is limited only by the available Au/mica substrates and the maximum area that can be homogeneously irradiated with electrons for cross-linking in the floodgun. A very large BPT nanosheet is shown in Figure 27; the area of the nanosheet is $\approx 5 \text{ cm}^2$.



4.1.4 Critical Point Dryer

The biggest problems associated with the preparation of large freestanding nanosheets in high yields are capillary forces and surface tension. Critical point drying (CPD) is a standard technique in the preparation of biological specimen for electron microscopy as well as the fabrication of MEMS. Using CPD for removal of the solvent after dissolution of the photoresist can enhance the yield significantly. Figure 29a shows the nanosheet on a 300mesh TEM grid by ways of manual rinsing and drying in air. This sample represents the highest yield out of many, in most cases it is significantly lower. (b) shows the largest freestanding sheets that were obtained by this method. In comparison (c) and (d) shows some of the very first samples that were prepared with the help of a critical point dryer. For a 300mesh TEM grid nearly all openings are covered and even for 100mesh about half of the membranes are intact. So far this is the largest freestanding nanosheet membrane. A higher resolution image is shown in Figure 28. The aspect ratio of this membrane is 1:225000, which is remarkable regarding its thickness of just 1 nm. It is likely that this yield and the size of the membranes can still be extended by further optimizing the conditions. However, for most applications a 300mesh TEM grid should have sufficiently large windows. Ruptured openings are also helpful for finding the right contrast settings for visualization of the sheet, as defect free samples would be difficult to distinguish from ones without nanosheet.



4.1.5 Summary

A method was developed for the transfer of nanosheets onto arbitrary new substrates, especially as freestanding membranes spanning over the large openings of standard TEM grids. Photoresist and PMMA can serve as a transfer medium that provides mechanical support during the process and can be dissolved afterwards. It was possible to transfer nanosheets made from silane as well as thiol based SAMs, and the method should be extendable to other substrate-SAM combinations as well. Of particular interest might be a SAM with a hydroxamic acid headgroup on iron substrates, as this would greatly reduce costs as compared to the thiol-gold system. It should also be possible to transfer different materials of similar thickness than the nanosheet. This could be graphene, and other layered minerals, but also more weakly bonded films, such as supramolecular aggregates that are held together by hydrogen bonds or even metal-organic frameworks (MOFs) if the etching conditions are optimized for the given material.

4.2 Asymmetric functionalization of nanosheets – Janus membranes

Self-assembled monolayers generally consist of amphiphilic molecules that are able to bind to a substrate with the “head” whereas the other end (the “tail”) is presenting a new interface. The properties of this interface can be modified by tailoring of these end-groups. This can either be achieved by using molecules with the desired end-group functionality, or by coupling reactions on the SAM in a second step.

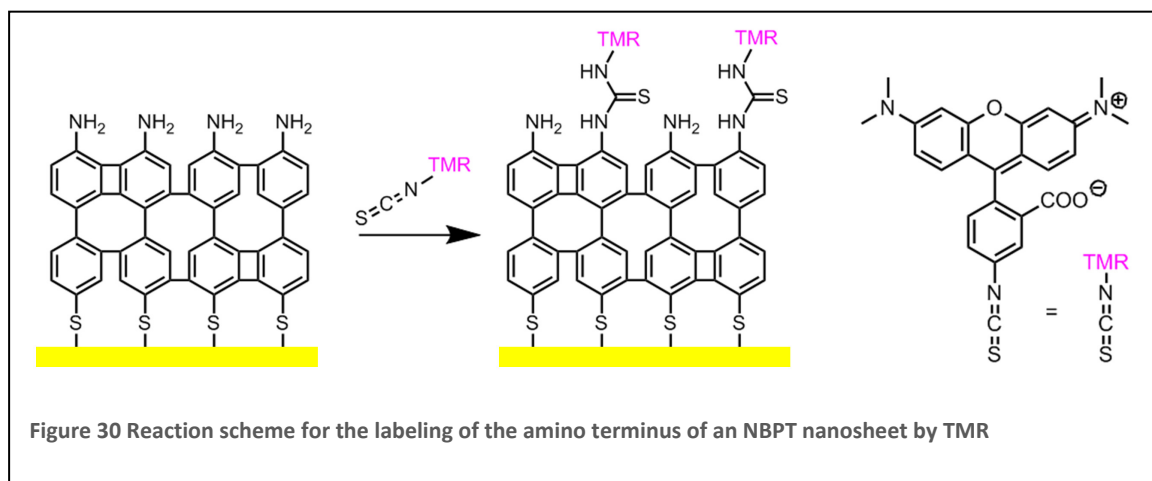
By releasing the nanosheet from the substrate, the SAMs head-group is no longer buried underneath the monolayer, but now presents a new interface. Its properties are ideally those of the amphiphilic molecules that originally formed the SAM. Nanosheets can thus be considered “Janus” membranes, as they have two distinct faces.^{viii} This term is usually used in the literature for particles with two sides of different chemistry (Janus particles) [62]. Such properties are extremely interesting for such thin membranes [2]. The asymmetric functionalization can possibly present a driving force for ion transport, similar to the proton- or ion pumps in biological systems [63-65]. To this end, it is thus necessary to selectively modify both faces of the nanosheet. In this chapter the feasibility is explored by functionalization with fluorescent dyes.

Another possible application for fluorescently labeled SAMs is chemical sensing [66-68]. The fluorescence is influenced by the interaction of the SAM with an analyte. Most studies on SAMs, however, have been performed on metal substrates. These are problematic for fluorescence applications, as the signal is quenched by energy transfer to the metal substrate. Recent studies that use fluorescently labeled SAMs for sensing applications, therefore make use of SAMs on glass substrates [69] or introduce a spacer layer that prevents/minimizes the quenching of the signal. The spacer layer can be the native oxide on a metal substrate [70] as well as an organic linker molecule [29], the fluorescence intensity is then increasing as a function of the spacer length. The problem of signal quenching can be circumvented by transferring cross-linked, labeled nanosheets to new insulating substrates.

^{viii} Janus is the Roman god of gates and doors, but also beginnings and endings, which is still present in the name of the month January. He is usually depicted with two faces or heads facing in opposite directions.

4.2.1 Modification of the Amino-terminus

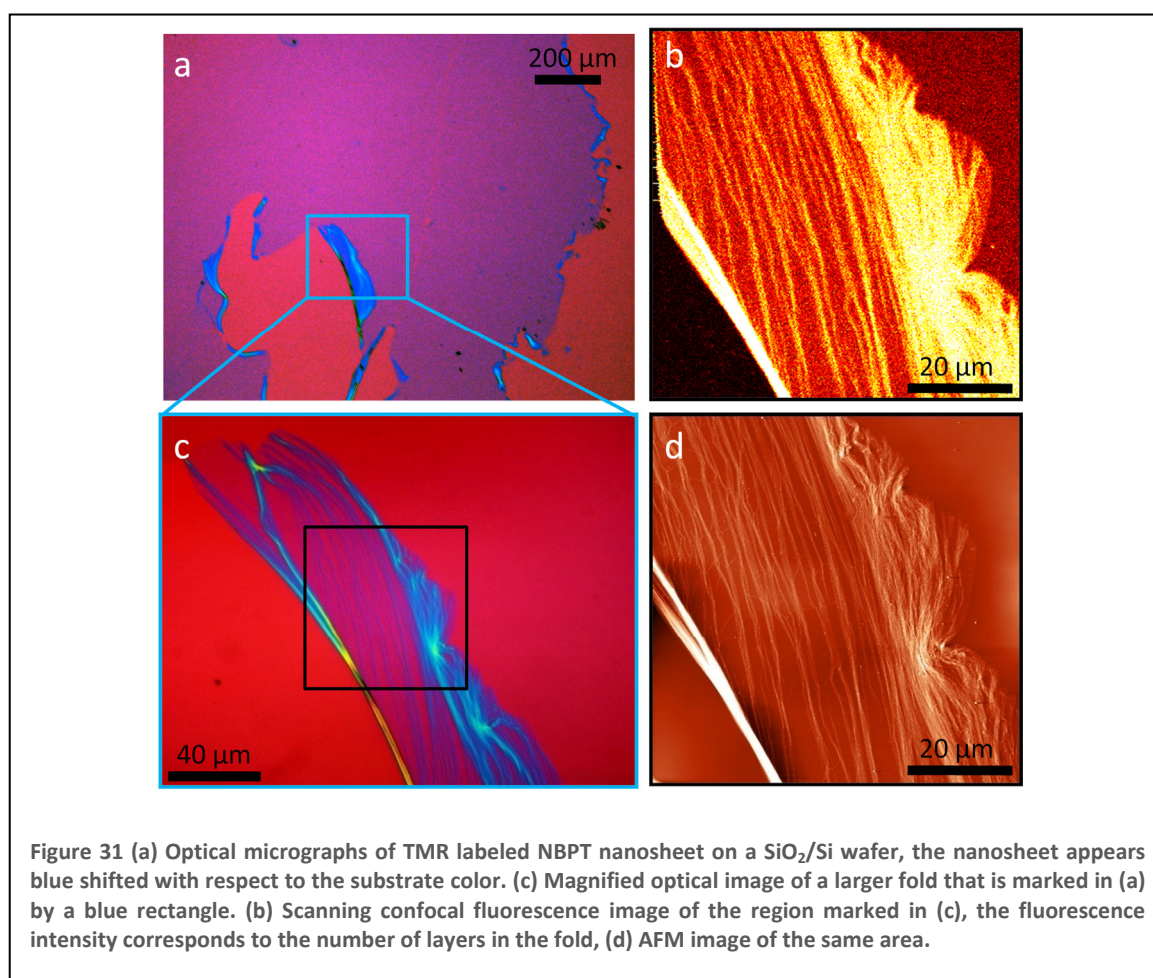
The functionalization of cross-linked NBPT SAMs with tetramethylrhodamine (TMR) was described previously by Geyer [23, 71]. Coupling to the amino group is achieved by using isothiocyanate as a linker to form a thiourea. The formation of a dithiocarbamate



(although these are unstable in aqueous solution) upon reaction of the isothiocyanate with a thiol is excluded by labeling the nanosheet before removal of the substrate, so that only the topmost interface is accessible to the dye. The reaction scheme is shown in Figure 30. The successful coupling can be monitored by atomic force microscopy for samples that were structured by proximity printing (see chapter 4.3.1). The coupling of the dye corresponds to a small increase in thickness (~ 0.5 nm) in the amino-terminated areas of the sample. It was not possible to obtain fluorescence images, presumably due to efficient quenching by the gold substrate.

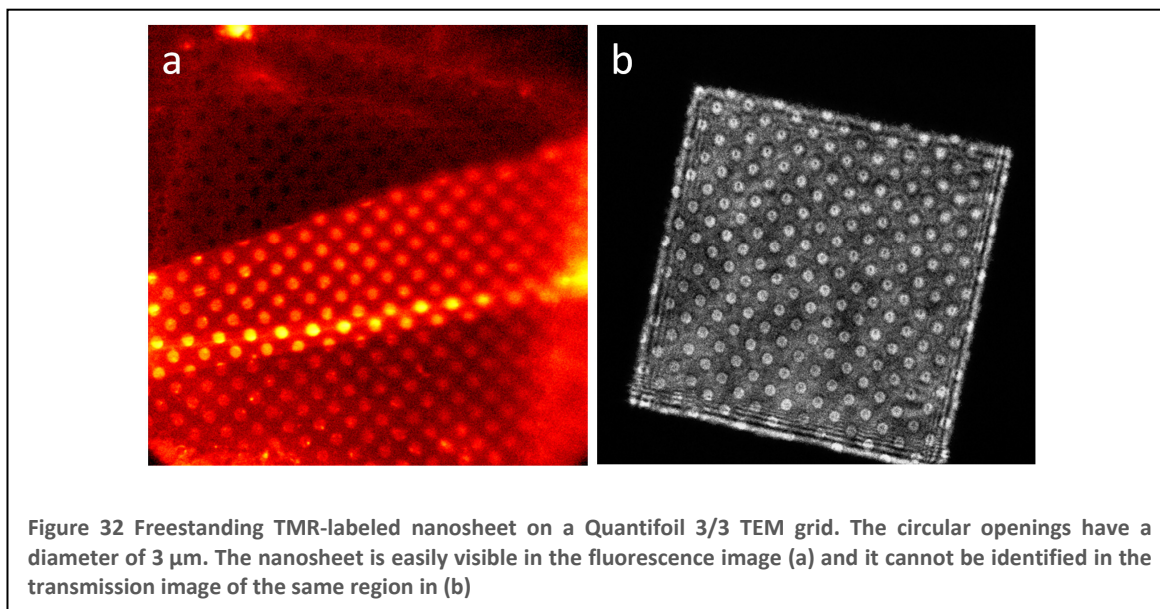
The labeled nanosheet can then be transferred to a SiO_2/Si wafer, where it can be imaged by optical microscopy. Figure 31a shows a large piece of TMR labeled NBPT nanosheet that shows a few folds and defects on the edges. One of these folds (marked blue) is shown magnified in (c). The color in this fold corresponds to the number of layers of the nanosheet. Figure 31b is a scanning confocal fluorescence image of the region that is marked in (c). The fluorescence intensity corresponds to the additional number of layers within the fold; the more layers of labeled nanosheet the higher is the detected fluorescence signal. This is confirmed by the AFM topography image that is shown in (d).

By transferring the labeled nanosheets, it is also possible to prepare them freestanding. This is demonstrated in the fluorescence image in Figure 32a, where the nanosheet is spanning over the holes in a quantifoil TEM grid. The size of the openings is $3\ \mu\text{m}$. The



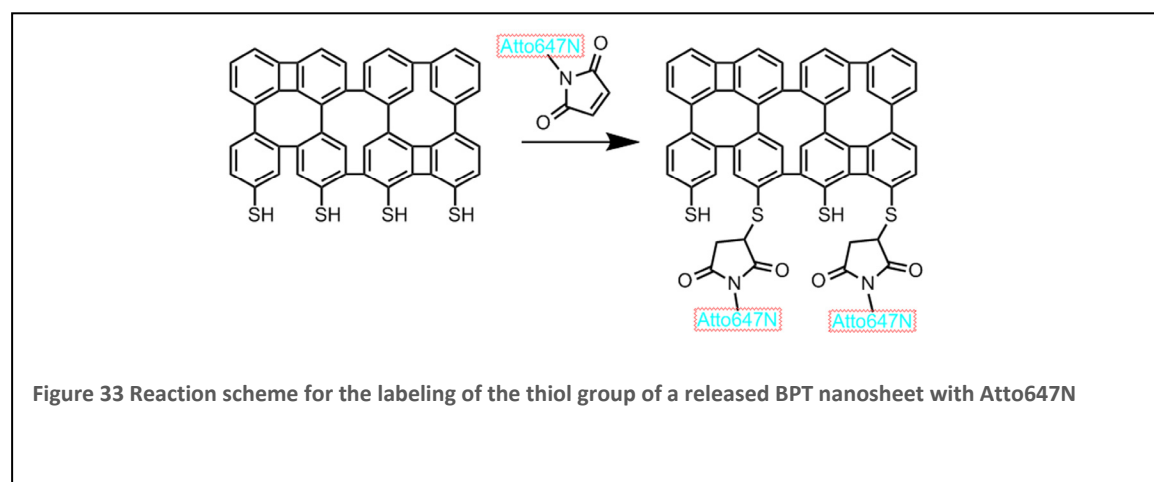
fluorescence is partially quenched by the carbon grid, so that the freestanding areas

appear brightest. (b) shows the same area in transmission mode, where it is not possible to see the nanosheet.



4.2.2 Modification of the thiol group

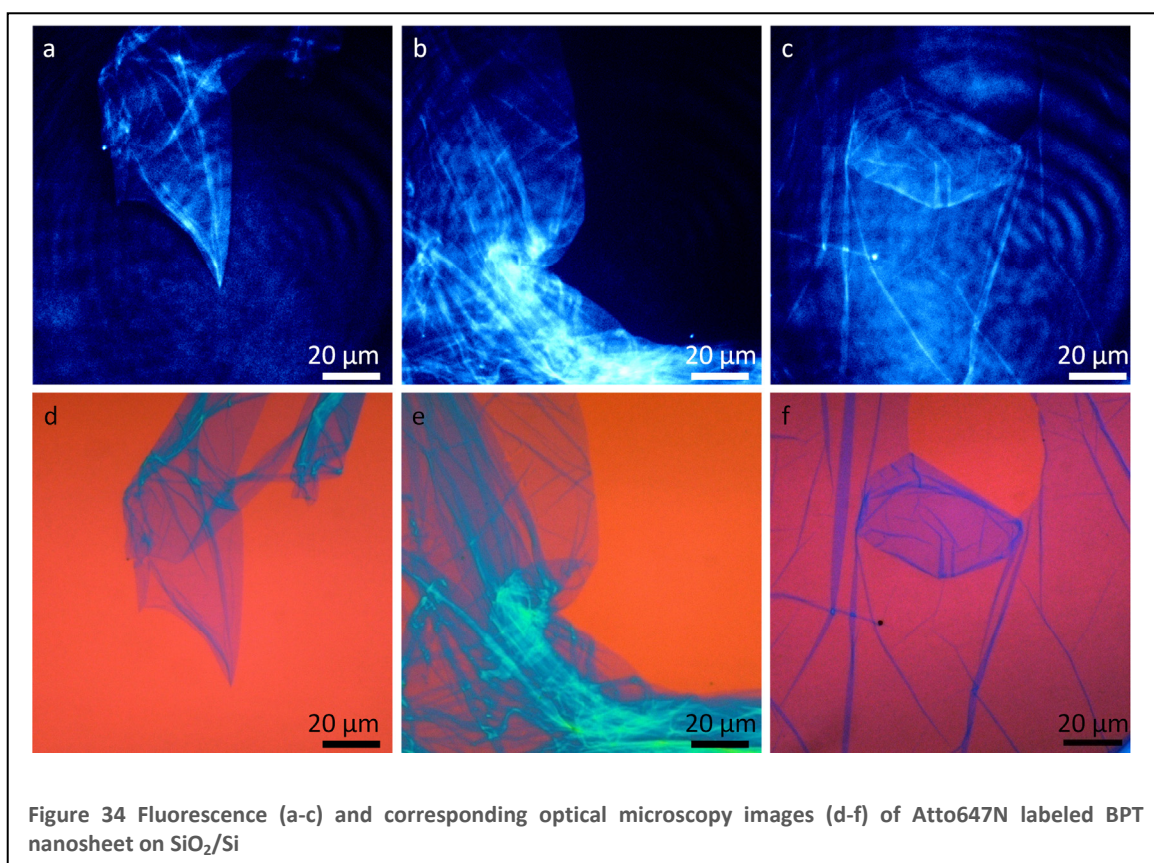
After showing that the selective labeling of the amino terminus and subsequent transfer to a new substrate is possible, the feasibility to also modify the thiol group can be studied. Thiols can generally be labeled by reaction with a maleimide to form a thioether. The reaction was conducted by letting the nanosheet/PMMA sandwich float on a buffered dye solution. Only the bottom side of the nanosheet was therefore exposed to the dye. Additionally, a BPT nanosheet was chosen for these experiments, as

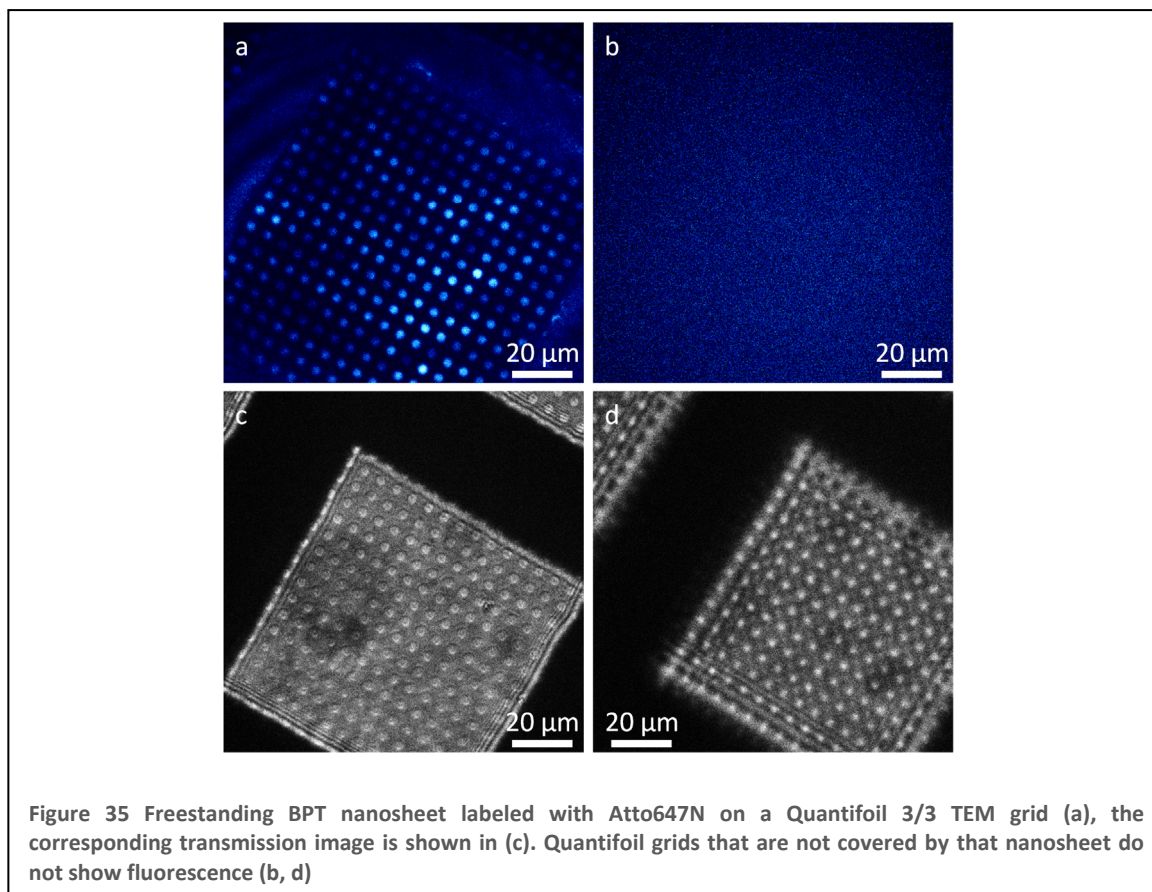


it has no other functional groups other than the thiol. The reaction scheme is shown in Figure 33, the exact structure of the dye is not disclosed by the manufacturer.

Some successfully labeled and transferred pieces of nanosheet are pictured in Figure 34. Folds are again chosen as they are clearly showing that the nanosheet is fluorescent. For comparison, optical micrographs of the same spots are also shown. The ring-like structures in the fluorescence images are artifacts (interference) due to the mounting of the samples on cover slides.

It is also possible to prepare freestanding membranes of labeled nanosheet. To this end it was transferred onto Quantifoil TEM grids and imaged by fluorescent microscopy (Figure 35). The openings in the grid appear brightest in the fluorescence image. This is most likely due to quenching in the areas of the carbon film, whereas no quenching is observed in the freestanding membranes. A Quantifoil grid that is not covered by the labeled nanosheet does not show any fluorescence.



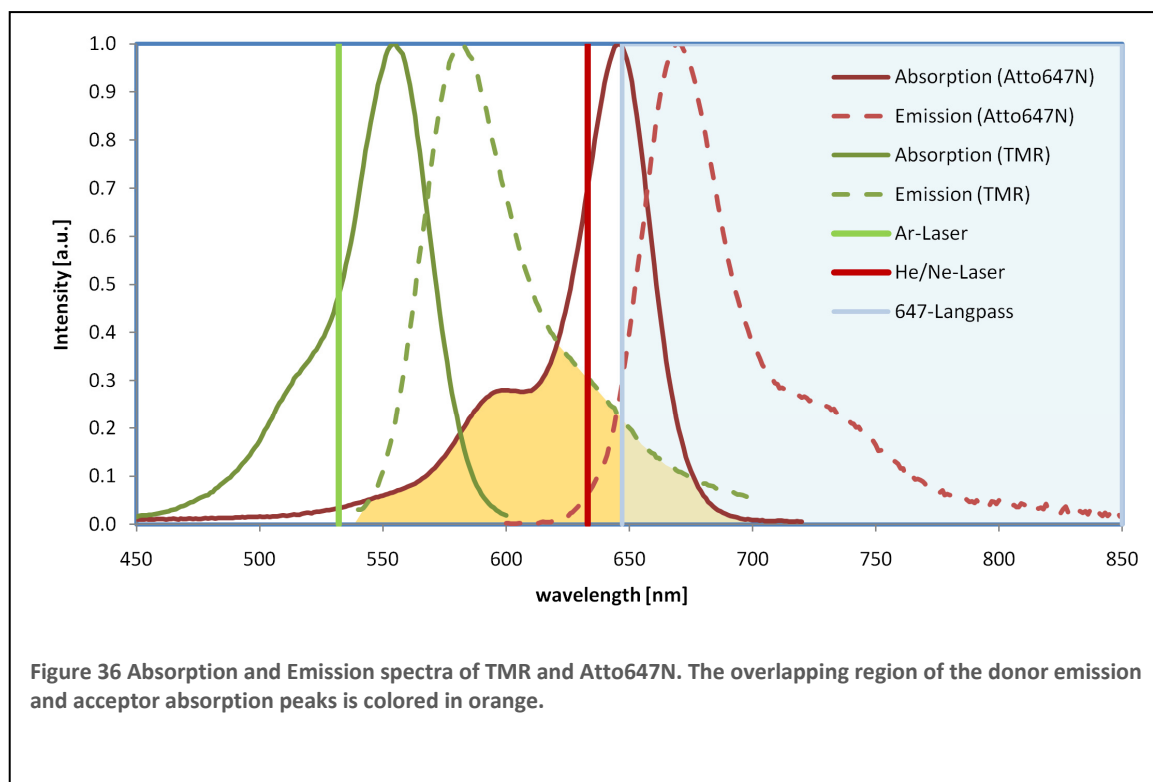


4.2.3 Doubly labeled nanosheets

Due to the thickness of the nanosheet the two dyes are in very close proximity if the nanosheet is labeled both on the amine and the thiol termini. At such short distances, it is expected that energy is transferred between the dyes by Förster resonance energy transfer (FRET). This is a nonradiative dipole-dipole interaction between two fluorophores with overlapping absorption (acceptor) and emission (donor) bands. For TMR and Atto647N the absorption and emission bands are shown in Figure 36, the overlapping region is colored orange. The efficiency E_{FRET} of the energy transfer is depending on the distance of the molecules r and decays by an inverse sixth power law:

$$E_{FRET} = \frac{1}{1 + \left(\frac{r}{R_0}\right)^6} \quad (30)$$

R_0 is called the Förster radius which is different for each donor-acceptor pair and is generally a few nanometers. It is defined as the distance where E_{FRET} is 50%. Due to this strong distance dependence, FRET can be used as a “nano-ruler” for measuring distances.



In order to verify that there is an energy transfer between the top and bottom side of the nanosheet, it is necessary to acquire images of both the singly labeled (TMR or Atto647N), as well as the doubly labeled (TMR and Atto647N) nanosheet at identical laser intensities for both excitation wavelengths. All following experiments were thus conducted with NBPT nanosheets to have both thiol- and amino-groups available for coupling to a dye. In Figure 36 the excitation wavelengths are shown as vertical lines for the respective laser. Images are taken using a 647 nm longpass filter (light blue).

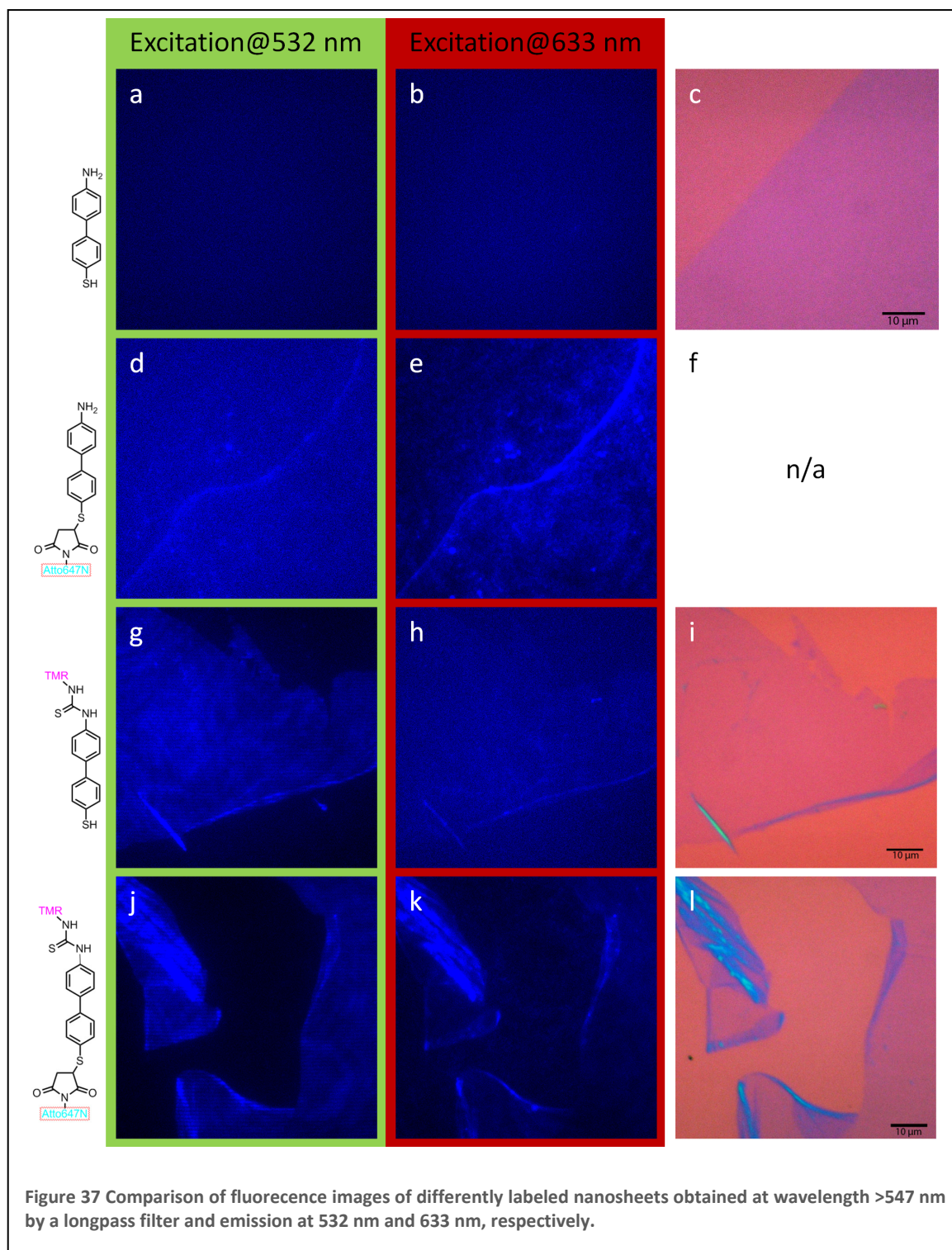
Representative fluorescence images are shown in Figure 37, a NBPT molecule is depicted in each row to show how the nanosheets are labeled. In the first row (a-c) images of an unlabeled nanosheet are included as a reference, no fluorescence is observed. The second row of images is from an Atto647N labeled nanosheet. Nearly no fluorescence is observed for excitation at 532 nm (d), only the edge of the nanosheet is visible but the intensity on both sides of the edge is identical. A weak contrast can be seen at 633 nm (e). For a TMR labeled nanosheet the case is reversed. Only at 532 nm the nanosheet shows fluorescence (g). Interestingly, the nanosheets contrast as compared to the background is higher than that of the Atto647N labeled nanosheet even though the longpass filter cuts off most of the emission line of TMR. This is a strong indication that there is a big difference in the labeling efficiency between the two dyes/faces of the

nanosheet. The last row in Figure 37 shows a doubly labeled nanosheet. Excitation at both 532 and 633 nm is sufficient to see the nanosheet. For successful FRET it is expected that the intensity is increased at excitation of 532 nm in (j) as compared to (g). The signal vs. background intensity within the images confirmed an energy transfer. The results are summarized in Table 1.

	Control	TMR	Atto647N	TMR+Atto647N
Green Excitation (532 nm)	-	160	0	220
Red Excitation (633 nm)	-	40	90	60

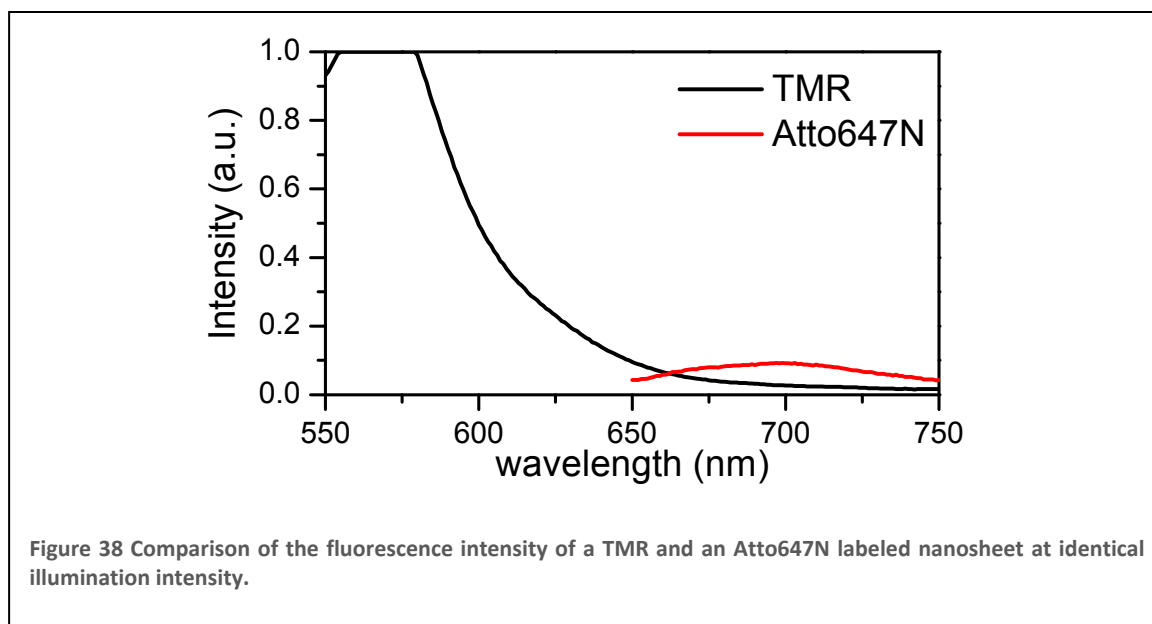
Table 1 Comparison of the fluorescence intensities (signal vs. background) for different samples measured at identical conditions. All values are given in counts.

For a better quantification than analyzing the fluorescence intensity within the images, it is also possible to use spectroscopy. To this end large labeled nanosheets have to be transferred onto pieces of quartz that can be introduced into the cuvette-holder of a standard fluorescence spectrometer. Figure 38 shows a comparison of the intensities obtained from a TMR- versus an Atto647N labeled sample. Again, it is clear that there is a strong difference between the two dyes' intensities.



A possible reason lies in the preparation of the nanosheet. During irradiation with electrons, new sulfur species are formed that are not accessible by thiol coupling chemistry. On the other hand, the remaining thiol groups can be oxidized by I_2 during the etching of the underlying gold. This could result in the formation of disulfides as well as higher oxidized species such as sulphones. A reduction of possible disulfides was attempted prior to labeling by dithioerythritol (DTE), but no increase of fluorescence

could be detected. Additionally, the quantum yields for fluorescence of the two dyes might not be the same. For further experiments a more detailed examination of the coupling process using different reduction methods should be conducted and monitored not only by fluorescence but also complementary techniques such as XPS.



4.2.4 Summary

In summary, it was shown that the two faces of the nanosheet are both accessible for coupling chemistry. The amino terminus can be modified by coupling with isothiocyanates, whereas the thiol can couple to maleimides. As a proof of principle, two different fluorescent dyes were attached and the resulting labeled nanosheets transferred to silicon oxide substrates as well as TEM grids. Even though the efficiency of the thiol coupling still needs to be improved, this method is promising for the fabrication of ultrathin bifunctional “Janus” membranes.

4.3 Patterning nanosheets

A variety of methods exist for generating laterally patterned SAMs. The most prominent technique is micro contact printing (μ CP), where an elastomeric stamp (i.e. polydimethylsiloxane, PDMS) is inked with a solution of an alkane thiol and then brought into contact with a clean Au surface [72, 73]. The SAM is then forming in the contact areas between the stamp and the surface. Other methods are inkjet printing, where the thiol solution is “shot” at the surface through a small capillary [74], and dip pen lithography (DPN) where the small tip of an AFM is used as a “fountain pen” to directly write the SAM onto the surface [75, 76]. All these methods have in common, that the patterning is achieved by selectively applying the thiol solution to confined areas on the sample. Patterning is therefore achieved *during* the formation of the SAM. As a result of the confinement of the solution, the resulting monolayers are often less ordered than those on continuous samples. However, for most applications this is not critical and is outweighed by the advantage of a fast and easy patterning method.

Patterning *after* the formation of continuous SAMs has also been demonstrated i.e. by mechanically removing the SAM with an AFM tip (“nanoshaving”) [77, 78], by exposure to reactive gases (ozone) through a mask [79], or by irradiation with light or electrons [80]. All these methods lead to destruction of alkane SAMs in the exposed areas, resulting in a “positive” pattern transfer.

For aromatic molecules (i.e. biphenylthiol) it is difficult to achieve patterned SAMs by μ CP. This is most likely due to the poor solubility of the molecules in ethanol and the significantly longer times that are necessary for SAM formation. The same arguments hold for other techniques that are forming patterns *during* the formation of the SAM. The method of choice is therefore to pattern aromatic SAMs *after* formation. Well established is the irradiation of homogeneous biphenyl SAMs with electrons, to achieve cross-linked nanosheets in the exposed areas (“negative” pattern transfer). This can be achieved by electron beam lithography (EBL) or by proximity printing using shadow masks [10, 23]. Recently it was shown that extreme ultraviolet (EUV) irradiation is also suitable for cross-linking biphenyl SAMs [81].

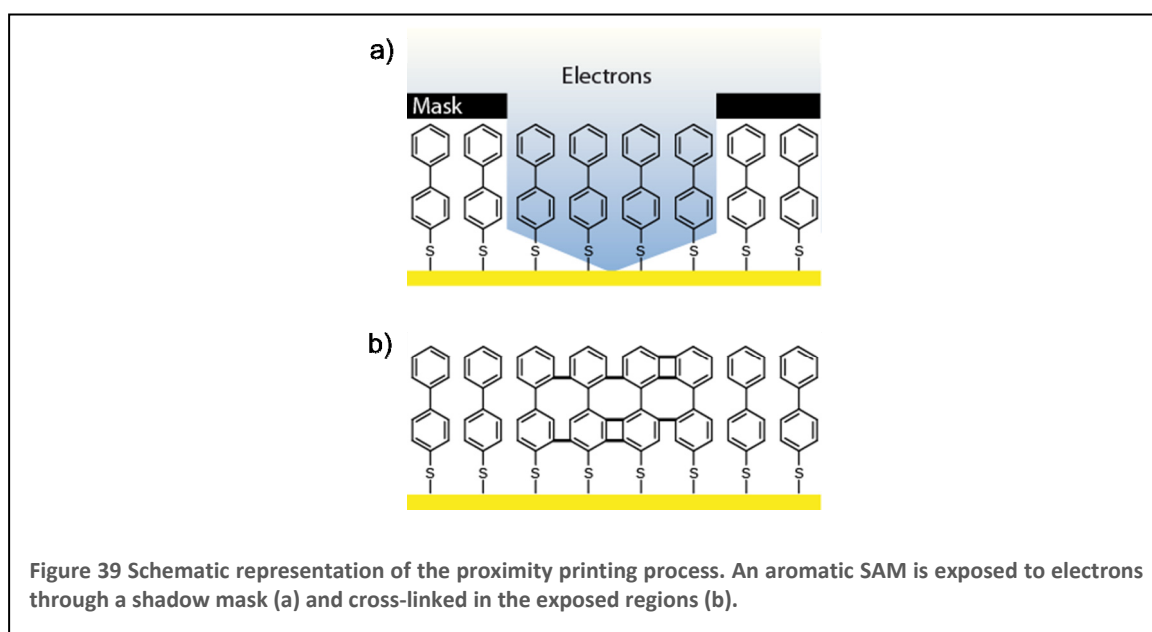
In this chapter, different pathways to pattern nanosheets are discussed, both before/during and after cross-linking. Generally two different types of structures are

possible: (i) areas of nanosheet that are separated from each other, and (ii) interconnected patterns that form a continuous film with defined holes. For different applications it is desirable to have means to achieve both types of structures with a variety of different methods. In the following, both proximity printing and EUV irradiation will be discussed. Additionally, the nanosheet is patterned by UV/ozone as well as oxygen plasma, both of which have not been used previously to generate patterned, cross-linked SAMs. Most importantly, it is shown for each patterning method, that the resulting nanosheet patterns can also be released from their original substrate and transferred to new substrates. The transfer medium then plays the important role of preserving the integrity of the patterns.

4.3.1 Irradiation through a shadow mask (proximity printing)

Proximity printing has been used for structuring SAMs with low-energy electrons for many years [82]. Generally a shadow mask is put in close contact with the SAM during the irradiation. The low-energy electrons (typically 50-100 eV) are not able to penetrate through the mask, and thus only the areas beneath the openings of the mask are exposed to the beam. Also for higher energy electron beams, a suitable mask can be generated. The process is schematically shown in Figure 39.

Patterns of cross-linked SAMs that were generated by proximity printing have been used

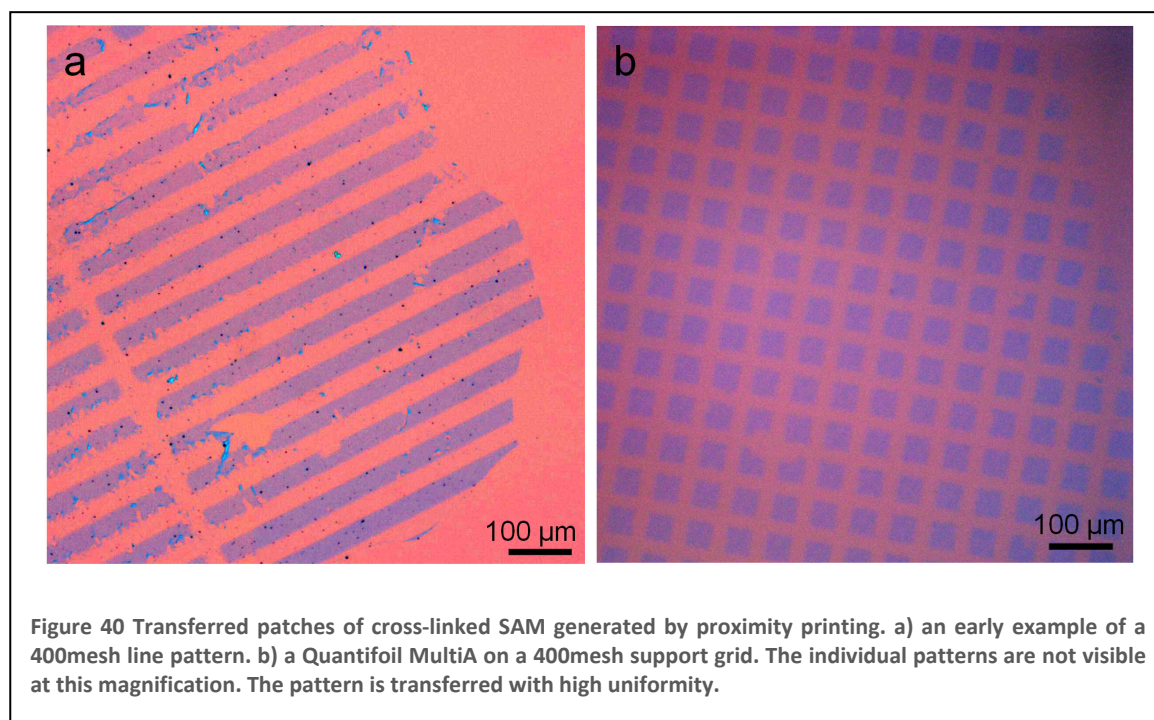


as a resist for selective etching of the substrate [10, 24], as well as selective electrochemical [21, 22] and electroless [28] deposition of metal, immobilization of

biomolecules [29, 30], and growth of polymer brushes [31]. Cross-linked patches can even be moved on the surface by sonication after cleaving the sulfur-gold bond by exposure to iodine vapor [32].

The size of the achievable patterns can be varied over a wide range by the use of suitable shadow masks. Conventional TEM grids are useful for patterns in the μm range, for patterns from 10-0.5 μm Quantifoil films can be used. Masks with smaller openings down to ~ 20 nm can be fabricated by focused ion beam etching of silicon nitride membranes [23]. However, such small structures can be written with higher accuracy by electron beam lithography.

Using the methods shown in chapter 4.1 the patterns can be transferred onto a new

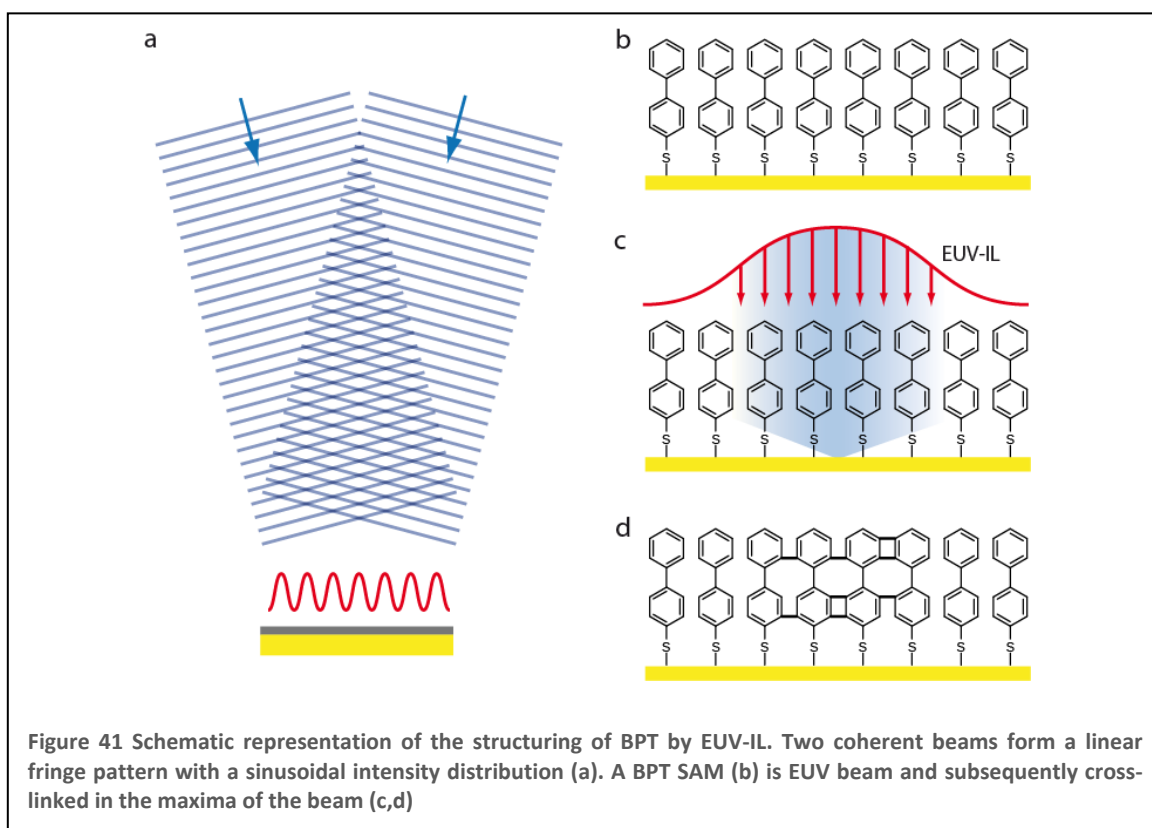


substrate. Figure 40 shows two samples where a biphenyl SAM is cross-linked by irradiation through a shadow mask. The first successful attempt of transferring such a pattern is shown in a). A copper grid with 400 mesh lines was used to pattern CBPS on silicon nitride. The pattern was then transferred to a SiO_2/Si wafer for visualization in an optical microscope. Even though some of the nanosheet ribbons are showing some defects, the overall structure of the TEM grid is well preserved. A highly uniform pattern of nanosheet made by irradiation of BPT through a Quantifoil Multi A grid is displayed in Figure 40b. Clearly visible is the structure of the supporting copper grid (400 mesh), the rim of the grid can be seen in the top right corner. The individual circular and elliptical

patches of nanosheet are not visible at this magnification. In both images the structural integrity of the pattern is preserved, even though the individual nanosheet patches are not interconnected.

Although proximity printing has been very useful for structuring SAMs in the past, the main drawback is the necessity to use shadow masks. It is hereby not possible to generate interconnecting patterns of nanosheet (“donut-problem”^{ix}). Interconnected patterns of nanosheet are desirable for example for preparing freestanding holey nanosheets. In the following, several methods are presented to overcome this problem.

4.3.2 EUV-IL



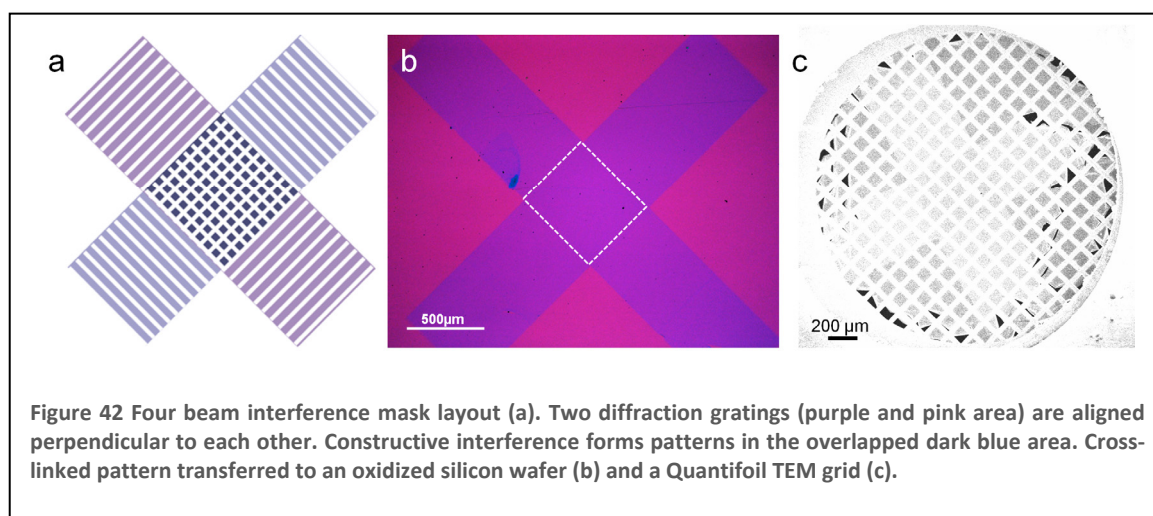
Extreme-ultraviolet interference lithography (EUV-IL) is a tool to generate periodic structures down to ≈ 13 nm over large areas in a parallel process [83, 84]. The coherent beam of a synchrotron is diffracted into multiple beams to generate interference fringes.

^{ix} This refers to the hole in the center of a donut. Such ring-like structures cannot be achieved by shadow masks, as the space in the center has no connection to the outside.

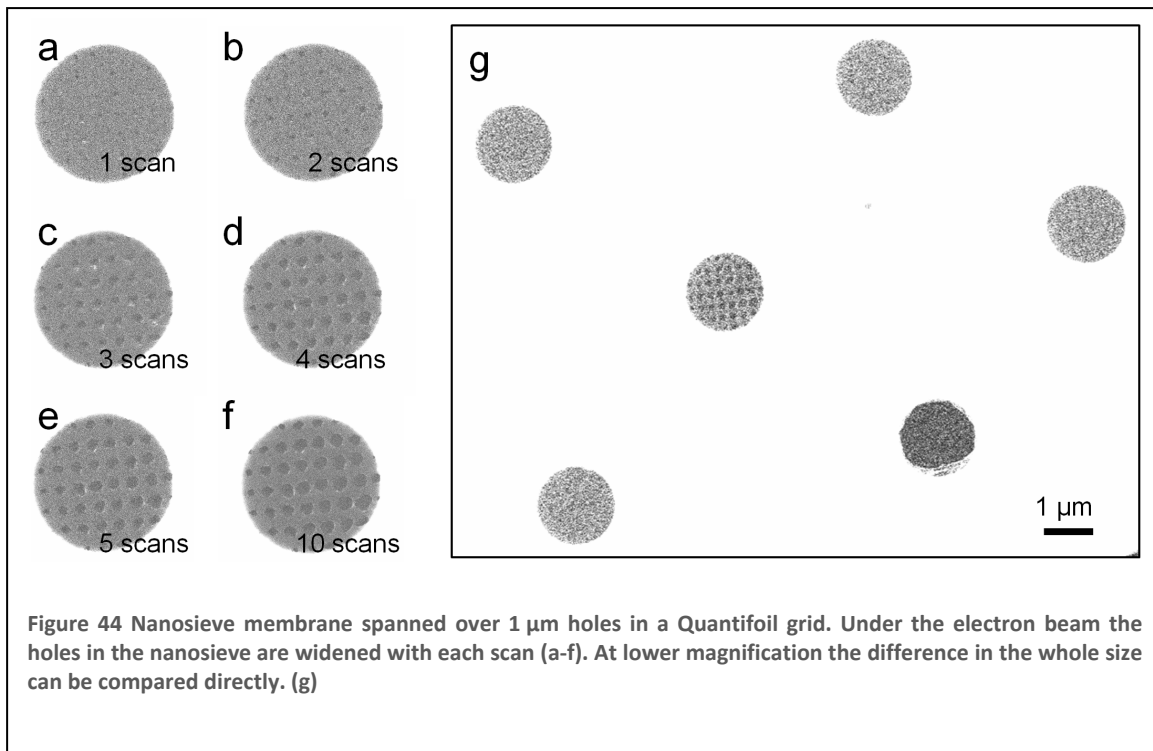
In comparison with electron beam lithography, proximity effects that lead to broadening of the patterns are negligible. Line patterns can be achieved by two beam interference, hexagonal arrays by three beams and square arrays by the interference of four beams [84].

This principle is shown in Figure 41 for a line pattern. Two coherent beams form a linear fringe pattern with a sinusoidal intensity distribution (a). Turchanin et al. have shown that this technique can also be applied to cross-link aromatic SAMs [30, 81]. If a BPT SAM (b) is exposed to the beam (c) it is cross-linked in the maxima of the beam (d).

By applying four-beam interference, it is possible to generate grids of cross-linked SAM with holes in the nanometer range [85]. If these grids can be released from the original substrate and prepared freestanding without degradation of the pattern, they might become valuable i.e. for membrane/separation applications as “nanosieves”, which are perforated membranes with nanometer thickness.

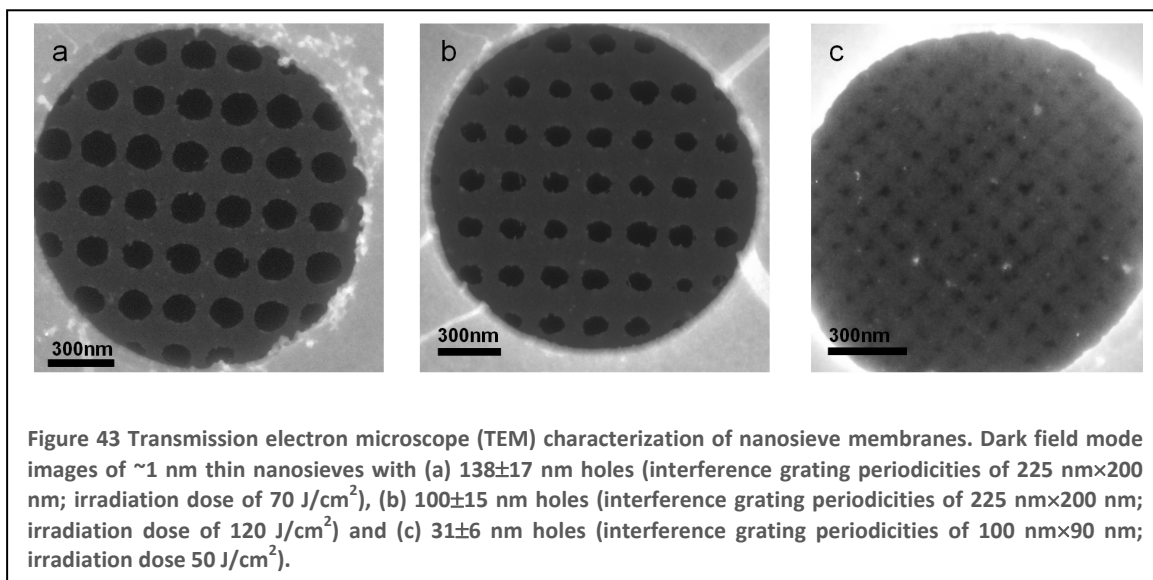


The results in this section were obtained together with Mark Schnietz, who did the EUV exposures at the Swiss Light Source. Figure 42 shows the successful transfer of the macroscopic pattern of the four-beam interference. The “swiss cross” formed by the two perpendicular interference patterns is shown schematically in (a), the purple and pink areas are representing the (overexposed) linear patterns from the different gratings. In the overlapping region (dark blue) the grid pattern is formed. In (b) this pattern can be seen in the nanosheet, transferred to a SiO₂/Si wafer. The overexposed areas and the



grid patterns are both appearing to be homogeneous by light microscopy. It is also possible to transfer this “swiss cross” to a Quantifoil TEM grid, where it can be seen in the overview scan of an SEM with steep contrast settings (c).

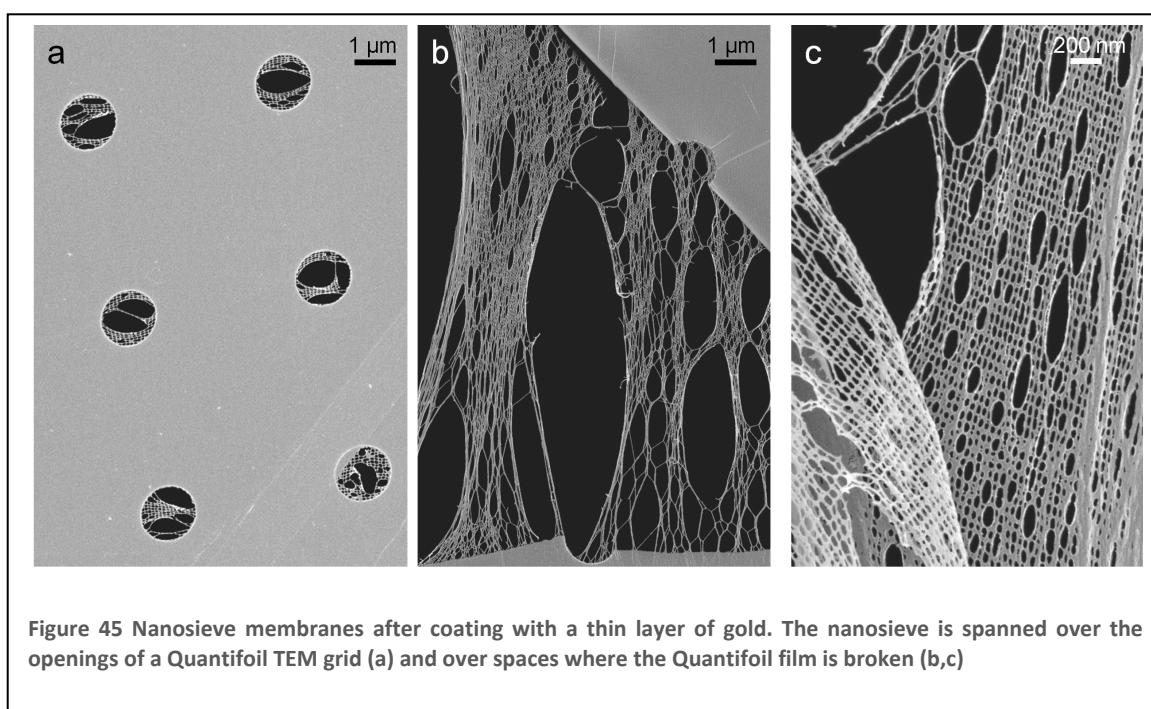
The grid/nanosieve itself can then be observed by zooming into the openings of the Quantifoil grid. However, it was found that it is difficult to observe the individual holes by slowly scanning at high magnification (at a beam energy of 3 kV), as the holes widened due to charging, leading to the destruction of the membrane. A sequence of images acquired in a fast scanning mode after each scan is shown in Figure 44a-f. The



holes are visible after the first scan and are subsequently getting bigger, further scanning lead to rupture of the membrane. Interestingly, the hole size increases within an image from top left to bottom right, which is the scanning direction of the electron beam. An overview with six different openings is shown in (g): four membranes are still intact, one is ruptured and one has enlarged holes due to previous scanning in this area.

It was found that the widening of the holes does not occur at the higher beam energy of a TEM. Images were acquired on a Philips TEM CM 200 FEG at 200 kV in dark field mode with a displaced aperture at the PTB in Braunschweig. Three different nanosieves with different hole sizes are shown in Figure 43. Both (a) and (b) were structured by the same interference gratings at different doses. The smaller holes of (b) were achieved by a grating with a different periodicity (see figure caption for details).

In principle these nanosieves can also be used as a template to fabricate composite materials. In a first experiment 2-5 nm gold were evaporated onto a nanosieve sample.



Due to the harsh conditions during evaporation, most of the membranes are damaged. Figure 45a shows some of these nanosieves spanned over a Quantifoil TEM grid and over larger openings, where the Quantifoil film is ripped (b,c). These large Au/nanosieve networks somewhat resemble broken stockings, with large areas still intact. From these results it seems promising to further pursue this route to the fabrication of composite nanosieves. Other than gold, different metals or oxides could be evaporated, tuning the

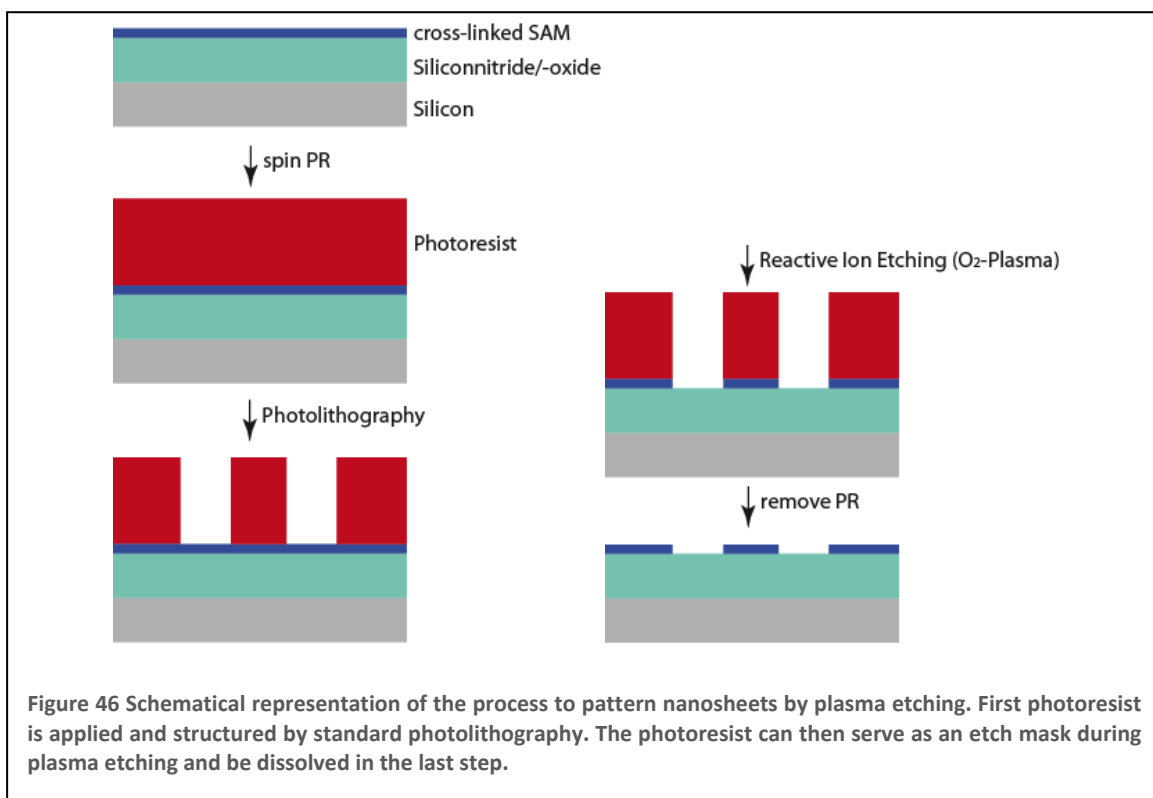
properties of the composite to the desired applications. Even polymer brushes could be grown on the functionalized surface of a NBPT nanosieve.

In summary, it was shown that the nanosheet patterns that are generated by EUV lithography can successfully be released from the Au substrate and transferred to TEM grids as nanosieves.

4.3.3 Plasma etching

Dry etching techniques are standard processes in microfabrication [49]. Generally, material from the substrate is transformed into a volatile compound that desorbs into the gas phase. In plasma etching this is achieved by generation of a plasma from reactive gases such as O_2 , Cl_2 , CF_4 , SF_6 , etc. The most important reactive species generated in the plasma are radicals. Selectivity for one over another material can be achieved by choosing a suitable reactive gas, which is able to form volatile compounds preferably with one of the materials. Polymeric organic materials can be removed by etching in an O_2 -plasma. The oxidizing etching conditions then lead to volatile compounds such as CO , CO_2 , H_2O , etc. that are easily desorbing from the surface.

This can be used for selectively removing nanosheet in areas that are exposed to the plasma. The process described here makes use of a fully cross-linked SAM (i.e. by a flood

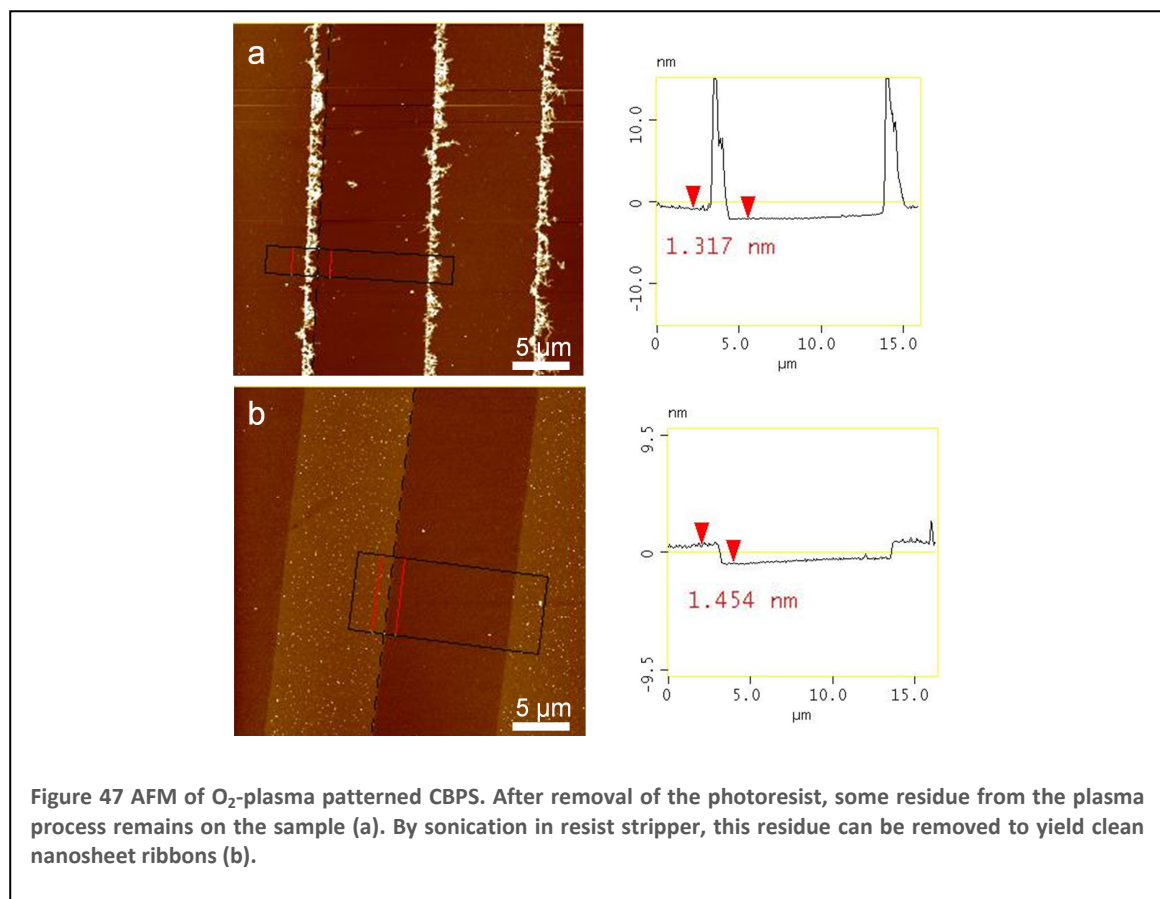


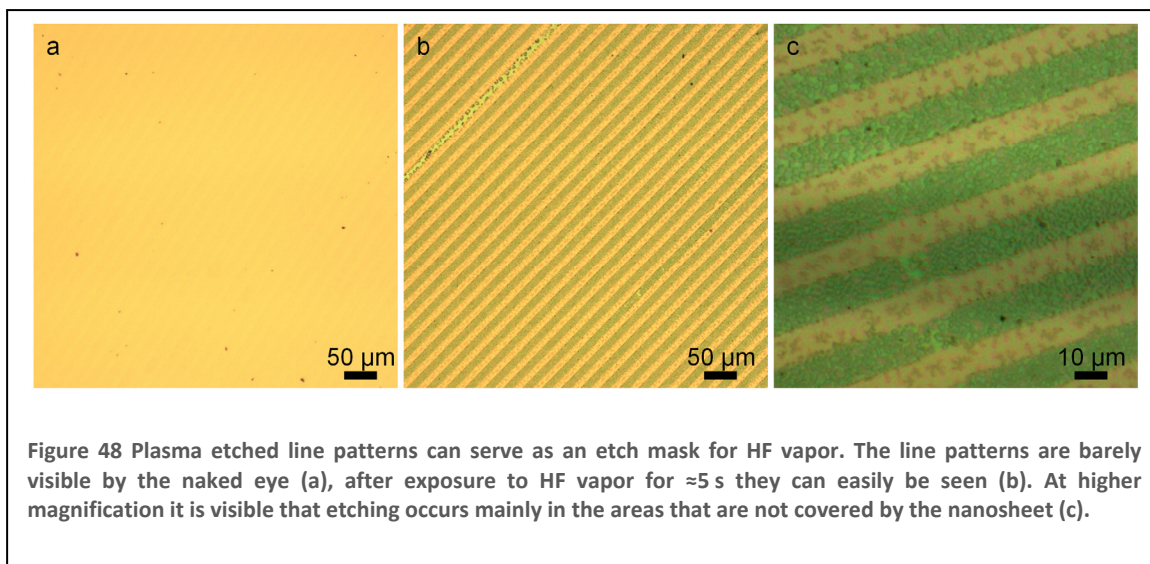
electron exposure). The following examples are based on CBPS SAMs on $\text{SiO}_2/\text{Si}_3\text{N}_4$, but the process is not limited to these. In general, all cross-linked SAMs can be structured in this manner, both before and after transfer to new substrates.

A schematic flow diagram of the whole process is shown in Figure 46. Starting with a cross-linked SAM/nanosheet, a layer of photoresist is spincast onto the sample. The desired pattern is then generated in the photoresist by standard photolithography. After development, the exposed nanosheet can be removed by oxygen-plasma etching. Finally, the remaining photoresist is dissolved in a suitable solvent.

The size of the features is limited to $>0.5\ \mu\text{m}$ due to the resolution limit of the photolithography step. Smaller features can be achieved by EBL, albeit with the drawback that the patterning of large areas is very time consuming. The biggest advantage of plasma etching for patterning of nanosheets is the high throughput together with the flexibility in the patterns that can be generated, as chrome masks can be custom made at low price.

Figure 47a shows an AFM micrograph of a CBPS nanosheet that has been patterned with





10 μm lines and spaces. Residues from the photo resist are visible on the edges of the lines. By sonication in photoresist stripper, these residues can also be removed (b), yielding clean ribbons of nanosheet. The corresponding line scans show that the height of the ribbons corresponds roughly to the thickness of the CBPS monolayer.

After structuring, the line patterns can also be seen by the naked eye on the silicon nitride substrate, though with very low contrast, Figure 48a. Similarly to the patterns that are generated by proximity printing, these patterns can then be used as a resist for etching the substrate. After exposure to hydrofluoric acid vapors for five seconds, the pattern is clearly visible (b). At higher magnification (c), crystallites of the etch products can be seen mostly in the areas that are not covered by the nanosheet. Etching of the nanosheet-protected nitride happens mostly from the sides and at defects in a dendritic fashion.

The nanosheet ribbons can now also be released from their original substrate and transferred to arbitrary new substrates. As mentioned earlier, the integrity of the pattern is preserved during the process.

Figure 49a and b show the 10 μm line pattern after transfer to SiO_2/Si . In (b) the edge of a transferred fragment is shown. In this case the photoresist broke into smaller pieces during the transfer procedure, resulting in irregularly shaped edges. Interestingly, the nanosheet ribbons are misaligned at this edge and are all pointing in the same direction, indicating bad contact to the substrate near the edge. During removal of the photoresist, the ribbons were then aligned by the direction of flow of the acetone.

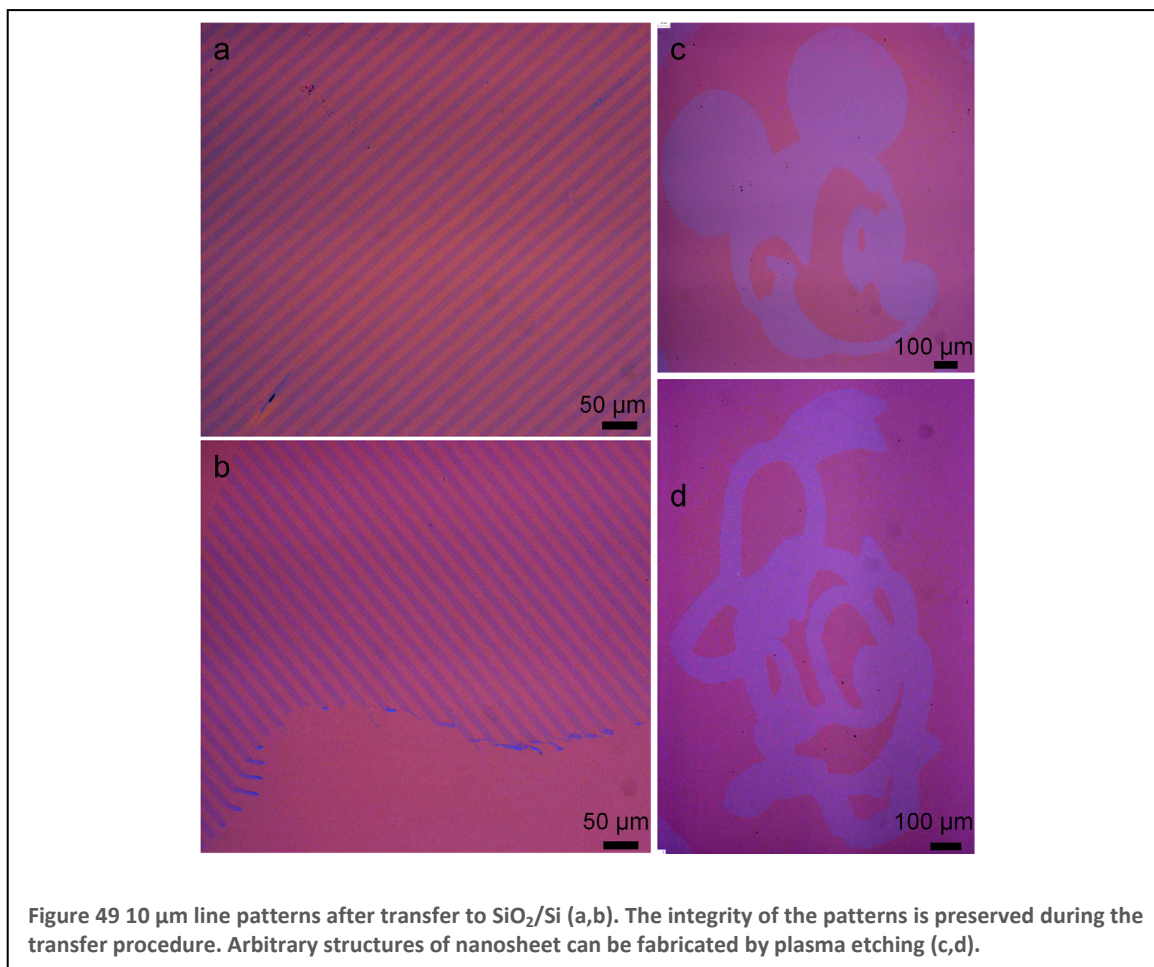
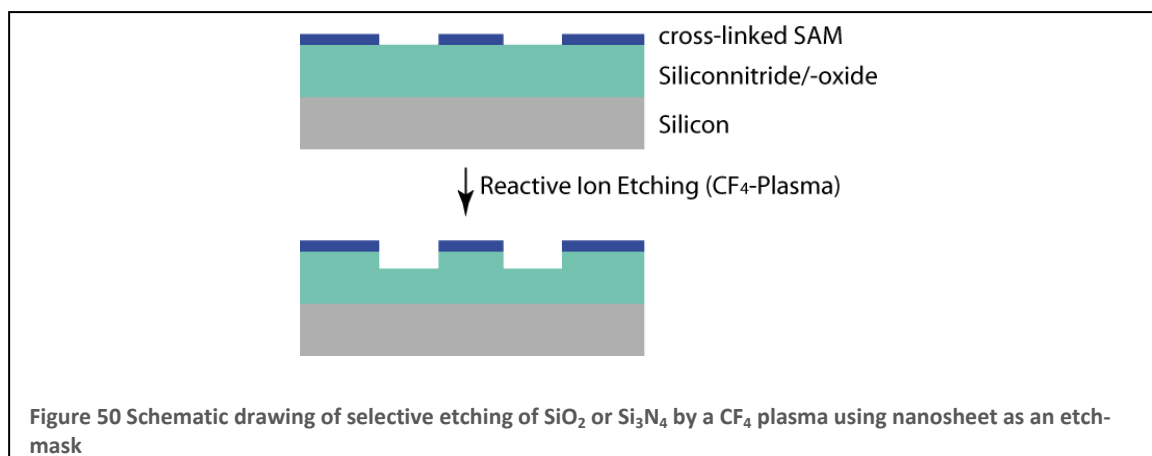


Figure 49 10 μm line patterns after transfer to SiO_2/Si (a,b). The integrity of the patterns is preserved during the transfer procedure. Arbitrary structures of nanosheet can be fabricated by plasma etching (c,d).

The versatility of this approach for patterning nanosheets is demonstrated in Figure 49c and d. A microfilm mask was used to obtain the “nanosheet-portraits” of Mickey Mouse and Donald Duck, the linewidth in this case is $\approx 50 \mu\text{m}$. Such structures are impossible to pattern by the proximity printing technique or EUV-IL and illustrate the versatility of the approach to pattern the nanosheet by photolithography and dry etching.

4.3.3.1 Nanosheets as resists for reactive ion etching

Self-assembled monolayers can be used as a resist to protect the underlying substrate from chemical etching. Selective etching of regions without a SAM has been demonstrated especially for alkane thiols on Au. Generally, the resistance against etchants is higher the better the quality of the SAM. Zhao et al. have used a highly selective etchant to visualize defects in closely packed SAMs [86]. Also, for best selectivity the etchant and etching conditions have to be chosen carefully. The stability of aromatic SAMs against etchants is strongly enhanced by cross-linking to form nanosheets. This has been shown for both thiols on gold [10], as well as



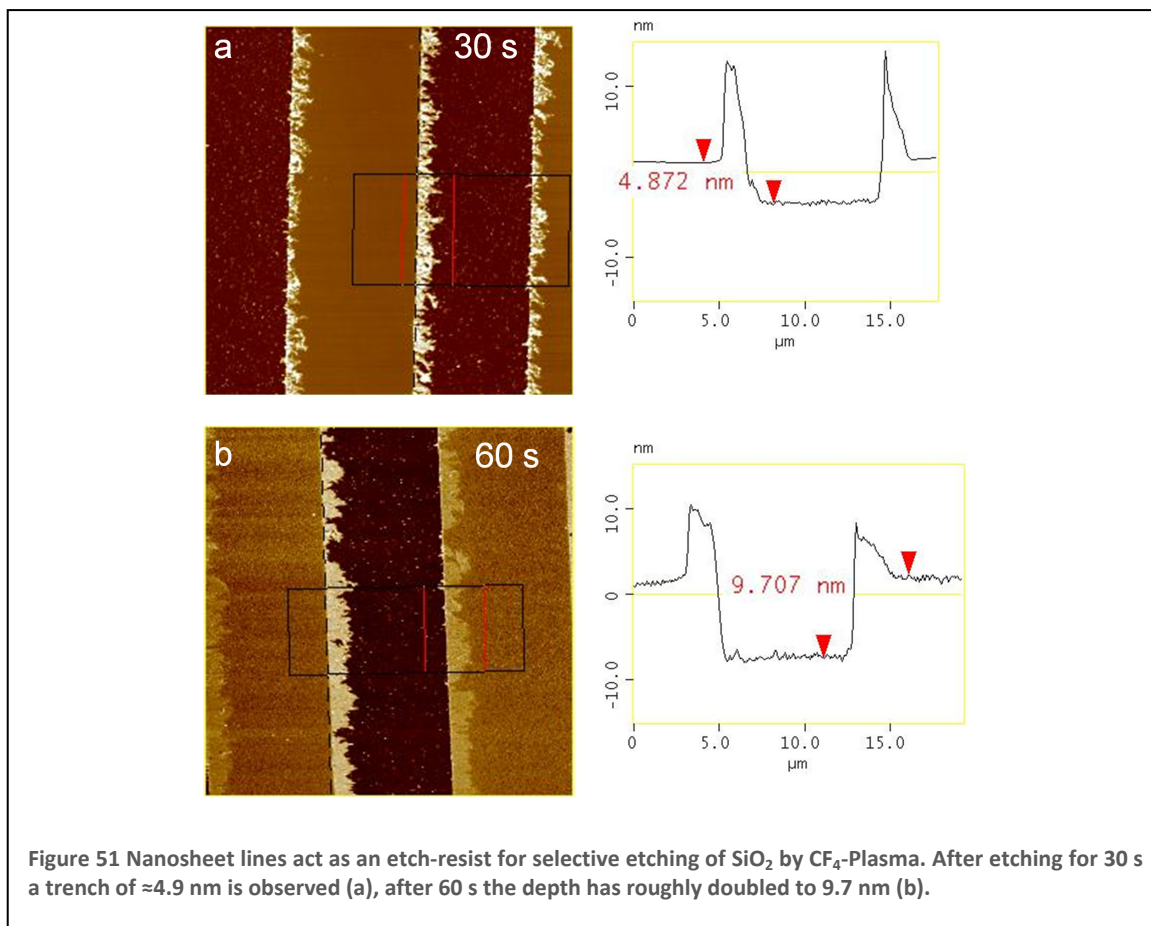
hydroxybiphenyls on silicon surfaces [87]. However, only for wet chemical etching this has been demonstrated so far.

It seemed promising to apply this enhanced stability also to plasma etching techniques. The process is shown schematically in Figure 50. As was shown earlier, oxidative conditions have to be avoided, as the monolayer is completely removed by an oxygen plasma. Selective etching of SiO_2 or Si_3N_4 can be achieved by using tetrafluoromethane (CF_4) [49].

Nanosheets were first structured by oxygen plasma according to 4.3.3. The resulting nanosheet ribbons were then used to test the etch-selectivity by treatment with a CF_4 plasma (100 W) at a CF_4 partial pressure of 50 mTorr and a flow of 40 sccm.

Figure 51 shows AFM images of the resulting line patterns. The fringed edges are photoresist residue from the oxygen plasma process (see Figure 47). After an etching time of 30 s (Figure 51a) a trench of ~ 4.9 nm is etched into the Si_3N_4 . Doubling the etching time roughly results in an increase of the trench's depth by a factor of two.

These results suggest that cross-linked SAMs (nanosheets) can be used as an etch-mask for selective plasma etching. However, several factors have to be considered. Firstly, only "clean" substrates can be patterned by this technique, as a small partial pressure of oxygen for the removal of organic contaminations would result in the destruction of the nanosheet. Secondly, it is not clear if selective etching is also possible if the SAM is not removed between the cross-linked regions. Further experiments are also necessary to test different reactive gases such as CF_3H .



4.3.4 UV/ozon

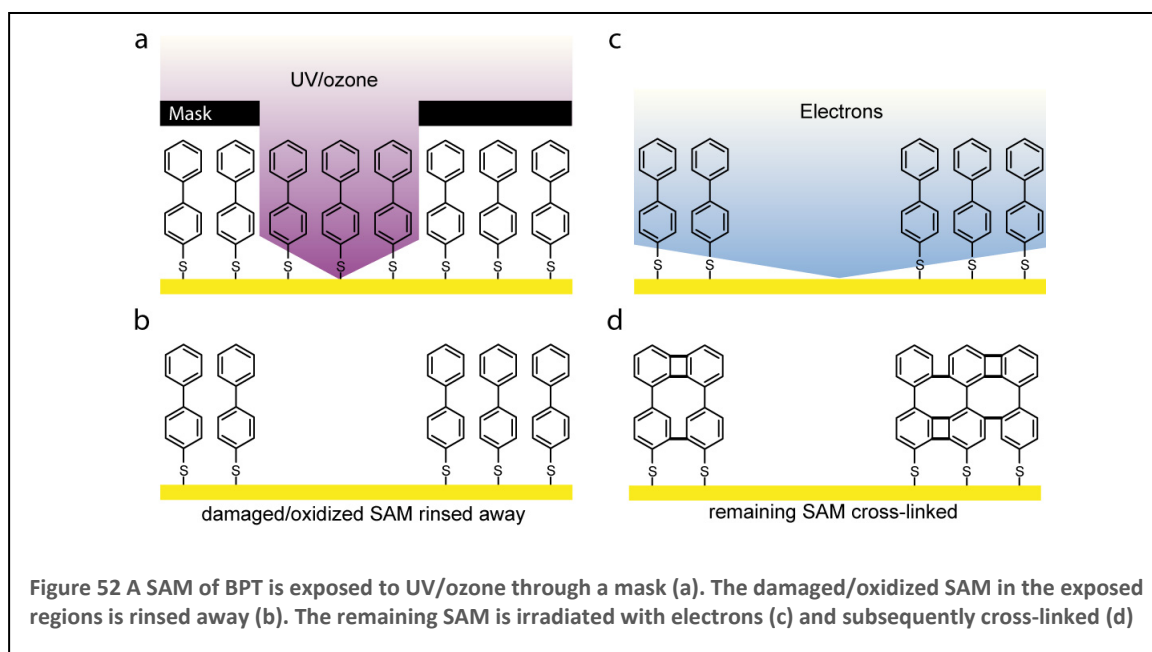
The previously described methods are sufficient for generating patterns for most applications. However, they are either expensive and of limited availability (EUV-IL) or require multiple processing steps (photolithography/plasma etching). Proximity printing is fast and easy, but lacks the possibility to generate interconnected patterns such as the nanosieves that can also be prepared freestanding. The straight forward way is structuring of the aromatic SAM prior to cross-linking. To this end, UV/ozone treatment through a mask (“positive” pattern transfer) followed by a flood electron exposure (cross-linking) is explored in this section.

Treatment of gold-samples with ozone generated from oxygen by UV-irradiation has become a standard cleaning procedure due to its ease of use [88-90]. Thiols as well as organic contaminants are oxidized by the ozone and subsequently washed away with ethanol or other polar solvents.

The technique, however, is not limited to cleaning the substrate. It can also be utilized for generating patterned SAMs if the UV/ozone exposure is locally restricted i.e. by using shadow masks [79]. Tarlov et al. have demonstrated that the exposed areas can be back-filled with differently functionalized thiols [91]. It is also possible to achieve local oxidation and removal of the SAM by irradiation through the small tip of a SNOM, as has been demonstrated by the group of Leggett [92]. The SAM can thus be considered a positive resist with respect to UV/ozone treatment, as the exposed areas are destroyed. By a subsequent cross-linking step the patterns will be of reversed contrast with respect to proximity printing, using the same shadow masks.

The process of generating a holey, cross-linked monolayer is shown schematically in Figure 52. A BPT SAM is formed by immersion of a Au substrate in a solution of BPT in DMF. The SAM is exposed to UV/ozone through a mask (a) and subsequently destroyed in the exposed areas by oxidation of the sulfur and ozonolysis, so that the fragments can be removed by rinsing in water and ethanol (b). The remaining SAM can then be irradiated with electrons (c) and completely cross-linked (d).

To monitor the effect of ozone on the monolayer, the change of contact angle was measured as a function of exposure time (Figure 53a). For a pristine BPT SAM the contact angle is $74.3 \pm 3.2^\circ$. After ozone exposure at a constant oxygen flux of 1 l/min for



2 minutes the surface becomes completely wetting with a contact angle of 0° , which is attributed to the oxidation of the monolayer. By subsequent rinsing of the sample with

ethanol it again goes up to $83.7 \pm 1.8^\circ$, which is in good agreement with the contact angle for a freshly cleaned gold substrate. To further evaluate the process, XPS was used to determine the degree of oxidation.

Figure 53 shows the C 1s, S 2p and O 1s regions of a pristine BPT SAM (top), a BPT SAM after 4 min UV/ozone treatment (center) and after rinsing with water and ethanol (bottom). The C 1s signal of the pristine SAM can be fitted with a peak at 284.2 eV (FWHM 1.15 eV) that is assigned to the 11 carbons in the aromatic ring and a peak at 285.3 eV (1.15 eV) that is assigned to the remaining sulfur bonded carbon. Two additional features at 286.4 and 290.0 eV (1.7 eV) are assigned to aromatic shake up satellites. The S 2p $3/2$ signal is found at 162.2 eV (1.2 eV) which is known for thiolate species. A small Oxygen signal at 532.1 eV can be found, which is likely due to contamination, as samples were not prepared in UHV. The thickness of the SAM was estimated by the attenuation of the Au 4f signal to $\sim 10.8 \text{ \AA}$.

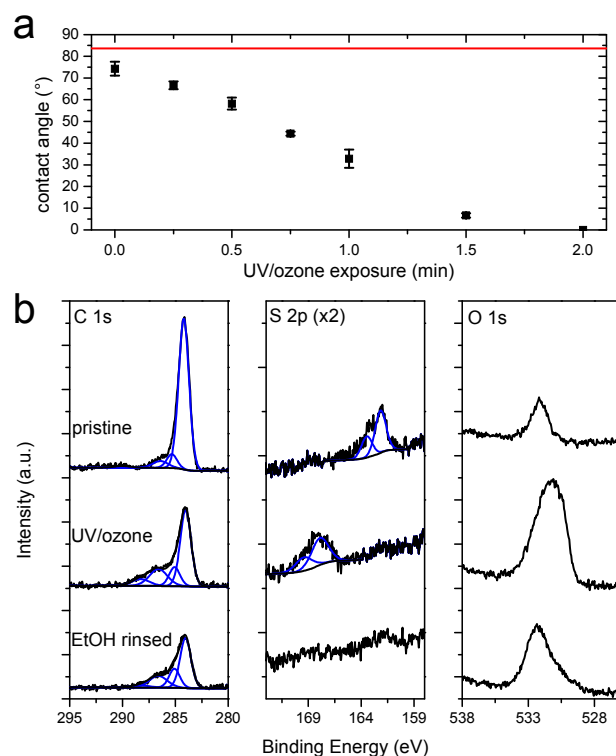
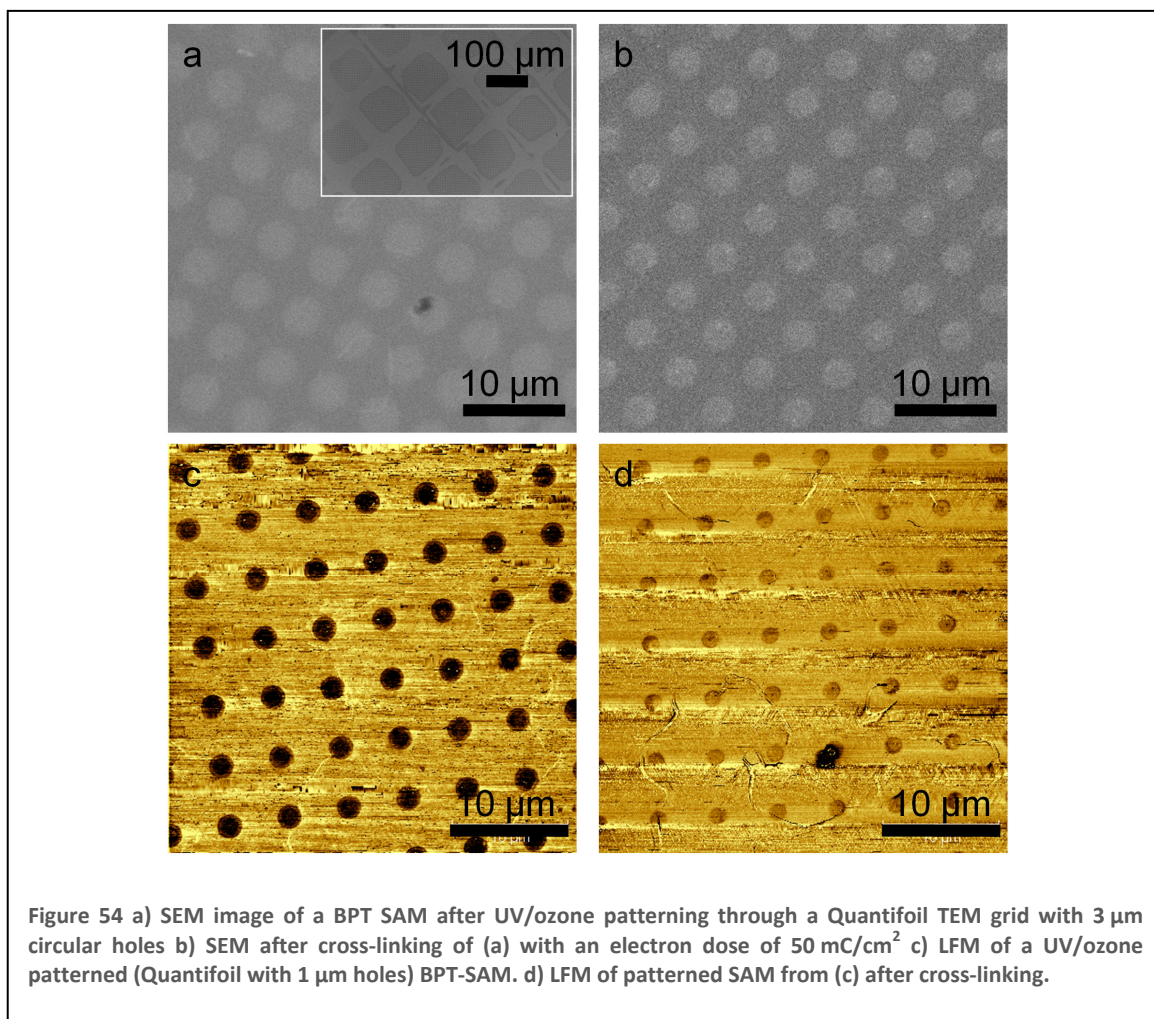


Figure 53 a) Contact angle of a BPT SAM as a function of UV/ozone exposure time at a O_2 flux of 1 l/min. The red line indicates the contact angle of a freshly cleaned gold substrate. b) top: XPS spectra of the C1s, S2p and O1s regions of a pristine BPT SAM. Middle: XPS spectra of the SAM after UV/ozone oxidation. Bottom: spectra of a sample after rinsing with water and ethanol to remove the SAM.

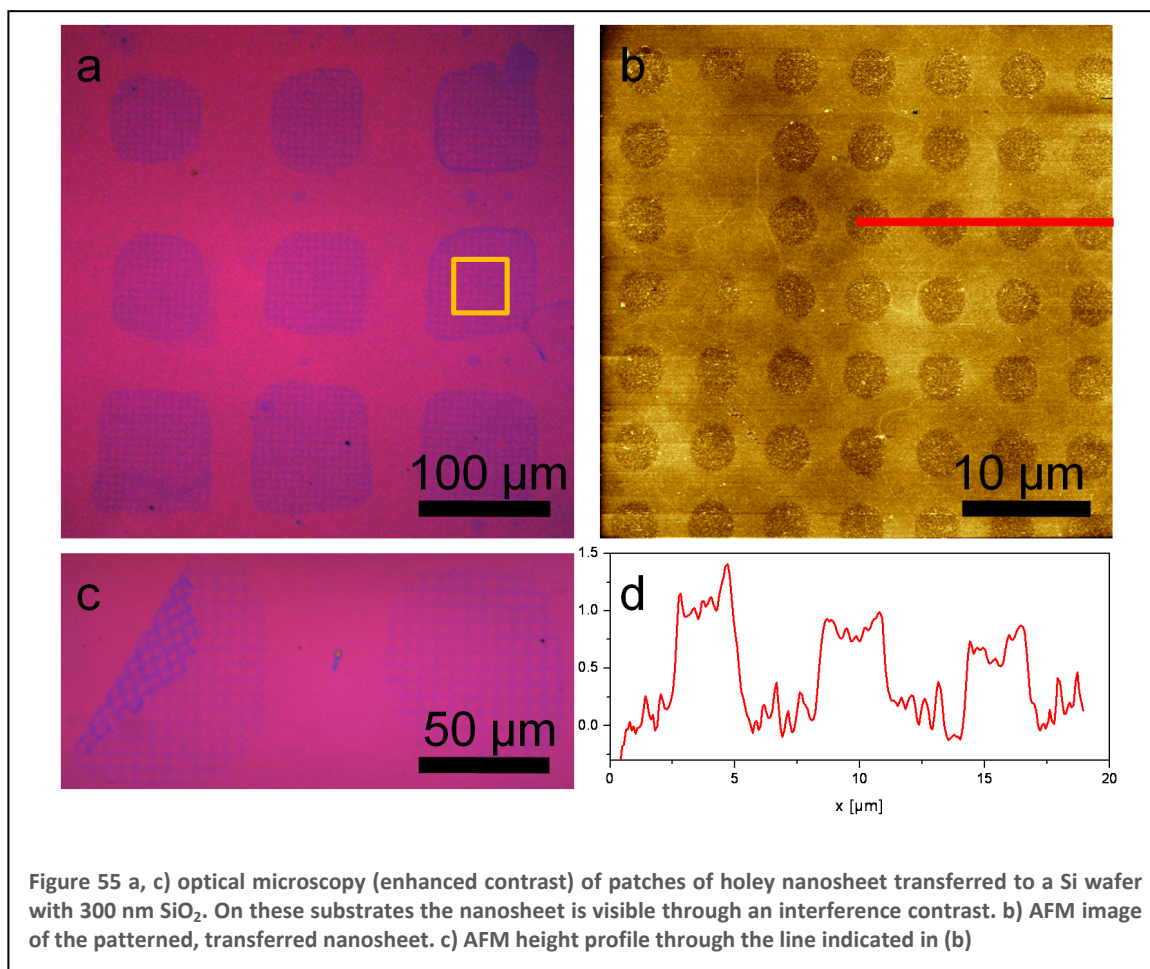
After exposure to UV/ozone for 4 minutes the C 1s signal intensity decreases. The signal develops a shoulder towards higher binding energies. The peaks at 286.6 and 288.3 eV can be assigned to oxidized carbon species (alcohols/ethers, carbonyls, carboxylic acids). The S 2p $3/2$ signal is shifted to 167.9 eV (1.2 eV) which is assigned to a sulfonate. Oxidation of the SAM is also apparent from an increase and broadening of the O 1s signal, we refrained from peak fitting due to the large variety of possible oxygen species. The thickness after UV/ozone treatment is ~ 5.2 Å. After rinsing with water and ethanol (bottom spectra), a sulfur signal is no longer found, indicating the removal of the SAM. The carbon and oxygen intensities are both decreased. A complete removal of carbon is not expected, as the sample preparation is done in ambient. From the shape of the residual carbon peaks, it is likely that some fragments from the ozonolysis are physisorbed to the Au. The thickness of the remaining contamination layer is ~ 2.0 Å. It can thus be concluded that the SAM in the exposed areas can be sufficiently removed to apply this method for structuring the monolayer.

To this end, a holey carbon coated TEM grid with circular openings (Quantifoil) was brought into contact with the sample and used as a mask for the UV/ozone exposure. The monolayer is only exposed to ozone in the openings of the mask. After removing the



mask and rinsing with ethanol, the pattern was observed with the inlens detector of a Leo1530 SEM at 3 kV (Figure 54a). The pattern can clearly be seen as the cleaned gold areas appear brighter than the surrounding monolayer. Low magnification (inset in Figure 54a) shows disconnected areas of patterned SAM that resemble the shape of the Cu-grid. This indicates that conformal contact between mask and sample is essential to protect the monolayer from the ozone in masked regions, which can be achieved by the flexible Quantifoil film, but not by the rigid Cu-grid. Figure 3c shows an AFM micrograph in lateral force mode of such a patterned region. The pattern is clearly visible; the areas that were exposed to ozone appear darker than the intact SAM.

Cross-linking of the patterned monolayer is achieved by large area electron exposure in a floodgun. By SEM no difference is observable; the pattern remains intact after cross-linking (Figure 54b). AFM lateral force mode shows a reduced contrast after electron exposure (Figure 54d), which indicates changes in the stiffness of the monolayer. To visualize the success of the cross-linking procedure, the cross-linked monolayer was released from the substrate and transferred to a silicon wafer with a 300 nm layer of thermal oxide. An optical micrograph of such a transferred holey nanosheet is shown in Figure 55a. The color of the patterned nanosheet is slightly shifted towards blue as compared to the background. Patches of holey nanosheet can easily be identified (compare to Figure 54a (inset)). Figure 55c shows a higher magnification of two of such patches. One of them got folded during the transfer procedure, hinting at its high mechanical stability [93]. An AFM image of one of the patches of holey nanosheet is shown in Figure 55b, the nanosheet appears to be smooth against the SiO_2 that is visible through the holes. The step height was measured (Figure 55d) to be around 1 nm, which is in good agreement with the length of the molecule and the thickness of the monolayer

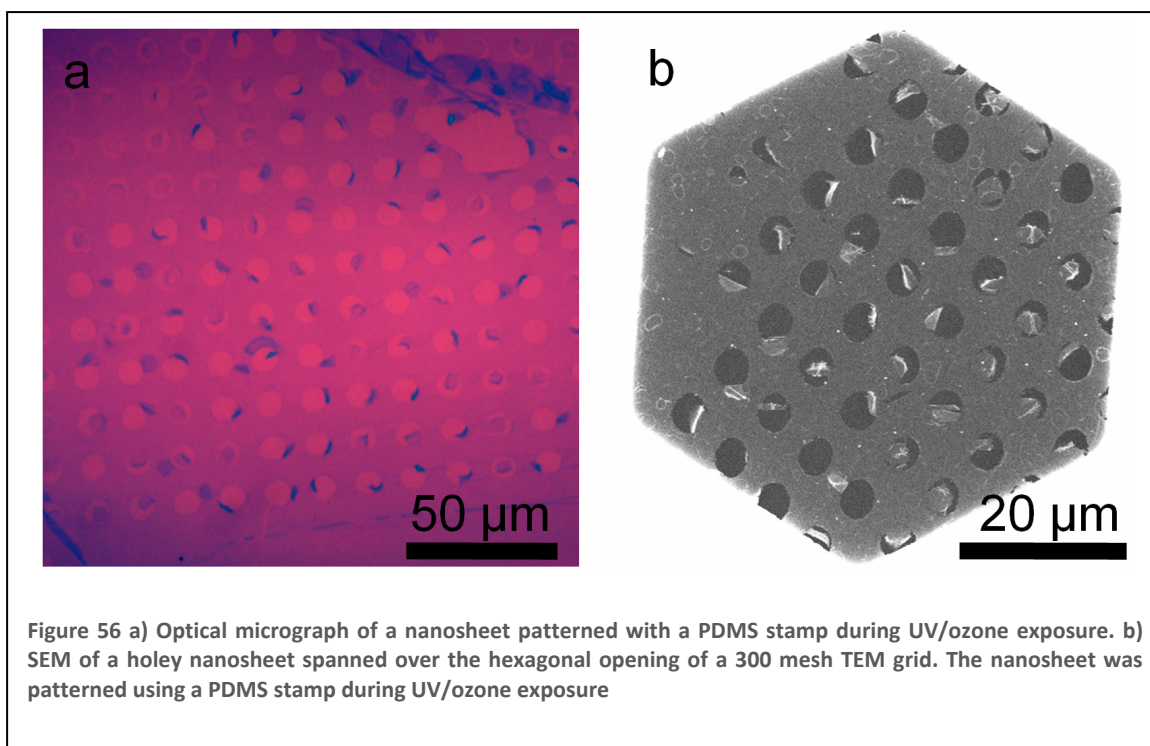


as measured by XPS [93].

4.3.4.1 PDMS stamps as masks for patterning

To maximize the UV/ozone patterned area and have access to a broader range of shapes and sizes of the patterns, the feasibility of using PDMS stamps as an alternative to TEM grids as shadow masks was studied. PDMS is widely used for micro-contact printing techniques [94]. Once a stamp is formed from a master, it can generally be used multiple times without degradation. Another advantage is that the stamp easily forms a conformal contact with the sample surface. Most importantly, PDMS shows the best transparency of commercial polymers in the far UV [95].

As it is difficult to form a shadow mask from PDMS, thin stamps were brought into contact with the surface under an oxygen enriched atmosphere. Ozone is presumably generated from the oxygen in the voids between the stamp and the sample. This way it is also possible to locally oxidize the SAM. It was found that significantly longer exposure times (~30-60 min) are necessary for achieving a patterned SAM where the exposed regions are totally destroyed. This can be attributed to a decreased UV intensity in the vicinity of the sample, but also to a lack of oxygen flow within the voids of the stamp. Figure 56a shows a successfully patterned monolayer using this method, which was cross-linked and transferred to an oxidized Si-wafer afterwards. The patterned holes are ring shaped, leaving a patch of nanosheet in the center, that is rolled up in most cases. This donut shape is due to sagging of the stamp [94]. By changing the aspect ratio of the stamp to a deeper relief structure, this effect becomes less pronounced. However, the photoresist used for the fabrication of the stamps limits the structure depth to ~3 μm , at which sagging is not yet eliminated. Nonetheless, the applicability of using PDMS stamps for patterning with UV/ozone is demonstrated. It is also possible to transfer these large holey nanosheets onto TEM grids (Figure 56b). A 300mesh Cu grid was used as a support; the holey nanosheet is spanned over the openings of the grid. Despite its extreme thinness, it is mechanically stable to span over ~60 μm openings of the grid.



In summary, the successful patterning of the nanosheet by UV/ozone exposure was demonstrated. The process is cheap and fast, and most of all easy to use. In addition to creating holey nanosheets, this method is also useable to fabricate nanosheets with chemical patterns, similarly to the ones presented in [96]. The advantage of this method is that the patterning is done prior to cross-linking. The areas where the SAM was removed by UVO exposure can easily be filled by differently functionalized molecules, so that the whole patterned nanosheet is cross-linked by an identical dose.

4.3.5 Summary

Four different methods have been shown to obtain laterally patterned nanosheets that can be transferred to new substrates while the integrity of the pattern is preserved. A graphical summary of these methods and the individual processing steps is shown in Figure 57. The first method, proximity printing, has already proven to be very useful for easily fabricating patches of nanosheet in the past. The major limitation is the need for shadow masks, both in terms of available patterns and because of the inability to form interconnected patterns (donut problem). These problems can be addressed by the other three methods that were discussed. EUV-IL is suitable for very small feature sizes: the fabrication of a freestanding nanosieve membrane was demonstrated. The main

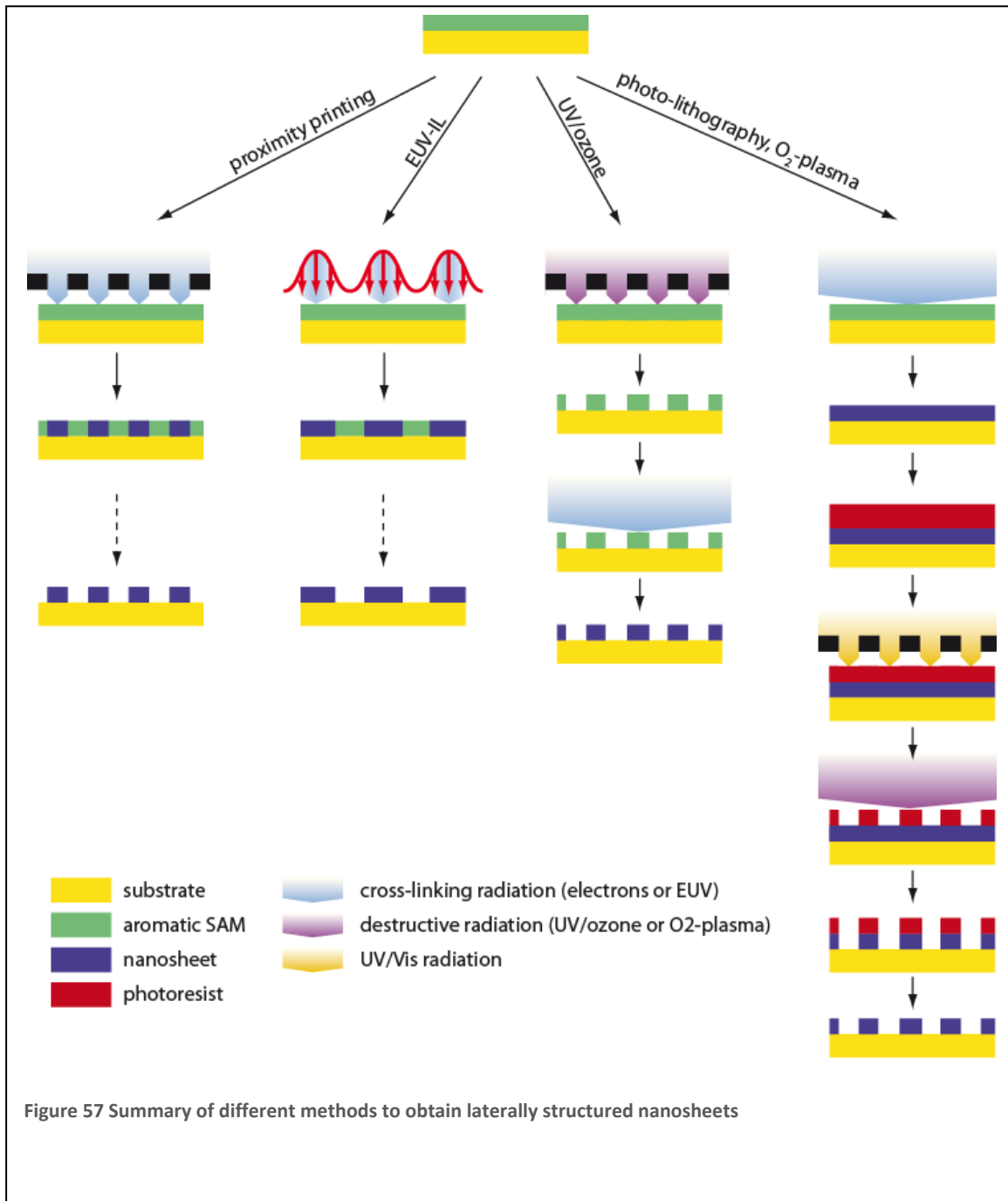
	Proximity printing	EUV-IL	Plasma etching	UV/ozone
Effect on exposed area	cross-linking	cross-linking	removal of nanosheet	removal of SAM
Possible structures	shadow mask	Interference patterns	arbitrary	arbitrary
Smallest features	$\approx 1 \mu\text{m}$	$\approx 30 \text{ nm}$	$\approx 1 \mu\text{m}$ ($\approx 10 \text{ nm}$ for EBL)	$\approx 1 \mu\text{m}$
Equipment	floodgun	synchrotron	floodgun photolithography plasma cleaner	UV/ozone cleaner floodgun

Table 2 Comparison of different methods to pattern nanosheets.

drawbacks are the low availability and high cost associated with a synchrotron based technique. Also, the possible patterns achievable by the interference method are very limited (lines, dots, etc.).

A viable alternative was developed using photolithography and plasma etching to pattern nanosheets after cross-linking. This approach is very versatile, as arbitrary shapes that are accessible by photolithography can be “carved” into the nanosheet. The fourth method makes use of the selective removal of the SAM in regions that are exposed to UV/ozone prior to cross-linking. Using shadow masks the contrast can thereby be reversed as compared to the proximity printing technique. Some of the features of the different methods are also summarized in Table 2.

In addition to the processes shown, combinations are also possible to imagine. Especially for the last two processes, the photoresist or shadow masks are to a large extent interchangeable. In total, there is now a whole toolbox of different methods available for patterning nanosheets for a variety of applications.



4.4 Nanosheet multilayers

Multilayer structures can be found in nature in a variety of layered minerals such as graphite, MoS, mica and clays. These generally have strong in-plane bonds and weak coupling between the planes, so that they can easily be cleaved along the layers. Recently it was shown that it is possible to even obtain single layers of such minerals [97]. By going the opposite direction, materials can be assembled from the “bottom up” by stacking up the single layers [2]. It is not necessary though to use “identical” building blocks for each of the layers. This opens up a route to totally new “synthetic” materials.

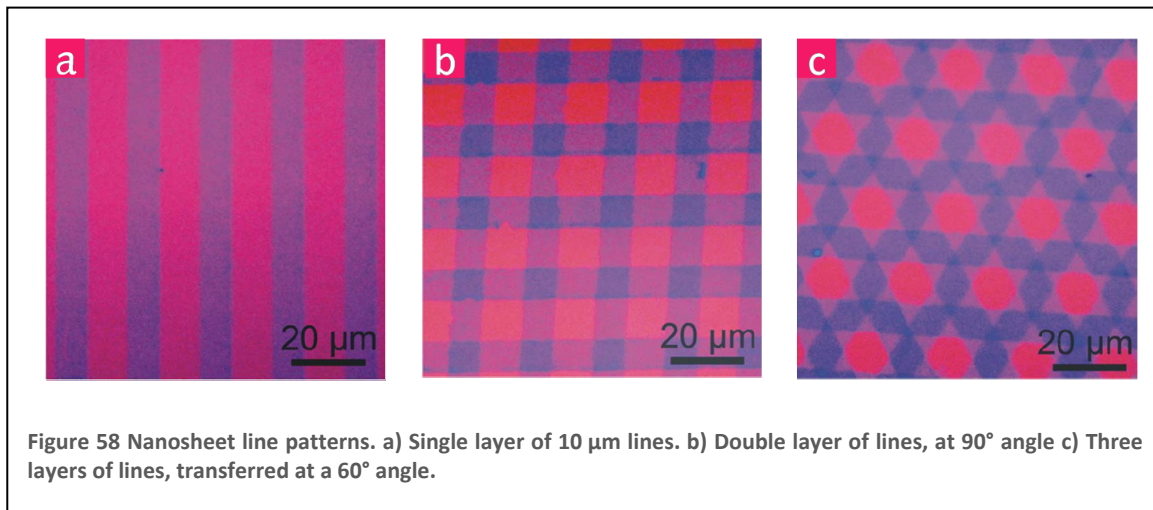
A technique that is already widely used for preparing multilayer stacks is the so-called layer-by-layer assembly (LbL) [98-101]. Generally, this involves complementary layers of for example positively and negatively charged polymeric solutions that are alternatingly applied to the substrate. Also, other specific molecular interactions such as hydrogen bonding or charge transfer interactions have been used for LbL.

Langmuir-Blodgett films can also be prepared as multilayers on solid substrates [102]. Here, the amphiphilic molecular layers bind to each other by hydrophilic and hydrophobic interactions. Thick layers have been used to make antireflective coatings [103]. The number of layers can be determined by the help of the color of the multilayer stack that can be compared with a suitable reference step gauge [104]. Recently, it was also demonstrated that freestanding films with thicknesses down to 3-4 nm can be prepared from polymer LB-films [105, 106]. With these films multilayer assemblies of several hundred layers were prepared [107].

In a similar fashion several layers of nanosheet can be stacked on top of each other by the transfer method that was described earlier (chapter 4.1). Here, no specific interactions between the layers are necessary, as the layers can easily be positioned on top of each other. In this chapter, first it is shown that multilayers can be prepared with high precision. Then, multilayers of BPT on SiO₂/Si substrates are characterized by XPS and UV-Vis spectroscopy and the origin of the optical visibility on these substrates is explored.

4.4.1 Structured nanosheet multilayers

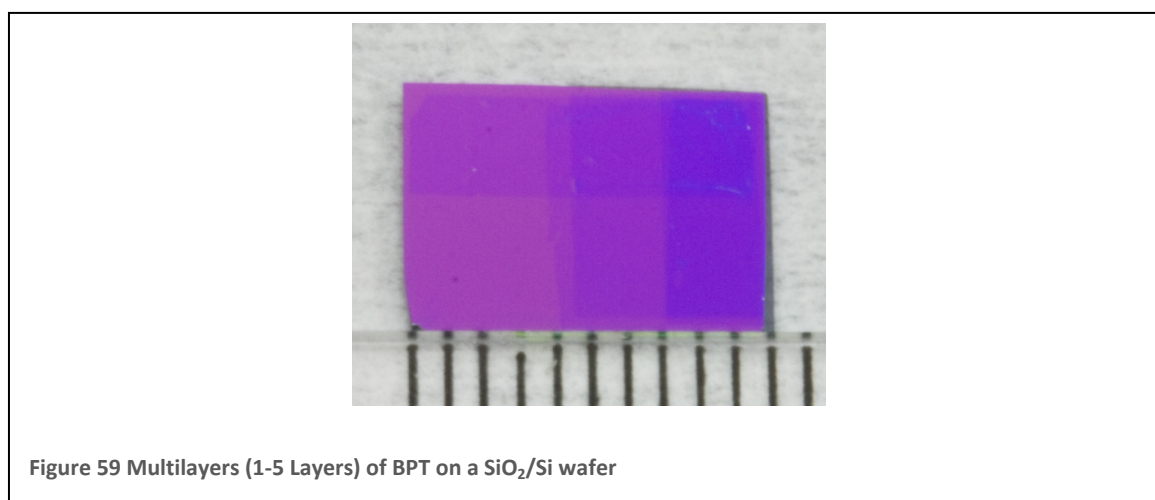
Nanosheet stripes of $10\ \mu\text{m}$ width with $10\ \mu\text{m}$ spaces have been prepared by photolithography and plasma etching, as was described in 4.3.3. An optical micrograph



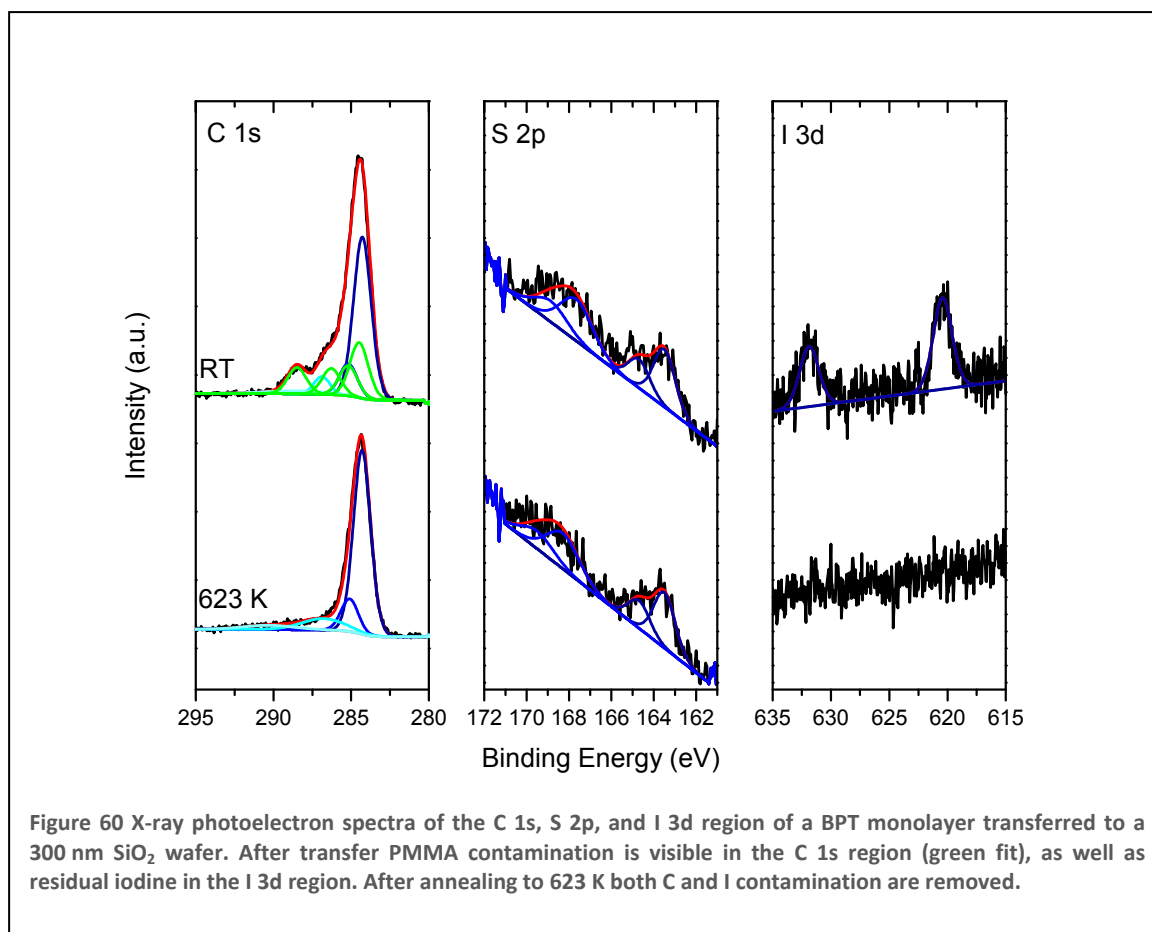
of such stripes after transfer is shown in Figure 58a. By transferring such line patterns on top of each other, multilayer structures can be generated as is shown in (b) and (c). The spatial orientation of the transferred nanosheet stripes is determined by the spatial orientation of the photoresist during transfer. Hence, the relative orientations of subsequent nanosheet layers can be fully controlled. In Fig. 3c an angle of 90° was chosen between two subsequent transfer steps. In Fig. 3d angles of 60° were chosen between three subsequent transfer steps. These results were obtained without the help of any alignment tool. However, the angles observed after the transfer deviate less than 3° from their intended values. Also note that the interference contrast changes with the addition of each new nanosheet layer and the increased local layer thickness corresponds to a further blue shift.

4.4.2 XPS evaluation of multilayer samples

As a first step for characterizing multilayers of nanosheet, XPS spectroscopy was used. Samples were prepared that allowed for measuring a reference signal together with the spectra of 1 to 5 layers of nanosheet. An example is shown in Figure 59. Binding energies were calibrated with respect to the C 1s signal of the nanosheet at 284.2 eV. For peak fitting a Shirley background and a Gaussian-Lorentzian line shape with 30% Lorentzian were used.

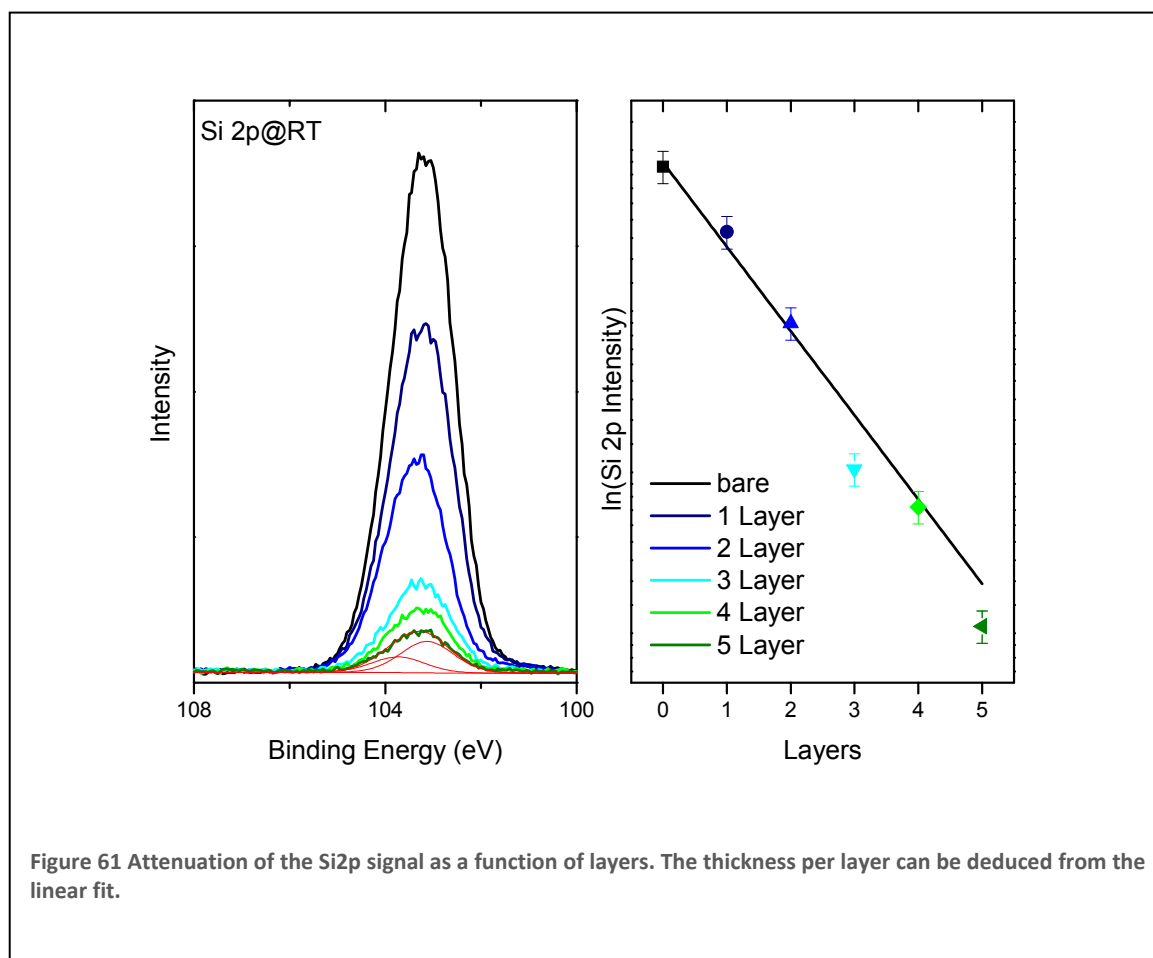


The C 1s peak consists of a main peak at 284.2 eV with a full width at half maximum (FWHM) of 1.3 eV that is assigned to the aromatic carbon atoms of the cross-linked BPT. Further a peak at 285.2 eV (FWHM 1.3 eV) that is generally attributed to the carbon directly bonded to sulfur. Additionally, it was found that the nanosheet was contaminated by a layer of polymethylmethacrylate that gives rise to signals at 284.5, 285.2, 286.3, and 288.5 eV (FWHM 1.4 eV) with an intensity ratio of 2:1.1:0.95:0.95 which is in good agreement with literature values [108, 109]. PMMA accounts for 40% (1 Layer) to 50% (5 Layers) of the carbon signal.



In the S 2p region, two sulfur species are found. The doublet at 163.5/164.7 eV (FWHM 1.2 eV) is assigned to thiolates or disulfides [110] and the doublet at 167.5/168.7 eV (FWHM 1.8 eV) can be attributed to oxidized sulfur species that were formed during or after transfer. Interestingly, the intensity of these oxidized sulfur species is roughly constant for 1 to 5 layers of nanosheet (see Figure 93). If oxidation was present in every layer, it would be expected that the signal is increasing with each additional layer. A constant intensity, however, might be due to oxidative processes during handling of the samples in air, which are mostly affecting the sulfur closest to the sample/air interface. Additionally, a residual iodine signal is found at 620.4/631.9 eV that originates from the Au-etchant.

The thickness of the carbon-layer (nanosheet + contamination) can be derived from the attenuation of the Si 2p peak of the SiO₂ substrate. An attenuation length of 3.43 nm was used. The average thickness per layer was found to be 1.7 ± 0.13 nm. Additionally, the thickness can be calculated from the attenuation of the O 1s peak of the SiO₂ substrate (attenuation length: 2.67 nm). As the PMMA contamination contains oxygen, this value (0.78 ± 0.09 nm) is too small.



In order to remove the contaminants, samples were annealed to 623 K. This temperature is sufficient for the thermal degradation of PMMA [111, 112] as can be seen from the C 1s spectra that were taken after annealing. The peak can be fitted by two components at 284.2 and 285.1 eV (FWHM 1.3 eV) and two satellites at 286.8 and 290.3 eV, which is expected for cross-linked BPT nanosheets [113]. Additionally, as can be seen from the I 3d region, no more iodine can be found. The intensity of the S 2p signal at 163.5/164.7 eV is generally slightly higher than before annealing, as is expected if the attenuating PMMA layer is removed. The oxidized sulfur species binding energy shifts to 168.3/169.5 eV, albeit with slightly lower intensity, indicating further oxidation and some diffusion into the vacuum. The average thickness per layer after annealing is found to be 0.85 ± 0.05 nm (0.77 ± 0.03 nm from O 1s). Hence, annealing to 623 K was sufficient to remove all contaminants.

4.4.3 Optical Properties

Similar to graphene, it is possible to see a single cross-linked nanosheet by the naked eye, if it is placed on top of an oxidized silicon wafer. The origin of this contrast has been described for single as well as multilayer graphene by Casiraghi [46] and Blake [61] and others [114-119]. It is dependent mostly on the thickness of the oxide layer that acts as a spacer, similarly to an interferometer. In order to understand the origin of this contrast for nanosheets, UV/Vis spectra were measured with a reflection probe. The reflection R_λ is given by

$$R_\lambda = \frac{I(\text{sample})}{I(\text{substrate})} \quad (31)$$

Casiraghi defines contrast (δ) as the difference between substrate and sample intensity, normalized to the substrate intensity. That means that regions that are darker than the substrate have a positive sign, so that

$$\delta = 1 - R_\lambda \quad (32)$$

Both terminologies are used in the following.

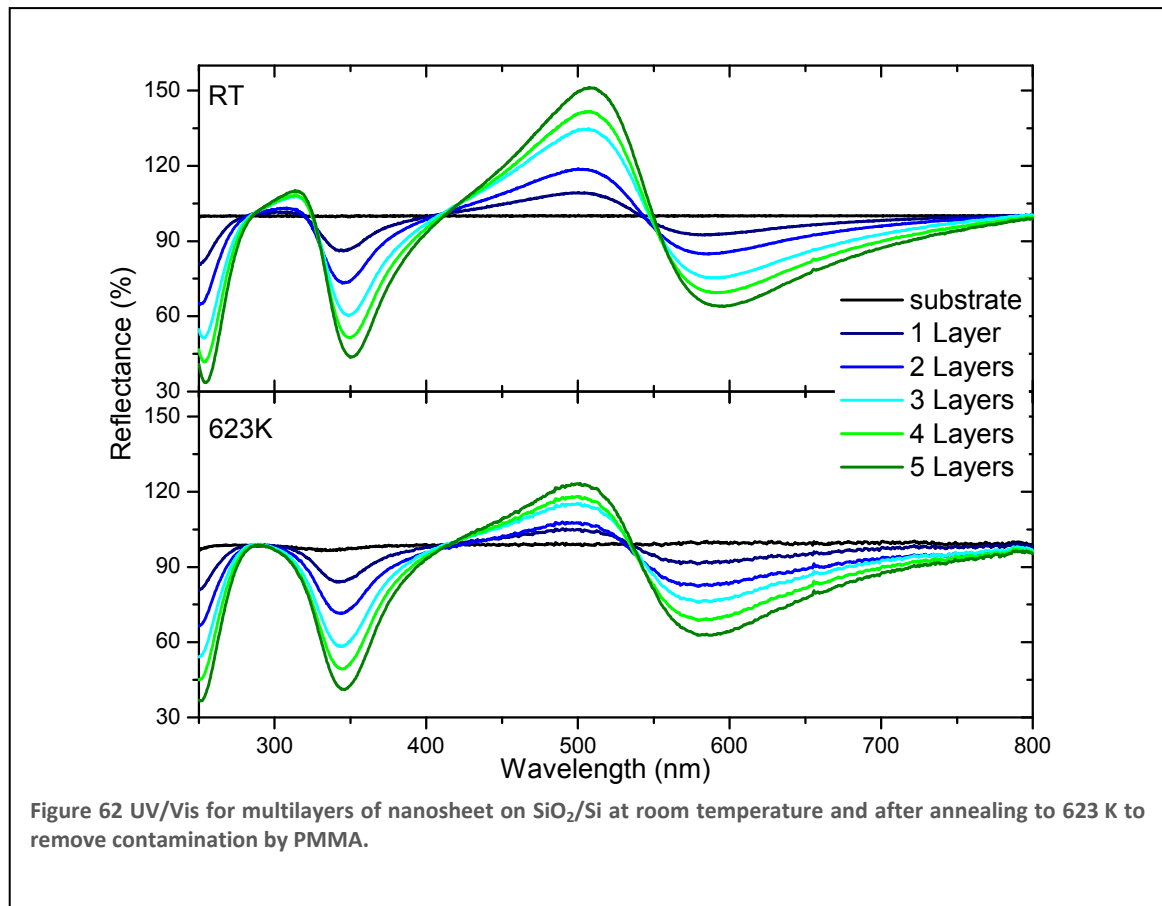
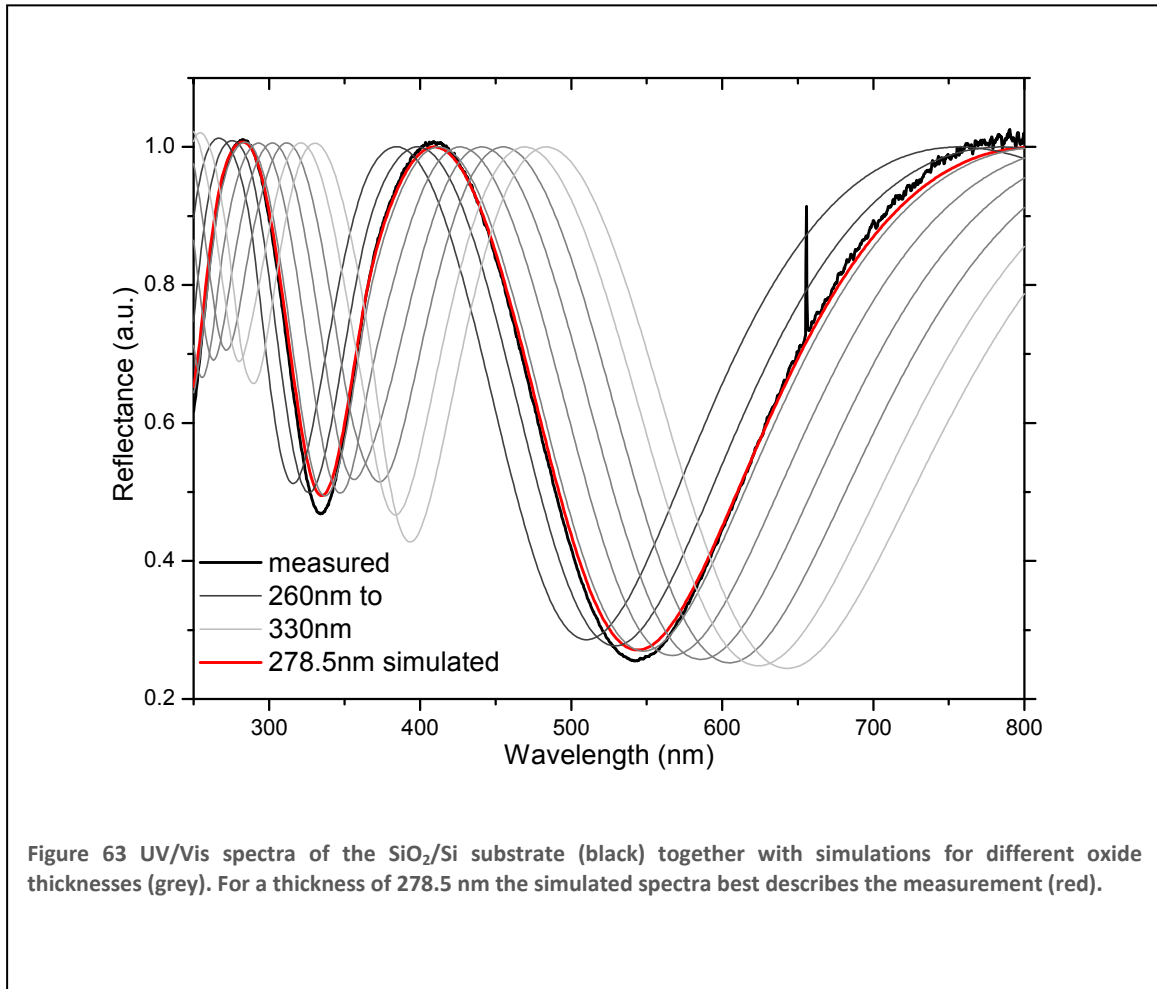


Figure 62 shows the spectra measured at room temperature and after annealing to 623 K to remove contaminants. The spectra have pronounced minima at $\lambda \approx 250$, 350 and 570 nm as well as a maximum at $\lambda \approx 500$ nm. A smaller maximum is found around 300 nm in the room temperature spectra that vanishes after annealing to 623 K. With each additional layer, the reflected intensity at the maxima (minima) is increasing (decreasing) roughly linearly and the position is slightly shifted towards higher wavelength. For the same amount of layers, the maximum intensity at $\lambda \approx 500$ nm is smaller in the annealed sample than at room temperature. This can be attributed to the removal of contamination during the annealing step.

4.4.3.1 Simulation

To understand the origin of the spectral features, it is necessary to simulate reflection spectra. As a first step, the spectrum of the SiO₂ substrate was measured using a freshly



etched Si wafer as a reference. Subsequently, different thicknesses of the SiO₂ layer were modeled, in order to determine the precise thickness that was used in the measurements. In order to accurately simulate the spectral data, it is necessary to use the wavelength dependent complex refractive indices of both Si and SiO₂ [120]. The simulation results are shown in Figure 63, the black curve represents the measured spectra and the grey spectra are simulated for SiO₂ thicknesses from 260 to 330 nm in steps of 10 nm. A thickness of 278.5 nm (red curve) was found to best describe the measured data, and was used for all further simulations.

As the refractive index is not known for the BPT nanosheet, it has to be estimated for simulations. Polymers generally have refractive indices between 1.3 and 1.7, polymers that contain aromatic units are mostly found on the high end. For the simulation two values were used: polystyrene: $n \approx 1.55$, and polyphenylene: $n \approx 1.7$. The refractive index was kept constant over the whole wavelength, for both values similar spectra were obtained, the only difference being a slightly higher magnitude at the minima/maxima for the higher refractive index. Figure 64 shows the simulated spectra for $n=1.7$, in the top spectra the layer thickness was set according to the XPS results (4.4.2), including the PMMA contamination. The bottom spectrum resembles a clean nanosheet with the nominal thickness of 1 nm. The features of the measured reflection data (Figure 62) can be described by these spectra for wavelength above 400 nm and even the magnitude is comparable, if the higher thickness of the layers is taken into account.

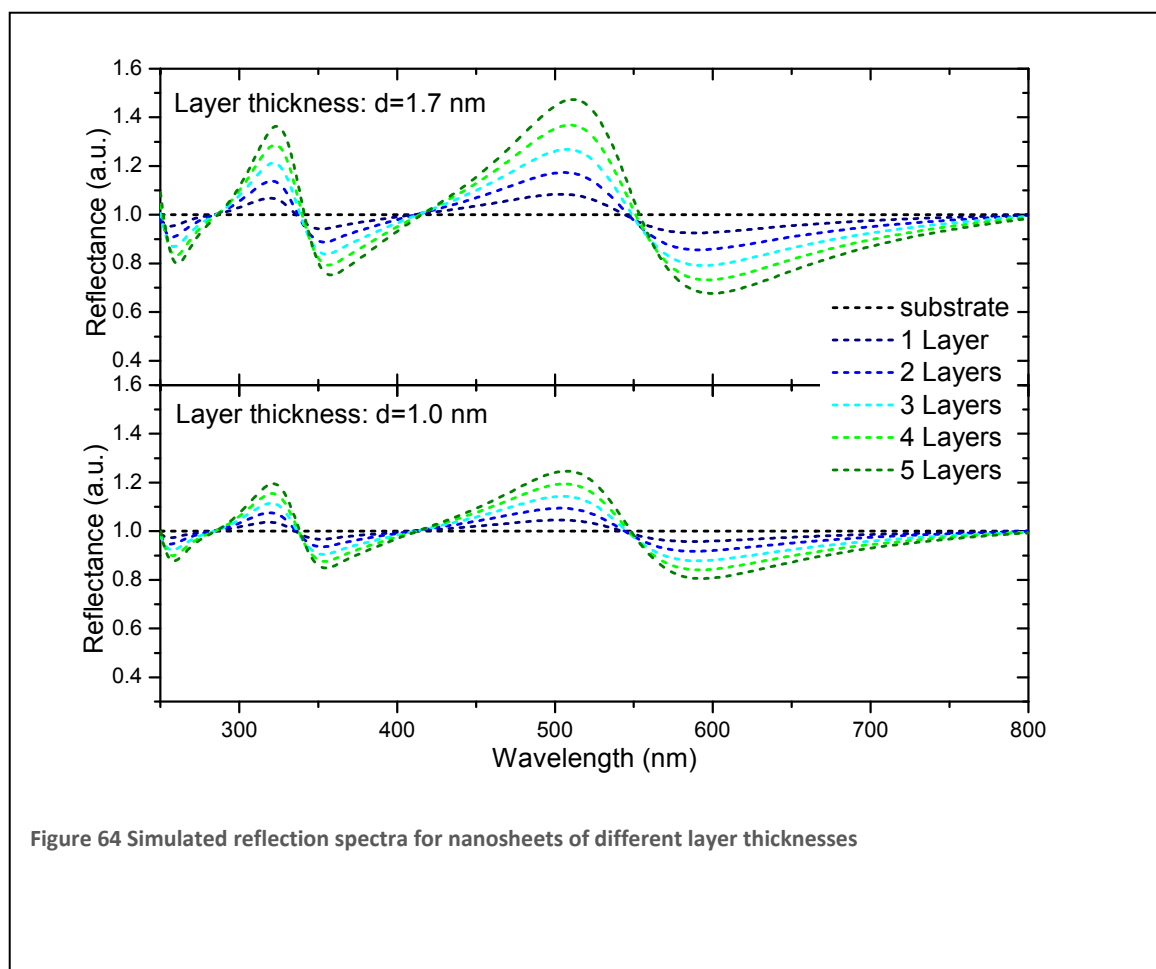
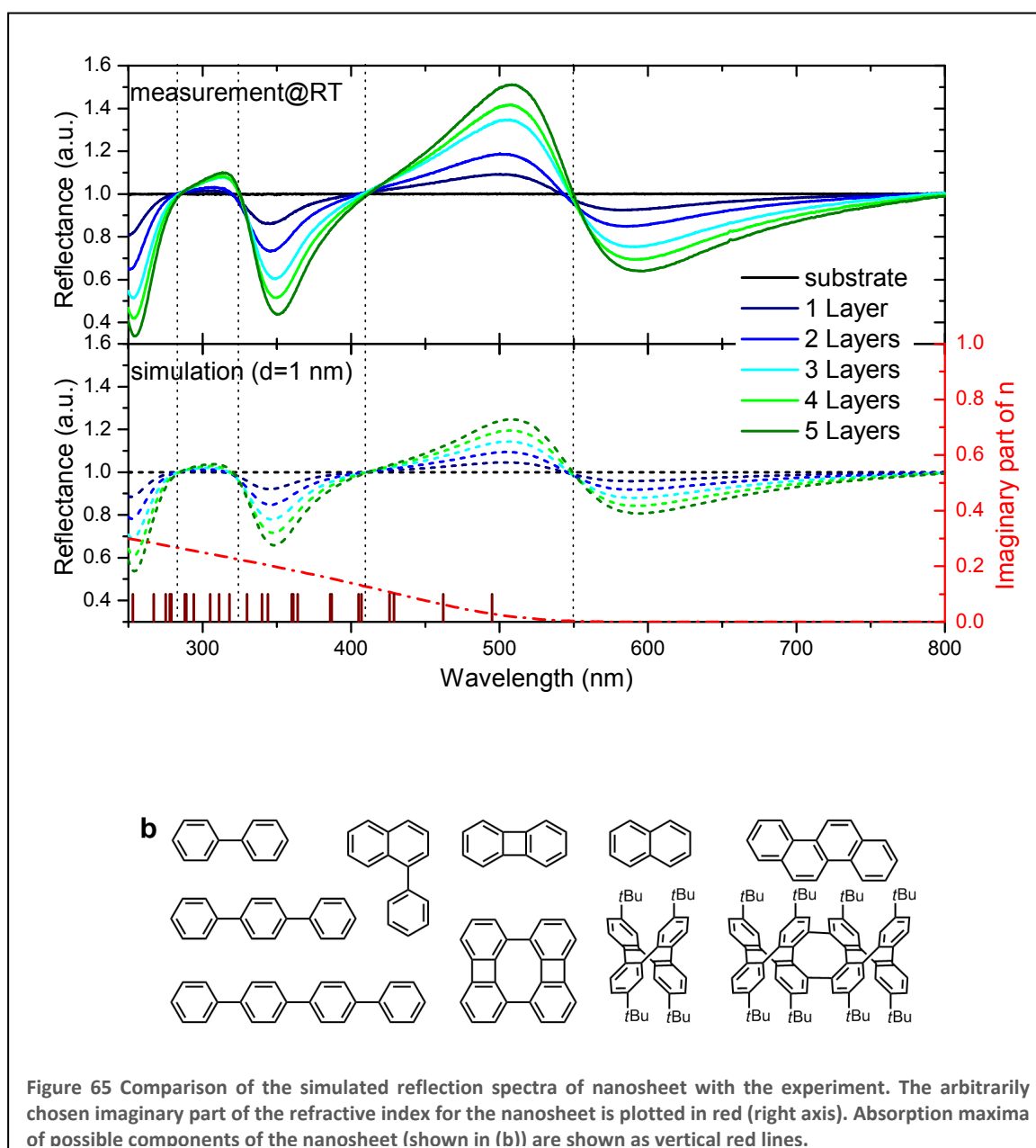
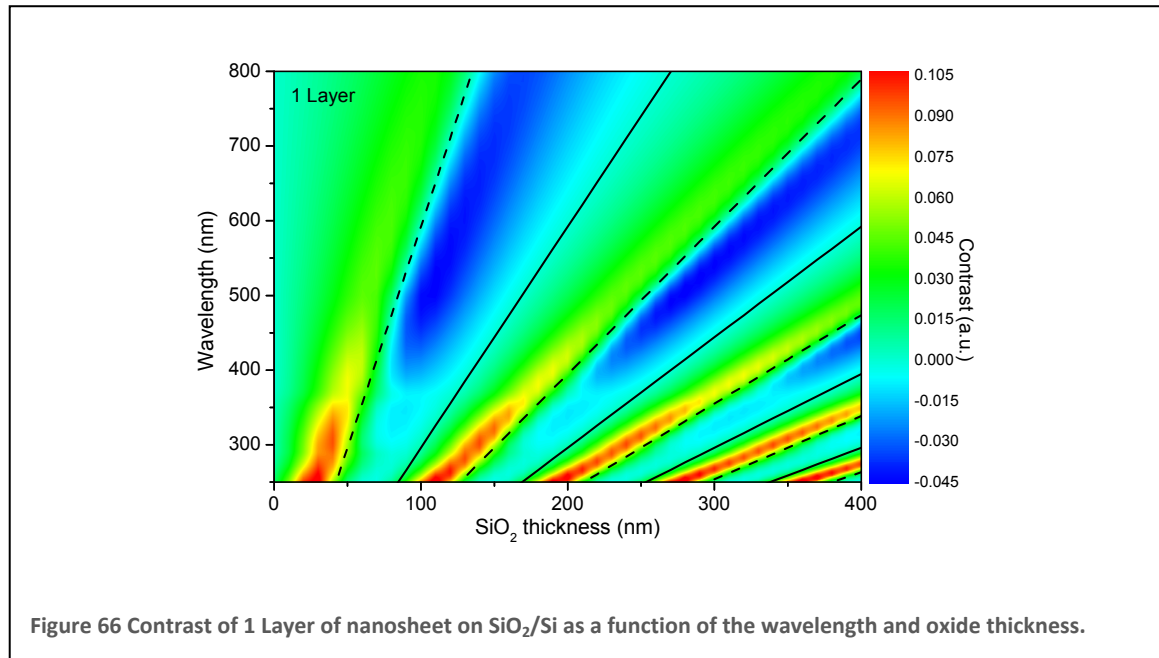


Figure 64 Simulated reflection spectra for nanosheets of different layer thicknesses



For better describing the spectral features in the UV range, the assumption that the refractive index is real and constant over the whole range of wavelengths can no longer hold. PMMA is known to be absorbing in the near UV-range. As was shown earlier, however, the PMMA can be completely removed by annealing to 623 K. The shape of the UV/Vis spectra though is not changing significantly in the near UV range (Figure 62), indicating an absorption due to the nanosheet. Thus, an imaginary part k was added arbitrarily to the refractive index below 500 nm. The absorption peaks of aromatic molecules that are possible candidates for being present in the cross-linked BPT nanosheet are lying in this range [121-123]. These are i.e. terphenyl, quaterphenyl, biphenylene, naphthalene, tetraphenylene, and others (Figure 65b) A few of the absorption maxima have been added as vertical red lines in the simulated spectra in

Figure 65a. The arbitrarily chosen imaginary part of n is shown as a red dashed line. Comparison of the simulated spectrum with the measured data at room temperature shows good agreement over the whole spectral range. For an even better agreement

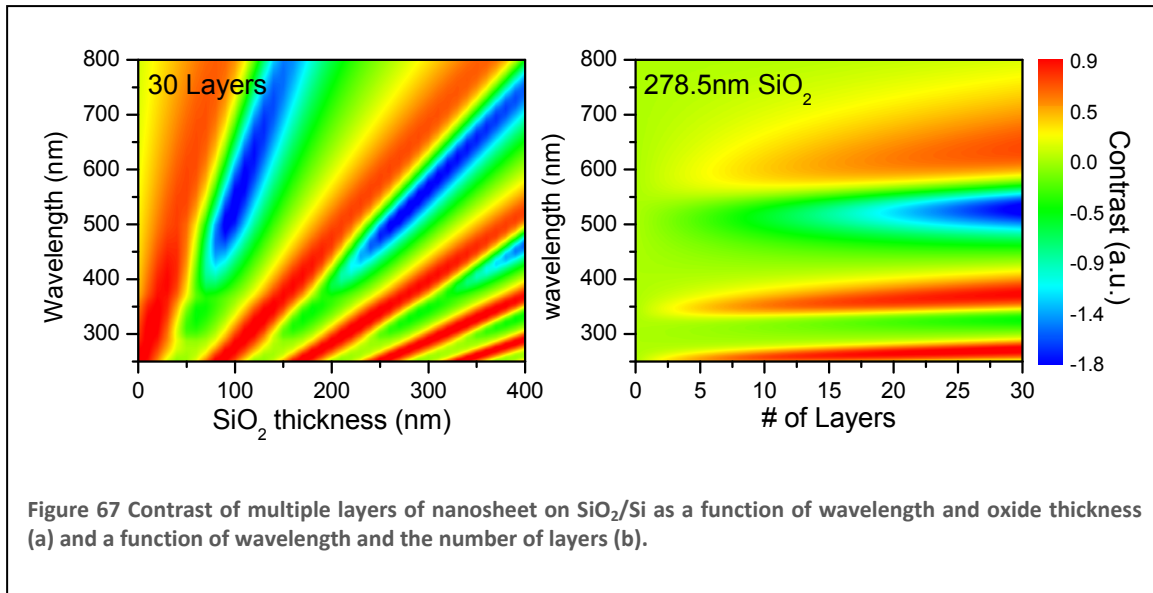


and more accurate description of the reflection data, the complex refractive index of the BPT nanosheet would have to be known. It should be possible to measure the refractive index of the nanosheet i.e. with spectral ellipsometry.

4.4.3.2 Dependence of contrast and thickness

Figure 66 shows the simulated contrast for one layer of BPT nanosheet as a function of wavelength and SiO₂ thickness. The general ray-like appearance is due to the shifting of the substrate spectra with higher oxide thicknesses. The rays follow the maxima and minima of the substrate spectra, as given by the criteria for constructive (straight line) and destructive (dashed line) interference in thin films (equations (9) and (10)). As the nanosheet is not absorbing in the visible range, and has a refractive index similar to the SiO₂ the reflection spectra shift slightly to higher wavelength by adding layers of nanosheet. The highest contrast is thus expected at the inflection points of the spectra.

Maximum contrast for all substrate thicknesses is found in the UV-range, which is due to absorption. Despite being of lower intensity, for all SiO₂ thicknesses a contrast in the visible range is expected. For thin oxide layers such as 10 nm the contrast is still between 0.005 and 0.01. Oxide layers of 70 nm or more are found to show both positive and negative contrast, depending on the wavelength.



Thicker layers give rise to a higher contrast, shown in Figure 67a for 30 layers. For such thick multilayer stacks no special substrate is necessary, as for each oxide thickness a very high contrast is observed. Figure 67b shows the contrast as a function of wavelength and the number of nanosheet layers at the given SiO₂ thickness of 278.5 nm. In this case the nanosheet layers significantly contribute to the optical path, the minima and maxima of contrast are shifted to higher wavelength with additional layers.

The strong wavelength dependence of the contrast makes it necessary to carefully choose the substrate in order to maximize visibility of a few layers of the BPT nanosheet. Contrast can be improved by the use of filters that can be chosen to achieve maximum contrast at a given substrate.

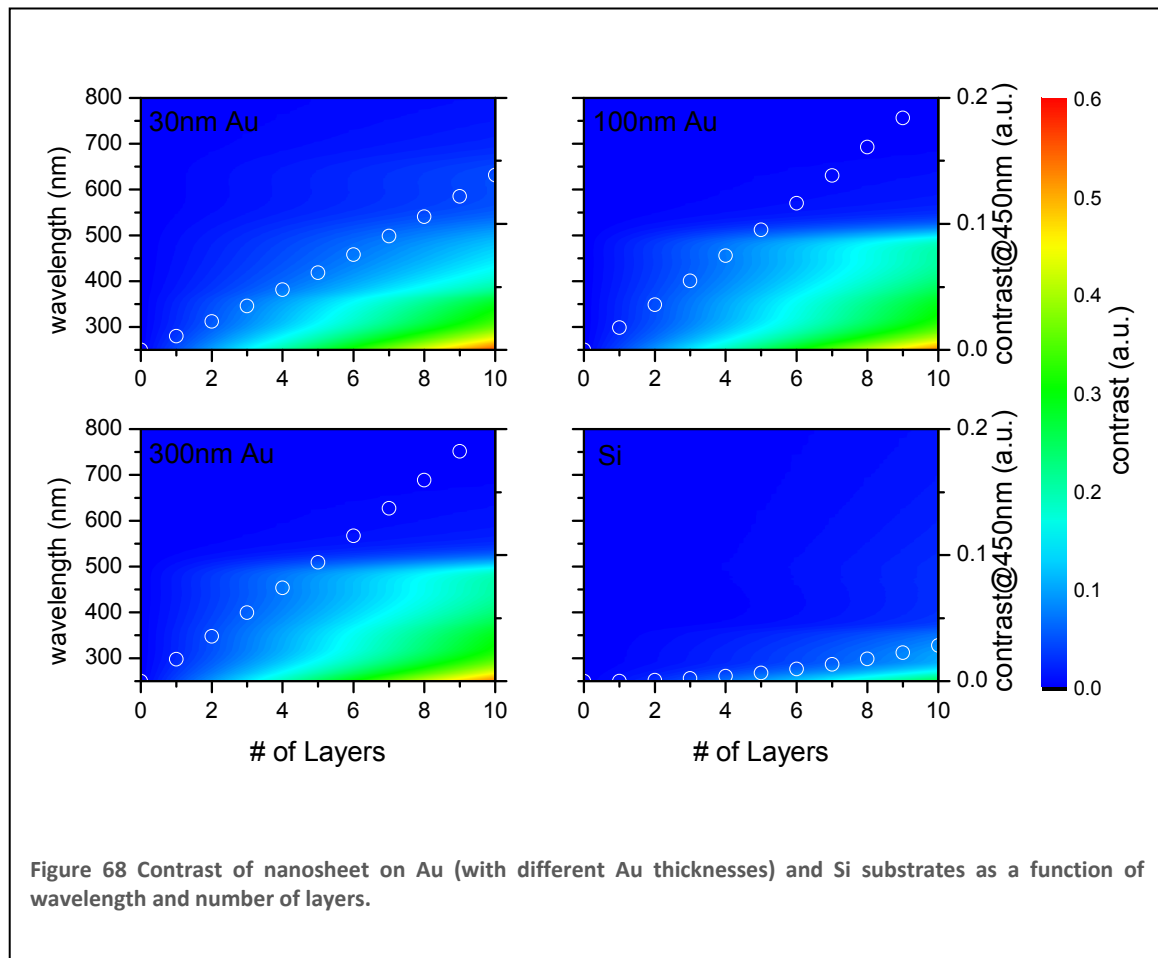


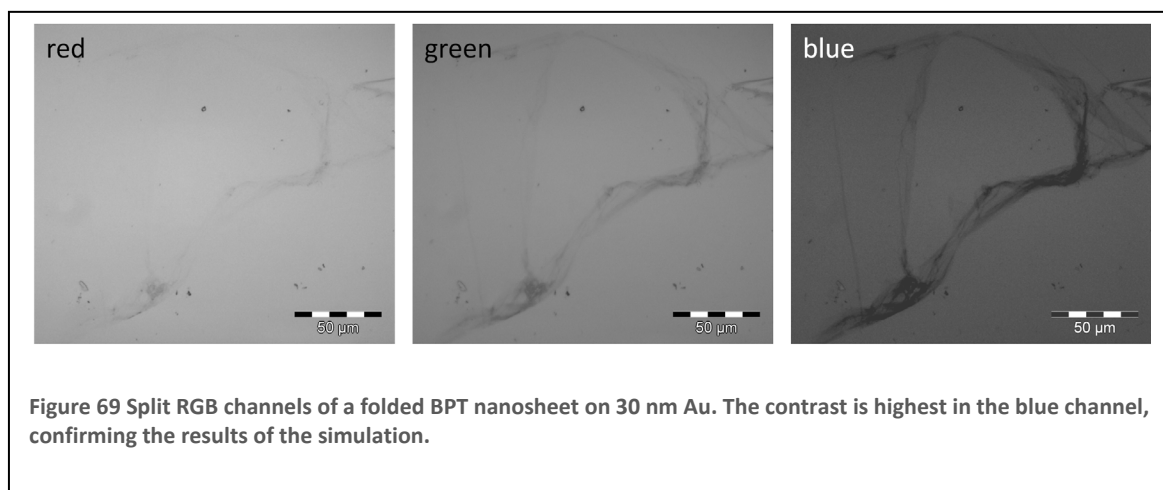
Figure 68 Contrast of nanosheet on Au (with different Au thicknesses) and Si substrates as a function of wavelength and number of layers.

4.4.3.3 Contrast on different substrates

It is now interesting to see, whether the role of the SiO_2 as an optical spacer is necessary to see the nanosheet by the naked eye. Other substrates that are generally used in our lab are Au (on silicon) substrates of different thicknesses as well as Si-wafers. The contrast on these substrates as a function of wavelength and the number of nanosheet layers is displayed in Figure 68a-d. For easier comparison, the contrast at 450 nm is added as white circles to each graph. Au is characterized by absorption in the UV to the blue visible range, which falls together with the absorption of the nanosheet. This leads to an enhanced contrast in blue light. In a cleanroom environment, where blue light is filtered, the nanosheet on Au is therefore invisible to the naked eye. Si on the other hand does not have such pronounced absorption in the UV-blue range, hence only thicker layers can be seen. The thickness of the Au layer seems to not have a big influence; both 100 and 300 nm Au give identical results. In the thinner 30 nm Au film the underlying Si is contributing, reducing the contrast. To check whether the simulation is able to predict the contrast of the nanosheet on Au, a piece of nanosheet was transferred to a Si wafer with a 30 nm Au layer. Figure 69 shows an optical micrograph of

a ripped and folded area of the nanosheet. The original image was split into the three channels red, green and blue. In agreement with the simulation, the contrast in the blue channel is highest, whereas in the red channel only the thickest multilayers of the folds are visible. This is strong evidence that the visibility of the nanosheet can be enhanced, if narrow band filters are used.

From the comparison of Au vs. Si substrates it is apparent that contrast enhancement is not limited to substrates that have a thin film coating with a thickness in the range of the wavelength of visible light. The contrast of gold originates from a strong change in the substrate absorption in the visible range, in this case around 450 nm. Such changes in absorption are characteristic of any colored materials; a contrast enhancement of nanosheet placed on top of these substrates is therefore expected.



4.4.3.4 Substrate independent contrast enhancement

It was shown in the previous sections that the visibility of the nanosheet depends strongly on the properties of the underlying substrate. It is favorable if the substrate is colored, showing a strong change in absorption in the visible range. The logical approach for enhancing the contrast of nanosheet on i.e. bare Si wafers is hence the coating with a thin film. The only requirement for these films is a thickness in the visible range to achieve thin film interference conditions.

Visibility of the nanosheet through the photoresist was first observed during development of the transfer procedure. In some cases the nanosheet was showing

defects, rips and folds after transfer. It was not clear, whether the damage occurred during transfer or later while dissolving the resist layer. Figure 70 shows optical micrographs of the transferred nanosheet/photoresist sandwich (in this case to an oxidized Si wafer) before and after dissolving the photoresist. The defects are clearly visible through the resist (a), and become more apparent when the contrast is enhanced (b). Figure 70c shows the same area of the sample after dissolving the resist in acetone. The size and shape of the defects are exactly matching the ones that are visible through the resist. Thick folds can even be seen as bright spots in the dark field image (not shown). This observation was then able to confirm that the dissolution was not responsible for the defects. It turned out that the damaged nanosheets were a result of incomplete/inhomogeneous cross-linking.

In addition to the detection of defects in large nanosheets, this technique would also be extremely useful for transfer of patterned nanosheets, as the integrity of the patterns can be monitored prior to dissolving the photoresist. As the contrast enhancement is not depending on the substrate, it might even be possible to check samples for defects while the nanosheet/photoresist sandwich is still swimming on top of the water, before applying it to the new substrate. Especially for procedures requiring multiple processing steps, such as the preparation of multilayer stacks, this could be very valuable.

Recently, this technique was also described by Teo et al., who simulated the contrast of graphene on a variety of different substrates using PMMA as the contrast enhancing top coating [124].

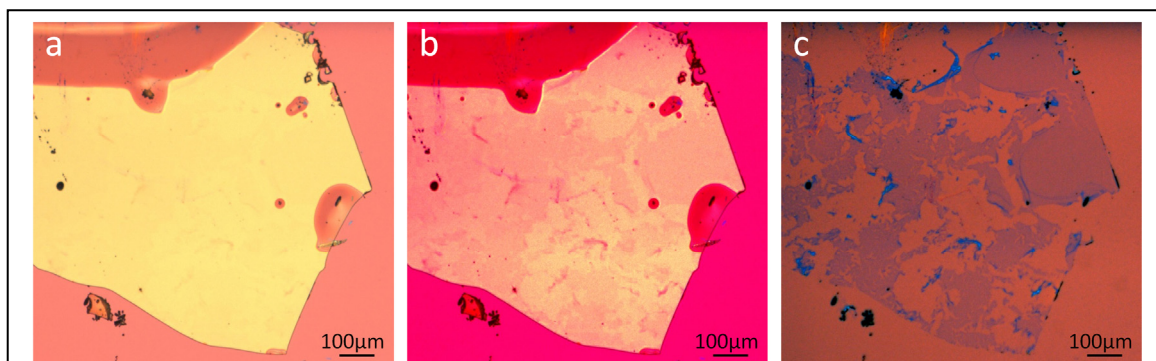
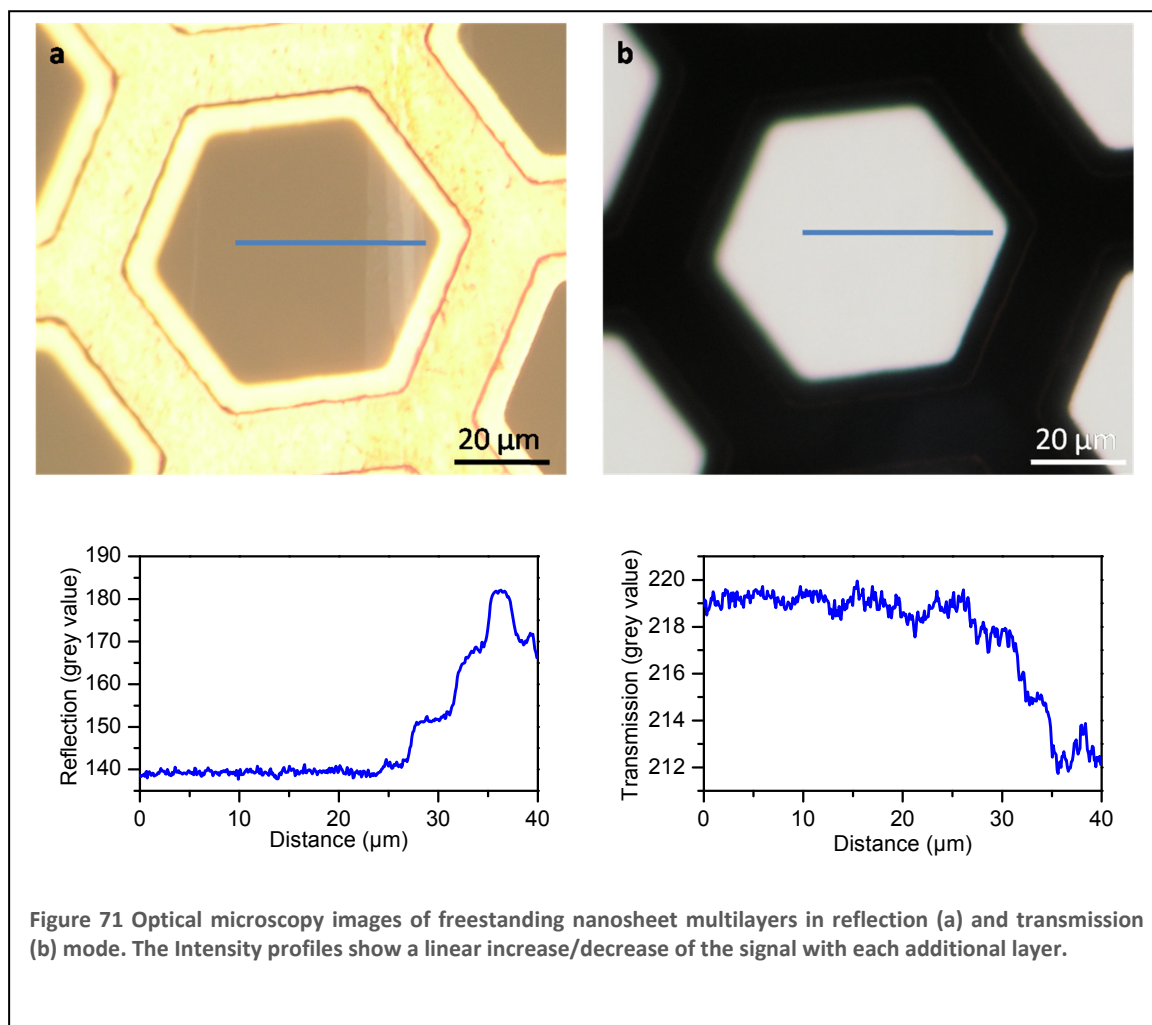


Figure 70 Contrast of nanosheet observed through the resist layer. The nanosheet is nearly invisible through the photoresist layer (a), but contrast enhancement can already show the defects (b) that are otherwise only visible after dissolution of the resist layer (c).

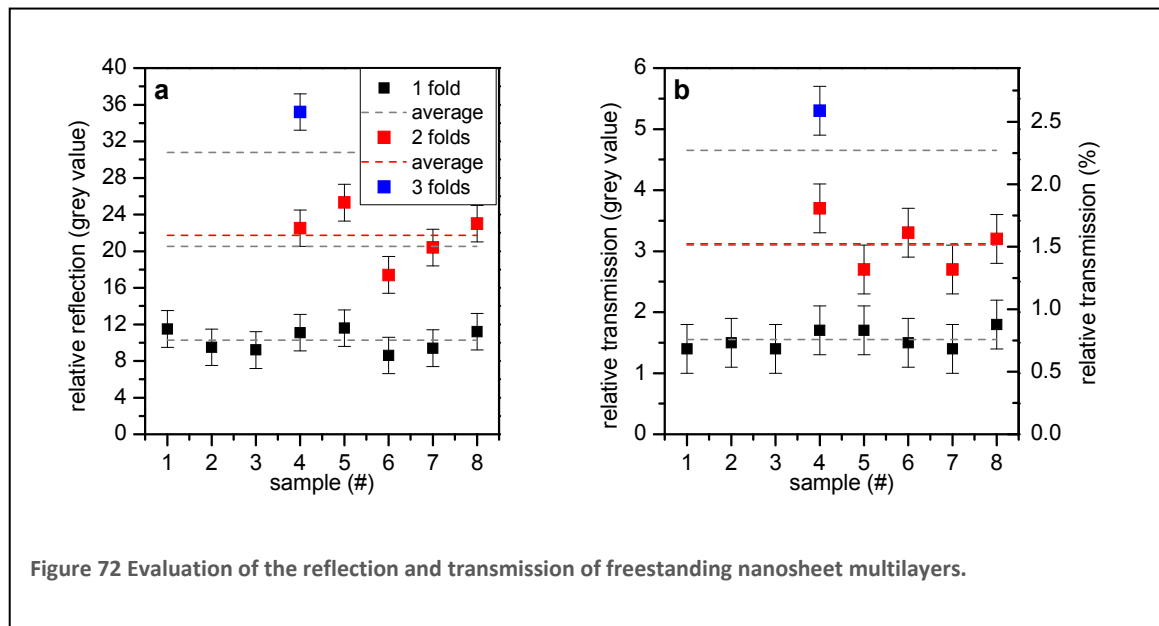
4.4.4 Optical Properties of freestanding nanosheets

If transferred to TEM grids, the nanosheet is practically invisible by means of optical microscopy. It is not possible to distinguish between holes that are covered with nanosheet from ones that are not. However, if holes are partly covered, i.e. if the nanosheet is ripped and still spanned over a corner, edges become visible presumably because they are rolled up and folded to thick layers. It is not possible to quantify this contrast though, as the thickness at the edges is not known.

This problem can be solved if folds on intact areas are found where each fold corresponds to an additional double layer. An image with a stack of such folds can be seen in Figure 71a, a corresponding averaged line scan of the grey values in the image is shown underneath. With each additional fold in the nanosheet the reflection is



increasing by roughly the same amount. In transmission (Figure 71b) this difference is not as pronounced, and not visible, however, in the line scan the steps can still be seen. Several of such folds were analyzed in the same way and the grey values plotted against the thickness of the folds (Figure 72). One fold always gives the same increase in reflectivity and the same decrease of transmission. For a double fold the variation is



slightly higher, but the average corresponds nicely to the twice the average of the single fold. A triple fold was only found in one sample, but was included for completeness, even though it is not enough data to further confirm the linearity of the contrast. Due to the lack of a reference in the image, the reflection data cannot be quantified beyond the grey value analysis. For transmission, however, the references are contained in the image. The nanosheet monolayer was used for 100% and the values at the copper grid for 0% transmission. The relative decrease for each layer of nanosheet can then be calculated as $\approx 0.38 \pm 0.09\%$

Similar measurements were described by Nair et al. for freestanding graphene [125]. Due to the unique electronic properties of graphene, they were able to derive the fine structure constant from the transmission data. Each layer of graphene contributes to a decrease of white light transmission of $\approx 2.3\%$, whereas the reflectivity is very small ($< 0.1\%$). This is in contrast to the high reflectivity and low transmittance of the nanosheet, due to its insulating character with low absorption in the visible range. It might be a valuable tool for the monitoring of the graphitization of freestanding

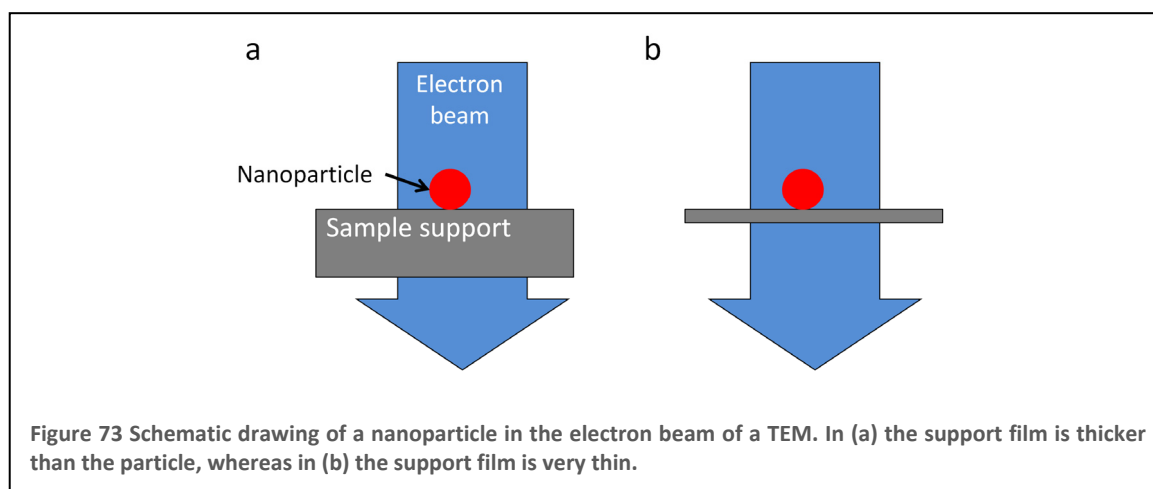
nanosheets by annealing, as the relative reflectivity is expected to be decreasing as the relative transmission is increasing.

4.4.5 Summary

By using the transfer method, it is now possible for the first time to fabricate multilayer stacks of cross-linked nanosheets. It was shown that this is possible in a very controlled way, such that defined multilayer geometries become possible with patterned nanosheets. Multilayer stacks of nanosheet show an increased optical contrast with respect to the SiO₂/Si substrate for each additional layer. The ability to prepare large areas of nanosheet with a defined number of layers makes it possible to measure optical reflection spectra over the UV/Vis range. By simulation of these spectra, the origin of the optical visibility can be explained by means of an interference effect. Interestingly, freestanding multilayers are also visible by optical microscopy.

4.5 Nanosheets as TEM sample supports

The resolution in the newest generation of transmission electron microscopes reaches about 0.08 nm [38, 39], which is sufficient to resolve single atomic columns in all crystalline materials. In the case of the imaging of nanoscale clusters, however, the experimental resolution frequently does not reach such values [126, 127]. The main difficulty arises from the need to place the cluster onto a thin sheet of a supporting material for imaging by the electron beam. The scattering of electrons from this



supporting material contributes to the overall detected scattering signal. For clusters with a size comparable to the thickness of the supporting material, this diminishes the image contrast and impedes the direct interpretation of transmission electron (TEM) or scanning transmission electron (STEM) micrographs (see Figure 73a). Hence, the foil thickness, thickness variations, chemical inertness and stability under high-energy electron beams must be considered when choosing a support for the study of nano- and subnano-sized objects. Most commonly used TEM foils are amorphous carbon, silicon oxide or silicon nitride film supported by a copper, nickel or gold grid. The usual thickness of these foils is ~ 10 nm, resulting in poor contrast of small nano-clusters. A strategy to enhance the imaging contrast is to reduce the support foil thickness (see Figure 73b). However, the thickness reduction diminishes the mechanical stability and increases its sensitivity against beam damage.

Higher stability foils might be achieved with a crystalline-like arrangement of atoms. Sheets of carbon atoms (graphene) were produced by mechanical cleavage of bulk graphite [97, 128] and a graphene sheet was freely suspended over metal grids and

imaged by TEM [129]. The current fabrication procedure, however, has limitations with respect to the yield, lateral shape and size of the suspended graphene sheets. After the complex fabrication by exfoliation, a sample usually consists of one graphene flake with a size of only a few microns. Another complication arises from the periodic arrangement of carbon atoms in graphene which results in a phase contrast in HRTEM micrographs which interferes with the contrast of objects onto the graphene layer. Therefore, an amorphous, very thin and stable support foil consisting of a light element is highly desired.

The nanosheet is able to fulfill these criteria as it can be prepared freestanding on standard TEM grids. Thus, in this chapter the use of freestanding nanosheets as TEM supports is explored. Nanosheet is used to image nanoscale cobalt and gold particles, and its performance is compared to conventional amorphous carbon supports.

4.5.1 Cobalt nanoparticles

SEM micrographs from a nanosheet deposited onto a ~15 nm thick carbon foil (Quantifoil) are shown in Figure 74a,b. The image contrast in (a) was chosen such that the sheet can only be seen on the amorphous carbon, whereas the circular holes of the Quantifoil that are also spanned by the sheet appear dark. In (b) the same region is imaged, however the contrast was adjusted to enhance the signal of the freestanding nanosheet within the holes. Similar to Figure 22c the freestanding nanosheet shows some folding that may result from handling of the SAM during its deposition onto the Quantifoil. Note that some folds in the nanosheet extend from the top of the carbon foil into the openings (see arrows).

Figure 74c shows a TEM micrograph of the edge of a 3 μm wide opening in the Quantifoil grid with the nanosheet spanning the opening. Cobalt nanoparticles (average diameter 6 nm) were deposited on the Quantifoil plus nanosheet composite. The thicker carbon foil in the left part of the image appears grey, whereas the right part of the micrograph

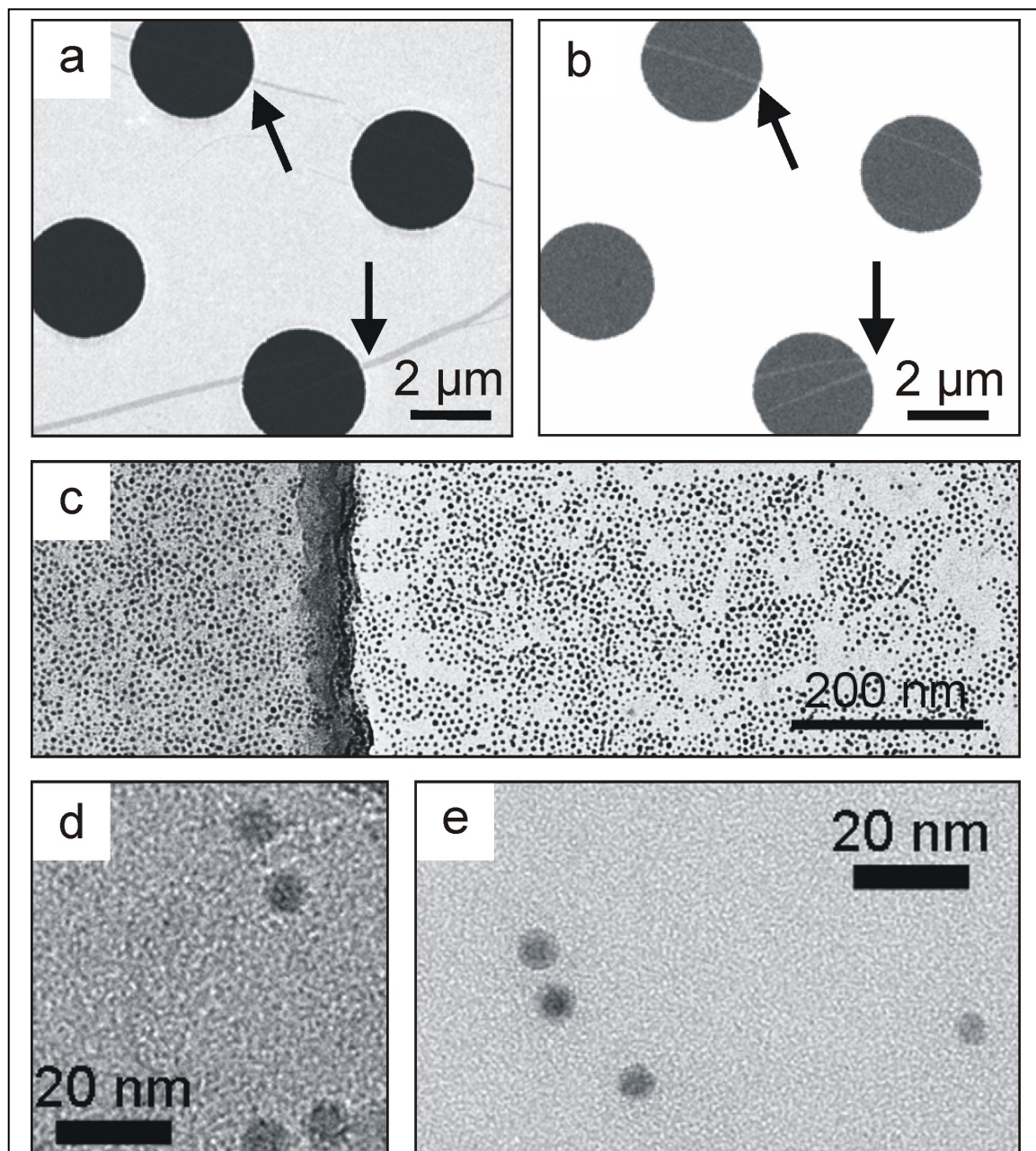
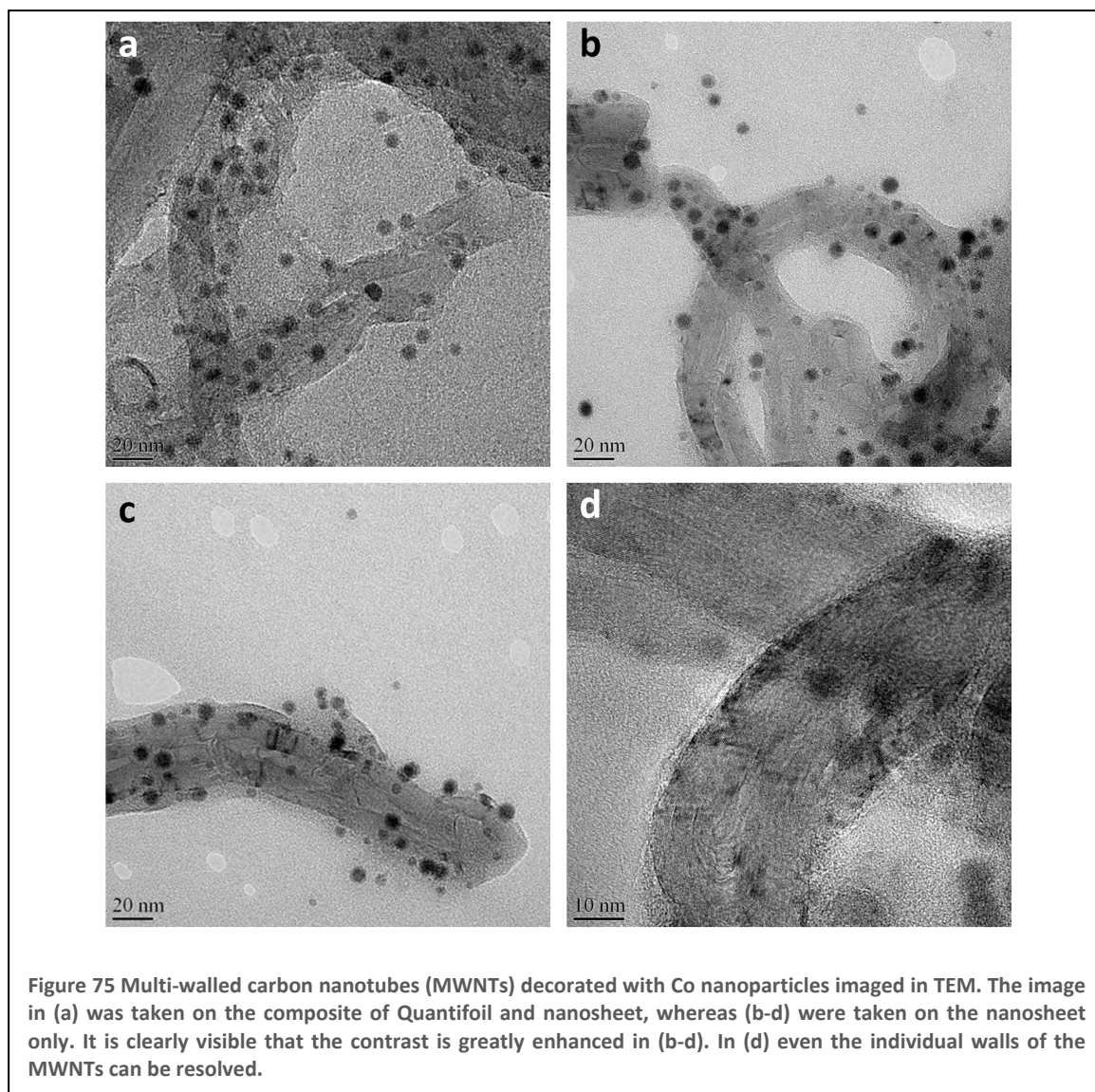


Figure 74 (a,b) SEM images of a nanosheet that has been spanned over circular 3 μm holes in a 15 nm thick carbon film with different contrast settings. (c-e) TEM images of Co nanoparticles deposited on nanosheets used as TEM support: (c) Low magnification image of Co particles (~ 6 nm diameter) deposited near the edge of a hole in the carbon film. Co particles are found on the conventional support (left) and on the nanosheet (right). The contrast is much higher for the particles on the nanosheet. (d,e) Higher magnification image of Co particles deposited on a 15 nm carbon film (d) and on a nanosheet (e) under identical imaging conditions at the Scherzer defocus. The contrast and sharpness of Co particles on the nanosheet are much higher and a distinct layer surrounding each particle can clearly be seen.

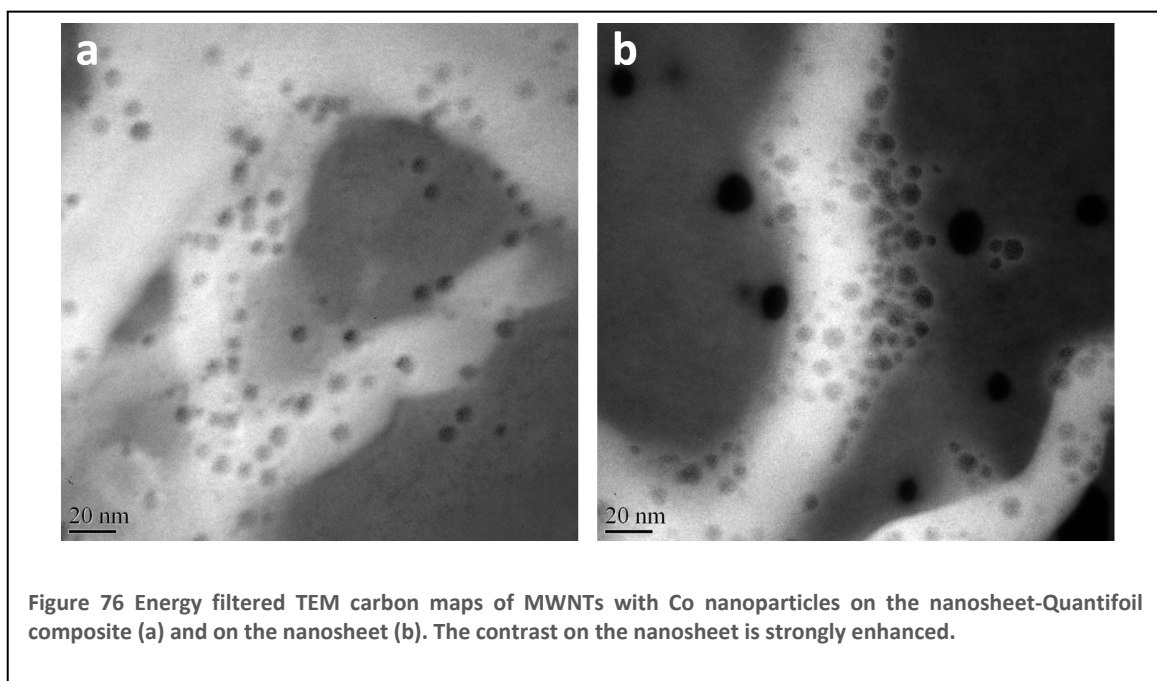
corresponds to the freestanding nanosheet area. It is evident that the contrast of Co particles supported by the bare nanosheet is much higher than that of the particles on the ~ 15 nm thick carbon foil plus the 1.6 nm thick nanosheet. Due to the thinness of the nanosheet, the electrons experience only little additional scattering, and the particles on the nanosheet are imaged with much higher contrast and sharpness.

TEM micrographs of Co particles supported by the carbon foil (Figure 74d), and by the freestanding nanosheet (Figure 74e) at higher magnification were also obtained. Both micrographs were taken under identical imaging conditions at Scherzer defocus. Again, the micrograph from the nanosheet area clearly reveals much higher contrast of the supported objects than the micrograph from the composite (Quantifoil plus nanosheet) area. Note that on the nanosheet, the imaged particles exhibit fine structural features that are likely to be caused by the ligands or an oxide shell surrounding each



nanoparticle.

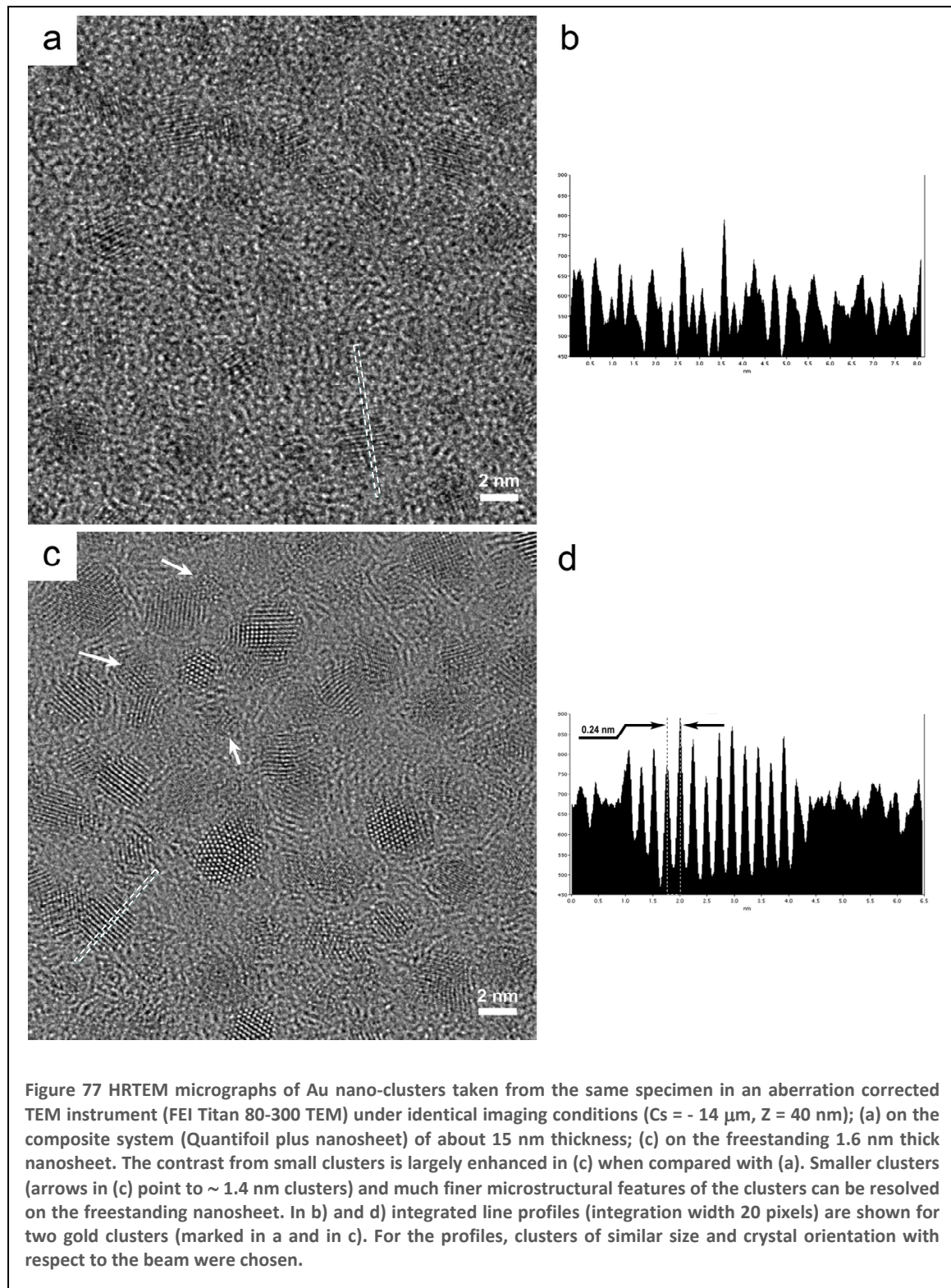
Figure 75 shows these Co particles together with multi-walled carbon nanotubes (MWNT), both on the composite (quantifoil plus nanosheet) (a) and the nanosheet (b,c,d). It is again visible that the contrast on the nanosheet alone is higher than on the composite. Especially, the contrast of the MWNTs is strongly enhanced, so that they are easily located. It is remarkable that even the individual layers of the MWNTs can be resolved (d). The lower background intensity of the nanosheet is also apparent in energy filtered (EFTEM) carbon maps (Figure 76). Here, high carbon content results in a lighter color. Thus the MWNTs appear nearly white, with dark spots where the Co particles are attached. The conventional sample support, due to its thickness, appears as a grey background, whereas the nanosheet appears nearly black.



4.5.2 Gold nanoclusters

The results of investigations of much smaller objects, Au nanoclusters, on the same composite system (Quantifoil plus nanosheet) are presented in Figure 77. The analysis of the nano-cluster size distribution showed that 1.4 nm sized clusters constitute the main yield of the synthesis reaction, though clusters of up to 5 nm in diameter were also detected. Two reasons are considered to be responsible for the observed cluster size distribution. Firstly, a finite size distribution is expected from the kinetics of the cluster formation process. Secondly, the TEM study itself can also affect the particle size. The drying process of the clusters on a TEM grid can cause size changes by inducing aggregation. Subsequently, the action of the high energy electron beam on the material is also very likely to influence the size distribution, because the ligand shell passivating the gold clusters is not stable under the high energy electron beam. This results in diffusion of gold atoms from one cluster to another and thus affects the cluster size distribution.

The high resolution micrographs of the gold nano-clusters were taken in an aberration corrected TEM instrument (FEI Titan 80-300 TEM) from a composite (Quantifoil plus nanosheet) area (Figure 77a) and from an area with freestanding nanosheet (Figure 77c). The imaging conditions were chosen in such a way, that the phase contrast produced by the support film was maximized, i.e. the value of the spherical aberration C_s was set to $-14 \mu\text{m}$ and a defocus of $+40 \text{ nm}$ was chosen (negative C_s imaging conditions, NCSI [21]). A comparison of the two micrographs, taken under identical imaging conditions, shows that the small clusters on the thick composite film are just barely perceptible (a). In contrast to this, high contrast information about morphological and structural features of the clusters can be obtained from the area with the freestanding nanosheet (c). The contrast of the nano-clusters is largely enhanced because of the lower background of the thinner support foil. As a result, much smaller objects can be visualized. For example, in (c) the presence of Au-clusters of about 1.4 nm in size (arrowed) can be verified under favorable imaging conditions, i.e. if they are imaged along a low-indexes zone axis. Figure 77b,d present integrated line profiles (over 20 pixels) of two gold clusters in (a) and (c) respectively (marked by dashed lines). For the profiles, clusters of similar size and crystal orientation with respect to the beam were chosen. The modulations of the integrated intensity in (b) indicate contrast variations caused by the lattice fringes, but

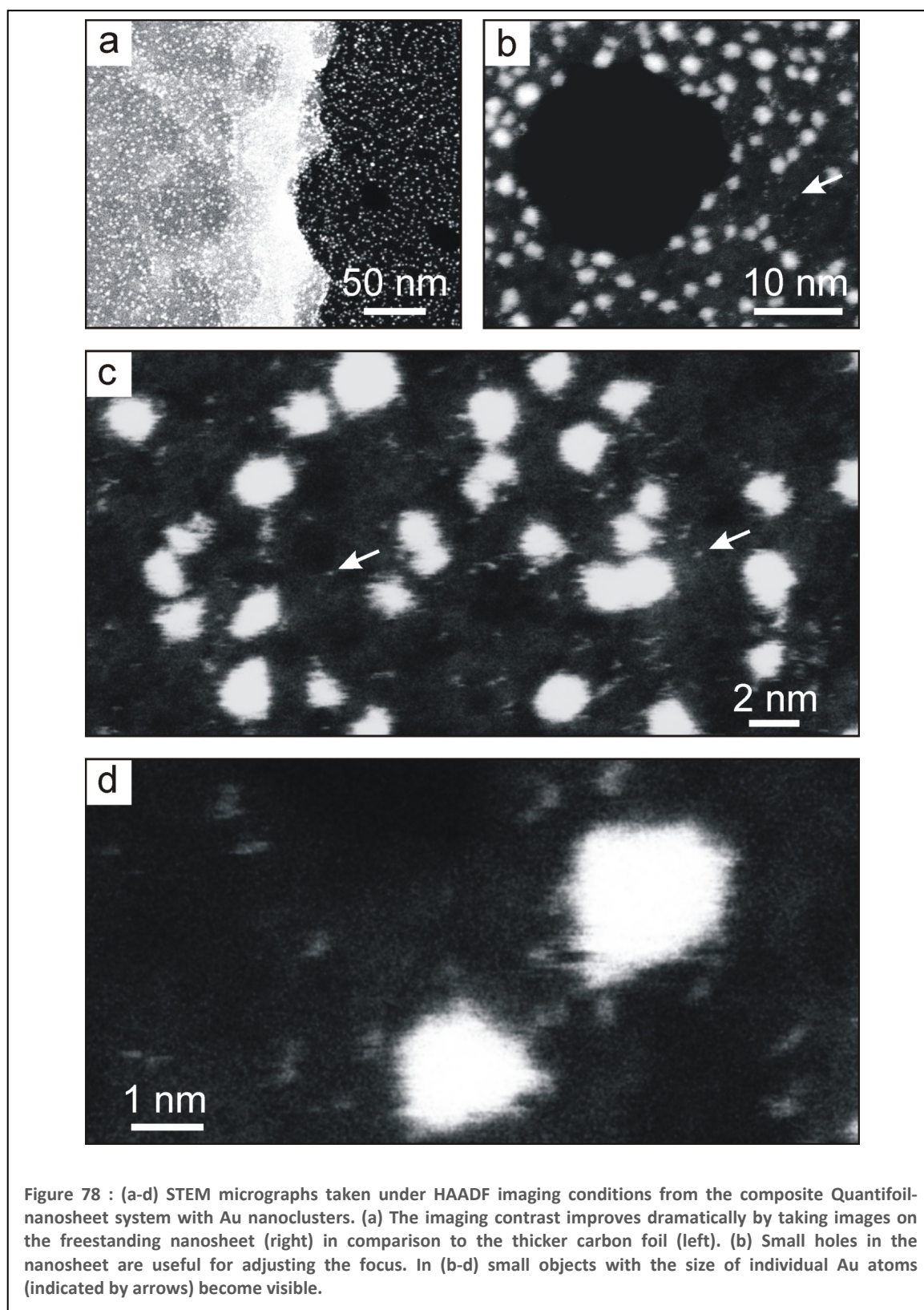


the profile is very irregular and noisy. In turn, the modulations of scattered integrated intensity in (d) are much more distinct, clearly show the period of contrast variations ($\sim 0.24 \text{ nm}$) and can be used for quantitative evaluations.

Still, imaging of nano-objects in high resolution TEM (HRTEM) is difficult when the size of the clusters becomes smaller than about 1.5–2 nm. In this case, the error of the particle

size estimation increases and statistical analysis of particle size distributions is better performed in scanning transmission electron microscopy (STEM) under high angle annular dark field (HAADF) imaging conditions.

The STEM micrograph depicted in Figure 78a presents a rim of a circular opening in the ~15 nm thick carbon foil (Quantifoil) covered by a nanosheet. In the left part of the image the nanoclusters are on the composite support system (Quantifoil plus nanosheet), whereas the right part of the micrograph presents clusters on the freestanding nanosheet. The difference in thickness of the support foil in the two areas of the same sample leads to a remarkable difference in the imaging contrast. Figure 78b-d show high resolution STEM micrographs taken on the FEI Titan 80-300 STEM from the Au nano-cluster material on the free-standing nanosheet. In addition to the clusters, very small strong scattering objects with a size of around 2 Å (which corresponds to the probe dimensions) can easily be recognized. It is assumed that these singular bright spots in the micrographs correspond to single Au atoms that have detached from the Au clusters under the high-energy electron beam. STEM observations at very high magnification showed that nanoclusters of these sizes are very sensitive to the high-energy electron beam. Subjected to exposure with the electron beam, the clusters change their shape, orientation and even size. This can be related to the fact that the decreasing volume/surface ratio leads to an increasing mobility of an effectively larger amount of less strongly bound surface atoms. It can be concluded that conformational changes of the atomistic structure of the clusters appear at time scales shorter than the typical exposure times, which explains the fact that the atomic structure is not resolved in such small clusters.



4.5.3 Summary

Carbon nanosheets from cross-linked SAMs with a thickness of 1.6 nm are fully stable under electron beam exposure and show an extraordinary performance as ultrathin supports, allowing for high contrast imaging of small supported objects. TEM images of cobalt nanoclusters and MWNTs reveal internal structures that were not visible by use of a conventional amorphous carbon support. By HRTEM imaging in a C_s -corrected TEM, it could be proven that the nanosheets exhibit a remarkable structural homogeneity which can be explained by the monolayer deposition process. This homogeneity is a strong advantage compared to carbon support films prepared by conventional deposition processes, which always show a strong intrinsic granularity. STEM imaging is capable to resolve single gold atoms diffusing on the nanosheet. In summary, carbon nanosheets are ultrathin foils, stable under electron irradiation. When used as a TEM support, they lead to a significant contrast enhancement during the imaging of very small objects.

4.6 Metallization of freestanding nanosheets

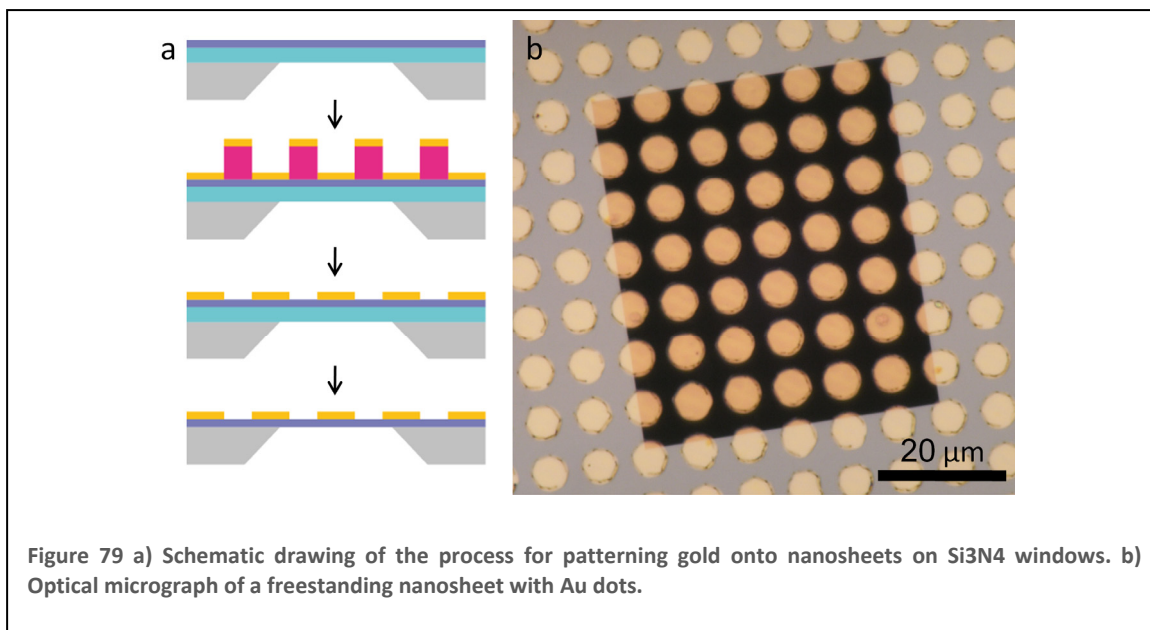
Possible applications for nanosheet membranes are pressure sensors and microphones. Due to their thickness, it is possible to minimize the size of the sensor, or enhance its sensitivity. One problem that needs to be solved is the read out of the membrane deflection. Both optical and electrical read out are possible candidates. An optical method could make use of a laser and a photodiode, similar to an AFM, but interferometry [130] also is a viable solution. An electrical read out could be realized by a strain gauge on top of the membrane. A common feature of these methods is that they require the metallization of the nanosheet (i.e. as a mirror or circuit).

Metallization of self-assembled monolayers has been the topic of intense research for many years [9, 131]. A variety of different methods have been discussed, ranging from evaporation over electrochemical to printing techniques. One of the main concerns was the penetration of the deposited metal through the SAM or reaction with the SAM, thus destroying the integrity of the monolayer. This might prohibit the preparation of freestanding metallized nanosheets. However, Tai et al. have recently shown that cross-linking prohibits metal penetration during evaporation [132]. Similarly, this is also true for electroless deposition [28].

In this chapter different pathways to fabricate metallized freestanding nanosheets are explored.

4.6.1 Underetching of metallized nanosheets

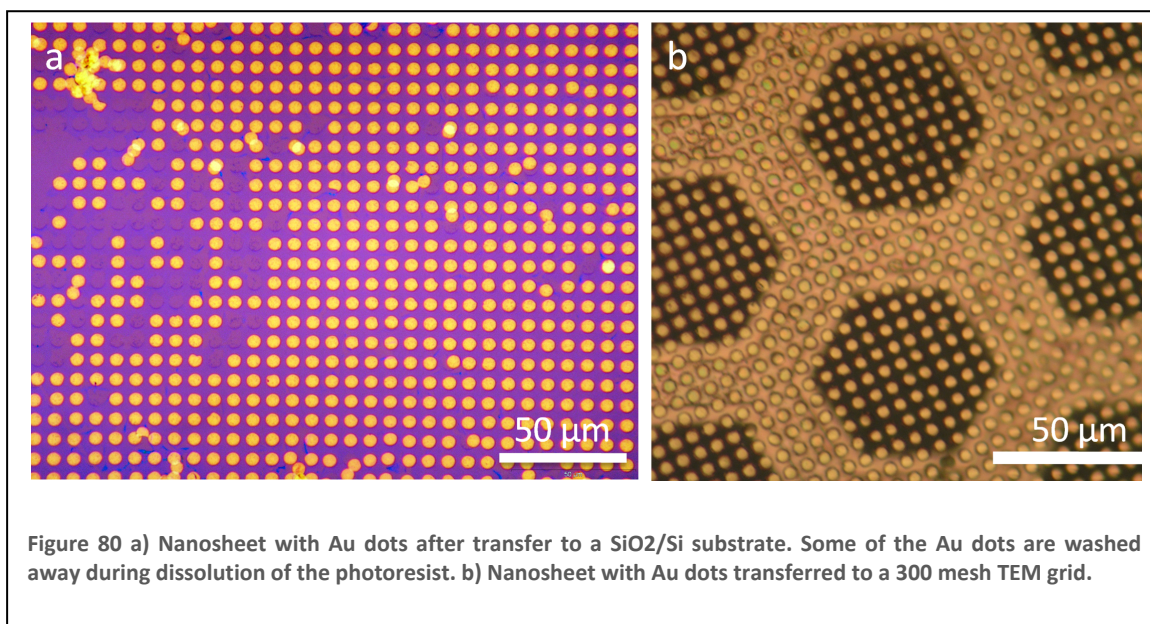
The straight forward route to pattern metal on top of the nanosheet is to do it on a solid support and subsequently underetching it. This has also been used to fabricate freestanding graphene devices [125, 129, 133, 134]. The process is schematically shown in Figure 79a. A self-assembled monolayer of CBPS is prepared on silicon nitride windows and the monolayer is cross-linked with electrons. A dot array (4 μm dots) is photolithographically patterned on top of the cross-linked monolayer using a negative tone resist. The sample is then coated by a layer of gold, followed by lift-off in acetone. Finally the Si_3N_4 is dissolved in hydrofluoric acid and rinsed in water and methanol, respectively to yield a freestanding nanosheet with a pattern of Au dots.



The gold pattern can then easily be seen using a conventional optical microscope (Figure 79b). It appears as if the gold dots are floating over the void, as the nanosheet is too thin to be visible. The integrity of the nanosheet is not destroyed during the lithographic patterning, so that this method is applicable for sensor fabrication. It is limited though to the Si₃N₄ material system.

4.6.2 Transfer of metallized nanosheets

In order to broaden the range of possible substrates, it should also be possible to transfer the nanosheet together with the Au dots. The process is basically the same as for the nanosheet alone. After patterning the Au dots, photoresist is spincoated onto the



substrate as a transfer medium. Special care has to be taken during the dissolution of the photoresist. If the solvent flow is too strong, the Au dots can be removed. The adhesion between the nanosheet and the SiO₂ substrate is not strong enough to hold the nanosheet and the Au dots in place. The Au dots then act as a “cookie cutter”, leaving behind a holey nanosheet, which is shown in Figure 80a. Some of the Au dots are still in close proximity of their original spot, only slightly shifted, whereas others are completely removed. A small heap of Au dots is located at the top left of the image. By carefully controlling the conditions during the dissolution of the photoresist, however, it is possible to prevent this “cookie cutter” effect. Figure 80b shows a successfully transferred nanosheet with an Au dot pattern on a 300 mesh TEM grid.

4.6.3 Evaporation onto freestanding nanosheets

The above described methods made use of patterning the metal onto the nanosheet prior to removing the substrate. In some cases, i.e. if the desired metal patterns are not withstanding the harsh processing conditions with hydrofluoric acid, these pathways are not viable. An alternative would be the direct evaporation of gold right onto the freestanding nanosheet. This is possible i.e. by using a shadow mask to define the pattern. To this end, freestanding nanosheets were prepared on a 300 mesh TEM grid (see scheme in Figure 81a) [135]. A second TEM grid with a regular pattern of holes (Quantifoil) was then brought in close proximity of the sample and used as a shadow mask during gold evaporation. After removing the shadow mask, a regular Au-pattern is deposited on the freestanding nanosheet. The optical micrograph in Figure 81b shows two of such freestanding nanosheets with Au dots of $\sim 1 \mu\text{m}$ in diameter. Not the whole

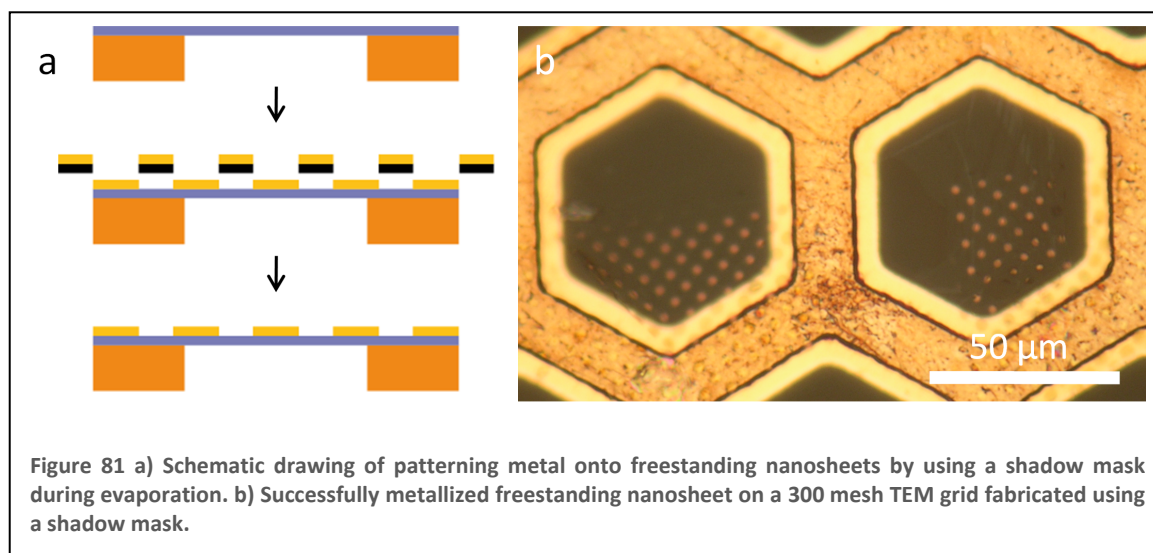


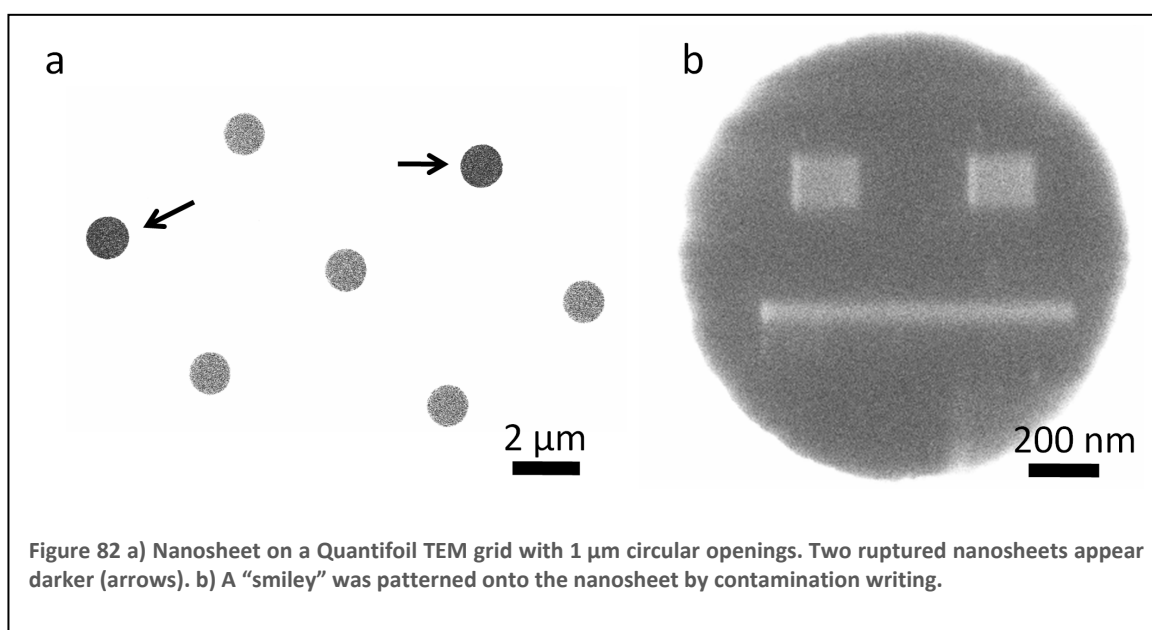
Figure 81 a) Schematic drawing of patterning metal onto freestanding nanosheets by using a shadow mask during evaporation. b) Successfully metallized freestanding nanosheet on a 300 mesh TEM grid fabricated using a shadow mask.

area of the nanosheet is covered with the Au pattern, due to incomplete overlap of the grid with the shadow mask.

4.6.4 Direct writing by electron beam induced deposition (EBID)

The main problem of using shadow masks for patterning metal onto freestanding nanosheets is that it is required that the shadow mask is in close proximity of the nanosheet in order to get well defined patterns with sharp edges. This can lead to sticking of the nanosheet to the shadow mask, so that destruction of the nanosheet is inevitable. A possible solution can be the direct writing of the metal pattern by electron beam induced deposition (EBID). By this technique metal patterns down to a few nm can be written using a suitable precursor gas [136, 137]. To show the feasibility of doing EBID on freestanding nanosheets, a closely related technique, contamination writing, was used. Here, instead of a specially tailored precursor gas, carbonaceous contamination from the sample as well as the residual gas is deposited on the sample by the electron beam.

To this end, the freestanding nanosheet was prepared on a TEM grid (Quantifoil) with circular openings of 1 μm in diameter. In order to image the nanosheet in an SEM, the contrast has to be set very high, so that the supporting film is saturated. The nanosheet then appears grey compared to the background. Figure 82a shows a few of such membranes together with two ruptured ones (arrows). Under high magnification on one of these circular openings the scanning area was then reduced on the nanosheet to write



a “smiley”-contamination pattern (b).

4.6.5 Summary

In summary it was shown that metal can be patterned onto freestanding nanosheets in a variety of ways. It is possible to lithographically pattern gold onto the nanosheet and subsequently removing the underlying substrate. The gold pattern together with the nanosheet can also be transferred to arbitrary new substrates, such as TEM grids. Finally, metal can also be structured directly on the freestanding nanosheet using shadow masks during metal evaporation or by directly writing the pattern using electron beam induced deposition (EBID). With this toolbox new applications for the nanosheet such as pressure sensors are one step closer.

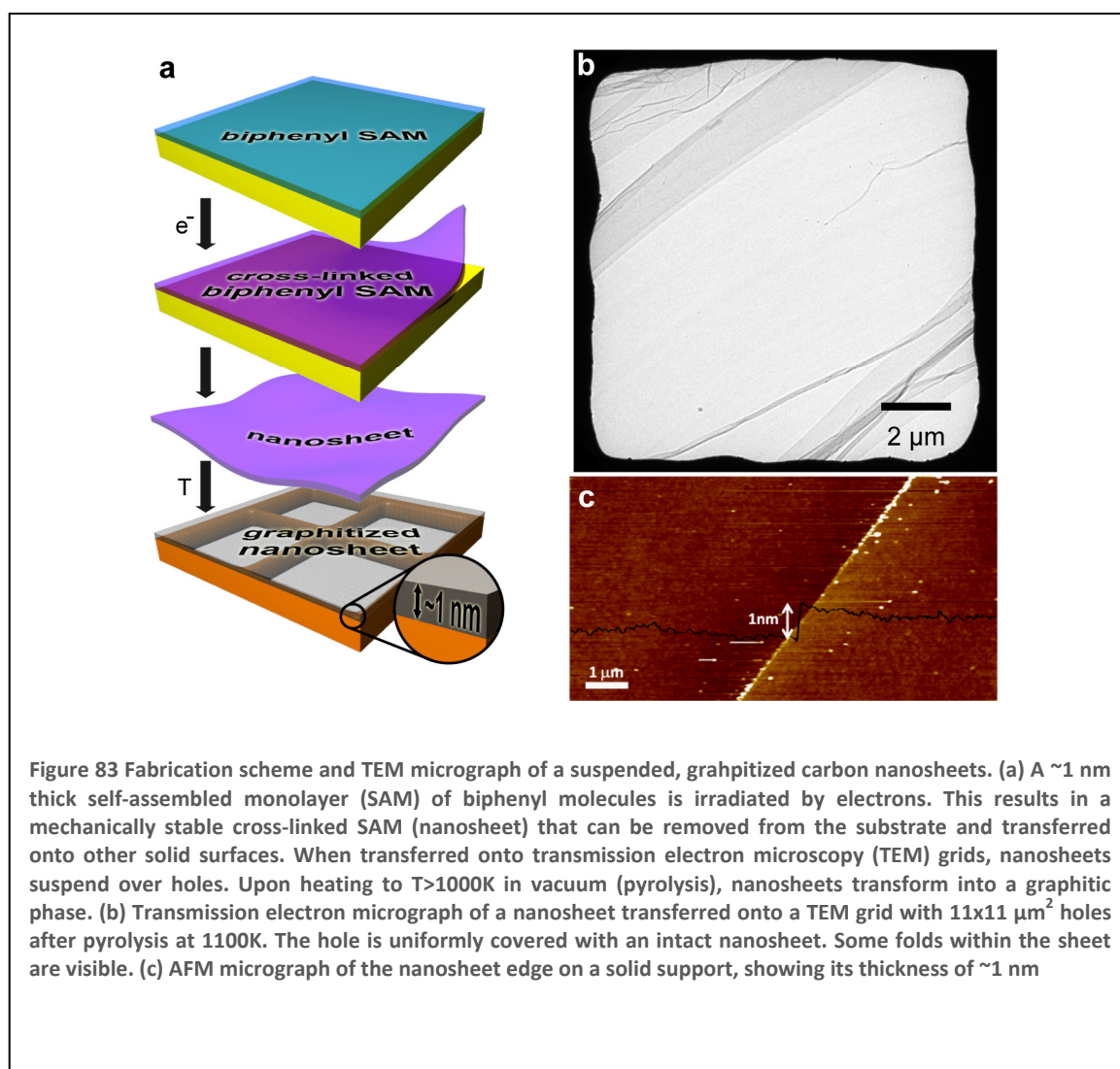
4.7 Annealing experiments

For centuries carbon allotropes have been identified with three-dimensional carbon phases like diamond and graphite. In the last few decades, nanoscopic zero-dimensional (fullerenes [138]) and one-dimensional (carbon nanotubes [139]) carbon allotropes generated a manifold of research due to their potential use in nanotechnology. The recent discovery of a two-dimensional carbon allotrope – graphene [140] – marks an important breakthrough in physics, since it has long been argued that free-standing atomically thin materials cannot exist at ambient conditions. The subsequent aim for novel applications of two-dimensional carbon ignited significant research efforts [128, 141-149]. For example, it is highly desirable to have atomically thin carbon sheets with tunable electrical, mechanical, and optical properties as well as with controllable size, shape and chemical functionality. Nanoscale electronics [128], nanoelectromechanical systems (NEMS) [146], as well as nano- and biosensors [150] could particularly benefit from the incorporation of such two-dimensional carbon sheets in composite materials and devices [128]. However, methods currently used for graphene fabrication such as mechanical exfoliation of highly oriented pyrolytic graphite [140], epitaxial methods [143, 148], or reduction of graphene oxide [145], can only partly fulfill these demands. Thus, there is a great need for novel paths to two-dimensional carbon allotropes.

Highly oriented pyrolytic graphite (HOPG) is the best ordered artificially made three-dimensional graphitic allotrope. It can be fabricated via pyrolysis of bulk aromatic polymers in the temperature range from 1000 K to 3000 K [151]. In analogy to this bulk transformation, we suggest that the pyrolysis of a molecular thin film of aromatic molecules is a promising path for the generation of two-dimensional carbon. Biphenylthiols form densely packed self-assembled monolayers (SAMs) with a thickness of ~ 1 nm on gold surfaces [152]. Such aromatic SAMs could act as suitable precursors in a pyrolytic reaction. However, due to the low thermal stability of thiolates [153], they desorb from the surface at temperatures that are much lower (350-450 K) than those required for pyrolysis. It was recently found that the temperature induced desorption of biphenylthiols on gold is inhibited [113], when biphenyls were cross-linked by electron irradiation in a molecular nanosheet [32]. In this chapter it is shown that vacuum pyrolysis can transform ~ 1 nm thick aromatic molecular nanosheets from an insulating to

a conducting state. The resulting carbon nanosheets are atomically thin and mechanically stable as suspended membranes even at temperatures above 1200 K and their resistivity and stiffness are determined by the annealing temperature.

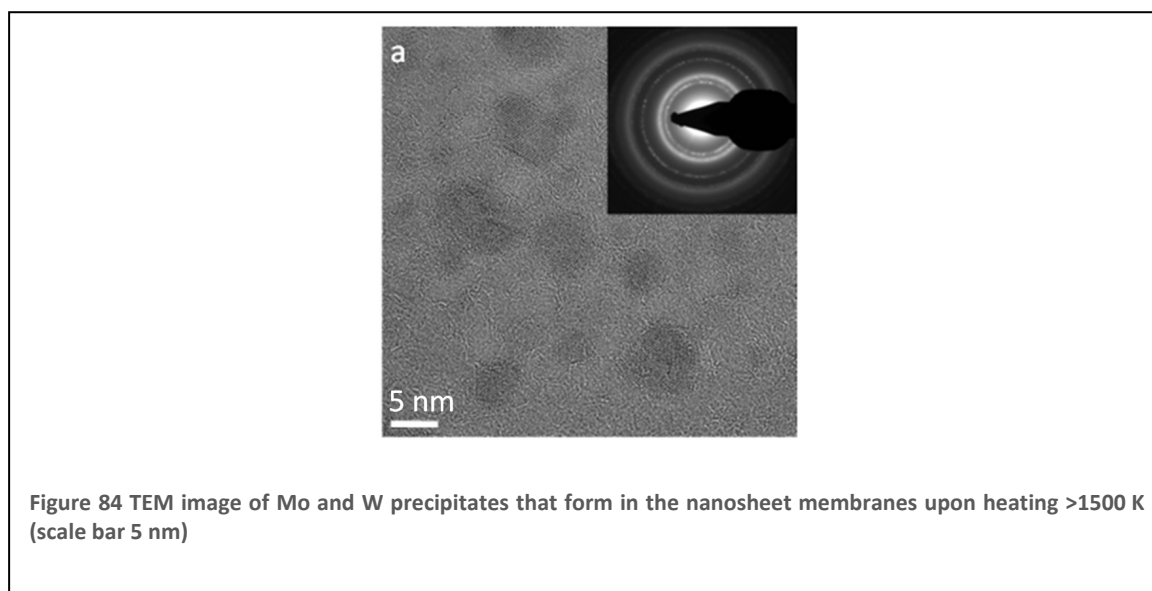
To prepare carbon nanosheets biphenyl molecules are self-assembled on a substrate from solution and subsequently cross-linked by electron irradiation, Figure 83A. Both size and shape of the nanosheets are determined by this initial exposure. Modern electron beam lithography and exposure tools allow the fabrication of sheets from macroscopic (cm^2) down to nanometer sizes and in arbitrary shapes [154]. The



nanosheets are then lifted from their surface and transferred, as described chapter 4.1, to another solid substrate or holey structures, such as transmission electron microscope (TEM) grids, where the nanosheets become suspended free-standing nanomembranes. The thickness of the nanosheet has been determined by X-ray photoelectron

spectroscopy and atomic force microscopy (AFM, Figure 83c) to be ≈ 1 nm, which is in good agreement with the height of a biphenyl molecule. Nanomembranes on TEM grids were pyrolysed at temperatures from ~ 800 K to ~ 1300 K. (c) shows a TEM micrograph of a cross-linked biphenyl nanosheet on a gold grid that has been annealed at ~ 1100 K in ultra high vacuum (UHV). An intact nanosheet (with a few folds) that spans an $11 \times 11 \mu\text{m}^2$ hole is clearly seen. This temperature stability is quite remarkable for a macroscopically large membrane with a thickness of only ~ 1 nm.

It was observed that the annealing of the nanosheets on Quantifoil-on-Mo TEM grids by e-beam heating at temperatures above 1500 K results in the formation of precipitates in the membranes, Figure 84. These are most likely carbides of Mo and W and may result from the hot Mo and W parts of the e-beam heater (W filament, Mo bottom plate of the



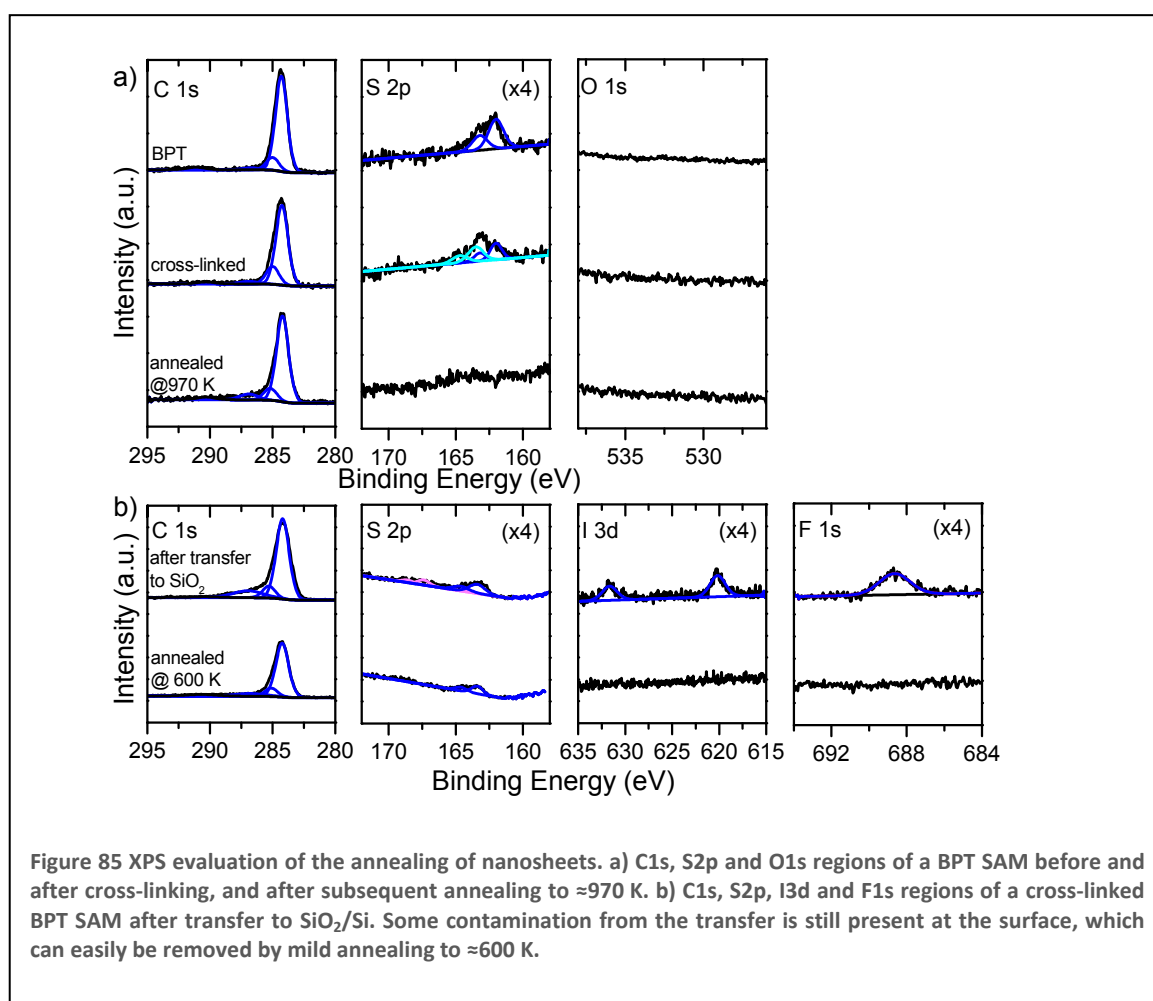
sample holder). All experiments were therefore conducted at annealing temperatures well below 1500 K.

4.7.1 XPS and scanning Auger microscopy

To pyrolyze nanosheets, we thermally annealed them in UHV and monitored the occurring changes by XPS (Fig. 2). The XP spectra of C1s, S2p and O1s regions for pristine, e-beam cross-linked and annealed BPT monolayers on Au are presented in Figure 85a. No other elements besides Au, C and S were identified from the overview spectra (not shown), showing the cleanliness of the samples. The effective thickness of a pristine

monolayer at room temperature is found to be ~ 1.0 nm. After electron irradiation (50 eV, 50 mC/cm²) and thermal annealing (1000 K), the film thickness decreases to ~ 0.7 nm, in agreement with a decrease of the C1s XP-intensity and thermal desorption of sulphur [110]. The C1s signal of a pristine BPT SAM consists of a main peak at 284.2 eV (FWHM 1.2 eV) and weaker peaks at 285.1 eV (1.2 eV), 286.9 eV (1.7 eV) and 290.3 eV (1.7 eV) [113]. The S2p signal shows the thiolate doublet with a S2p_{3/2} peak at 162.0 eV (FWHM 0.9 eV). After electron irradiation, an additional sulphur species at S2p_{3/2} = 163.5 eV appears that is due to electron irradiation induced changes at the SAM/Au interface [110]. Upon annealing above 800 K, sulphur desorbs completely from the surface of Au and from the nanosheet.

The nanosheet was prepared on gold substrates and then transferred onto oxidized Si wafers. Figure 85b shows the C1s, S2p, I3d and F1s regions of the carbon nanosheet after transfer. The spectra indicate the presence of transfer related contaminants: The C1s signal shows a broad shoulder at 287.0 eV, resulting from PMMA residues. Oxidized



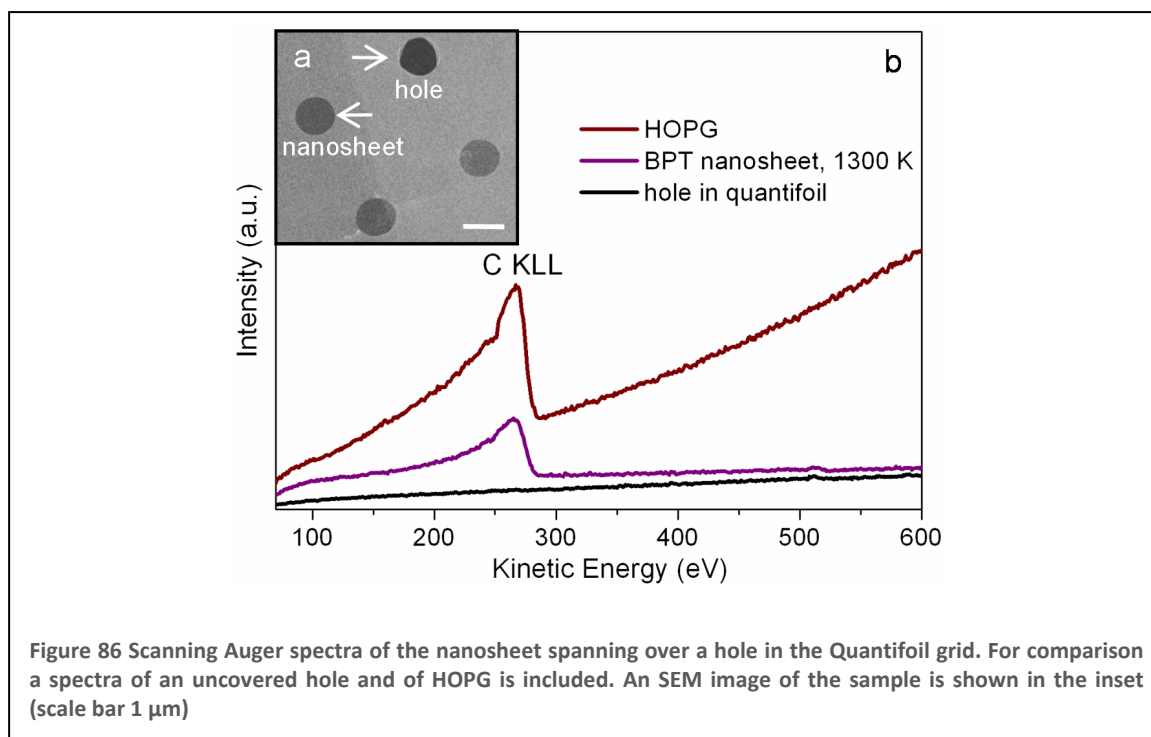


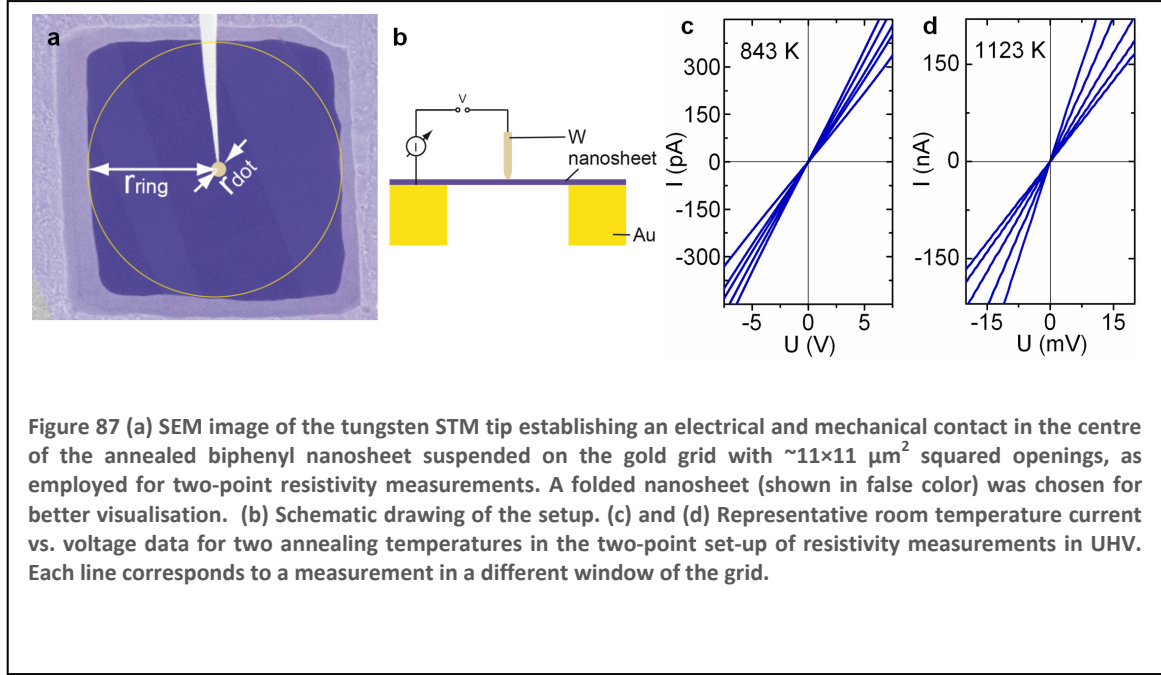
Figure 86 Scanning Auger spectra of the nanosheet spanning over a hole in the Quantifoil grid. For comparison a spectra of an uncovered hole and of HOPG is included. An SEM image of the sample is shown in the inset (scale bar 1 μm)

sulphur at $S2p_{3/2} = 167.4$ eV as well as traces of iodine and fluorine are detected. However, these contaminants are easily removed by mild (600 K) annealing in UHV. AFM of the nanosheet after transfer onto SiO_2 shows a thickness of ~ 1 nm (Figure 83c).

The chemical composition of annealed suspended membranes on TEM grids was analysed with a scanning Auger microscope. Figure 86 presents an Auger spectrum of a BPT nanosheet annealed at ~ 1300 K on a Quantifoil-on-Mo TEM grid by e-beam heating in vacuum for 5 min. For comparison the Auger spectra of highly oriented pyrolytic graphite (HOPG) and a hole in Quantifoil (space without nanosheet) are presented. Besides the C KLL Auger line no other Auger transitions can be seen in the spectrum of the annealed nanosheet. Thus it consists of only carbon.

4.7.2 Electrical properties

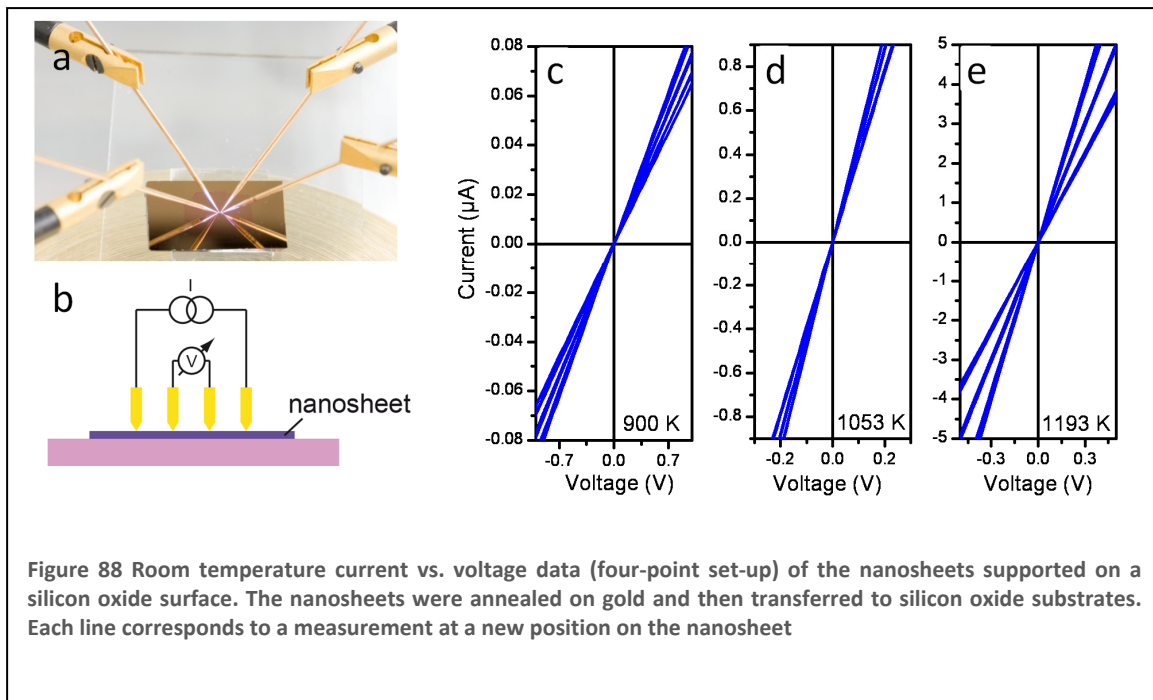
In the next step, the electrical properties of the heated nanosheets in suspended (membranes) and supported states (films) were explored. The resistivity was determined at room temperature after the respective annealing steps. Nanosheets suspended on a gold grid were contacted by the tip of a scanning tunneling microscope; resistance was then determined by a two-point measurement in UHV. Figure 87a shows a scanning electron micrograph of a tungsten tip touching a nanosheet that suspends over an $11 \times 11 \mu\text{m}^2$ squared opening. A schematic representation of the setup is shown in (b).



A bias voltage was then applied between the tip and the gold grid, resulting in a linear current response. The sheet resistivity can be extracted from such measurements by applying a simple model. First it is assumed that a homogenous film is contacted by two electrodes; one electrode, a circular dot, is placed at the centre of a ring-like second electrode that confines the measured area, cf. Figure 87a. The current-voltage-characteristics can be easily calculated for this setup if contact resistances are neglected. Thus, the sheet resistivity ρ_S is determined by

$$\rho_S = \frac{2\pi}{\ln\left(\frac{r_{ring}}{r_{dot}}\right)} \frac{V}{I} \quad (33)$$

with the inner radius of the ring electrode r_{ring} and the radius of the dot electrode r_{dot} . The contact area of the STM tip is not exactly known and the outer electrode is a square-like frame. However, as the ratio of radii enters only as the argument of a logarithmic function, the sheet resistivity is not drastically affected by the electrode geometry. We therefore approximated our setup with this model using a ring electrode radius r_{ring} of $5 \mu\text{m}$ and a dot electrode radius r_{dot} of 100 nm . Assuming that the true contact area of the tip equals a circle with a radius of 1 \AA , our approximation leads to an overestimation of the sheet resistivity by a factor of less than three. This overestimation is not critical, as changes in the resistivity of more than five orders of magnitude are discussed. The current-voltage curves show a linear dependence. Representative curves for two samples at a low and a high annealing temperature are shown in Figure 87c and d.



Additional resistivity measurements were carried out under ambient conditions. To this end, large pieces ($\sim\text{mm}^2$) of nanosheets heated directly on gold substrate in UHV where transferred onto silicon oxide and their sheet resistance was determined under ambient conditions by a four-point measurement [93]. Four probe tips were equidistantly arranged in a line and contacted the film as shown in Figure 88a and b. A current I was driven through the two outer needles and the voltage drop V between the two inner needles was measured. In this setup the sheet resistance ρ_S is given by [155]:

$$\rho_S = \frac{\pi}{\ln(2)} \frac{V}{I} = 4.532 \frac{V}{I} \Omega/\text{square} \quad (34)$$

The current-voltage curves for all studied samples also show a linear dependence, Figure 88c-e.

The sheet resistivity values measured in UHV and in ambient are in a very good agreement. Figure 89 summarizes the results as a function of annealing temperature. A measurable electrical current is detected after annealing at above ~ 800 K. Here the sheet resistivity corresponds to $\sim 10^7$ k Ω /sq. Increasing the annealing temperature to ~ 1200 K drops the sheet resistivity to ~ 100 k Ω /sq, which demonstrates the clear metallic nature of the film. This resistivity is only one order of magnitude higher than that of a defect free graphene monolayer [141], and ~ 100 times lower than the sheet resistivity of

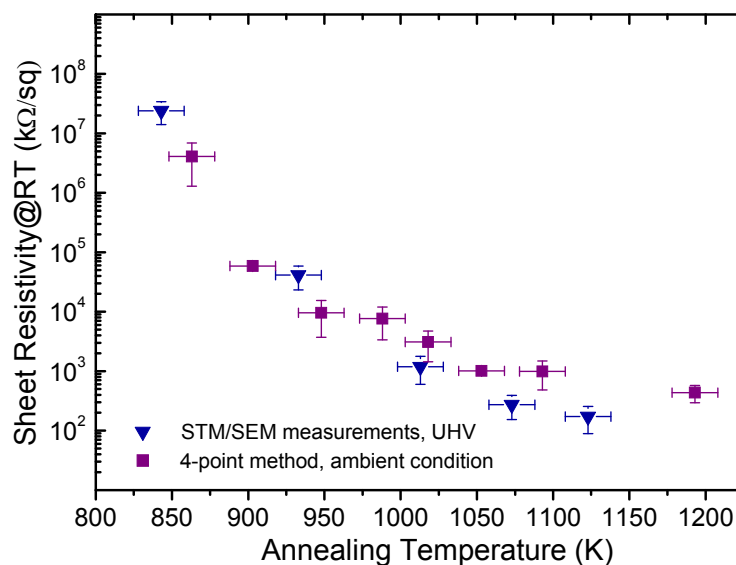


Figure 89 Summary of the room temperature sheet resistivity as a function of annealing temperature. All samples were annealed for 30 min at the respective temperatures.

single chemically reduced graphene oxide sheets [156], which are currently most favored for mass production of graphene [145].

4.7.3 Raman

The structural transformations that occur upon annealing in the cross-linked aromatic monolayer were investigated by Raman spectroscopy. Again, nanosheets supported on silicon oxide substrates and films suspended on TEM grids were analyzed at room temperature after annealing. For annealing temperatures above 700 K, two peaks at ~ 1350 and ~ 1590 cm^{-1} are observed in the Raman spectrum (Figure 90). These bands are referred to as the so-called D- and G-peaks which are characteristic for sp^2 -bonded, honeycomb structured carbon allotropes [157]. Their positions, shapes and the intensity ratio $I(\text{D})/I(\text{G})$ provide information about the degree of order in the carbon network [158]. At ~ 730 K the D-peak has its maximum intensity at 1350 cm^{-1} while the G-peak has its maximum intensity at 1592 cm^{-1} and shows a shoulder at 1570 cm^{-1} . At higher annealing temperatures, the shoulder in the G peak disappears. The band narrows and its position successively shifts to higher wave numbers reaching 1605 cm^{-1} at ~ 1200 K. Simultaneously, the ratio $I(\text{D})/I(\text{G})$ increases from ~ 0.75 to ~ 1 (Figure 90b).

The maximum of the D-peak almost remains at the same wave number while above ~ 950 K a shoulder appears at ~ 1180 cm^{-1} . The observed temperature dependent changes in the Raman spectra are characteristic for a phase transition from an amorphous to a nanocrystalline carbon network [158]. Considering the thickness of the carbon nanosheet (1 nm), it is reasonable to attribute these changes to the formation of a nanosize graphene network. The Raman spectra also correlate very well with the successive decrease of the sheet resistivity for increasing annealing temperatures.

4.7.4 TEM

The occurrence of structural ordering in the annealed sheets can also be observed by HRTEM studies of suspended membranes. For non-annealed membranes, both high resolution imaging and selected area electron diffraction (SAED) show only the presence of amorphous material, Figure 91a and b. In annealed specimens, extended areas with curvy, nearly parallel fringes indicating the presence of graphitic material were found, Figure 91c. The areas where fringes are observed, alternate with areas where they are not present. These observations clearly indicate that distinct

structural changes occur in the nanosheet upon annealing and that the intrinsic properties of this two-dimensional material must vary accordingly [129, 159]. The line profiles across the regions with fringes (Figure 91c 1,2) give a periodicity of 0.35 ± 0.03 nm, which is close to the interplanar spacing of the close-packed planes in graphite (0.342 nm). In our experiments, the scattered intensity modulations corresponding to the 0.35 ± 0.03 nm periodicity of the fringes could not be found in the diffraction patterns

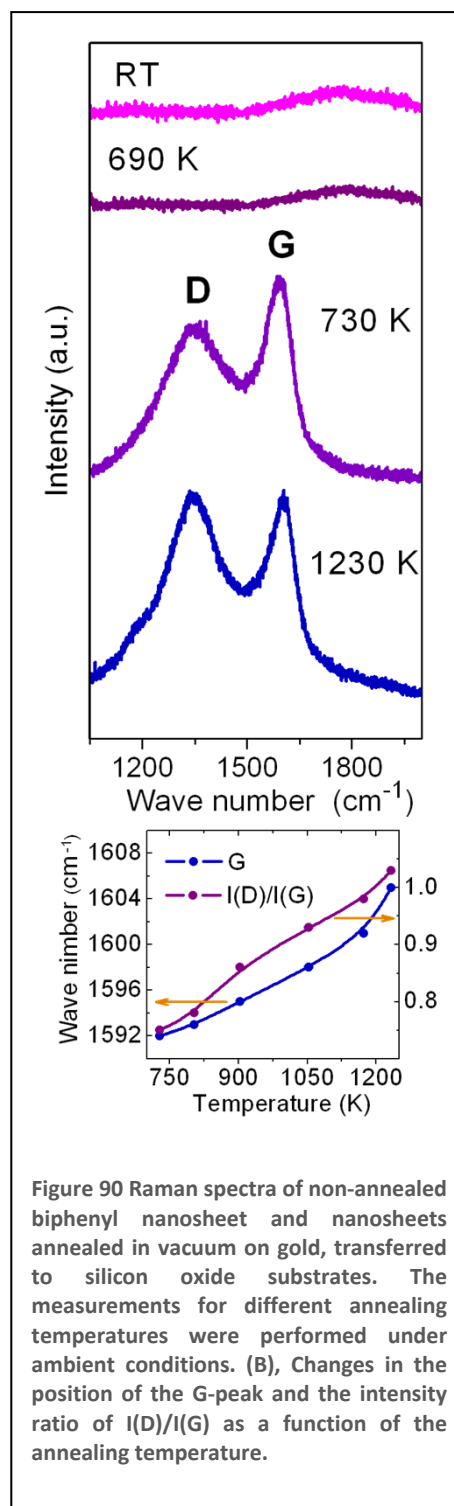
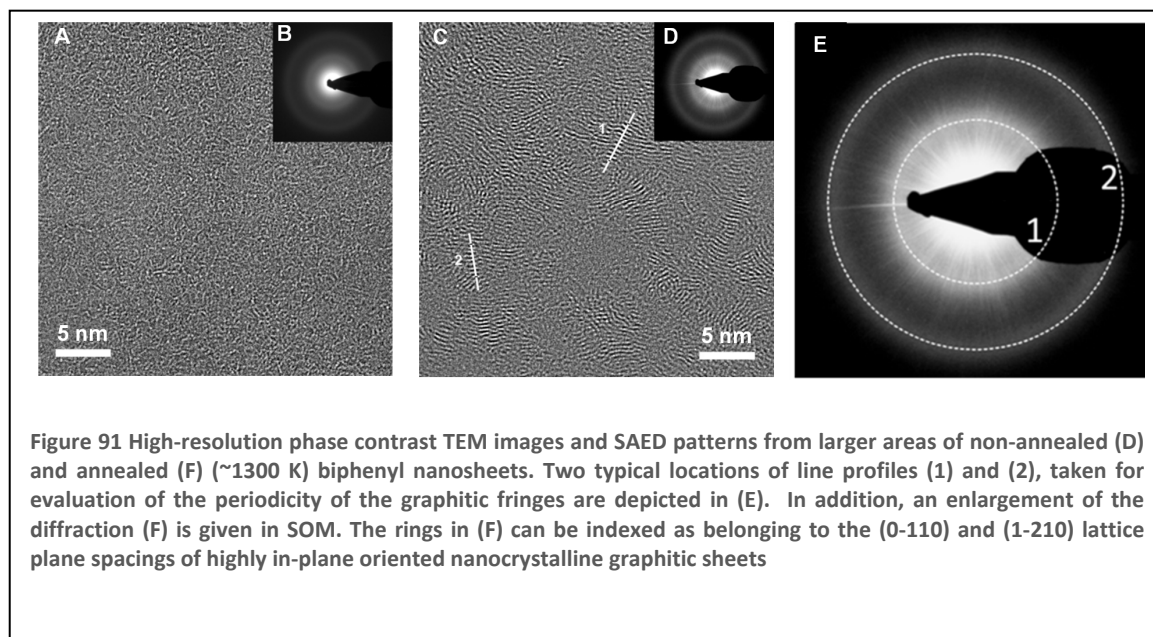


Figure 90 Raman spectra of non-annealed biphenyl nanosheet and nanosheets annealed in vacuum on gold, transferred to silicon oxide substrates. The measurements for different annealing temperatures were performed under ambient conditions. (B), Changes in the position of the G-peak and the intensity ratio of $I(D)/I(G)$ as a function of the annealing temperature.

from the investigated areas. Our evaluation showed that the corresponding reciprocal distance still lies within the strong tails of the central beam of the diffraction pattern. However, the enlargement of the SAED pattern (d, e) taken from a much larger area as depicted in (c) shows two distinct rings (marked 1 and 2) corresponding to the real space periodicities of 0.11 ± 0.02 nm (ring 2) and 0.20 ± 0.02 nm (ring 1). These can be interpreted as to correspond to the major indices (0-110) (1.23 \AA spacing) and (1-210) (2.13 \AA spacing) of highly in-plane oriented nanocrystalline graphitic sheets observed along the [0002] zone axis. The sharpness and intensity of the rings increase in specimens annealed at higher temperatures indicating progressing ordering in the nanomembrane.



4.7.5 Outlook and Conclusion

Since nanomembranes are elastic and mechanically stable at ambient conditions they can be further utilized as sensitive diaphragms in various applications. Conducting nanomembranes may act as transducers in nanoelectromechanical systems (NEMS) and open an opportunity to build highly miniaturized pressure sensors that might eventually lead to microphones with nanometer dimensions. The possibility to chemically functionalize nanosheets by chemical lithography [27] further permits their use as highly

sensitive chemical sensors that change their electromechanical characteristics upon the adsorption of distinct molecules.

In conclusion, a simple method to produce ultrathin (~ 1 nm) conducting carbon films and membranes based on molecular self-assembly, electron irradiation and pyrolysis was shown. Upon annealing, cross-linked aromatic monolayers undergo a transition to a mechanically stable graphitic phase. The above experiments demonstrate a variety of applications that take advantage from the fact that size, shape and conductivity of the films and nanomembranes are easily controlled.

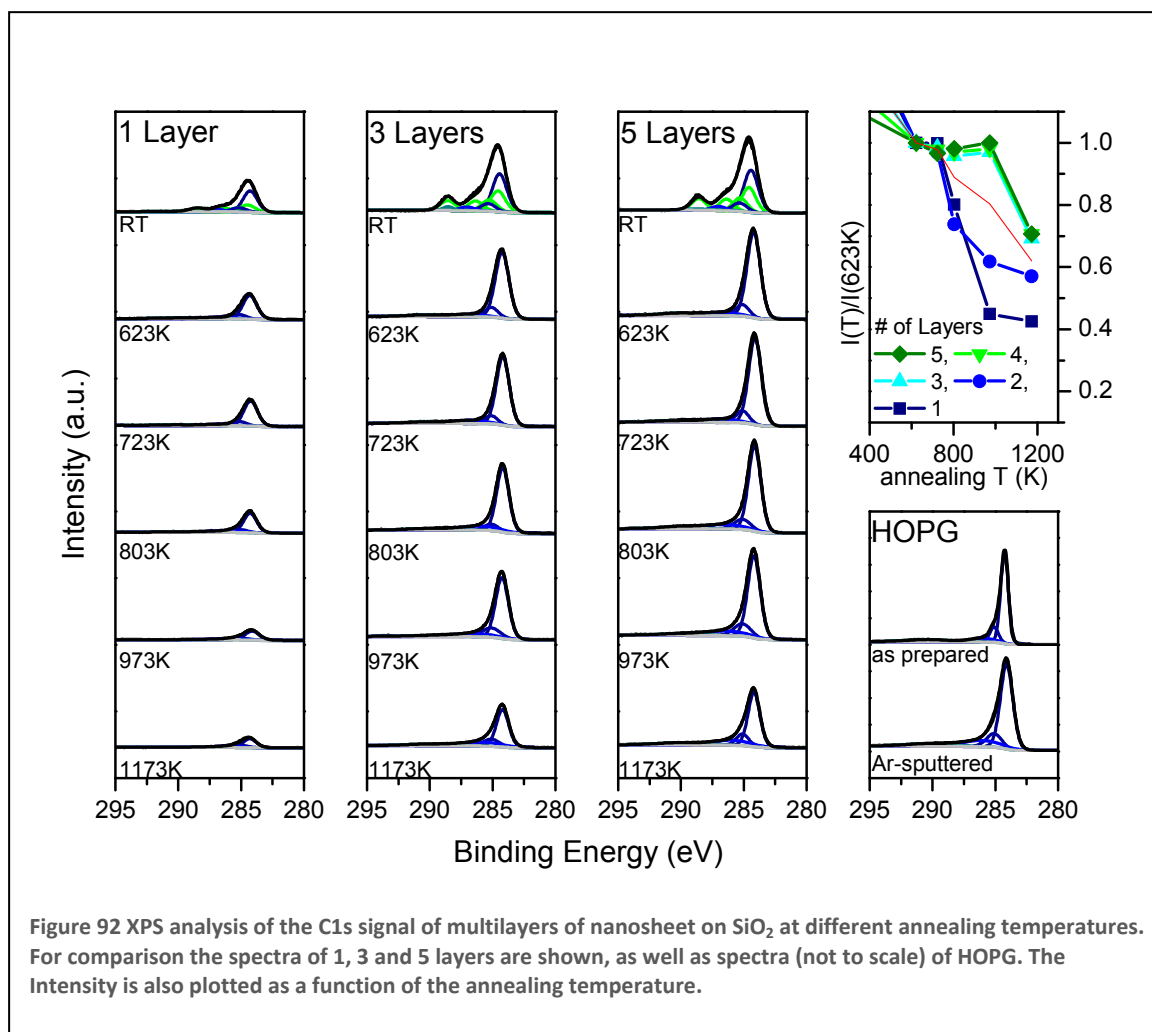
4.8 Annealing experiments on multilayers

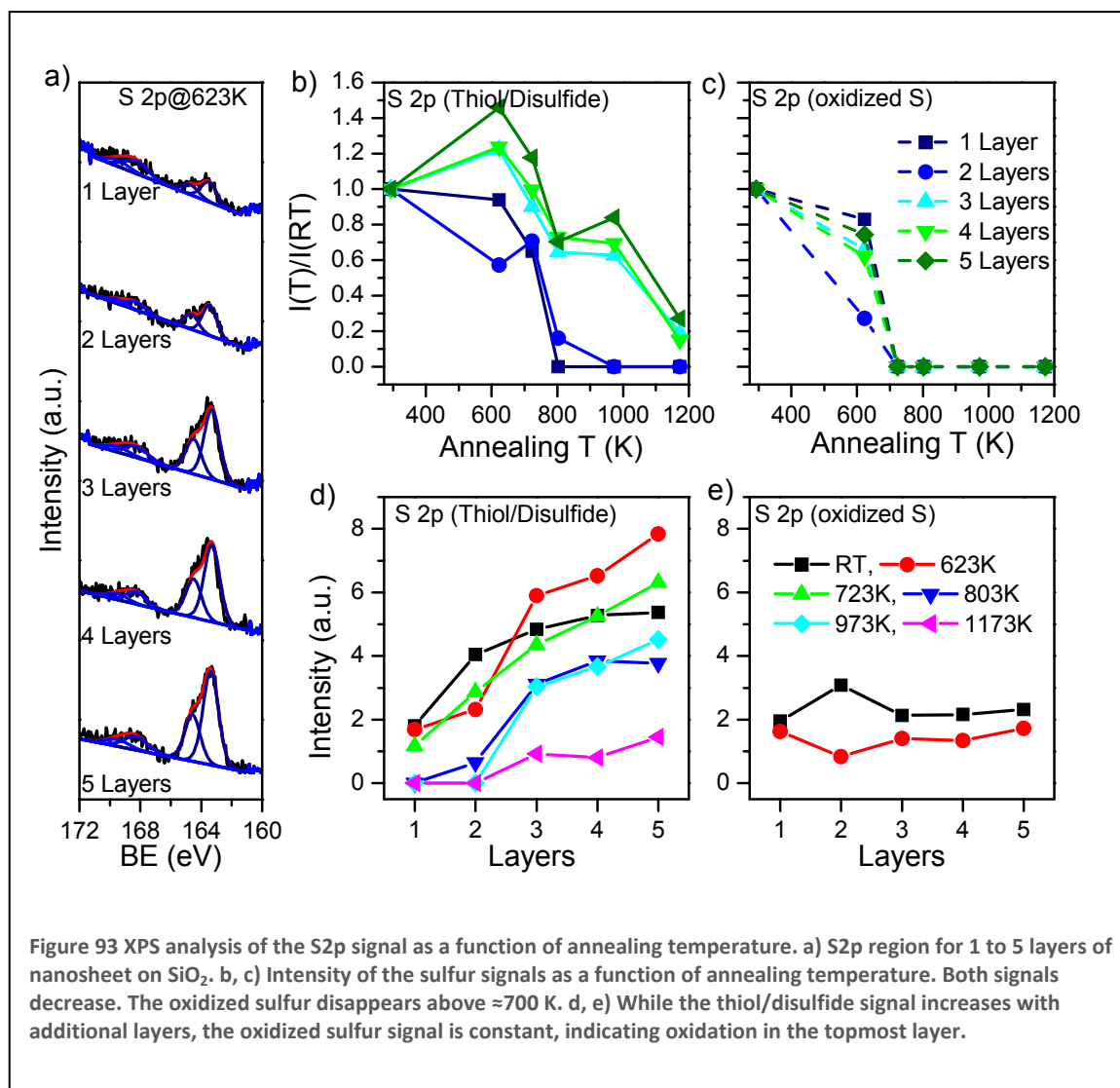
In the previous chapter it was shown that nanosheets can be transformed into a nanocrystalline graphitic material upon annealing in UHV. Annealing was performed on gold substrates and the graphitized nanosheets then had to be transferred to silicon oxide wafers for electrical characterization. This is a cumbersome process, especially for samples that were annealed at temperatures above 1000 K, as the supporting mica decomposes and at even higher temperatures (>1200 K) the gold film is no longer stable and melts. For technical applications it would thus be interesting to graphitize the nanosheets after transfer to the silicon oxide wafer. Higher temperatures should be reachable to further increase the crystallite size and thus decrease the sheet resistivity. Also, this would permit easy fabrication of ultrathin conductive coatings over large areas. Such coatings could possibly replace indium tin oxide for use as a transparent electrode in display technology, as indium supplies are limited.

In this chapter, nanosheets on silicon oxide wafers are annealed in UHV and characterized by XPS, Raman and UV/Vis spectroscopy as well as conductivity measurements. All experiments were conducted on multilayer stacks to find out how this influences the properties of the annealed films.

4.8.1 XPS evaluation

Evolution of the C 1s region as a function of annealing temperature is displayed in Figure 92. All signals were displayed for one, three, and five layers, in order to visualize their relative intensities. They were all fitted with the same peaks that were described previously for the C 1s peak after annealing to 623 K. Further annealing to 1173 K leads to a decrease of the overall intensity. For one and two layers the normalized intensity drops at temperatures above 723 K and levels off at 1173 K at ≈ 0.4 (one layer) and ≈ 0.6 (two layers), respectively. Thicker arrangements of three to five layers are seemingly more temperature resistant, as the normalized intensity stays nearly constant up to 973 K and only drops to ≈ 0.7 at 1173 K. The shape of the peak is changing only slightly. The main signal at 284.2 eV remains unaltered, but the component at 285.1 eV broadens to a FWHM of 1.5 eV. The two satellites are also broadening to a FWHM of 4 eV. As graphitization is expected to take place upon annealing, HOPG was measured for comparison. Graphite is known to have a peak shape that can be described by a Doniach-



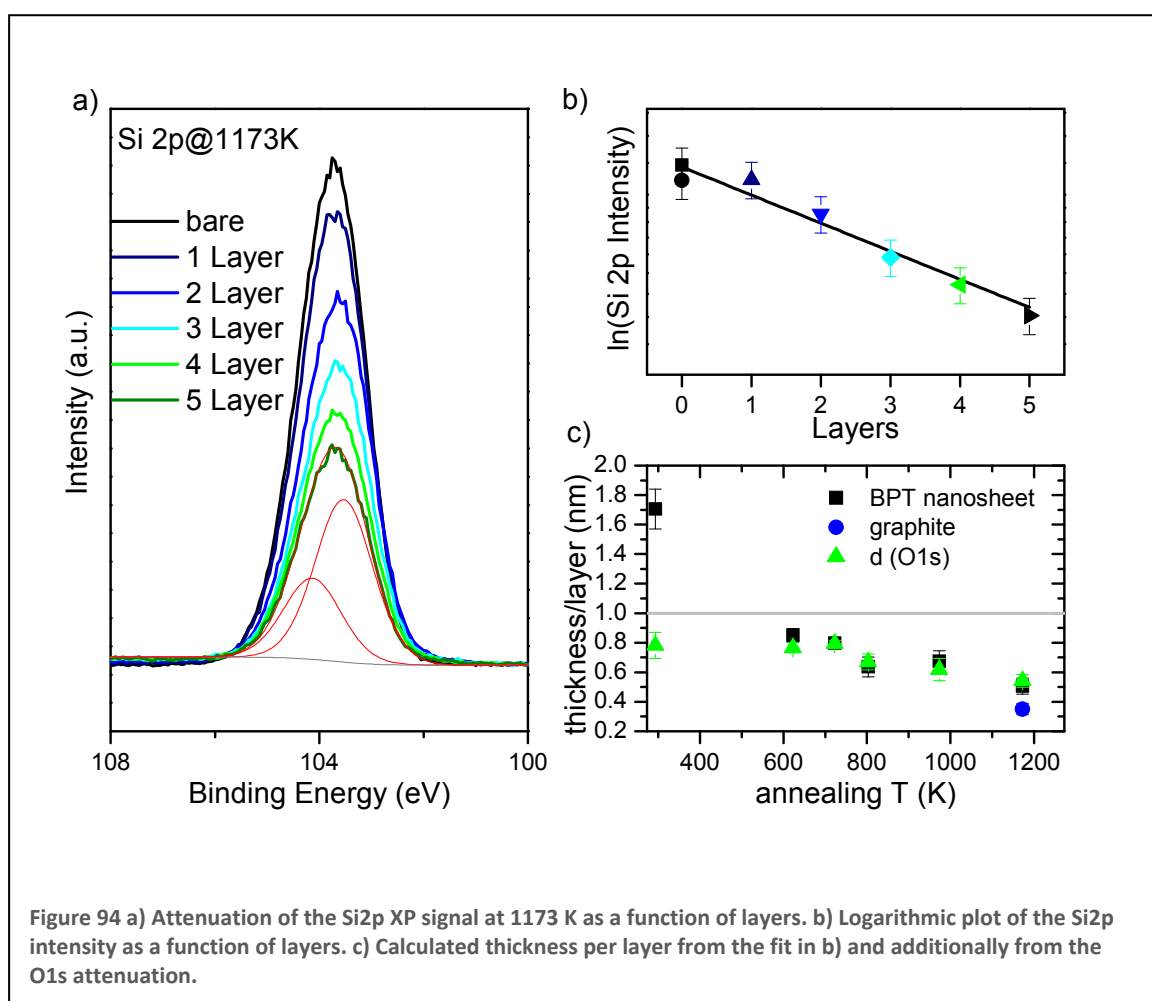


Sunjic asymmetry [160-162]. For ease of fitting, the asymmetric shape of the peak was modeled with Gaussian-Lorentzian components [162] at the same energies as the BPT nanosheet. This fit is able to describe the shape of the graphite peak (of freshly cleaved HOPG) quite well, only the FWHM was found to be significantly smaller (0.7 eV). Sputtering with Ar-ions was then used to introduce disorder at the surface of the HOPG sample and to break it down to smaller crystallites. The FWHM of the two main components at 284.2 and 285.1 eV is increased to 1.3 eV, which is in good agreement with the annealed nanosheet.

The fate of sulfur during annealing is displayed in Figure 93. Two sulfur peaks, that are assigned to thiols/disulfides and oxidized species, are still found after the first annealing step (see chapter 4.4.2), Figure 93a. The evolution of both signals as a function of annealing temperature is shown in Figure 93b, c and as a function of the number of

layers in Figure 93d, e. The oxidized species are completely vanished at 723 K, whereas the thiols/disulfides are only reduced in intensity by $\approx 25\%$. Further heating to 803 K is sufficient to remove the sulfur from the monolayer. The two layer sample also exhibits a significant decrease and vanishes at 973 K. At this temperature still around 70% of the room temperature intensity are observed for the three, four and five layer samples. Even annealing to 1173 K is not able to remove all sulfur from those multilayer stacks. It is reasonable to assume that higher annealing temperatures lead to a subsequent carbon-sulfur bond cleavage, such that the sulfur can diffuse to the interface and into the vacuum. Multilayer stacks pose as a (thicker) diffusion barrier, therefore slowing the loss of sulfur.

The average layer thickness of the multilayer samples can be determined from the attenuation of the Si 2p peaks for each annealing temperature. Figure 94a shows the spectra for 1173 K and the respective exponential fit (Figure 94b). The thickness as a function of annealing temperature is displayed in Figure 94c. The values derived from the Si 2p and O 1s attenuation are in good agreement with each other. For the highest



annealing temperature (1173 K) the thickness calculated with the attenuation length for graphite 0.35 ± 0.04 nm ($\lambda = 2.37$ nm [163]) is shown in blue. Interestingly, it is close to the thickness of a single graphene layer (0.33 nm). Note that the thickness derived by this method is an effective thickness, as the density of the annealed nanosheets is not necessarily the same as in graphite.

4.8.2 Raman

Multilayers that were annealed to 1173 K were also measured by Raman spectroscopy for additional information about the graphitization process. Raman spectroscopy has been widely used to study the order in graphitic materials [164]. This is possible because single crystalline graphite (such as large crystallites or graphene) exhibits a single major feature around 1590 cm^{-1} , the so called G band. Additionally, in less ordered graphitic materials, the so called D (around 1350 cm^{-1}), D' (1620 cm^{-1}), and G' (in the range of $2500 - 2800$ cm^{-1}) bands are observed. The G' band represents the overtone of the D band, whereas the D and D' bands are associated with defects/disorder in the material.

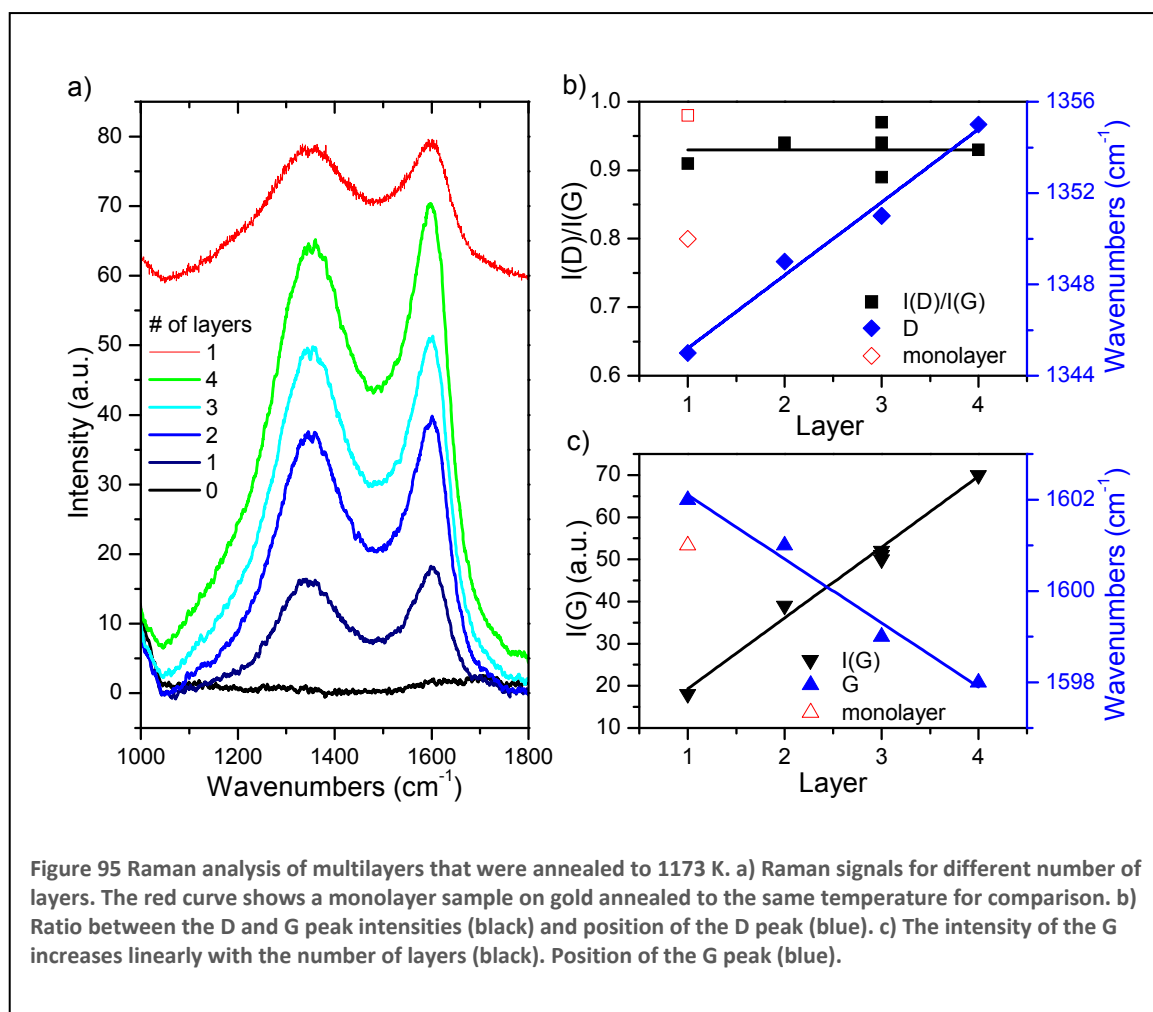


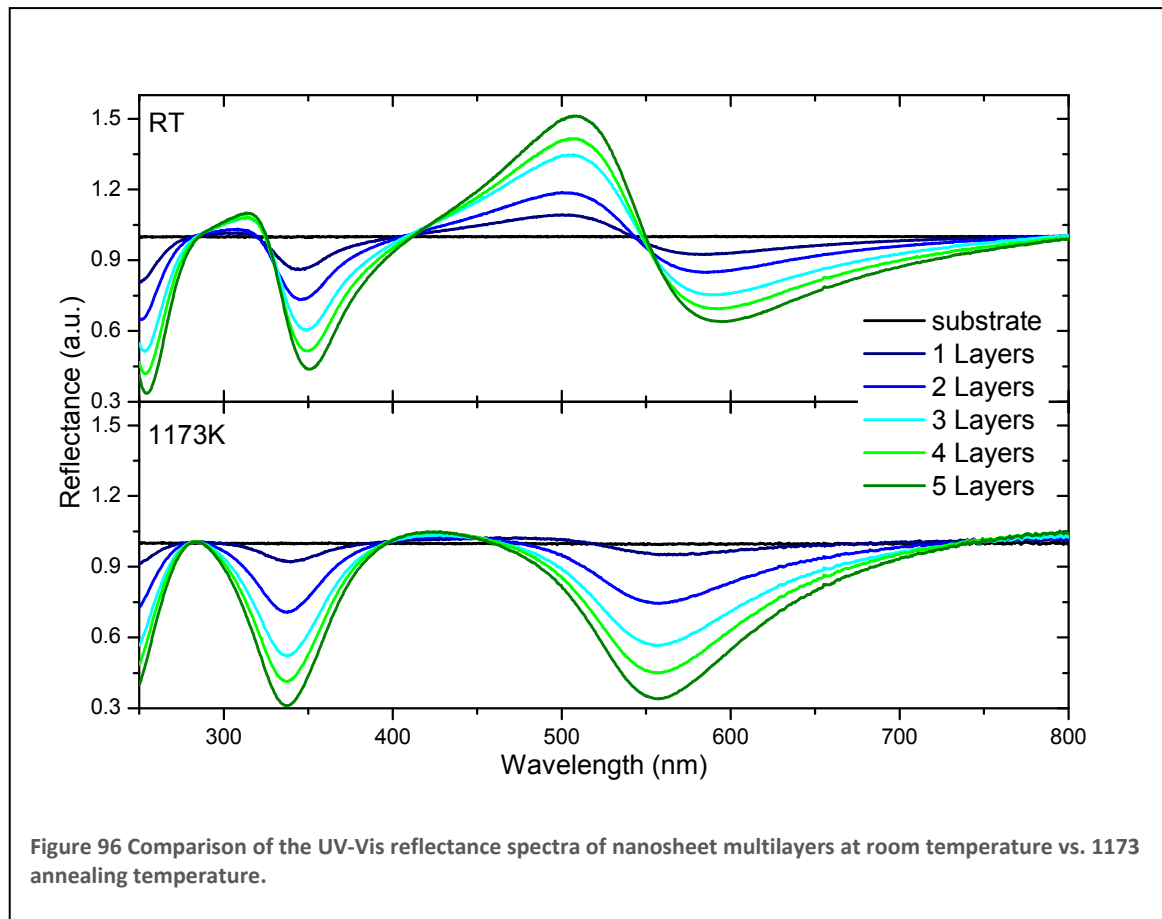
Figure 95 Raman analysis of multilayers that were annealed to 1173 K. a) Raman signals for different number of layers. The red curve shows a monolayer sample on gold annealed to the same temperature for comparison. b) Ratio between the D and G peak intensities (black) and position of the D peak (blue). c) The intensity of the G band increases linearly with the number of layers (black). Position of the G peak (blue).

The ratio of the intensities between the D and G band $I(D)/I(G)$ is thus used to characterize the defect quantity of a given sample. It has also been used to estimate the size of the crystallites in nanographite materials [158, 164].

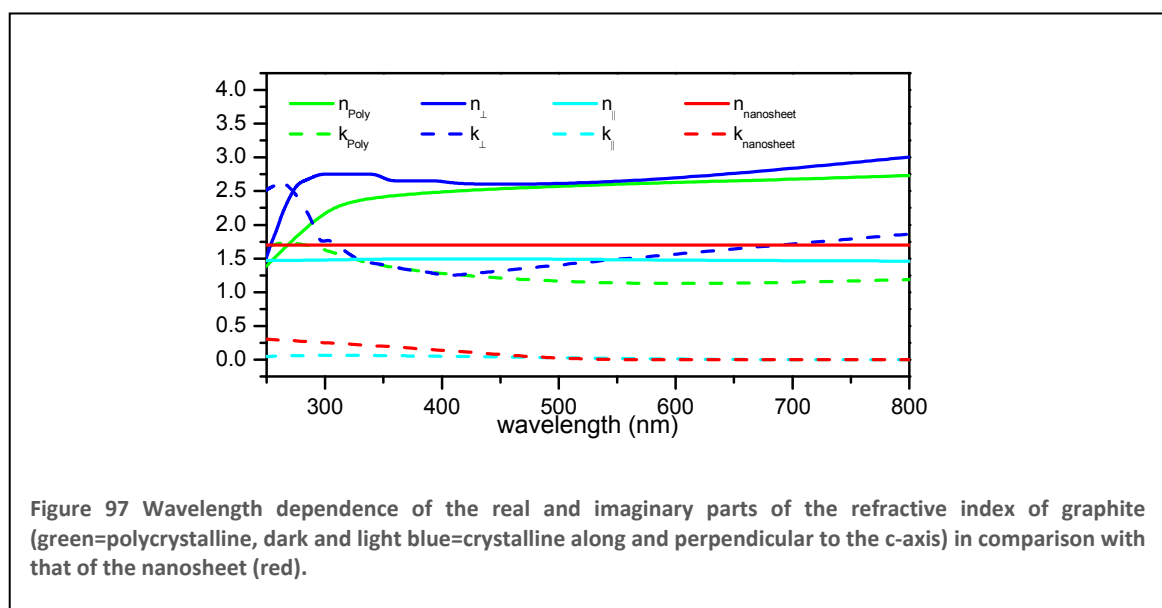
Figure 95a shows the G and D Raman bands of the multilayer samples after annealing to 1173 K, for comparison a spectra of a monolayer (red) annealed to the same temperature on a Au substrate was included (see chapter 4.7.3 for details). An increase of intensity with each additional layer can be observed. This increase is roughly linear, which can be seen in the intensity of the G band (Figure 95c). The shape of the signals closely resembles that of the monolayer, indicating that the graphitization process is independent of the chosen substrate. The ratio $I(D)/I(G)$ can be considered constant at 0.93 within the variation of the experiment, as all measurements led to values between 0.89 and 0.97, which were both measured for the three-layer sample (Figure 95b) in different positions. The values are all slightly smaller than what was found for the monolayers annealed at the same temperature on Au (chapter 4.7.3). This can be attributed to a small difference in the actual annealing temperature or time. The D band linearly shifts to higher wavenumbers with additional layers, whereas the G band shifts to lower wavenumbers (Figure 95b, c). Both shifts are very small as compared to shifts generally observed for the transition to amorphous carbon [158]. It can thus be concluded from the Raman data, that the graphitization process for multilayer samples is similar to that of monolayers and that nanocrystalline graphite is formed.

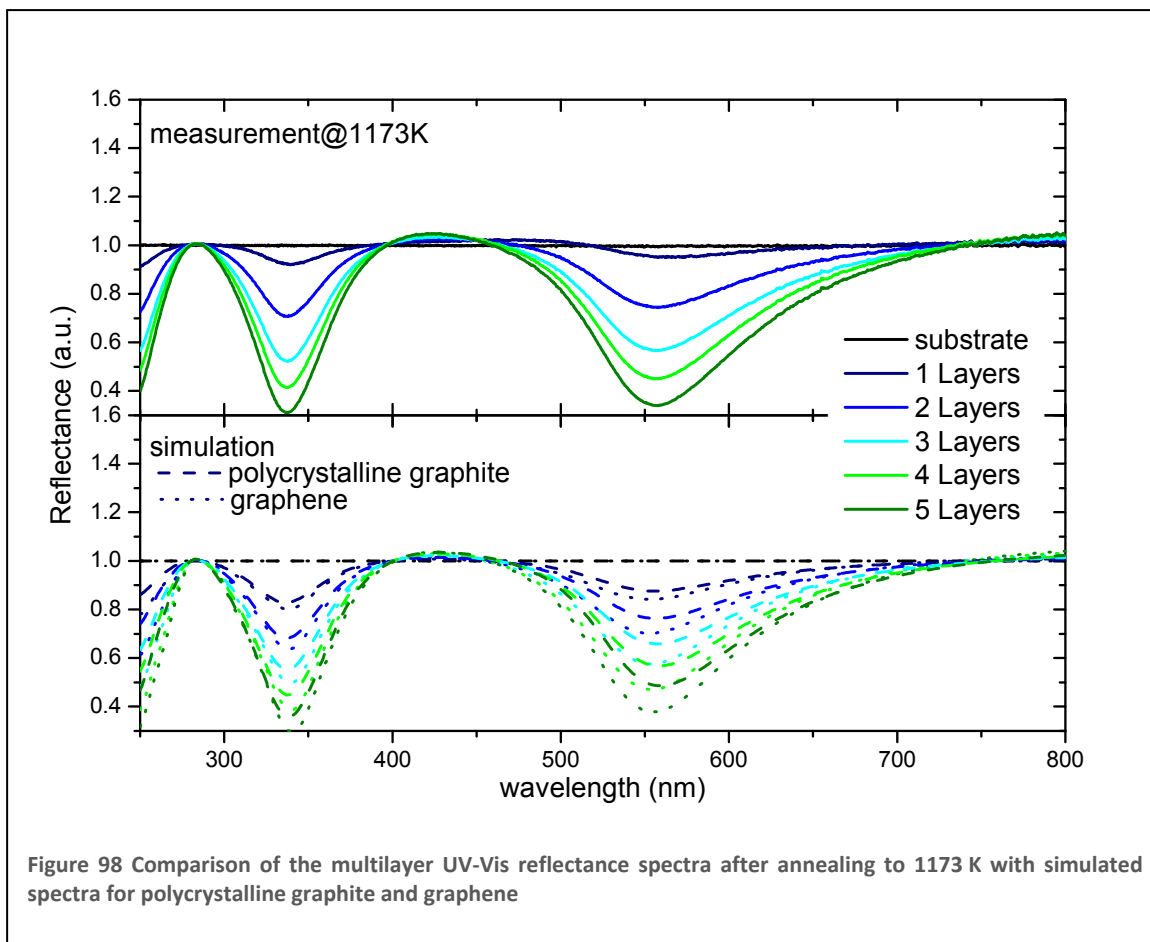
4.8.3 Optical Properties

The process of graphitization of the nanosheet multilayers by annealing is also reflected in their optical properties. After annealing the visibility by the naked eye is greatly enhanced, the nanosheet appears to be darker. In the UV-Vis spectra in Figure 96 it can be seen that the maxima with higher reflectance than the substrate disappear. The magnitude of the minima is increased and shifted to lower wavelengths.



All these changes can be attributed to the difference of the refractive indices of graphite vs. nanosheet. Graphite's refractive index is anisotropic due to the layered structure. It can be described with a part that is parallel (n_{\parallel}) and one that is perpendicular (n_{\perp}) to the c-axis, where only n_{\perp} is strongly absorbing. This has to be taken into account for ordered,

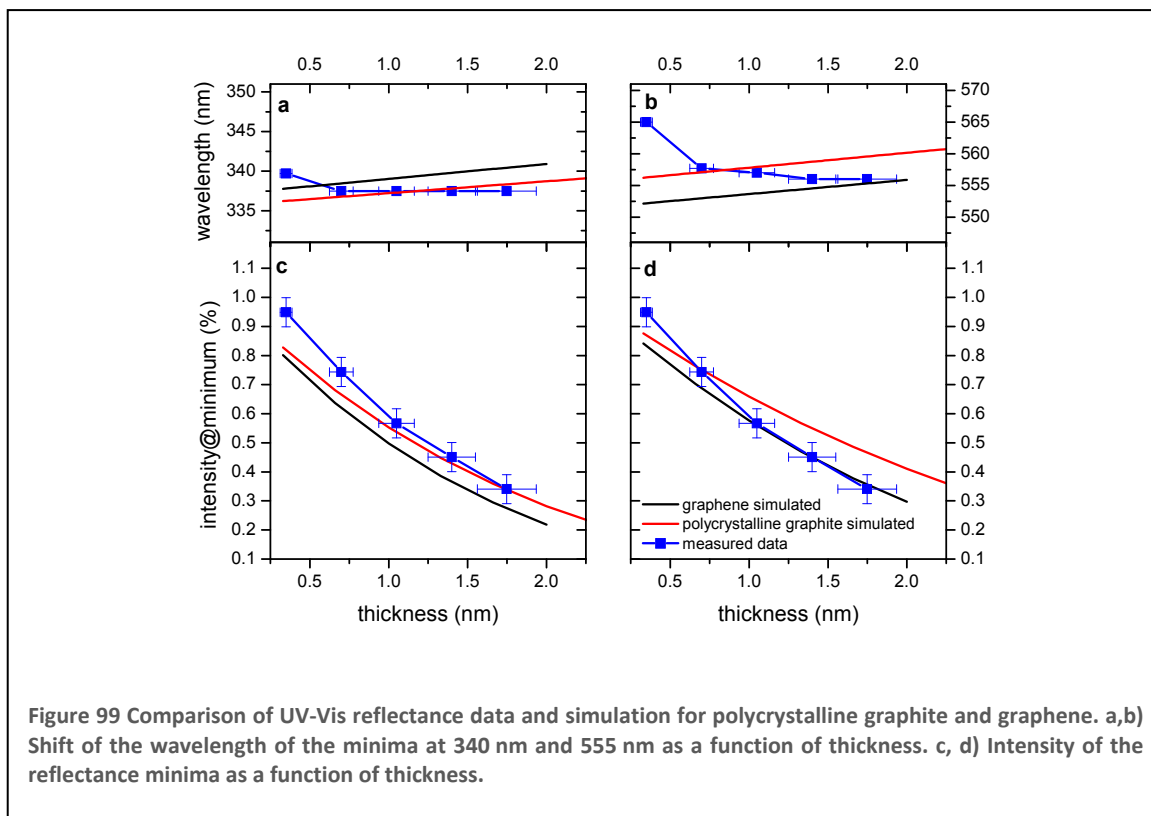




single crystalline graphite, such as graphene. For polycrystalline graphite the anisotropy can be neglected. Figure 97 shows the wavelength dependency of both the real and imaginary parts of n_{poly} , n_{\parallel} , and n_{\perp} and for comparison also $n_{\text{nanosheet}}$.

By using these refractive indices, the UV-Vis spectra for thin graphite layers on SiO_2 can be simulated. Both graphene and polycrystalline graphite layers were considered. In the latter case simulation is straight forward, whereas for graphene, simulations have to be done separately for s- and p-polarized light due to the anisotropy, as is described by Casiraghi et al. [46]. For s-polarization, the refractive index to be used is $n_s = n_{\perp}$, for p-polarization, however, it is angle dependent $n_p^{-2} = n_{\perp}^{-2} \cos^2 \theta + n_{\parallel}^{-2} \sin^2 \theta$. For best comparison with measured data, the average layer thickness as determined by XPS was used for simulation.

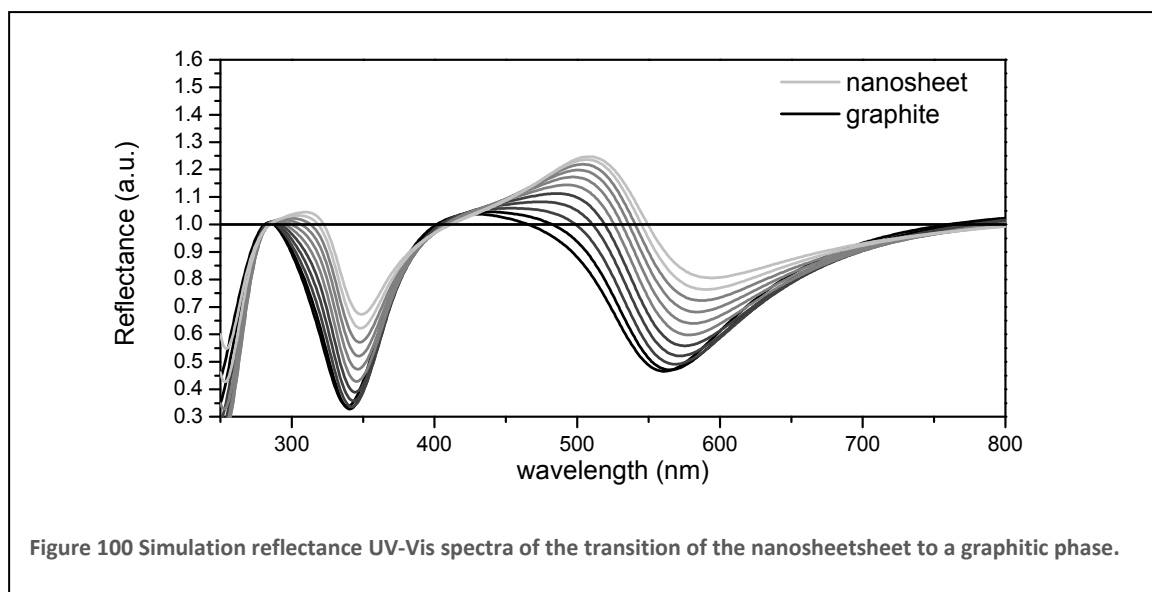
The simulated spectra in Figure 98 are able to describe the overall shape of the measured data quite nicely. The minima are shifted to lower wavelength and the magnitude is slightly higher in the case of graphene. To compare these features in more detail, both the reflected intensity and wavelength at the minima were plotted as a



function of the thickness (Figure 99). Both minima are shifting towards higher wavelength with additional layers, whereas the measured data shifts towards lower wavelength. This could hint at a higher degree of graphitization for thicker layers, as this change is also associated with the graphitization process. The change in reflected intensity of the measured data follows that of the simulations closely for three to five layers, the deviation in one and two layers could also be associated with lower degree of graphitization for these layers. It can be concluded though that the difference between poly- or nanocrystalline graphite and graphene is very small in terms of the reflectance spectrum and is not sufficient to distinguish between the two allotropes.

In principal, the spectra measured at annealing temperatures below 1173 K can be modeled by assuming a homogenous mixture of graphite and polymeric nanosheet. This could be i.e. graphitic clusters in a polymeric matrix. The optical properties of such mixtures can be described in terms of a new refractive index that is calculated from the refractive indices of both components. The most commonly used mixing rule is the so called Lorentz-Lorenz formula, which was also used here [45, 165, 166].

Simulated spectra for the transition from nanosheet to polycrystalline graphite in steps of 10% are shown in Figure 100 for the case of five layers. The layer thickness for the



graphitic spectra was derived from the XPS spectra at 1173 K, the nanosheet thickness was assumed to be 1 nm. All intermediate thicknesses were calculated assuming a homogeneous mixture.

By comparison of these simulated spectra with the measured data at different temperatures, an approximate degree of graphitization can be estimated for each annealing step. At 623 K already 35% of the nanosheet is transformed into graphite, 55% at 723 K, and 80% at 803 K. At 973 K the transformation is 90% complete and reaching 100% at 1173 K. These values are rough estimates based on the position and intensity of the peaks. Especially for 623 K no graphitic carbon is expected from Raman data for monolayers (see 4.7.3, ref. [93]). Based on these Raman measurements the onset of graphitization lies somewhere between 690 and 740 K. The deviation can be explained by the uncertainties in the refractive index of the nanosheet, as well as the thickness (from XPS) and intensity (difference between measurement and simulation, see Figure 63). However, these values can serve as a guide to simply estimate the degree of graphitization from the shape of an optical reflectance spectrum.

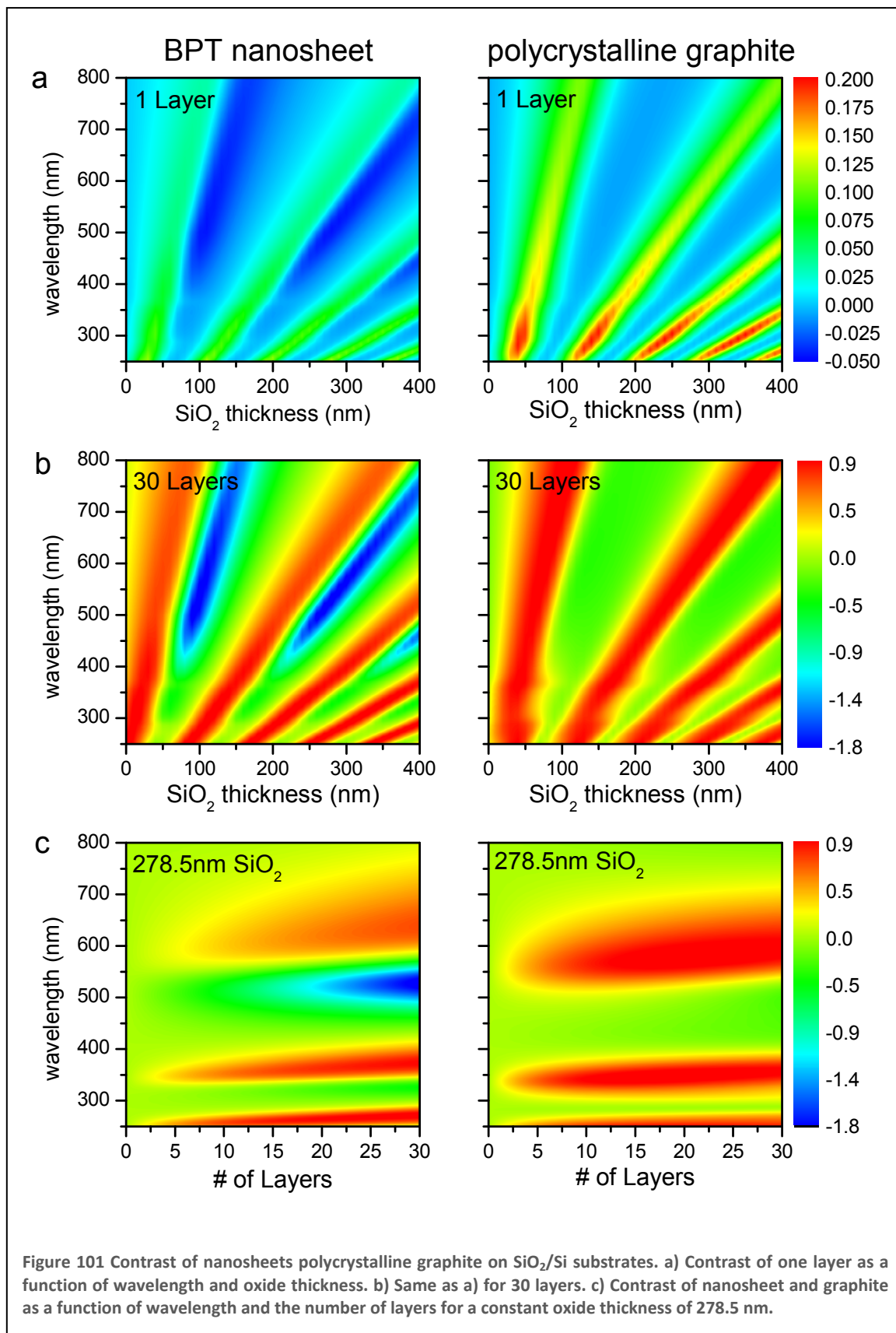
4.8.3.1 Dependence of contrast and thickness

From Figure 96 and Figure 100 it is apparent that the BPT nanosheet and graphite give rise to different spectral features on the SiO_2 substrate. The most prominent difference is the maximum in reflectance of the nanosheet around 500 nm, where the reflected intensity is higher than that of the SiO_2 substrate. In the graphite spectra no such feature can be observed. For better comparison, the contrast was plotted against the SiO_2

thickness, the wavelength and the number of layers for both pristine nanosheet as well as polycrystalline graphite in Figure 101 (the contrast scale was set the same for nanosheet and graphite). The layer thickness for polycrystalline graphite was set to the thickness of the annealed nanosheet as determined by XPS.

For one layer (a) the contrast of graphite is higher over the whole spectral range and all substrate thicknesses. The highest maximum is found in the UV range, which can be attributed to the $\pi \rightarrow \pi^*$ transition of graphite [46, 167]. However, the difference in contrast between maxima and minima is similar for nanosheet and graphite. Interestingly, other than for the nanosheet, the maxima in contrast for graphite closely follow the lines of destructive interference of the substrate. This is due mostly to the strong absorption of graphite. The minima are the most sensitive points, therefore giving the highest contrast.

For thicker layers (b,c) the contrast for graphite saturates in the maxima, whereas for the nanosheet it still grows in the minima.



4.8.4 Electrical properties

By graphitization of nanosheet multilayers, the electrical properties are expected to change drastically as a function of the degree of graphitization, similarly to the monolayers that were annealed on Au (chapter 4.7.2). Thus for each annealing step the conductivity of annealed multilayer stacks has been studied by means of 4-probe measurements. The probes were equidistantly spaced on the sample. If the distance between the probes is small compared to the lateral dimensions of the sample, the sheet resistivity ρ_{\square} for a thin film can be calculated by [168]

$$\rho_{\square} \left(\frac{\Omega}{\square} \right) = \frac{\rho}{t} = \frac{\pi}{\ln(2)} \frac{U}{I} = 4.53 \frac{U}{I} \quad (35)$$

where the resistivity ρ , the thickness of the thin film t , the Voltage U , and the current I .

All samples showed a linear current-voltage response, which is plotted in Figure 102b for an annealing temperature of 973 K. The calculated sheet resistivity as a function of annealing temperature is plotted in Figure 102a, the error bars represent the standard

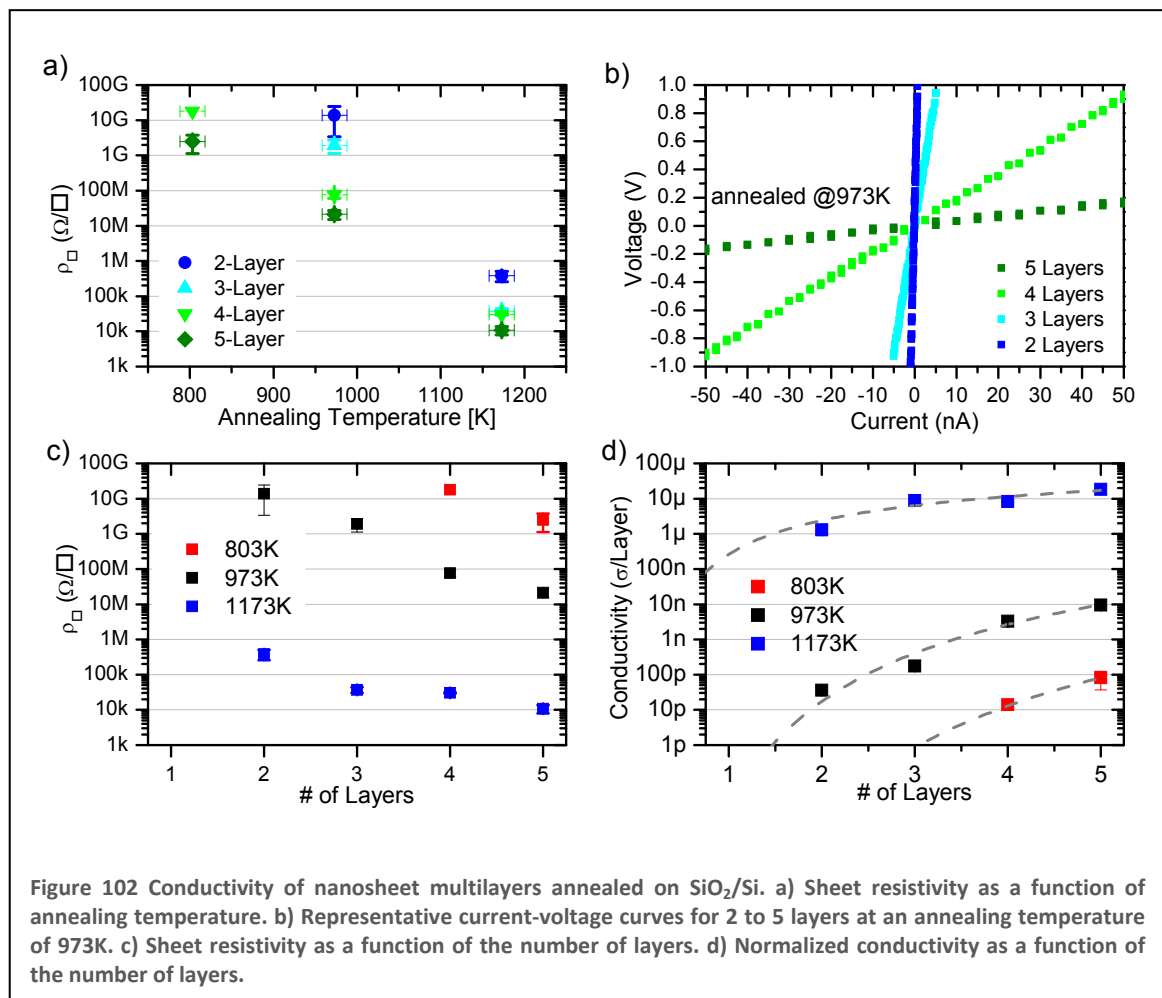


Figure 102 Conductivity of nanosheet multilayers annealed on SiO₂/Si. a) Sheet resistivity as a function of annealing temperature. b) Representative current-voltage curves for 2 to 5 layers at an annealing temperature of 973K. c) Sheet resistivity as a function of the number of layers. d) Normalized conductivity as a function of the number of layers.

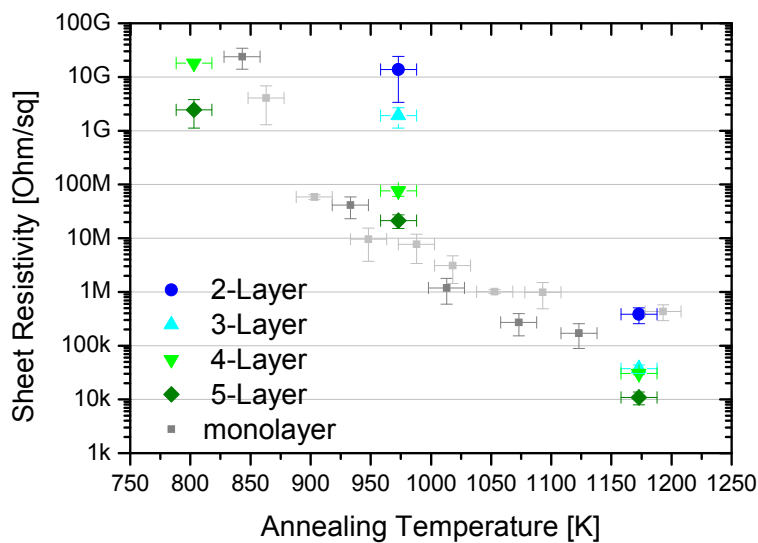


Figure 103 Comparison of the sheet resistivity obtained for monolayers of nanosheet annealed on Au and multilayers annealed on SiO_2/Si .

deviation between measurements at different spots on the samples. The onset of conductivity is found at an annealing temperature of 803 K, the four layer sample has a sheet resistivity ρ_{\square} of 18 $\text{G}\Omega/\square$, which is right at the resolution limit of the measurement. Some of the measured spots on this sample were found to be insulating as well. In the five layer sample, the sheet resistivity is already lower by one order of magnitude ($2.5 \pm 1.3 \text{ G}\Omega/\square$). After annealing to 973 K it drops by two orders of magnitude to $21 \pm 6 \text{ M}\Omega/\square$ for five layers, and $76 \pm 16 \text{ M}\Omega/\square$ for four layers, respectively. Also, the three and two layer samples are now conductive with a sheet resistivity ρ_{\square} of $1.9 \pm 0.8 \text{ G}\Omega/\square$ and $14 \pm 10 \text{ G}\Omega/\square$, respectively. Upon annealing to 1173 K it drops further to 10.8 ± 2.9 , 30.3 ± 1.4 , and $37.2 \pm 6.8 \text{ k}\Omega/\square$ for five, four and three layers. The two layer sample has a ρ_{\square} of $0.38 \pm 0.13 \text{ M}\Omega/\square$. The single layer sample is still insulating at this temperature. It seems that for the thicker layers (three to five) the graphitization is complete and the resistivity is going into saturation. This tendency is better shown in Figure 102c, where the sheet resistivity is plotted as a function of layer number.

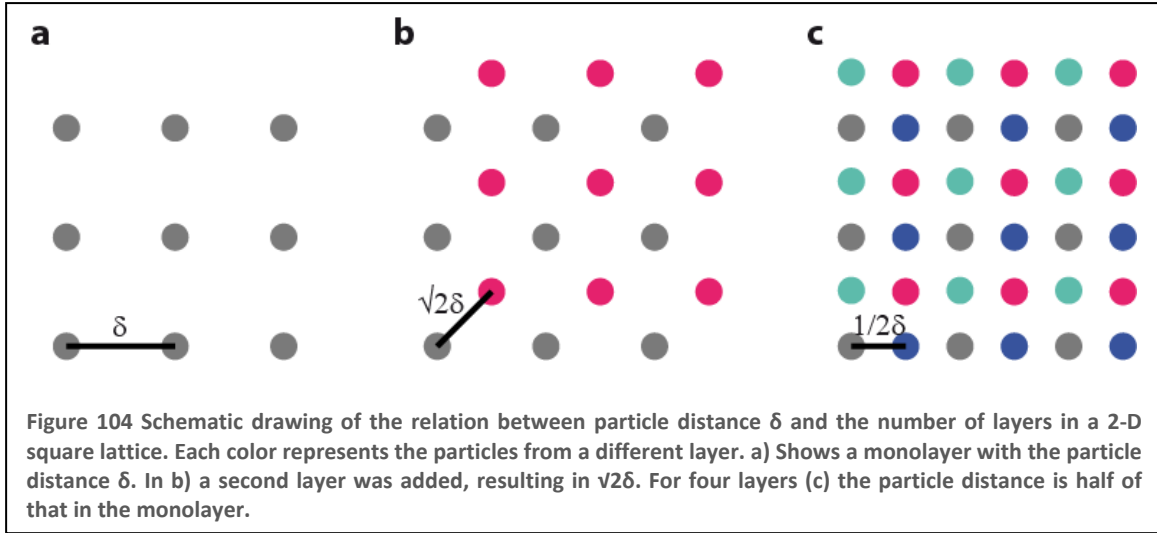
Multiplication with the layer thickness yields a mean resistivity of $\approx 33 \pm 8 \mu\Omega\text{m}$ for five, four and three layers at 1173 K. Literature values for graphite are 1-9.8 $\mu\Omega\text{m}$ perpendicular and 41 $\mu\Omega\text{m}$ parallel to the c-axis [169], for graphene theoretical values as low as 0.01 $\mu\Omega\text{m}$ have been reported [170]. Generally the resistivity decreases with annealing temperature in pyrolytic graphite, as the average crystallite size is

increasing[164, 171]. It can thus be expected that higher annealing temperatures are sufficient to further reduce the resistivity of the graphitized nanosheet.

A comparison of the obtained sheet resistivities with those that were measured for a single layer of nanosheet that was annealed on Au and transferred afterwards, is shown in Figure 103. It is found that the values are generally higher than those of the previous experiment. The monolayer annealed on SiO₂ was not found to be conductive even after annealing to 1173 K, where a sheet resistivity of $\approx 100 \text{ k}\Omega/\square$ would be expected. These differences might be an indication for a different mechanism of the graphitization on SiO₂. It might be possible that the amorphous SiO₂ prevents the formation of graphite crystallites at the interface, so that the first layer acts as a buffer layer that enables the formation of graphitic films for thicker layers. The effect could also be due to surface roughness that induces defects and therefore prevents the formation of a continuous film. As the origin of the differences is speculative, care should be taken when comparing samples annealed on SiO₂ with ones annealed freestanding or on Au.

In addition, the large differences in resistivity between different numbers of layers at the same annealing temperature cannot be explained if the samples have identical properties, only with a different thickness. For example, in the case of separated layers that are connected in parallel the total resistance R_{tot} is given by $1/R_{\text{tot}} = 1/R_1 + 1/R_2 + \dots$, therefore the resistance of five layers should be 4/5th of one with four layers. The observed difference between four and five layers at both 803 K and 973 K is about an order of magnitude though.

One can consider the nanosheet as a polymeric matrix, in which with higher annealing temperature more and bigger graphitic crystallites are dispersed. Three situations are then possible: the crystallites have no contact to each other, they are in close proximity, and they are in physical contact. The resistivity is then simply a function of the “filling factor” [172]. In the first case the resulting material will be insulating, in the last case it will have the properties of graphite. If they are in close proximity, however, electrons are able to move between the particles by a hopping mechanism. This can be understood as a thermally activated tunneling mechanism that can be described by the Arrhenius relation [173-177]:



$$\sigma(\delta, T) = \sigma_0 \exp(-\beta\delta) \exp\left(-\frac{E_A}{k_B T}\right) \quad (36)$$

where σ is the conductivity, β an electron tunneling coefficient, δ the average particle distance, and E_A the activation energy. Figure 102d plots the conductivity σ in units of $\Omega^* \text{Layer}$, which is independent of the actual layer thickness, allowing comparison between values obtained at different annealing temperatures.

At constant temperature the activation energy term can be neglected for high temperatures [176]. Assuming that the nanosheet's tunneling coefficient β is constant, the difference in conductivity can be explained by a change in the inter particle distance δ of the graphite crystallites. δ is related to the density q of the crystallites in the insulating matrix by:

$$\delta \propto \frac{1}{\sqrt[D]{q}} \quad (37)$$

where D is the dimensionality. Assuming that all measured multilayer stacks can be treated as 2-dimensional, and that the number of layers N is proportional to the density q (see Figure 104 for details), the conductivity data (Figure 102d) can be fitted by

$$\sigma(N, b) = \sigma_0 \exp\left(-\frac{b}{\sqrt[2]{N}}\right) \quad (38)$$

σ_0 was kept constant at an approximate value for the conductivity of graphite [169], the fitting parameter b is a scaling factor that is depending on the annealing temperature and also includes the tunneling coefficient β , which is unknown for the nanosheets. As β can be considered constant, b is a measure for the average particle distance per layer at

a given annealing temperature. The fits are describing the data very well, only the one layer conductivity at 1173 K would be expected at about 100 nS/Layer. Most likely the lacking conductivity at this point is due to defects in the layer rather than being an intrinsic property of the annealed nanosheet. From the fits it can be deduced that the particle distance at 973 K is 3.2 times larger (4.6 times at 803 K) than at 1173 K. Hence, as expected intuitively, the density of particles increases with higher annealing temperature.

Further insights into the graphitization process and the mechanism of conductivity could be gained by temperature dependent measurements. In the simplified Arrhenius model (equation (36)) it is expected that the conductivity decreases with decreasing temperature by $\log(\sigma) \propto -1/T$. Also, the higher the crystallinity of the annealed nanosheets, the less pronounced the temperature dependence should be. Ideally there is an annealing temperature at which the conductivity changes to metallic behavior.

4.8.5 Summary

It was shown that the graphitization of nanosheets can also be carried out on silicon oxide substrates for multilayer stacks. Changes in the optical spectra clearly reflect the transformation to a graphitic phase. Raman measurements indicate a similar mechanism of the graphitization, however, the sheet resistivity, especially of a monolayer, deviates from the results in the previous chapter. To explain the large difference in the resistivity of different layer thicknesses, a model was developed. For a better understanding of the material properties and the mechanism of graphitization, it is necessary though to perform additional microscopic experiments such as STM or TEM together with the electrical transport measurements.

5 Conclusion and Outlook

The present work deals with carbon nanosheets that are made by electron irradiation of biphenyl based SAMs. Such nanosheets constitute a new class of two-dimensional polymeric materials, which is characterized by its uniform molecular thickness, and high chemical, mechanical, and thermal stability. A method was developed to release such nanosheets from their original substrate and transfer them to arbitrary new substrates. This is achieved by the application of a polymeric layer (i.e. photoresist) as a transfer medium onto the nanosheet and subsequent dissolution of the substrate or a sacrificial layer. The transfer medium provides mechanical support during the whole process and can easily be dissolved in a final step.

The transfer procedure was shown for two types of SAMs: silanes on silicon oxide and silicon nitride substrate as well as thiols on gold. However, the procedure is not limited to these, as SAMs can assemble on a variety of different substrates through their specific headgroups. This is of particular interest with respect to the minimization of substrate cost and safety hazards. For example, SAMs with hydroxamic acid headgroups can assemble on iron substrates, which can be easily etched without the need for hydrofluoric acid.

In addition, the transfer method is not limited to nanosheets. In general it can be adapted to a wide variety of ultrathin films that are prepared on solid supports by using methods such as vapor deposition, spin coating, and electrodeposition. It is also possible to transfer graphene films and maybe even more weakly bound films such as supramolecular aggregates that are held together by hydrogen bonds or metal-organic frameworks (MOFs). The only requirement is the use of a sacrificial substrate. This could even be a water soluble polymer, as long as the transfer medium and the thin film are stable to the processing conditions. Some experiments were already carried out using gelatin, which can easily be dissolved by warm water, as a support for gold films. It is also possible to substitute the transfer medium by i.e. metal deposition. A thin gold film could provide stability during the transfer process and can be etched away afterwards. It must be ensured though, that the evaporation does not damage the material to be transferred.

The versatility of the transfer procedure was also demonstrated by transferring structured nanosheets. To this end, several different routes have been demonstrated that can produce patterned nanosheets on various length scales and geometries. Other than using these structures as an ultrathin resist material, it might be possible to use them as templates for “nano origami”. Nanosheet ribbons can roll themselves together to nanosheet tubes, if they are underetched. It might be interesting to study their properties in comparison with carbon nanotubes. It was shown in this work that nanosheets can be selectively functionalized on both sides to form “Janus”-membranes. Rolling up such functionalized ribbons, would lead to core-shell tubes. In a different approach, hollow nanosheet objects could be fabricated by preparing cross-linked SAMs on the convex surfaces of nanowires or particles and dissolving the support. Fascinating three-dimensional materials might be possible if nanosheets can be prepared on sponge-like supports with high inner surface area.

Nanosheets can be seen by the naked eye, if they are placed on oxidized silicon wafers. Folds of several layers appear to be darker and blue shifted with respect to the substrate color. This effect is very useful for sample fabrication, as it is not necessary to monitor every step by SEM. It was shown that nanosheets can be transferred with high precision to form multilayer stacks. This allowed a systematical study of the origin of the contrast by means of UV/Vis reflection spectroscopy and simulation. It was found that the contrast depends on the wavelength of light as well as the thickness of the oxide layer, which acts as an optical spacer, similar to an interferometer.

The controlled fabrication of multilayers also opens up a new route to assemble materials from the bottom up, simply by stacking layers. The advantage over existing techniques such as layer-by-layer assembly (LbL) is the possibility to stack layers without the need for specific interactions between the layers. Also, the individual nanosheet layers are very homogeneous in thickness and surface functionalization. By stacking different types of nanosheets or even other ultrathin films alternately, it is possible to “synthesize” totally new materials.

In addition, nanosheets can help in the characterization of other materials. Freestanding nanosheets have been used as a sample support in transmission electron microscopy. With Co nanoparticles and Au nanoclusters, it was shown that compared with

conventional supports the contrast of the particles is strongly enhanced. It was possible to resolve single gold atoms as well as the individual layers of multi-walled carbon nanotubes.

Apart from electron microscopy, a variety of other applications could benefit from freestanding nanosheets. The first experiments with nanosheets as sample supports for holography have already been carried out by collaborators at the free electron laser. Secondly, nanosheets can be used in ion-beam experiments: On the one hand the energy loss of highly charged ions traveling through the nanosheet can be studied as a function of the layer thickness. On the other hand, ion beam experiments might also help to gain more insight into the structure of the nanosheet. The impact of highly charged ions can lead to fragmentation, which can be analyzed by time-of-flight mass spectrometry. Initial experiments in this direction have already been carried out by Dr. Udo Werner together with collaborators. Thirdly, due to its thickness, only very few secondary electrons are generated in the nanosheet during electron irradiation. This is beneficial in lithographic patterning and can be used in EBID to obtain very small features. Such structures are particularly interesting for optical experiments, as the supporting nanosheet is practically “invisible”.

Another field of applications is filtration and separation, especially if the pore size in the nanosheets can be flexibly adjusted. For separation of gases, very small pores are necessary that might be present in the nanosheet as intermolecular voids. Conversely, gas permeation experiments could thus also help to gain a better understanding of the structure of the nanosheet. Larger pores could be introduced by adding a small fraction of molecules into the SAM that does not contribute to the cross-linked network upon electron irradiation, thus leaving voids. That way, the generation of pores up to several nanometers in diameter should be possible. Together with the techniques presented in chapter 4.3, methods are then available to produce nanosheets with pores from the sub-nanometer to the micron range.

Such membranes with defined pore size could be useful in biological applications. The pores could be utilized to study ion transport similar to cell membranes. Compared with lipid bilayers, the nanosheet is mechanically and chemically very robust. It might even be possible to incorporate biological ion pumps to study their function in different

environments. Also, by different functionalization of the nanosheet on both sides, a gradient could be created to facilitate transport in one direction, thus creating an artificial ion pump.

Thin membranes with defined pore sizes might also be useful in fuel cells. Fuel cells generally use a polymeric membrane as an electrolyte, and the cells performance depends critically on the properties of these membranes. Similarly, electrodes have to be separated by an ion-permeable membrane in lithium ion batteries. The selectivity of such membranes could be enhanced by suitable functionalization of the nanosheets, i.e. by polymer brushes that are tailored towards the specific application. The nanosheet then also provides a mechanically stable template.

Nanosheets could also prove useful as ultrathin dielectric layers, i.e. in transistors or capacitors. To this end the conduction perpendicular to the nanosheet layers must be examined, and first experiments are ongoing. The dielectric properties might even be adjustable by introducing functional groups into the SAM.

Nanosheets might also find use as sensors and actuators. This ranges from microphones and accelerometers to gas sensors. The critical step is to have a mechanism to read out the signal easily. An optical readout could be realized by positioning the nanosheet membrane close to a reflective surface, so that the membrane deflection gives rise to an interference contrast. By monitoring the resulting color and the number of interference fringes, the deflection can be calculated. However, for technical applications an electrical readout is desirable, so that the device can be used in integrated circuits. Several methods that lead towards an electrical readout were demonstrated in this work. On the one hand, metallic patterns can be fabricated on top of freestanding nanosheets. On the other hand the nanosheet can be made conductive by annealing in vacuum, where it undergoes a transition to a nanocrystalline graphitic phase. The conductivity can be flexibly adjusted by varying the annealing temperature. So far the lowest sheet resistivity that was obtained at ≈ 1200 K was ≈ 100 k Ω /sq; however, it might be possible to obtain a higher degree of crystallinity, and thus lower resistivity, by going to higher annealing temperatures or possibly the use of a suitable catalyst/catalytic surface. That way it might be possible to even produce graphene sheets.

On solid substrates the annealed nanosheets might find use as transparent conductive coatings. Such materials are in high demand i.e. for the fabrication of displays, as the resources for the current indium-tin-oxide (ITO) coatings are limited. Another disadvantage of ITO is its low mechanical strength, which is especially important as touch screen displays are becoming increasingly common. Due to the nanosheets elasticity, it might also be useable in flexible displays and other electronic devices.

Carbon nanosheets are a new type of 2D material with the thickness of only one molecule. Although more work has to be done to determine their exact structure, nanosheets have possible applications in a variety of different industries, the most promising being sensors, filtration membranes, sample supports, and conductive coatings. The work presented in this thesis is an important step in this direction and opens up opportunities for future research on this material system.

6 References

1. Moore, G.E., *Cramming more components onto integrated circuits*. Electronics, 1965. **38**(8).
2. Sakamoto, J., et al., *Two-Dimensional Polymers: Just a Dream of Synthetic Chemists?* Angewandte Chemie International Edition, 2009. **48**(6): p. 1030-1069.
3. Pockels, A., *Surface Tension*. Nature, 1891. **43**(1115): p. 437-439.
4. Langmuir, I., *The constitution and fundamental properties of solids and liquids. II. Liquids. 1*. Journal of the American Chemical Society, 1917. **39**(9): p. 1848-1906.
5. Blodgett, K.B., *Monomolecular films of fatty acids on glass*. Journal of the American Chemical Society, 1934. **56**(2): p. 495-495.
6. Gee, G., *Reactions in Monolayers of Drying Oils. II. Polymerization of the Oxidized Forms of the Maleic Anhydride Compound of β -Elaeostearin*. Proceedings of the Royal Society of London. Series A - Mathematical and Physical Sciences, 1935. **153**(878): p. 129-141.
7. Gee, G. and E.K. Rideal, *Reactions in Monolayers of Drying Oils. I. The Oxidation of the Maleic Anhydride Compound of β -Elaeostearin*. Proceedings of the Royal Society of London. Series A - Mathematical and Physical Sciences, 1935. **153**(878): p. 116-128.
8. Watanabe, H., R. Vendamme, and T. Kunitake, *Development of Fabrication of Giant Nanomembranes*. Bulletin of the Chemical Society of Japan, 2007. **80**(3): p. 433-440.
9. Love, J.C., et al., *Self-assembled monolayers of thiolates on metals as a form of nanotechnology*. Chemical Reviews, 2005. **105**(4): p. 1103-1169.
10. Geyer, W., et al., *Electron-induced crosslinking of aromatic self-assembled monolayers: Negative resists for nanolithography*. Applied Physics Letters, 1999. **75**(16): p. 2401-2403.
11. Sagiv, J., *Organized Monolayers by Adsorption, I. Formation and Structure of Oleophobic Mixed Monolayers on Solid Surfaces*. J. Am. Chem. Soc., 1980. **102**: p. 92.
12. Nuzzo, R.G. and D.L. Allara, *Adsorption of bifunctional organic disulfides on gold surfaces*. Journal of the American Chemical Society, 1983. **105**: p. 4481.
13. Ulman, A., *Formation and Structure of Self-Assembled Monolayers*. Chem Rev., 1996. **96**: p. 1533--1554.
14. Ulman, A., et al., *Self-assembled monolayers of rigid thiols*. Reviews in Molecular Biotechnology, 2000. **74**: p. 175-188.
15. Schreiber, F., *Structure and growth of self-assembling monolayers*. Prog. Surf. Sci., 2000. **65**: p. 151--256.
16. Müller, H.U., et al., *Low-Energy Electron-Induced Damage in Hexadecanethiolate Monolayers*. Journal of Physical Chemistry B, 1998. **102**: p. 7949--7959.
17. Zharnikov, M., et al., *Modification of Alkanethiolate Monolayers by Low Energy Electron Irradiation: Dependence on the Substrate Material and on the Length and Isotopic Composition of the Alkyl Chains*. Langmuir, 2000. **16**: p. 2697--2705.
18. Zharnikov, M., et al., *Modification of alkanethiolate monolayers on Au-substrate by low energy electron irradiation: Alkyl chains and the S/Au interface*. Physical Chemistry Chemical Physics, 1999. **1**(13): p. 3163-3171.
19. Huethorst, J.A.M.S., H.R.J. van Helleputte, and L.G.J. Fokkink, *Generation of electrochemically deposited metal patterns by means of electron beam*

- (nano)lithography of self-assembled monolayer resists. *Applied Physics Letters*, 1994. **64**: p. 285--287.
20. SondagHuethorst, J.A.M. and L.G.J. Fokkink, *Galvanic copper deposition on thiol-modified gold electrodes*. *Langmuir*, 1995. **11**(12): p. 4823-4831.
 21. Kaltenpoth, G., et al., *Electrode modification by electron-induced patterning of self-assembled monolayers*. *Journal of Vacuum Science & Technology B*, 2002. **20**(6): p. 2734-2738.
 22. Völkel, B., et al., *Electrodeposition of copper and cobalt nanostructures using self-assembled monolayer templates*. *Surface Science*, 2005. **597**(1-3): p. 32-41.
 23. Geyer, W., *Strukturierung selbstaggregierender Monolagen mit Elektronen*. 2001, Universität Heidelberg.
 24. Götzhäuser, A., et al., *Nanoscale patterning of self-assembled monolayers with electrons*. *Journal of Vacuum Science & Technology B*, 2000. **18**(6): p. 3414-3418.
 25. Tai, Y., et al., *Depth Distribution of Irradiation-Induced Cross-Linking in Aromatic Self-Assembled Monolayers*. *Langmuir*, 2004. **20**: p. 7166--7170.
 26. Eck, W., et al., *Generation of surface amino groups on aromatic self-assembled monolayers by low energy electron beams - a first step towards chemical lithography*. *Advanced Materials*, 2000. **12**: p. 805--808.
 27. Götzhäuser, A., et al., *Chemical nanolithography with electron beams*. *Advanced Materials*, 2001. **13**(11): p. 806--809.
 28. Nottbohm, C.T., A. Turchanin, and A. Götzhäuser, *Metallization of Organic Monolayers: Electroless Deposition of Cu onto Cross-Linked Aromatic Self-Assembled Monolayers*. 2008. **222**(5-6/2008): p. 917-926.
 29. Biebricher, A., et al., *Controlled three-dimensional immobilization of biomolecules on chemically patterned surfaces*. *Journal of Biotechnology*, 2004. **112**(1-2): p. 97-107.
 30. Turchanin, A., et al., *Molecular self-assembly, chemical lithography, and biochemical tweezers: A path for the fabrication of functional nanometer-scale protein arrays*. *Advanced Materials*, 2008. **20**(3): p. 471-+.
 31. Schmelmer, U., et al., *Surface-initiated polymerization on self-assembled monolayers: Amplification of patterns on the micrometer and nanometer scale*. *Angewandte Chemie-International Edition*, 2003. **42**(5): p. 559-+.
 32. Eck, W., et al., *Freestanding nanosheets from crosslinked biphenyl self-assembled monolayers*. *Advanced Materials*, 2005. **17**(21): p. 2583-+.
 33. Briggs, D. and J.C. Riviere, *Practical Surface Analysis Volume 1: Auger and X-Ray Photoelectron Spectroscopy*, D. Briggs and M.P. Seah, Editors. 1990, Wiley.
 34. *Surface Analysis by Auger and X-ray Photoelectron Spectroscopy*, ed. D. Briggs and J.T. Grant. 2003: IM Publications and SurfaceSpectra Limited.
 35. Egerton, R.F., *Physical Principles of Electron Microscopy: An Introduction to TEM, SEM, and AEM*. 2008: Springer.
 36. Knoll, M. and E. Ruska, *Das Elektronenmikroskop*. *Zeitschrift für Physik A Hadrons and Nuclei*, 1932. **78**(5): p. 318-339.
 37. de Broglie, L., *Recherches sur la théorie des quanta*. *Ann. Phys.*, 1925. **3**(22).
 38. O'Keefe, M.A., et al., *Sub-Angstrom high-resolution transmission electron microscopy at 300 keV*. *Ultramicroscopy*, 2001. **89**(4): p. 215-241.
 39. O'Keefe, M.A., et al., *Sub-angstrom resolution of atomistic structures below 0.8 angstrom*. *Philosophical Magazine B-Physics of Condensed Matter Statistical*

- Mechanics Electronic Optical and Magnetic Properties, 2001. **81**(11): p. 1861-1878.
40. von Ardenne, M., *Das Elektronen-Rastermikroskop*. Zeitschrift für Physik A Hadrons and Nuclei, 1938. **109**(9): p. 553-572.
 41. Meschede, D., *Gerthsen Physik*. 2006: Springer, Berlin.
 42. Hecht, E., *Optics*. 2001: Addison Wesley. 680.
 43. Sernelius, B.E., *Surface Modes in Physics*. 2001: Wiley-VCH.
 44. Dobrowolski, J.A., *Optical properties of films and coatings*, in *Handbook/Optics*, M. Bass, Editor. 1994, McGraw-Hill Professional.
 45. Born, M. and E. Wolf, *Principles of Optics: Electromagnetic Theory of Propagation Interference and Diffraction of Light*. 1980: Pergamon. 808.
 46. Casiraghi, C., et al., *Rayleigh Imaging of Graphene and Graphene Layers*. Nano Letters, 2007. **7**(9): p. 2711-2717.
 47. Larouche, S. and L. Martinu, *OpenFilters: open-source software for the design, optimization, and synthesis of optical filters*. Appl. Opt., 2008. **47**(13): p. C219-C230.
 48. Atkins, P.W., *Physikalische Chemie*. 1996: Wiley-VCH.
 49. Köhler, M., *Ätzverfahren für die Mikrotechnik*. 1998: Wiley-VCH.
 50. Hellmich, W., et al., *Poly(oxyethylene) Based Surface Coatings for Poly(dimethylsiloxane) Microchannels*. Langmuir, 2005. **21**(16): p. 7551.
 51. Puentes, V.F., K.M. Krishnan, and A.P. Alivisatos, *Science*, 2001. **291**: p. 2115 - 2117.
 52. Ennen, I., *Magnetische Nanopartikel als Bausteine für granulare Systeme : Mikrostruktur, Magnetismus und Transporteigenschaften*. 2008, Bielefeld.
 53. Schmidt, G., *Chemical Review*, 1992. **92**: p. 1709.
 54. Panhorst, M., *On-chip manipulation and positioning of biomolecules with magnetic beads*, in *Physik*. 2005, Universität Bielefeld.
 55. Haugland, R.P. *Molecular Probes - The Handbook*. 2009 [cited; Available from: <http://www.invitrogen.com/site/us/en/home/References/Molecular-Probes-The-Handbook.html>].
 56. Loo, Y.-L., et al., *Electrical Contacts to Molecular Layers by Nanotransfer Printing*. Nano Letters, 2003. **3**(7): p. 913-917.
 57. Meitl, M.A., et al., *Transfer printing by kinetic control of adhesion to an elastomeric stamp*. Nature Materials, 2006. **5**: p. 33--38.
 58. Vilan, A. and D. Cahen, *Soft Contact Deposition onto Molecularly Modified GaAs. Thin Metal Film Flotation: Principles and Electrical Effects*. Advanced Functional Materials, 2002. **12**(11-12): p. 795-807.
 59. Shimizu, K.T., et al., *Soft Deposition of Large-Area Metal Contacts for Molecular Electronics*. Advanced Materials, 2006. **18**(12): p. 1499-1504.
 60. Küller, A., *Von der Chemischen Nanolithographie zur Dreidimensionalen Lithographie und freistehenden Nanofolien*. 2006, Universität Heidelberg.
 61. Blake, P., et al., *Making graphene visible*. Applied Physics Letters, 2007. **91**(6).
 62. Walther, A. and A.H.E. Muller, *Janus particles*. Soft Matter, 2008. **4**(4): p. 663-668.
 63. Kosztin, I. and K. Schulten, *Fluctuation-Driven Molecular Transport Through an Asymmetric Membrane Channel*. Physical Review Letters, 2004. **93**(23): p. 238102.

64. Astumian, R.D. and I. Derényi, *Fluctuation driven transport and models of molecular motors and pumps*. European Biophysics Journal, 1998. **27**(5): p. 474-489.
65. Matthias, S. and F. Muller, *Asymmetric pores in a silicon membrane acting as massively parallel brownian ratchets*. Nature, 2003. **424**(6944): p. 53-57.
66. Mancin, F., et al., *Self-Assembled Fluorescent Chemosensors*. Chemistry - A European Journal, 2006. **12**(7): p. 1844-1854.
67. Basabe-Desmonts, L., et al., *A Simple Approach to Sensor Discovery and Fabrication on Self-Assembled Monolayers on Glass*. Journal of the American Chemical Society, 2004. **126**(23): p. 7293-7299.
68. Lavigne, J.J. and E.V. Anslyn, *Sensing A Paradigm Shift in the Field of Molecular Recognition: From Selective to Differential Receptors*. Angewandte Chemie International Edition, 2001. **40**(17): p. 3118-3130.
69. Crego-Calama, M. and D.N. Reinhoudt, *New Materials for Metal Ion Sensing by Self-Assembled Monolayers on Glass*. Advanced Materials, 2001. **13**(15): p. 1171-1174.
70. Chen, S.H. and C.W. Frank, *Fluorescence probe studies of self-assembled monolayer films*. Langmuir, 1991. **7**(8): p. 1719-1726.
71. Geyer, W., et al., *Electron induced chemical nanolithography with self-assembled monolayers*. Journal of Vacuum Science & Technology B, 2001. **19**: p. 2732--2735.
72. Wilbur, J.L., et al., *Microfabrication by microcontact printing of self-assembled monolayers*. Advanced Materials, 1994. **6**(7-8): p. 600-604.
73. Xia, Y. and G.M. Whitesides, *Soft lithography*. Annual Review of Materials Science, 1998. **28**: p. 153-184.
74. Bietsch, A., et al., *Inkjet Deposition of Alkanethiolate Monolayers and DNA Oligonucleotides on Gold: Evaluation of Spot Uniformity by Wet Etching*. Langmuir, 2004. **20**(12): p. 5119-5122.
75. Huck, W.T.S., *Self-Assembly Meets Nanofabrication: Recent Developments in Microcontact Printing and Dip-Pen Nanolithography*. Angewandte Chemie International Edition, 2007. **46**(16): p. 2754-2757.
76. Salaita, K., Y. Wang, and C.A. Mirkin, *Applications of dip-pen nanolithography*. Nat Nano, 2007. **2**(3): p. 145-155.
77. Liu, M., N.A. Amro, and G.-y. Liu, *Nanografting for Surface Physical Chemistry*. Annual Review of Physical Chemistry, 2008. **59**(1): p. 367-386.
78. Garcia, R., R.V. Martinez, and J. Martinez, *Nano-chemistry and scanning probe nanolithographies*. Chemical Society Reviews, 2006. **35**(1): p. 29-38.
79. Huang, J.Y., D.A. Dahlgren, and J.C. Hemminger, *Photopatterning of self-assembled alkanethiolate monolayers on gold - a simple monolayer photoresist utilizing aqueous chemistry*. Langmuir, 1994. **10**(3): p. 626-628.
80. Mendes, P.M. and J.A. Preece, *Precision chemical engineering: integrating nanolithography and nanoassembly*. Current Opinion in Colloid & Interface Science, 2004. **9**: p. 236--248.
81. Turchanin, A., et al., *Fabrication of molecular nanotemplates in self-assembled monolayers by extreme-ultraviolet-induced chemical lithography*. Small, 2007. **3**(12): p. 2114-2119.
82. David, C., et al., *Low energy electron proximity printing using a self-assembled monolayer resist*. Microelectronic Engineering, 1996. **30**(1-4): p. 57-60.

83. Solak, H.H., et al., *Photon-beam lithography reaches 12.5 nm half-pitch resolution*. Journal of Vacuum Science & Technology B: Microelectronics and Nanometer Structures, 2007. **25**(1): p. 91-95.
84. Auzelyte, V., et al., *Extreme ultraviolet interference lithography at the Paul Scherrer Institut*. Journal of Micro/Nanolithography, MEMS and MOEMS, 2009. **8**(2): p. 021204-10.
85. Schnietz, M., et al., *Chemically functionalized nanosieve membranes with a thickness of 1 nm* submitted, 2009.
86. Zhao, X.-M., J.L. Wilbur, and G.M. Whitesides, *Using Two-Stage Chemical Amplification To Determine the Density of Defects in Self-Assembled Monolayers of Alkanethiolates on Gold*. Langmuir, 1996. **12**(13): p. 3257-3264.
87. Küller, A., et al., *Nanostructuring of silicon by electron-beam lithography of self-assembled hydroxybiphenyl monolayers*. Applied Physics Letters, 2003. **82**(21): p. 3776-3778.
88. Huang, J.Y. and J.C. Hemminger, *Photooxidation of thiols in self-assembled monolayers on gold*. Journal of the American Chemical Society, 1993. **115**(8): p. 3342-3343.
89. Worley, C.G. and R.W. Linton, *Removing sulfur from gold using ultraviolet/ozone cleaning*. Journal of Vacuum Science & Technology A: Vacuum, Surfaces, and Films, 1995. **13**(4): p. 2281-2284.
90. Zhang, Y.M., et al., *Ozonolysis is the primary cause of UV photooxidation of alkanethiolate monolayers at low irradiance*. Journal of the American Chemical Society, 1998. **120**(11): p. 2654-2655.
91. Tarlov, M.J., D.R.F. Burgess, and G. Gillen, *UV photopatterning of alkanethiolate monolayers self-assembled on gold and silver*. Journal of the American Chemical Society, 1993. **115**(12): p. 5305-5306.
92. Leggett, G.J., *Scanning near-field photolithography-surface photochemistry with nanoscale spatial resolution*. Chemical Society Reviews, 2006. **35**(11): p. 1150-1161.
93. Turchanin, A., et al., *One Nanometer Thin Carbon Nanosheets with Tunable Conductivity and Stiffness*. Advanced Materials, 2009. **21**(12): p. 1233-1237.
94. Xia, Y. and G.M. Whitesides, *Soft Lithography*. Angewandte Chemie International Edition, 1998. **37**(5): p. 550-575.
95. Rohr, T., et al., *Surface Functionalization of Thermoplastic Polymers for the Fabrication of Microfluidic Devices by Photoinitiated Grafting*. Advanced Functional Materials, 2003. **13**(4): p. 264-270.
96. Beyer, A., et al., *Fully cross-linked and chemically patterned self-assembled monolayers*. Phys. Chem. Chem. Phys., 2008. **10**: p. 7233-7238.
97. Novoselov, K.S., et al., *Two-dimensional atomic crystals*. Proceedings of the National Academy of Sciences of the United States of America, 2005. **102**: p. 10451-10453.
98. Ariga, K., J.P. Hill, and Q. Ji, *Layer-by-layer assembly as a versatile bottom-up nanofabrication technique for exploratory research and realistic application*. Physical Chemistry Chemical Physics, 2007. **9**(19): p. 2319-2340.
99. Jiang, C., S. Markutsya, and V.V. Tsukruk, *Compliant, Robust, and Truly Nanoscale Free-Standing Multilayer Films Fabricated Using Spin-Assisted Layer-by-Layer Assembly*. Advanced Materials, 2004. **16**(2): p. 157-161.

100. Jiang, C.Y., et al., *Freely suspended nanocomposite membranes as highly sensitive sensors*. Nature Materials, 2004. **3**(10): p. 721-728.
101. Markutsya, S., et al., *Freely Suspended Layer-by-Layer Nanomembranes: Testing Micromechanical Properties*. Advanced Functional Materials, 2005. **15**(5): p. 771-780.
102. Blodgett, K.B., *Film structure and method of preparation*. 1940: USA.
103. Blodgett, K.B., *Low-reflectance glass*. 1940: USA.
104. Blodgett, K.B., *Step gauge for measuring thickness of thin films*. 1952: USA.
105. Mitsuishi, M., J. Matsui, and T. Miyashita, *Functional Organized Molecular Assemblies Based on Polymer Nano-sheets*. Polymer Journal, 2006. **38**(9): p. 877-896.
106. Mitsuishi, M., J. Matsui, and T. Miyashita, *Photofunctional thin film devices composed of polymer nanosheet assemblies*. Journal of Materials Chemistry, 2009. **19**(3): p. 325-329.
107. Kado, Y., M. Mitsuishi, and T. Miyashita, *Fabrication of Three-Dimensional Nanostructures Using Reactive Polymer Nanosheets*. Advanced Materials, 2005. **17**(15): p. 1857-1861.
108. Wagner, C.D., et al. *NIST X-ray Photoelectron Spectroscopy Database NIST Standard Reference Database 20, Version 3.4 (Web Version)*. 2003 [cited].
109. Ton-That, C., et al., *XPS and AFM surface studies of solvent-cast PS/PMMA blends*. Polymer, 2001. **42**(3): p. 1121-1129.
110. Turchanin, A., et al., *Molecular mechanisms of electron-induced cross-linking in aromatic SAMs*. Langmuir, 2009. **in print**.
111. Hirata, T., T. Kashiwagi, and J.E. Brown, *Thermal and oxidative degradation of poly(methyl methacrylate): weight loss*. Macromolecules, 1985. **18**(7): p. 1410-1418.
112. Meisters, A., et al., *Thermal stability of poly(methyl methacrylate)*. Polymer Bulletin, 1988. **20**(5): p. 499-503.
113. Turchanin, A., M. El-Desawy, and A. Götzhäuser, *High thermal stability of cross-linked aromatic self-assembled monolayers: Nanopatterning via selective thermal desorption*. Applied Physics Letters, 2007. **90**(5).
114. Ni, Z.H., et al., *Graphene Thickness Determination Using Reflection and Contrast Spectroscopy*. Nano Letters, 2007. **7**(9): p. 2758-2763.
115. Roddaro, S., et al., *The Optical Visibility of Graphene: Interference Colors of Ultrathin Graphite on SiO₂*. Nano Letters, 2007. **7**(9): p. 2707-2710.
116. Jung, I., et al., *Simple Approach for High-Contrast Optical Imaging and Characterization of Graphene-Based Sheets*. Nano Letters, 2007. **7**(12): p. 3569-3575.
117. Gray, A., et al., *Optical detection and characterization of graphene by broadband spectrophotometry*. Journal of Applied Physics, 2008. **104**(5): p. 053109.
118. Akcoltekin, S., et al., *Graphene on insulating crystalline substrates*. Nanotechnology, 2009(15): p. 155601.
119. Gaskell, P.E., et al., *Counting graphene layers on glass via optical reflection microscopy*. APPLIED PHYSICS LETTERS, 2009. **94**(14): p. 143101.
120. Edited by: Palik, E.D., *Handbook of Optical Constants of Solids*. 1998: Elsevier. 3227.
121. Perkampus, H.-H., *UV-VIS Atlas of Organic Compounds (2nd ed.)*. 1992: Wiley VCH.

122. Rajca, A., et al., *Biphenylene Dimer. Molecular Fragment of a Two-Dimensional Carbon Net and Double-Stranded Polymer*. Journal of the American Chemical Society, 1996. **118**(31): p. 7272-7279.
123. Rajca, A., et al., *Doppelhelicales Octaphenylene*. Angewandte Chemie, 1997. **109**(5): p. 504-507.
124. Teo, G., et al., *Visibility study of graphene multilayer structures*. Journal of Applied Physics, 2008. **103**(12): p. 124302.
125. Nair, R.R., et al., *Fine structure constant defines visual transparency of graphene*. Science, 2008. **320**(5881): p. 1308-1308.
126. Konkar, A., et al., Nanoletters, 2005. **5**(5): p. 969 - 973.
127. Menard, L.D., et al., J. Phys. Chem. B, 2006. **110**: p. 12874 - 12883.
128. Geim, A.K. and K.S. Novoselov, *The rise of graphene*. Nature Materials, 2007. **6**(3): p. 183-191.
129. Meyer, J.C., et al., *The structure of suspended graphene sheets*. Nature, 2007. **446**(7131): p. 60-63.
130. Hoogenboom, B.W., et al., *A Fabry--Perot interferometer for micrometer-sized cantilevers*. Applied Physics Letters, 2005. **86**(7): p. 074101.
131. Akkerman, H.B. and B.d. Boer, *Electrical conduction through single molecules and self-assembled monolayers*. J. Phys.: Condens. Matter, 2008. **20**: p. 013001.
132. Tai, Y., et al., *Fabrication of stable metal films on the surface of self-assembled monolayers*. Advanced Materials, 2005. **17**(14): p. 1745-1749.
133. Du, X., et al., *Approaching ballistic transport in suspended graphene*. Nat Nano, 2008. **3**(8): p. 491-495.
134. Gass, M.H., et al., *Free-standing graphene at atomic resolution*. Nature Nanotechnology, 2008. **3**(11): p. 676-681.
135. Nottbohm, C.T., et al., *Novel carbon nanosheets as support for ultrahigh-resolution structural analysis of nanoparticles* Ultramicroscopy, 2008. **108**(9): p. 885-892.
136. Koops, H.W.P., et al., *High-resolution electron-beam induced deposition*. Journal of Vacuum Science & Technology B: Microelectronics and Nanometer Structures, 1988. **6**(1): p. 477-481.
137. Dorp, W.F.v. and C.W. Hagen, *A critical literature review of focused electron beam induced deposition*. Journal of Applied Physics, 2008. **104**(8): p. 081301.
138. Kroto, H.W., et al., *C-60 - Buckminsterfullerene*. Nature, 1985. **318**(6042): p. 162-163.
139. Iijima, S., *Helical microtubules of graphitic carbon*. Nature, 1991. **354**(6348): p. 56-58.
140. Novoselov, K.S., et al., *Electric Field Effect in Atomically Thin Carbon Films*. Science (Washington, DC, United States), 2004. **306**: p. 666--669.
141. Novoselov, K.S., et al., *Two-dimensional gas of massless Dirac fermions in graphene*. Nature, 2005. **438**(7065): p. 197-200.
142. Zhang, Y.B., et al., *Experimental observation of the quantum Hall effect and Berry's phase in graphene*. Nature, 2005. **438**(7065): p. 201-204.
143. Berger, C., et al., *Electronic confinement and coherence in patterned epitaxial graphene*. Science, 2006. **312**(5777): p. 1191-1196.
144. Ohta, T., et al., *Controlling the electronic structure of bilayer graphene*. Science, 2006. **313**(5789): p. 951-954.

145. Stankovich, S., et al., *Graphene-based composite materials*. Nature, 2006. **442**(7100): p. 282-286.
146. Bunch, J.S., et al., *Electromechanical resonators from graphene sheets*. Science, 2007. **315**(5811): p. 490-493.
147. Li, X.L., et al., *Chemically derived, ultrasMOOTH graphene nanoribbon semiconductors*. Science, 2008. **319**(5867): p. 1229-1232.
148. Coraux, J., et al., *Structural coherency of graphene on Ir(111)*. Nano Letters, 2008. **8**(2): p. 565-570.
149. Schultz, M.J., et al., PNAS, 2008. **105**(21): p. 7353-7358.
150. Striemer, C.C., et al., *Charge- and size-based separation of macromolecules using ultrathin silicon membranes*. Nature, 2007. **445**(7129): p. 749-753.
151. Kyotani, T., N. Sonobe, and A. Tomita, *Formation of highly oriented graphite from polyacrylonitrile by using a two-dimensional space between montmorillonite lamellae*. Nature, 1988. **331**(6154): p. 331-333.
152. Sabatani, E., et al., *Thioaromatic monolayers on gold - a new family of self-assembled monolayers*. Langmuir, 1993. **9**(11): p. 2974-2981.
153. Bain, C.D., et al., *Formation of monolayer films by the spontaneous assembly of organic thiols from solution onto gold*. Journal of the American Chemical Society, 1989. **111**(1): p. 321-335.
154. Lercel, M.J., et al., *Sub-10 nm lithography with self-assembled monolayers*. Applied Physics Letters, 1996. **68**(11): p. 1504-1506.
155. Plummer, J.D., M.D. Deal, and P.B. Griffin, in *Silicon VLSI Technology*. 2000, Prentice Hall: Upper Saddle River, NJ, USA. p. 114.
156. Gomez-Navarro, C., et al., *Electronic transport properties of individual chemically reduced graphene oxide sheets*. Nano Letters, 2007. **7**(11): p. 3499-3503.
157. Weber, W.H. and R. Merlin, eds. *Raman Scattering in Materials Science*. Materials Science. 2000, Springer: Heidelberg. 492.
158. Ferrari, A.C. and J. Robertson, *Resonant Raman spectroscopy of disordered, amorphous, and diamondlike carbon*. Physical Review B, 2001. **64**(7): p. 075414.
159. Fasolino, A., J.H. Los, and M.I. Katsnelson, *Intrinsic ripples in graphene*. Nature Materials, 2007. **6**(11): p. 858-861.
160. Sette, F., et al., *Lifetime and screening of the C 1s photoemission in graphite*. Physical Review B, 1990. **41**(14): p. 9766.
161. Jackson, S.T. and R.G. Nuzzo, *Determining hybridization differences for amorphous carbon from the XPS C 1s envelope*. Applied Surface Science, 1995. **90**(2): p. 195-203.
162. Blyth, R.I.R., et al., *XPS studies of graphite electrode materials for lithium ion batteries*. Applied Surface Science, 2000. **167**(1-2): p. 99-106.
163. S. Tanuma, C.J.P.D.R.P., *Calculations of electron inelastic mean free paths*. Surface and Interface Analysis, 2005. **37**(1): p. 1-14.
164. Pimenta, M.A., et al., *Studying disorder in graphite-based systems by Raman spectroscopy*. Physical Chemistry Chemical Physics, 2007. **9**(11): p. 1276-1290.
165. Lorenz, L., *Über die Refraktionsconstante*. Ann. Phys., 1880. **11**: p. 70-103.
166. Lorentz, H.A., *Über die Beziehung zwischen der Fortpflanzungsgeschwindigkeit des Lichtes der K^rperdichte*. Ann. Phys., 1880. **9**: p. 641-665.
167. Djuricic, A.B. and E.H. Li, *Optical properties of graphite*. Journal of Applied Physics, 1999. **85**(10): p. 7404-7410.
168. Plummer, V.J.D., M.D. Deal, and P.B. Griffin, *Silicon VLSI Technology*.

169. Powell, R.L. and G.E. Childs, in *American Institute of Physics Handbook*. 1972. p. 4-142 to 4-160.
170. Chen, J.-H., et al., *Intrinsic and extrinsic performance limits of graphene devices on SiO₂*. *Nat Nano*, 2008. **3**(4): p. 206-209.
171. Kinchin, G.H., *The Electrical Properties of Graphite*. Proceedings of the Royal Society of London. Series A. Mathematical and Physical Sciences, 1953. **217**(1128): p. 9-26.
172. Bigg, D.M., *Electrical Properties of Metal-Filled Polymer Composites*. 1986.
173. Wuelfing, W.P. and R.W. Murray, *Electron Hopping through Films of Arenethiolate Monolayer-Protected Gold Clusters*. *The Journal of Physical Chemistry B*, 2002. **106**(12): p. 3139-3145.
174. Wuelfing, W.P. and R.W. Murray, *Electron Hopping through Films of Arenethiolate Monolayer-Protected Gold Clusters*. *The Journal of Physical Chemistry B*, 2003. **107**(24): p. 6018-6018.
175. Wessels, J.M., et al., *Optical and Electrical Properties of Three-Dimensional Interlinked Gold Nanoparticle Assemblies*. *Journal of the American Chemical Society*, 2004. **126**(10): p. 3349-3356.
176. Strelniker, Y.M., *Effective resistance of systems with hopping conductivities in the case of many neighbors*. *Physical Review B (Condensed Matter and Materials Physics)*, 2006. **73**(15): p. 153407.
177. Terrill, R.H., et al., *Monolayers in Three Dimensions: NMR, SAXS, Thermal, and Electron Hopping Studies of Alkanethiol Stabilized Gold Clusters*. *Journal of the American Chemical Society*, 1995. **117**(50): p. 12537-12548.

7 Publikations

Kaltenpoth, G.; Völkel, B.; **Nottbohm, C.T.**; Gölzhäuser, A.; Buck, M. „Electrode modification by electron induced patterning of self-assembled monolayers”, *J. Vac. Sci. Technol. B*, 2002, 20, 2734-2738.

Völkel, B.; Kaltenpoth, G.; Handrea, M.; Sahre, M.; **Nottbohm, C.T.**; Küller, A.; Paul, A.; Kautek, W.; Eck, W.; Gölzhäuser, A.; „Electrodeposition of copper and cobalt nanostructures using self-assembled monolayer templates”, *Surf. Sci.*, 2005, 597, 32-41.

Nottbohm, C.T.; Beyer, A.; Gölzhäuser, A.; Patentantrag, DE 10 2007 016 995.9-54.

Nottbohm, C.T., Turchanin, A. Gölzhäuser, A.; „Metallization of organic monolayers: Electroless deposition of Cu onto cross-linked aromatic self-assembled monolayers”, *Z. Phys. Chem.*, 2008, 222, 917-926.

Nottbohm, C.T.; Beyer, A.; Sologubenko, A.S.; Ennen, I.; Hütten, A.; Rösner, H.; Eck, W.; Mayer, J.; Gölzhäuser, A.; „Novel carbon nanomembranes as support for ultrahigh resolution structural analysis of nanoparticles”, *Ultramicroscopy*, 2008, 108, 885-892.

Beyer, A.; Godt, A.; Amin, I.; **Nottbohm, C.T.**; Schmidt, C.; Zhao, J.; Gölzhäuser, A.; „Fully cross-linked and chemically patterned self-assembled monolayers”, *Phys. Chem. Chem. Phys.*, 2008, 10, 7233-7238.

Turchanin, A.; Beyer, A.; **Nottbohm, C.T.**; Zhang, X.; Stosch, R.; Sologubenko, A.; Mayer, J.; Hinze, P.; Weimann, T.; Gölzhäuser, A.; „One nanometer thin carbon nanosheets with tunable conductivity and stiffness”, *Adv. Mater.*, 2009, 21, 1233-1237.

Nottbohm, C.T.; Beyer, A.; Turchanin, A.; Gölzhäuser, A.; „Direct e-beam writing of 1 nm thin graphitic nanoribbons”, *submitted*.

Schnietz, M.; Turchanin, A.; **Nottbohm, C.T.**; Beyer, A.; Solak, H.H.; Hinze, P.; Weimann, T.; Gölzhäuser, A.; „Nanosieve membranes with a thickness of 1 nm”, *Small*, *accepted*.

8 Abbreviations

2D	two-dimensional
μCP	micro contact printing
AFM	atomic force microscopy
BPT	1,1'-biphenyl-4-thiol
CBPS	4'-[(3-Trimethoxysilyl)propoxy]-[1,1'-biphenyl]-4-carbonitril
CPD	critical point drying
DMF	dimethylformamide
DNQ	diazonaphtaquinone
DPN	dip pen nanolithography
DTE	dithioerytritol
EBID	electron beam induced deposition
EBL	electron beam lithography
EFTEM	energy filtered TEM
EUV	extreme ultraviolet
EUV-IL	extreme ultraviolet interference lithography
FRET	Förster resonance energy transfer
FWHM	full width half maximum
HAADF	high angle annular dark field
HEPES	4-(2-hydroxyethyl)-1-piperazineethanesulfonic acid
HF	hydrofluoric acid
HOPG	highly ordered pyrolytic graphite
HR TEM	high resolution TEM
HV	high vacuum
ITO	Indium-tin-oxide
LB-film	Langmuir-Blodgett film
LbL	layer-by-layer assembly
LOFO	lift-off float-on
MEMS	micro electromechanical systems
MOF	metal-organic frameworks
MWNT	multi-walled carbon nanotubes
NA	numerical aperture
NBPT	4'-Nitro-1,1'-biphenyl-4-thiol
NEMS	nanoelectromechanical systems
PALO	polymer assisted lift-off
PDMS	polydimethylsiloxane
PMMA	polymethylmethacrylate
PR	photoresist
SAED	selected area electron diffraction
SAM	self-assembled monolayer
SEM	scanning electron microscopy

SNOM	scanning nearfield optical microscope
STEM	scanning transmission electron microscopy
TEM	transmission electron microscopy
THF	tetrahydrofurane
TMR	tetramethylrhodamine
TOPO	trioctylphosphin oxide
TPP	triphenylphosphine
UHV	ultra high vacuum
UV	ultraviolet
Vis	visible
XPS	x-ray photoelectron spectroscopy

9 List of Figures

Figure 1 Schematic picture of a self-assembled monolayer (SAM)	5
Figure 2 Effect of electron irradiation on the structure of SAMs. Aliphatic SAMs are destroyed by the electron beam (a), whereas aromatic SAMs undergo cross-linking to nanosheets.....	6
Figure 3 Patches of cross-linked SAM (nanosheet) have moved on the substrate after cleavage of the Au-sulfur bond with iodine vapor. b,c) An intact and a broken nanosheet membrane that was prepared by dissolving the thin silicon nitride window substrate. (SEM images from reference [32]).....	7
Figure 4 a) XPS is based on the generation of electrons from core states by irradiation with x-rays. b) Following the photoemission, an outer electron can fill the vacancy and second electron can be emitted (Auger process).....	7
Figure 5 Fundamental characteristic curve for the attenuation lengths of electrons in solids as a function of electron energy (from ref [33]).....	8
Figure 6 Design of a TEM (a) and SEM (b) from ref [36] and [40].	10
Figure 7 Different operation modes of an AFM in terms of their position on a force-distance-curve.....	12
Figure 8 Schematic drawing of interference in a thin film of the thickness d and a refractive index n	14
Figure 9 Optical properties of multilayer stacks. a) Schematic drawing of a multilayer stack consisting of different layers with thicknesses d_i and refractive index n_i . b) Every layer m has both incoming and reflected waves from both sides. c) The layer stack for nanosheet on SiO_2/Si is schematically shown.	15
Figure 10 Comparison between reflection microscopy using an objective lens (a) vs. spectroscopy using an optical fiber (b) vs. a reflection probe with separate illumination and detection fibres (c).....	17
Figure 11 Reflection probe consisting of six illuminating fibers around one detection fiber (Ocean Optics).....	18

Figure 12 The angular distribution of the reflection probe depends on the probe sample distance	20
Figure 13 Schematic drawing of patterning with positive and negative tone photoresists	21
Figure 14 Transfer of a photoresist pattern into the substrate by metal deposition and lift-off, etching and stripping of the resist.	22
Figure 15 Chemistry of Novolak based photoresists	22
Figure 16 Monomer of the SU8 negative tone photoresist.	23
Figure 17 General procedure for the transfer of nanosheets.....	35
Figure 18 XPS spectra of a CBPS sample after irradiation with $\sim 40\text{mC/cm}^2$ (blue) and after spincoating and subsequent removal (red) of a Novolak based photoresist (Shipley S1808).....	36
Figure 19 Schematical drawing of the transfer procedure for silane based nanosheets on $\text{SiO}_2/\text{Si}_3\text{N}_4$ (left) as well as for thiol based nanosheets on Au (right).....	37
Figure 20 First example of a transferred nanosheet on a structured Si-wafer before (a, optical microscopy) and after removal of the photoresist (b-d, SEM).	38
Figure 21 First freestanding membranes prepared by transfer of the nanosheet. (a) shows an optical micrograph of the transferred nanosheet before dissolution of the photoresist spanning over a small window in the silicon substrate (red arrow). In (b) a SEM image is shown of a similar sample after the resist is dissolved in acetone. Due to incomplete rinsing, the membrane appears rather dirty. With optimal process parameters, clean membranes can be obtained with few folds (c).	39
Figure 22 SEM images of a nanosheet deposited onto a conventional TEM grid (Au, 1500mesh). (a) Large area overview: the transferred sheet appears as a grey shade, covering the interior of the grid, as well as the outer, circular rim. (b) Low magnification image: Most openings in the mesh appear grey, revealing the presence of the freely-suspended nanosheet. A few squares appear black, indicating holes not covered by the nanosheet, most likely caused by rupture during transfer. (c) High magnification image of several openings in the Au mesh: The nanosheet covering the openings is visible as a grey film with a few folds that serve as a guide to the eye.	40

Figure 23 Nanosheets on SiO ₂ are visible by an optical microscope due to an interference contrast.	41
Figure 24 Defects in nanosheets are visible by placement on SiO ₂ /Si-substrates (a,b). Preparation of such defective nanosheets as freestanding membranes leads to interesting, though undesired, structures.	42
Figure 25 XP spectra of a NBPT SAM after cross-linking and after spincoating and subsequent removal of photoresist as well as PMMA	43
Figure 26 First example of a NBPT nanosheet after release from the Au substrate and transfer to SiO ₂	44
Figure 27 Optical micrograph of an extremely large (~5 cm ²) cross-linked BPT nanosheet transferred on a 300 nm silicon oxide layer on silicon. Only few defects and very few folds and wrinkles are visible.....	44
Figure 28 Largest freestanding nanosheet to date.....	46
Figure 29 Comparison between samples prepared with manual rinsing and the help of a critical point dryer.....	46
Figure 30 Reaction scheme for the labeling of the amino terminus of an NBPT nanosheet by TMR	50
Figure 31 (a) Optical micrographs of TMR labeled NBPT nanosheet on a SiO ₂ /Si wafer, the nanosheet appears blue shifted with respect to the substrate color. (c) Magnified optical image of a larger fold that is marked in (a) by a blue rectangle. (b) Scanning confocal fluorescence image of the region marked in (c), the fluorescence intensity corresponds to the number of layers in the fold, (d) AFM image of the same area.....	51
Figure 32 Freestanding TMR-labeled nanosheet on a Quantifoil 3/3 TEM grid. The circular openings have a diameter of 3 μm. The nanosheet is easily visible in the fluorescence image (a) and it cannot be identified in the transmission image of the same region in (b)	52
Figure 33 Reaction scheme for the labeling of the thiol group of a released BPT nanosheet with Atto647N.....	52

- Figure 34 Fluorescence (a-c) and corresponding optical microscopy images (d-f) of Atto647N labeled BPT nanosheet on SiO₂/Si53
- Figure 35 Freestanding BPT nanosheet labeled with Atto647N on a Quantifoil 3/3 TEM grid (a), the corresponding transmission image is shown in (c). Quantifoil grids that are not covered by that nanosheet do not show fluorescence (b, d).....54
- Figure 36 Absorption and Emission spectra of TMR and Atto647N. The overlapping region of the donor emission and acceptor absorption peaks is colored in orange.55
- Figure 37 Comparison of fluorescence images of differently labeled nanosheets obtained at wavelength >547 nm by a longpass filter and emission at 532 nm and 633 nm, respectively.57
- Figure 38 Comparison of the fluorescence intensity of a TMR and an Atto647N labeled nanosheet at identical illumination intensity.58
- Figure 39 Schematic representation of the proximity printing process. An aromatic SAM is exposed to electrons through a shadow mask (a) and cross-linked in the exposed regions (b).60
- Figure 40 Transferred patches of cross-linked SAM generated by proximity printing. a) an early example of a 400mesh line pattern. b) a Quantifoil MultiA on a 400mesh support grid. The individual patterns are not visible at this magnification. The pattern is transferred with high uniformity.61
- Figure 41 Schematic representation of the structuring of BPT by EUV-IL. Two coherent beams form a linear fringe pattern with a sinusoidal intensity distribution (a). A BPT SAM (b) is EUV beam and subsequently cross-linked in the maxima of the beam (c,d)62
- Figure 42 Four beam interference mask layout (a). Two diffraction gratings (purple and pink area) are aligned perpendicular to each other. Constructive interference forms patterns in the overlapped dark blue area. Cross-linked pattern transferred to an oxidized silicon wafer (b) and a Quantifoil TEM grid (c).63
- Figure 43 Transmission electron microscope (TEM) characterization of nanosieve membranes. Dark field mode images of ~1 nm thin nanosieves with (a) 138±17 nm holes (interference grating periodicities of 225 nm×200 nm; irradiation dose of 70 J/cm²), (b) 100±15 nm holes (interference grating periodicities of 225 nm×200 nm; irradiation dose

of 120 J/cm^2) and (c) $31 \pm 6 \text{ nm}$ holes (interference grating periodicities of $100 \text{ nm} \times 90 \text{ nm}$; irradiation dose 50 J/cm^2).	64
Figure 44 Nanosieve membrane spanned over $1 \mu\text{m}$ holes in a Quantifoil grid. Under the electron beam the holes in the nanosieve are widened with each scan (a-f). At lower magnification the difference in the whole size can be compared directly. (g)	64
Figure 45 Nanosieve membranes after coating with a thin layer of gold. The nanosieve is spanned over the openings of a Quantifoil TEM grid (a) and over spaces where the Quantifoil film is broken (b,c)	65
Figure 46 Schematical representation of the process to pattern nanosheets by plasma etching. First photoresist is applied and structured by standard photolithography. The photoresist can then serve as an etch mask during plasma etching and be dissolved in the last step.....	66
Figure 47 AFM of O_2 -plasma patterned CBPS. After removal of the photoresist, some residue from the plasma process remains on the sample (a). By sonication in resist stripper, this residue can be removed to yield clean nanosheet ribbons (b).....	67
Figure 48 Plasma etched line patterns can serve as an etch mask for HF vapor. The line patterns are barely visible by the naked eye (a), after exposure to HF vapor for $\approx 5 \text{ s}$ they can easily be seen (b). At higher magnification it is visible that etching occurs mainly in the areas that are not covered by the nanosheet (c).....	68
Figure 49 $10 \mu\text{m}$ line patterns after transfer to SiO_2/Si (a,b). The integrity of the patterns is preserved during the transfer procedure. Arbitrary structures of nanosheet can be fabricated by plasma etching (c,d).....	69
Figure 50 Schematic drawing of selective etching of SiO_2 or Si_3N_4 by a CF_4 plasma using nanosheet as an etch-mask	70
Figure 51 Nanosheet lines act as an etch-resist for selective etching of SiO_2 by CF_4 -Plasma. After etching for 30 s a trench of $\approx 4.9 \text{ nm}$ is observed (a), after 60 s the depth has roughly doubled to 9.7 nm (b).	71
Figure 52 A SAM of BPT is exposed to UV/ozone through a mask (a). The damaged/oxidized SAM in the exposed regions is rinsed away (b). The remaining SAM is irradiated with electrons (c) and subsequently cross-linked (d)	72

- Figure 53 a) Contact angle of a BPT SAM as a function of UV/ozone exposure time at a O₂ flux of 1 l/min. The red line indicates the contact angle of a freshly cleaned gold substrate. b) top: XPS spectra of the C1s, S2p and O1s regions of a pristine BPT SAM. Middle: XPS spectra of the SAM after UV/ozone oxidation. Bottom: spectra of a sample after rinsing with water and ethanol to remove the SAM..... 74
- Figure 54 a) SEM image of a BPT SAM after UV/ozone patterning through a Quantifoil TEM grid with 3 μm circular holes b) SEM after cross-linking of (a) with an electron dose of 50 mC/cm² c) LFM of a UV/ozone patterned (Quantifoil with 1 μm holes) BPT-SAM. d) LFM of patterned SAM from (c) after cross-linking. 75
- Figure 55 a, c) optical microscopy (enhanced contrast) of patches of holey nanosheet transferred to a Si wafer with 300 nm SiO₂. On these substrates the nanosheet is visible through an interference contrast. b) AFM image of the patterned, transferred nanosheet. c) AFM height profile through the line indicated in (b) 76
- Figure 56 a) Optical micrograph of a nanosheet patterned with a PDMS stamp during UV/ozone exposure. b) SEM of a holey nanosheet spanned over the hexagonal opening of a 300 mesh TEM grid. The nanosheet was patterned using a PDMS stamp during UV/ozone exposure..... 78
- Figure 57 Summary of different methods to obtain laterally structured nanosheets 80
- Figure 58 Nanosheet line patterns. a) Single layer of 10 μm lines. b) Double layer of lines, at 90° angle c) Three layers of lines, transferred at a 60° angle..... 82
- Figure 59 Multilayers (1-5 Layers) of BPT on a SiO₂/Si wafer 83
- Figure 60 X-ray photoelectron spectra of the C 1s, S 2p, and I 3d region of a BPT monolayer transferred to a 300 nm SiO₂ wafer. After transfer PMMA contamination is visible in the C 1s region (green fit), as well as residual iodine in the I 3d region. After annealing to 623 K both C and I contamination are removed..... 84
- Figure 61 Attenuation of the Si2p signal as a function of layers. The thickness per layer can be deduced from the linear fit. 85
- Figure 62 UV/Vis for multilayers of nanosheet on SiO₂/Si at room temperature and after annealing to 623 K to remove contamination by PMMA. 87

Figure 63 UV/Vis spectra of the SiO ₂ /Si substrate (black) together with simulations for different oxide thicknesses (grey). For a thickness of 278.5 nm the simulated spectra best describes the measurement (red).	88
Figure 64 Simulated reflection spectra for nanosheets of different layer thicknesses.....	89
Figure 65 Comparison of the simulated reflection spectra of nanosheet with the experiment. The arbitrarily chosen imaginary part of the refractive index for the nanosheet is plotted in red (right axis). Absorption maxima of possible components of the nanosheet (shown in (b)) are shown as vertical red lines.....	90
Figure 66 Contrast of 1 Layer of nanosheet on SiO ₂ /Si as a function of the wavelength and oxide thickness.....	91
Figure 67 Contrast of multiple layers of nanosheet on SiO ₂ /Si as a function of wavelength and oxide thickness (a) and a function of wavelength and the number of layers (b).....	92
Figure 68 Contrast of nanosheet on Au (with different Au thicknesses) and Si substrates as a function of wavelength and number of layers.	93
Figure 69 Split RGB channels of a folded BPT nanosheet on 30 nm Au. The contrast is highest in the blue channel, confirming the results of the simulation.....	94
Figure 70 Contrast of nanosheet observed through the resist layer. The nanosheet is nearly invisible through the photoresist layer (a), but contrast enhancement can already show the defects (b) that are otherwise only visible after dissolution of the resist layer (c).	95
Figure 71 Optical microscopy images of freestanding nanosheet multilayers in reflection (a) and transmission (b) mode. The Intensity profiles show a linear increase/decrease of the signal with each additional layer.	96
Figure 72 Evaluation of the reflection and transmission of freestanding nanosheet multilayers.	97
Figure 73 Schematic drawing of a nanoparticle in the electron beam of a TEM. In (a) the support film is thicker than the particle, whereas in (b) the support film is very thin.	99
Figure 74 (a,b) SEM images of a nanosheet that has been spanned over circular 3 μm holes in a 15 nm thick carbon film with different contrast settings. (c-e) TEM images of	

Co nanoparticles deposited on nanosheets used as TEM support: (c) Low magnification image of Co particles (~6 nm diameter) deposited near the edge of a hole in the carbon film. Co particles are found on the conventional support (left) and on the nanosheet (right). The contrast is much higher for the particles on the nanosheet. (d,e) Higher magnification image of Co particles deposited on a 15 nm carbon film (d) and on a nanosheet (e) under identical imaging conditions at the Scherzer defocus. The contrast and sharpness of Co particles on the nanosheet are much higher and a distinct layer surrounding each particle can clearly be seen.....101

Figure 75 Multi-walled carbon nanotubes (MWNTs) decorated with Co nanoparticles imaged in TEM. The image in (a) was taken on the composite of Quantifoil and nanosheet, whereas (b-d) were taken on the nanosheet only. It is clearly visible that the contrast is greatly enhanced in (b-d). In (d) even the individual walls of the MWNTs can be resolved.....102

Figure 76 Energy filtered TEM carbon maps of MWNTs with Co nanoparticles on the nanosheet-Quantifoil composite (a) and on the nanosheet (b). The contrast on the nanosheet is strongly enhanced.103

Figure 77 HRTEM micrographs of Au nano-clusters taken from the same specimen in an aberration corrected TEM instrument (FEI Titan 80-300 TEM) under identical imaging conditions ($C_s = -14 \mu\text{m}$, $Z = 40 \text{ nm}$); (a) on the composite system (Quantifoil plus nanosheet) of about 15 nm thickness; (c) on the freestanding 1.6 nm thick nanosheet. The contrast from small clusters is largely enhanced in (c) when compared with (a). Smaller clusters (arrows in (c) point to ~1.4 nm clusters) and much finer microstructural features of the clusters can be resolved on the freestanding nanosheet. In b) and d) integrated line profiles (integration width 20 pixels) are shown for two gold clusters (marked in a and in c). For the profiles, clusters of similar size and crystal orientation with respect to the beam were chosen.105

Figure 78 : (a-d) STEM micrographs taken under HAADF imaging conditions from the composite Quantifoil-nanosheet system with Au nanoclusters. (a) The imaging contrast improves dramatically by taking images on the freestanding nanosheet (right) in comparison to the thicker carbon foil (left). (b) Small holes in the nanosheet are useful

for adjusting the focus. In (b-d) small objects with the size of individual Au atoms (indicated by arrows) become visible.	107
Figure 79 a) Schematic drawing of the process for patterning gold onto nanosheets on Si ₃ N ₄ windows. b) Optical micrograph of a freestanding nanosheet with Au dots.	110
Figure 80 a) Nanosheet with Au dots after transfer to a SiO ₂ /Si substrate. Some of the Au dots are washed away during dissolution of the photoresist. b) Nanosheet with Au dots transferred to a 300 mesh TEM grid.	110
Figure 81 a) Schematic drawing of patterning metal onto freestanding nanosheets by using a shadow mask during evaporation. b) Successfully metallized freestanding nanosheet on a 300 mesh TEM grid fabricated using a shadow mask.	111
Figure 82 a) Nanosheet on a Quantifoil TEM grid with 1 μm circular openings. Two ruptured nanosheets appear darker (arrows). b) A “smiley” was patterned onto the nanosheet by contamination writing.	112
Figure 83 Fabrication scheme and TEM micrograph of a suspended, graphitized carbon nanosheets. (a) A ~1 nm thick self-assembled monolayer (SAM) of biphenyl molecules is irradiated by electrons. This results in a mechanically stable cross-linked SAM (nanosheet) that can be removed from the substrate and transferred onto other solid surfaces. When transferred onto transmission electron microscopy (TEM) grids, nanosheets suspend over holes. Upon heating to T>1000K in vacuum (pyrolysis), nanosheets transform into a graphitic phase. (b) Transmission electron micrograph of a nanosheet transferred onto a TEM grid with 11x11 μm ² holes after pyrolysis at 1100K. The hole is uniformly covered with an intact nanosheet. Some folds within the sheet are visible. (c) AFM micrograph of the nanosheet edge on a solid support, showing its thickness of ~1 nm.	115
Figure 84 TEM image of Mo and W precipitates that form in the nanosheet membranes upon heating >1500 K (scale bar 5 nm)	116
Figure 85 XPS evaluation of the annealing of nanosheets. a) C1s, S2p and O1s regions of a BPT SAM before and after cross-linking, and after subsequent annealing to ≈970 K. b) C1s, S2p, I3d and F1s regions of a cross-linked BPT SAM after transfer to SiO ₂ /Si. Some	

contamination from the transfer is still present at the surface, which can easily be removed by mild annealing to ≈ 600 K.117

Figure 86 Scanning Auger spectra of the nanosheet spanning over a hole in the Quantifoil grid. For comparison a spectra of an uncovered hole and of HOPG is included. An SEM image of the sample is shown in the inset (scale bar $1 \mu\text{m}$).....118

Figure 87 (a) SEM image of the tungsten STM tip establishing an electrical and mechanical contact in the centre of the annealed biphenyl nanosheet suspended on the gold grid with $\sim 11 \times 11 \mu\text{m}^2$ squared openings, as employed for two-point resistivity measurements. A folded nanosheet (shown in false color) was chosen for better visualisation. (b) Schematic drawing of the setup. (c) and (d) Representative room temperature current vs. voltage data for two annealing temperatures in the two-point set-up of resistivity measurements in UHV. Each line corresponds to a measurement in a different window of the grid.119

Figure 88 Room temperature current vs. voltage data (four-point set-up) of the nanosheets supported on a silicon oxide surface. The nanosheets were annealed on gold and then transferred to silicon oxide substrates. Each line corresponds to a measurement at a new position on the nanosheet.....120

Figure 89 Summary of the room temperature sheet resistivity as a function of annealing temperature. All samples were annealed for 30 min at the respective temperatures...121

Figure 90 Raman spectra of non-annealed biphenyl nanosheet and nanosheets annealed in vacuum on gold, transferred to silicon oxide substrates. The measurements for different annealing temperatures were performed under ambient conditions. (B), Changes in the position of the G-peak and the intensity ratio of $I(\text{D})/I(\text{G})$ as a function of the annealing temperature.122

Figure 91 High-resolution phase contrast TEM images and SAED patterns from larger areas of non-annealed (D) and annealed (F) (~ 1300 K) biphenyl nanosheets. Two typical locations of line profiles (1) and (2), taken for evaluation of the periodicity of the graphitic fringes are depicted in (E). In addition, an enlargement of the diffraction (F) is given in SOM. The rings in (F) can be indexed as belonging to the (0-110) and (1-210) lattice plane spacings of highly in-plane oriented nanocrystalline graphitic sheets.....123

Figure 92 XPS analysis of the C1s signal of multilayers of nanosheet on SiO ₂ at different annealing temperatures. For comparison the spectra of 1, 3 and 5 layers are shown, as well as spectra (not to scale) of HOPG. The Intensity is also plotted as a function of the annealing temperature.	126
Figure 93 XPS analysis of the S2p signal as a function of annealing temperature. a) S2p region for 1 to 5 layers of nanosheet on SiO ₂ . b, c) Intensity of the sulfur signals as a function of annealing temperature. Both signals decrease. The oxidized sulfur disappears above ≈700 K. d, e) While the thiol/disulfide signal increases with additional layers, the oxidized sulfur signal is constant, indicating oxidation in the topmost layer.	127
Figure 94 a) Attenuation of the Si2p XP signal at 1173 K as a function of layers. b) Logarithmic plot of the Si2p intensity as a function of layers. c) Calculated thickness per layer from the fit in b) and additionally from the O1s attenuation.	128
Figure 95 Raman analysis of multilayers that were annealed to 1173 K. a) Raman signals for different number of layers. The red curve shows a monolayer sample on gold annealed to the same temperature for comparison. b) Ratio between the D and G peak intensities (black) and position of the D peak (blue). c) The intensity of the G increases linearly with the number of layers (black). Position of the G peak (blue).....	129
Figure 96 Comparison of the UV-Vis reflectance spectra of nanosheet multilayers at room temperature vs. 1173 annealing temperature.	131
Figure 97 Wavelength dependence of the real and imaginary parts of the refractive index of graphite (green=polycrystalline, dark and light blue=crystalline along and perpendicular to the c-axis) in comparison with that of the nanosheet (red).....	131
Figure 98 Comparison of the multilayer UV-Vis reflectance spectra after annealing to 1173 K with simulated spectra for polycrystalline graphite and graphene	132
Figure 99 Comparison of UV-Vis reflectance data and simulation for polycrystalline graphite and graphene. a,b) Shift of the wavelength of the minima at 340 nm and 555 nm as a function of thickness. c, d) Intensity of the reflectance minima as a function of thickness.	133
Figure 100 Simulation reflectance UV-Vis spectra of the transition of the nanosheetsheet to a graphitic phase.....	134

Figure 101 Contrast of nanosheets polycrystalline graphite on SiO₂/Si substrates. a) Contrast of one layer as a function of wavelength and oxide thickness. b) Same as a) for 30 layers. c) Contrast of nanosheet and graphite as a function of wavelength and the number of layers for a constant oxide thickness of 278.5 nm.....136

Figure 102 Conductivity of nanosheet multilayers annealed on SiO₂/Si. a) Sheet resistivity as a function of annealing temperature. b) Representative current-voltage curves for 2 to 5 layers at an annealing temperature of 973K. c) Sheet resistivity as a function of the number of layers. d) Normalized conductivity as a function of the number of layers....137

Figure 103 Comparison of the sheet resistivity obtained for monolayers of nanosheet annealed on Au and multilayers annealed on SiO₂/Si.138

Figure 104 Schematic drawing of the relation between particle distance δ and the number of layers in a 2-D square lattice. Each color represents the particles from a different layer. a) Shows a monolayer with the particle distance δ . In b) a second layer was added, resulting in $\sqrt{2}\delta$. For four layers (c) the particle distance is half of that in the monolayer.140

10 Acknowledgements

First I would like to thank my advisor Prof. Dr. Armin Gölzhäuser for letting me work in his group and giving me the opportunity to also spend time to do research at the University of Illinois at Urbana Champaign. He was always supportive of my ideas and helped with his constructive criticism and his view of the “big picture”.

Dr. André Beyer and Dr. Andrey Turchanin were always willing to discuss problems and experiments extensively. Of my coworkers I would especially like to thank Dirk Weber, Mark Schnietz, Matthias Büenfeld and Heiko Muzik for lots of (more or less) valuable discussions and Nils Mellech for sputter coating samples with gold. A big thank you also goes to the rest of the group, it was always nice to work with you.

Dr. Berthold Völkel always had helpful ideas and the necessary parts for improvising experimental setups and fix problems quickly. If Berthold’s vast supply was not enough, Dr. Udo Werner most likely was able to help out. I also have to thank the team in the mechanical workshop, it would have been difficult without their expertise at times.

I would also like to thank my undergraduate students: Ran Sopher for helping me with labeling nanosheets, Marius for his efforts to prepare flat gold substrates and his help with building the contact angle device and Sebastian for his experiments with UV/ozone.

Especially, I want to thank Frau Lorentzen for her help with all the administrative details and her warm-hearted words.

A lot of experiments were only possible with the help of people from other groups within the physics department. Inga Ennen and Andreas Hütten helped using the nanosheets as supports for their Co nanoparticles. Robert Kasper, Mike Heilemann, and Markus Sauer introduced me to fluorescence microscopy and helped with obtaining images. Jan Regtmeier helped with initial UV exposures and always let me use the oxygen plasma with very short notice. From the chemistry department I would like to thank Christian Schmidt and Prof. Dr. Godt for letting me borrow the Kugelrohr and sublimation apparatus. For letting me use the UV/Vis spectrometer, I would like to thank Michael Schlegler and Uwe Güth from the group of Prof. Dr. Heberle. From the biology department, I am indebted to Renate Feist, who let me use the critical point dryer.

I also want to thank the collaborators from Aachen (Dr. Alla Sologubenko and Prof. Dr. Joachim Mayer) and Braunschweig (Peter Hinze, Dr. Thomas Weimann and Dr. Rainer Stosch) for their valuable contributions. From Heidelberg I would like to thank Dr. Alexander Küller for lots of helpful discussions and the supply of several of his precious chemicals, as well as Dr. Wolfgang Geyer for introducing me to the secrets of surface science.

I would like to thank Profs. John A. Rogers und Ralph G. Nuzzo for letting me work in their groups in Illinois, giving me the opportunity to learn a lot about soft lithography and an unconventional way of thinking about materials. From their groups I especially want to thank Sakulsuk Unarunotai, Xiaoyu Zhang, and Zhengtao Zhu for their help. I am also indebted to Rick Haasch for letting me put an electron gun in his precious XPS preparation chamber.

Finally I want to thank my parents who were always encouraging me and supporting me in my decisions and most importantly my wife Amanda for her patience and support through all these years.